UC Berkeley
UC Berkeley Electronic Theses and Dissertations

Title

Particle Transport in non-Markovian Stochastic Media

Permalink

https://escholarship.org/uc/item/63k8705h

ISBN

9798173787170

Author

Lioce, Dominic Andrew

Publication Date

2026-08-10

Peer reviewed|Thesis/dissertation

eScholarship.org Powered by the California Digital Library
University of California

Particle Transport in non-Markovian Stochastic Media

by

Dominic Andrew Lioce

A dissertation submitted in partial satisfaction of the

requirements for the degree of

Doctor of Philosophy

in

Nuclear Engineering

in the

Graduate Division

of the

University of California, Berkeley

Committee in charge:

Professor Jasmina Vujic, Co-Chair
Professor Anil Prinja, Co-Chair
Professor Daniel Siefman
Professor Panayiotis Papadopoulos

Summer 2026

Particle Transport in non-Markovian Stochastic Media

Copyright 2026
by
Dominic Andrew Lioce

Abstract

Particle Transport in non-Markovian Stochastic Media

by

Dominic Andrew Lioce

Doctor of Philosophy in Nuclear Engineering

University of California, Berkeley

Professor Jasmina Vujic, Co-Chair

Professor Anil Prinja, Co-Chair

Particle transport in stochastic media is important in the simulation of many applications, including inertial confinement fusion, pebble bed nuclear reactors, atmospheric science, and supernovae explosions. Classical stochastic media transport models often assume Markovian mixing statistics, in which material chord lengths are exponentially distributed and the current material label is sufficient to determine the probability of encountering the next material interface. Many physically relevant random media, however, contain finite inclusions, grains, droplets, or other structured features whose chord length distributions are not necessarily exponential. In these non-Markovian media, the probability of crossing a material interface depends on the distance already traveled through the current material, so accurate transport models must retain additional geometric memory.

This dissertation develops age-based particle transport methods for binary stochastic media described by an alternating renewal statistical process. The central idea is to augment the joint stochastic state space with an age variable, defined as the distance traveled since the previous material interface. For transport in purely absorbing media, this augmented state yields a Markovian description in the expanded stochastic state space, allowing for the derivation of a generalized master equation for transport in renewal media. A stochastic simulation algorithm based on this formulation is shown to reproduce benchmark leakage quantities, scalar flux moments, and transmission distributions for several non-exponential chord length distributions. These results demonstrate that replacing renewal statistics with a Markovian approximation can produce significant errors even when mean chord lengths and volume fractions are preserved.

The age-based framework is then extended to include particle scattering in 1D planar geometry. Scattering introduces an additional transport memory effect because particles may reverse direction and move back toward previously sampled material. Several Monte Carlo

algorithms are developed to approximate the age update after scattering, including the Backscatter-Resample and Age-Decreasing methods, and these methods are compared with the heuristic renewal statistics extensions of the Markovian stochastic media algorithms Chord Length Sampling (CLS) and Local Realization Preserving (LRP). The results show that methods preserving more local geometric memory generally improve accuracy relative to the benchmark in leakage values and scalar flux, with the Age-Decreasing method often producing accuracy comparable to LRP while retaining a simpler memory structure.

The methods are also extended to 3D stochastic media and tested against explicit spherical inclusion benchmark calculations. In 3D, material interfaces are sampled along full particle trajectories, and the treatment of local geometric memory after scattering becomes approximate because scalar interface memory cannot fully describe the surrounding 3D geometry. Deterministic and probabilistic memory-update treatments are compared, and the probabilistic rule is adopted for consistency with previous 3D LRP implementations. The 3D results show the same broad method ordering observed in 1D, with the Age-Decreasing method and LRP generally improving accuracy relative to the Backscatter-Resample method and FLRP. The spherical inclusion benchmarks also show that a randomly distributed radius can influence scalar flux and leakage, emphasizing the importance of accurate characterization of real-world stochastic media transport applications.

Overall, this work provides an extension of stochastic media transport that preserves prescribed chord length distributions for renewal statistical media more directly than previous heuristic adaptations of Markovian models. The resulting age-based methods provide a computationally efficient framework for modeling ensemble-averaged transport in non-Markovian media.

To my parents

Without your unwavering support and encouragement, none of this would have been possible. Thanks for letting me be me, Mom and Pap.

Contents

Contents **ii**

List of Figures **iv**

List of Tables **ix**

1 Introduction **1**

2 General Considerations of Transport in Immiscible Random Media **5**
2.1 Introduction 5
2.2 Transport on a Fixed Realization 8
2.3 The Benchmark Method: Realization Sampling and Ensemble Averaging . . 10
2.4 Summary 11

3 Statistics of Markovian and Non-Markovian Random Media **13**
3.1 Introduction 13
3.2 Renewal Processes and Alternating Renewal Media 14
3.3 Markov Processes and Markovian Media 22
3.4 Summary 29

4 Transport in Markovian Random Media **31**
4.1 Introduction 31
4.2 The Atomic Mix Approximation 31
4.3 The Levermore-Pomraning Closure 33
4.4 Chord Length Sampling: The Monte Carlo Analog to Levermore-Pomraning 37
4.5 Adapting CLS and LRP to Renewal Statistics 43
4.6 Previous Heuristic Adaptations to Renewal Media 44
4.7 Summary 46

5 Generalized Master Equation Approach to Transport in Renewal Media **47**
5.1 Introduction 47
5.2 Definitions for Transport in Renewal Media 48
5.3 Generalized Master Equation 50

5.4 Numerical Implementation 63
5.5 Conclusions 75

6 Extension of Age-Based Transport in Renewal Statistical Media to Include Particle Scatter 78
6.1 Introduction 78
6.2 Theory and Methods 79
6.3 Results 89
6.4 Summary 124

7 Extension of Age-Based Transport in Renewal Statistical Media to 3D 125
7.1 Introduction 125
7.2 3D Benchmark Generation Procedure 126
7.3 Adapting the Methods to 3D Media 128
7.4 Results 130
7.5 Summary 168

8 Conclusions and Future Work 169
8.1 Conclusions 169
8.2 Future Work 171

Bibliography 174

List of Figures

2.1 Example of a stochastic geometry arising from a Rayleigh-Taylor turbulent instability with surface tension leading to immiscibility [20]. 6
2.2 Example of a Markovian realization generally used as a benchmark for transport in stochastic media [21]. 6
2.3 Example of a stochastic geometry arising from the inside of a pebble in a pebble bed reactor. The TRISO fuel pellets are randomly dispersed throughout the carbon pebble [22]. 7
2.4 Example of a stochastic geometry arising from a thermal spray microstructure. Voids and layers of molten, oxidized, or unmolten material are located randomly throughout [23]. 7
2.5 Example of a stochastic geometry used for studying thermal radiation flow in stochastic media for the X-ray Flow Over Lumps (XFOL) project at Los Alamos National Laboratory [1]. 8

3.1 Chord length probability density functions/distributions $f_i(s)$ considered in this dissertation, from Eqs. (3.16) through (3.19). 18
3.2 Hazard functions $h_i(s)$ considered in this dissertation, from Eqs. (3.16) through (3.19). 18

4.1 Example of a particle history for CLS algorithm. 39
4.2 Example of a particle history for LRP algorithm. 42

5.1 Convergence of cases 1 and 3 as a function of step size Δx for ramp-ramp mixing. 67
5.2 Sampled equilibrium age distribution from model compared with analytic solution for ramp distribution. 69
5.3 Comparison of interior flux quantities for SSA model vs. analytic benchmark for case 3 with exponential-exponential (Markov) mixing. 70
5.4 Comparison of interior flux quantities for SSA model vs. analytic benchmark for case 3 with ramp-ramp mixing and a boundary source of particles at $x = 0$. . . . 71
5.5 Comparison of interior flux quantities for SSA model vs. analytic benchmark for case 3 with exponential-ramp mixing and a boundary source of particles at $x = 0$. 71
5.6 Comparison of interior flux quantities for SSA model vs. analytic benchmark for case 3 with exponential-exponential radii mixing and a boundary source of particles at $x = 0$. 72

5.7 Comparison of interior flux quantities for SSA model vs. analytic benchmark for case 3 with exponential-uniform radii mixing and a boundary source of particles at $x = 0$. 72
5.8 Comparison of interior flux quantities for SSA model vs. analytic benchmark for case 3 with ramp-ramp mixing and a random interior source of particles with $q_0 = 0.1,\ q_1 = 1.0$. 73
5.9 Comparison of interior flux quantities for SSA model vs. analytic benchmark for case 3 with ramp-ramp mixing and a random interior source of particles with $q_0 = 1.0,\ q_1 = 0.1$. 73
5.10 Distribution of transmission values for case 2 with ramp-ramp mixing and incident boundary flux. 74
5.11 Material dependent transmittance PDFs with incident boundary flux. 75
5.12 Relative difference between benchmark interior fluxes for Markov (exponential-exponential) and exponential-ramp media. 76
5.13 Relative difference between benchmark interior fluxes for spherical inclusion geometries with constant radii (exponential-ramp) and spherical inclusion geometries with randomly distributed radii (exponential-uniform radii and exponential-exponential radii) for case 1. 77

6.1 Scalar flux for the GME method and the benchmark in Case 3c with Ramp-Ramp mixing, considering particles moving only in the forward direction. 83
6.2 Example of a particle history for the Backscatter-Resample method. 85
6.3 Example of a particle history for the Age-Decreasing method. 88
6.4 Relative error of leakage quantities for Suite I, Exponential-Exponential distributions. 91
6.5 Relative error of leakage quantities for Suite I, Ramp-Ramp distributions. 92
6.6 Relative error of leakage quantities for Suite I, Exponential-Ramp distributions. 93
6.7 Relative error of leakage quantities for Suite I, Exponential-Uniform-Radii distributions. 94
6.8 Relative error of leakage quantities for Suite I, Exponential-Exponential-Radii distributions. 95
6.9 Scalar flux distributions for Case 1a (Suite I) comparing five material mixing statistics: Exponential-Exponential, Ramp-Ramp, Exponential-Ramp, Exponential-Uniform-Radii, and Exponential-Exponential-Radii. 101
6.10 Scalar flux distributions for Case 2b (Suite I) comparing five material mixing statistics: Exponential-Exponential, Ramp-Ramp, Exponential-Ramp, Exponential-Uniform-Radii, and Exponential-Exponential-Radii. 102
6.11 Scalar flux distributions for Case 3c (Suite I) comparing five material mixing statistics: Exponential-Exponential, Ramp-Ramp, Exponential-Ramp, Exponential-Uniform-Radii, and Exponential-Exponential-Radii. 103

6.12 Relative error of the scalar flux for Case 1a (Suite I), comparing five material mixing statistics: Exponential-Exponential, Ramp-Ramp, Exponential-Ramp, Exponential-Uniform-Radii, and Exponential-Exponential-Radii. All methods are shown relative to the benchmark solution. 104
6.13 Relative error of the scalar flux for Case 2b (Suite I), comparing five material mixing statistics: Exponential-Exponential, Ramp-Ramp, Exponential-Ramp, Exponential-Uniform-Radii, and Exponential-Exponential-Radii. All methods are shown relative to the benchmark solution. 105
6.14 Relative error of the scalar flux for Case 3c (Suite I), comparing five material mixing statistics: Exponential-Exponential, Ramp-Ramp, Exponential-Ramp, Exponential-Uniform-Radii, and Exponential-Exponential-Radii. All methods are shown relative to the benchmark solution. 106
6.15 Relative error of transmission (T) for Suite II, Exponential-Exponential distributions. 108
6.16 Relative error of transmission (T) for Suite II, Ramp-Ramp distributions. 109
6.17 Relative error of transmission (T) for Suite II, Exponential-Ramp distributions. 110
6.18 Relative error of transmission (T) for Suite II, Exponential-Uniform-Radii distributions. 111
6.19 Relative error of transmission (T) for Suite II, Exponential-Exponential-Radii distributions. 112
6.20 Scalar flux distributions for Case 1a (Suite II) comparing five material mixing statistics: Exponential-Exponential, Ramp-Ramp, Exponential-Ramp, Exponential-Uniform-Radii, and Exponential-Exponential-Radii. 113
6.21 Scalar flux distributions for Case 2b (Suite II) comparing five material mixing statistics: Exponential-Exponential, Ramp-Ramp, Exponential-Ramp, Exponential-Uniform-Radii, and Exponential-Exponential-Radii. 114
6.22 Scalar flux distributions for Case 3c (Suite II) comparing five material mixing statistics: Exponential-Exponential, Ramp-Ramp, Exponential-Ramp, Exponential-Uniform-Radii, and Exponential-Exponential-Radii. 115
6.23 Relative error of the scalar flux for Case 1a (Suite II), comparing five material mixing statistics: Exponential-Exponential, Ramp-Ramp, Exponential-Ramp, Exponential-Uniform-Radii, and Exponential-Exponential-Radii. All methods are shown relative to the benchmark solution. 116
6.24 Relative error of the scalar flux for Case 2b (Suite II), comparing five material mixing statistics: Exponential-Exponential, Ramp-Ramp, Exponential-Ramp, Exponential-Uniform-Radii, and Exponential-Exponential-Radii. All methods are shown relative to the benchmark solution. 117
6.25 Relative error of the scalar flux for Case 3c (Suite II), comparing five material mixing statistics: Exponential-Exponential, Ramp-Ramp, Exponential-Ramp, Exponential-Uniform-Radii, and Exponential-Exponential-Radii. All methods are shown relative to the benchmark solution. 118

6.26 Pointwise relative scalar-flux difference from Exponential-Ramp mixing for Case 1a, Suite I. . . . 119
6.27 Pointwise relative scalar-flux difference from Exponential-Ramp mixing for Case 2b, Suite I. . . . 120
6.28 Pointwise relative scalar-flux difference from Exponential-Ramp mixing for Case 3c, Suite I. . . . 120
6.29 Pointwise relative scalar-flux difference from Exponential-Ramp mixing for Case 1a, Suite II. . . . 121
6.30 Pointwise relative scalar-flux difference from Exponential-Ramp mixing for Case 2b, Suite II. . . . 121
6.31 Pointwise relative scalar-flux difference from Exponential-Ramp mixing for Case 3c, Suite II. . . . 122
6.32 Maximum relative difference in scalar flux as a function of scattering fraction for Exponential Radius Distribution and Constant Radius. . . . 123

7.1 2D representations of various spherical inclusion geometries used for 3D benchmarks. . . . 127
7.2 Scalar flux distributions for Case 1a with sphere volume fraction $p_1 = 0.10$, comparing constant, exponential, and uniform spherical inclusion radius distributions. 144
7.3 Scalar flux distributions for Case 1a with sphere volume fraction $p_1 = 0.20$, comparing constant, exponential, and uniform spherical inclusion radius distributions. 145
7.4 Scalar flux distributions for Case 1a with sphere volume fraction $p_1 = 0.30$, comparing constant, exponential, and uniform spherical inclusion radius distributions. 146
7.5 Scalar flux distributions for Case 2b with sphere volume fraction $p_1 = 0.10$, comparing constant, exponential, and uniform spherical inclusion radius distributions. 147
7.6 Scalar flux distributions for Case 2b with sphere volume fraction $p_1 = 0.20$, comparing constant, exponential, and uniform spherical inclusion radius distributions. 148
7.7 Scalar flux distributions for Case 2b with sphere volume fraction $p_1 = 0.30$, comparing constant, exponential, and uniform spherical inclusion radius distributions. 149
7.8 Scalar flux distributions for Case 3c with sphere volume fraction $p_1 = 0.10$, comparing constant, exponential, and uniform spherical inclusion radius distributions. 150
7.9 Scalar flux distributions for Case 3c with sphere volume fraction $p_1 = 0.20$, comparing constant, exponential, and uniform spherical inclusion radius distributions. 151
7.10 Scalar flux distributions for Case 3c with sphere volume fraction $p_1 = 0.30$, comparing exponential and uniform spherical inclusion radius distributions. Constant radius not included, see Section 7.2. . . . 152
7.11 Relative scalar flux error for Case 1a with sphere volume fraction $p_1 = 0.10$, comparing constant, exponential, and uniform spherical inclusion radius distributions. 153
7.12 Relative scalar flux error for Case 1a with sphere volume fraction $p_1 = 0.20$, comparing constant, exponential, and uniform spherical inclusion radius distributions. 154
7.13 Relative scalar flux error for Case 1a with sphere volume fraction $p_1 = 0.30$, comparing constant, exponential, and uniform spherical inclusion radius distributions. 155

7.14 Relative scalar flux error for Case 2b with sphere volume fraction $p_1 = 0.10$, comparing constant, exponential, and uniform spherical inclusion radius distributions. 156
7.15 Relative scalar flux error for Case 2b with sphere volume fraction $p_1 = 0.20$, comparing constant, exponential, and uniform spherical inclusion radius distributions. 157
7.16 Relative scalar flux error for Case 2b with sphere volume fraction $p_1 = 0.30$, comparing constant, exponential, and uniform spherical inclusion radius distributions. 158
7.17 Relative scalar flux error for Case 3c with sphere volume fraction $p_1 = 0.10$, comparing constant, exponential, and uniform spherical inclusion radius distributions. 159
7.18 Relative scalar flux error for Case 3c with sphere volume fraction $p_1 = 0.20$, comparing constant, exponential, and uniform spherical inclusion radius distributions. 160
7.19 Relative scalar flux error for Case 3c with sphere volume fraction $p_1 = 0.30$, comparing exponential and uniform spherical inclusion radius distributions. Constant radius not included, see Section 7.2. 161
7.20 Effect of spherical inclusion radius distribution on the benchmark scalar flux for Case 1a. The signed relative difference is computed relative to the constant radius benchmark. 164
7.21 Effect of spherical inclusion radius distribution on the benchmark scalar flux for Case 1b. The sensitivity is larger than in Case 1a because the optically thick inclusion material is absorbing while the background material is scattering. . . . 165
7.22 Effect of spherical inclusion radius distribution on the benchmark scalar flux for Case 2a. The radius-distribution effect remains relatively modest compared with the absorbing-inclusion and uniformly scattering cases. 166
7.23 Effect of spherical inclusion radius distribution on the benchmark scalar flux for Case 2c. The uniformly scattering case shows that radius-distribution effects can remain significant when particles undergo many collisions before leakage or absorption. 167

8.1 Example Rayleigh-Taylor mixing problem with miscible materials from Ref. [20]. 173

List of Tables

5.1 Material parameters 67
5.2 Numerical results for leakage values. 70

6.1 Leakage Comparison Between GME Model and Benchmark for forward moving particles only with Ramp-Ramp mixing. 83
6.2 Material Properties for the Standard Benchmark Cases [9] 90
6.3 Methods Comparison for Exp-Exp Distributions (Suite I). 96
6.4 Methods Comparison for Ramp-Ramp Distributions (Suite I). 97
6.5 Methods Comparison for Exp-Ramp Distributions (Suite I). 98
6.6 Methods Comparison for Exp-Unif Rad Distributions (Suite I). 99
6.7 Methods Comparison for Exp-Exp Rad Distributions (Suite I). 100
6.8 RMSE Comparison (Suite I). 100
6.9 Methods Comparison for Exp-Exp Distributions (Suite II). 108
6.10 Methods Comparison for Ramp-Ramp Distributions (Suite II). 109
6.11 Methods Comparison for Exp-Ramp Distributions (Suite II). 110
6.12 Methods Comparison for Exp-Unif Rad Distributions (Suite II). 111
6.13 Methods Comparison for Exp-Exp Rad Distributions (Suite II). 112
6.14 RMSE Comparison (Suite II). 113

7.1 Leakage RMSE comparison by geometric memory treatment for volume fraction 0.10. 129
7.2 Material properties for the 3D spherical inclusion benchmark cases [44]. The material case numbers correspond to the Brantley spherical inclusion mean chord length cases. The quantity λ_0^* denotes the background mean chord length for sphere volume fraction $p_1 = 0.10$, with λ_0 at other volume fractions computed using Eq. (7.4). The scattering cases a and b are added in this chapter, while case c corresponds to the scattering ratio used in the original 3D spherical inclusion calculations. 132
7.3 Methods comparison for Exp-Constant Radius distributions, volume fraction 0.10. 134
7.4 Methods comparison for Exp-Uniform Radius distributions, volume fraction 0.10. 135
7.5 Methods comparison for Exp-Exp Radius distributions, volume fraction 0.10. . . 136
7.6 Methods comparison for Exp-Constant Radius distributions, volume fraction 0.20. 137
7.7 Methods comparison for Exp-Uniform Radius distributions, volume fraction 0.20. 138

7.8 Methods comparison for Exp-Exp Radius distributions, volume fraction 0.20. . . 139
7.9 Methods comparison for Exp-Constant Radius distributions, volume fraction 0.30. 140
7.10 Methods comparison for Exp-Uniform Radius distributions, volume fraction 0.30. 141
7.11 Methods comparison for Exp-Exp Radius distributions, volume fraction 0.30. . . 142
7.12 Leakage RMSE comparison by volume fraction. 143

Acknowledgments

I would first like to thank my primary technical advisor, Dr. Anil Prinja, for guiding me through the complex world of transport in stochastic media. His mentorship not only shaped the technical direction of this dissertation, but also introduced me to research and showed me the most interesting parts of nuclear engineering. I am also incredibly grateful for the opportunities, advice, and professional connections he helped provide throughout my graduate studies.

Immense credit is also owed to Dr. Jasmina Vujic and Dr. Daniel Siefman for helping give me the tools needed to succeed in graduate school at UC Berkeley. Their support and advice have meant a great deal to me. I'd also like to thank Dr. Panos Papadopoulos for his help in reviewing this dissertation.

I would also like to thank my mentors at the national laboratories, especially Dr. Todd Urbatsch, Dr. Aaron Olson, and Dr. Patrick Brantley. Each of them encouraged my curiosity by giving me the freedom to follow technical questions down rabbit holes, and helped me understand what it means to be an expert, a professional, and a contributor in a national laboratory setting. I hope to live up to the examples they have set in my own career.

This work was supported by the Department of Energy National Nuclear Security Administration under Award Number DE-NA0003996.

Chapter 1

Introduction

Radiation transport in random media is a fundamental problem in nuclear science and engineering. In many applications, the material composition and associated interaction properties are not known as deterministic functions of space, but instead exhibit spatial variability that must be described statistically. Such stochastic media arise in high-energy-density physics and inertial confinement fusion, where hydrodynamic instabilities and turbulent mixing can generate complex heterogeneous material structures [1, 2]; in atmospheric radiative transfer, where cloud density and opacity can vary randomly in space [3]; in reactor applications, where particle transport may occur through statistically heterogeneous fuel, coolant, or moderator configurations [4, 5]; and in shielding problems involving concrete or other heterogeneous materials [6, 7, 8]. In these systems, the particle flux depends not only on the volume fractions and material properties of the constituents, but also on their spatial arrangement along particle trajectories.

A direct approach to stochastic media transport is to sample many independent material realizations, solve the deterministic transport equation on each realization, and then ensemble average the resulting quantities of interest [9, 10]. This realization-based procedure provides a natural benchmark for mean particle fluxes, reflection and transmission probabilities, and higher moments of the flux. Benchmark calculations have therefore played a central role in the development and assessment of stochastic media transport models [11, 12, 10, 13, 4]. However, explicit realization sampling is expensive: each material realization requires a transport solve, and many realizations may be needed to obtain statistically converged estimates of ensemble-averaged quantities of interest. As a result, benchmark calculations are typically used for code comparison and method assessment rather than routine analysis.

The central objective of stochastic media transport theory is therefore to approximate ensemble-averaged transport quantities without the expense of fully resolving an ensemble of random material realizations. The simplest such approximation is atomic mix, in which random material cross sections are replaced by volume-fraction-weighted averages. Atomic mix is computationally attractive because it reduces the problem to an ordinary deterministic transport calculation. It can be appropriate when the particle mean free path is large compared with the characteristic material chord lengths, so that particles traverse many

material regions between collisions and experience an effectively homogenized medium [8, 10]. Outside this limit, however, atomic mix neglects important spatial correlation effects, particularly in systems containing relatively large material chunks or strongly contrasting material properties.

More detailed stochastic media models retain information about the material state encountered by a particle. The Levermore-Pomraning (LP) model, also called the Markovian model, provides coupled equations for material-conditioned ensemble-averaged fluxes in binary random media [7, 14, 9, 8]. Derivative Monte Carlo algorithms, such as Chord Length Sampling (CLS), model the random material sequence encountered by a particle by sampling distances to material interfaces along its trajectory [15, 10, 16, 17]. The LP model and CLS are exact in purely absorbing Markovian media, but become approximate when particle scattering is introduced because the Markov property no longer applies: the particle flux at a point x depends on the flux solution at a point beyond x in space. In the case of CLS, this manifests in non-physical events where particles can traverse locations in the geometry in one material that were previously defined as the other material. Local Realization Preserving (LRP) is then an extension to CLS that incorporates local geometric memory to avoid some of the nonphysical events stemming from repeated resampling of geometric features, thereby improving accuracy [15, 10, 18, 6]. Together, these deterministic and Monte Carlo methods form the classical foundation for approximate particle transport in binary stochastic media.

Much of this classical theory is built on Markovian mixing statistics. In a Markovian binary medium, material chord lengths are exponentially distributed, and the probability of encountering the next material interface is independent of the distance already traveled through the current material. This memoryless property makes the material label itself a sufficient statistical descriptor of the medium along a particle trajectory. It is also what allows the Levermore-Pomraning model and CLS-type algorithms to be formulated in relatively simple forms. While the Markovian assumption is mathematically convenient and has been widely used, it is not generally representative of heterogeneous materials with finite inclusions, grains, droplets, or other structured features [1, 5].

Many realistic random media are more naturally described by non-exponential chord-length statistics. In high-energy-density physics, radiation flow experiments often involve heterogeneous or mixed materials that are not naturally memoryless [1, 2]. Reactor applications involving randomly dispersed fuel particles or pebbles provide another important example, since chord lengths through finite particles or inclusions are determined by geometry rather than by an exponential distribution [5]. It has been shown that, for randomly distributed disks and spheres, chord lengths through the inclusions are not exponentially distributed, and even the background chord length statistics can depart from exponential behavior as the volume fraction of inclusions becomes sufficiently large [5]. These observations motivate stochastic media models that retain more information about material geometry than is contained in the mean chord lengths alone.

Renewal statistics provide a natural generalization of Markovian mixing. In a renewal medium, material chord lengths can be sampled from any arbitrary probability distribution, not just the exponential distribution. The Markovian model is recovered as the special case

in which each chord length distribution is exponential. In the more general renewal case, however, the probability of material transition depends on the distance already traveled through the current material. Accurate transport representations, therefore, require some geometric memory; the material state alone is no longer sufficient to describe the local material transition probability. This additional memory is the central feature distinguishing non-Markovian renewal media from classical Markovian mixtures.

Previous work extended stochastic media transport beyond the classical Markovian setting by modifying Markovian closure models to account for renewal material statistics [11, 12]. These approaches improved the treatment of non-Markovian mixtures and demonstrated that transport observables can depend on the full chord length distributions, not only on volume fractions or mean chord lengths. However, the resulting models do not preserve the renewal material distributions along particle trajectories. Rather than representing material transitions through the actual non-exponential interface statistics, they introduce approximate corrections to Markovian equations. As a result, they may improve ensemble-averaged predictions while still failing to accurately represent the material distributions that define the stochastic medium. Other work has treated spherical inclusion geometries more directly by combining CLS in the matrix material with explicit transport through constant-radius inclusions [19]. Such methods are useful for modeling spherical inclusion geometries, but they do not generalize to any arbitrary chord length distribution, and they are difficult to incorporate into existing stochastic media transport frameworks due to the mixed implicit and explicit representation of the geometry.

This dissertation develops particle transport methods for non-Markovian stochastic media described by renewal statistics. The central idea is to augment the material-conditioned transport description with an age variable, defined as the distance traveled since the most recent material interface. This age variable carries the geometric memory needed to describe general renewal statistical media, Markovianizing the joint stochastic state space and allowing for the development of a model analogous to LP for renewal media that is exact in a pure absorber and approximate with particle scatter. When the chord length distributions are exponential, the age dependence disappears and the classical Markovian description is recovered. When the chord length distributions are non-exponential, the age variable enables the development of transport models and Monte Carlo algorithms that accurately represent the mixing statistics of the medium and provide ensemble-averaged particle fluxes efficiently.

The dissertation proceeds as follows. Chapter 2 introduces transport on fixed material realizations and describes the benchmark ensemble-averaging procedure used to assess approximate stochastic media methods. Chapter 3 develops the statistical framework needed for transport in Markovian and renewal binary media. Chapter 4 reviews classical stochastic media transport approximations, including atomic mix, the Levermore-Pomraning model, CLS, LRP, and previous heuristic adaptations to renewal statistics. Chapter 5 derives an age-dependent generalized master equation formulation that is exact for purely absorbing renewal statistical media and demonstrates its relationship to the classical Markovian theory. Chapter 6 extends the age-based approach to include particle scattering, develops Monte Carlo algorithms for one-dimensional (1D) renewal statistical media, and provides

comparisons against benchmarks. Chapter 7 extends the analysis to three-dimensional (3D) stochastic media, largely focusing on spherical inclusion geometries. Chapter 8 summarizes the main conclusions of the dissertation and discusses directions for future work.

Chapter 2

General Considerations of Transport in Immiscible Random Media

2.1 Introduction

This chapter introduces the basic transport setting used throughout this dissertation. The focus here is on immiscible binary mixtures, in which two materials are separated by randomly located interfaces. For any particular realization of the medium, transport is deterministic. The challenge lies in computing ensemble-averaged quantities over all admissible realizations of the random geometry.

The central objective of stochastic media transport is not merely to solve the transport equation on one possible realization of the random medium, but to predict quantities averaged over the ensemble of possible material configurations. In practice, one is usually interested in ensemble-averaged observables such as the mean angular flux, scalar flux, reflection, transmission, absorption, and higher moments. A direct benchmark approach samples realizations of the stochastic medium, solves the transport equation on each realization, and then performs post-realization ensemble averaging. This is conceptually straightforward but very computationally expensive, particularly when material segments are small relative to the domain or when the geometry is multidimensional. Examples of stochastic geometries, seen in Figures 2.1 through 2.5, exemplify the complexity of real-world stochastic geometries. The motivation for ensemble-averaged transport models is therefore clear: rather than solve transport on many random realizations and average afterward, it is advantageous to develop equations for the ensemble-averaged intensity directly. This general viewpoint is also emphasized in Pomraning's discussion of stochastic transport theory [8].

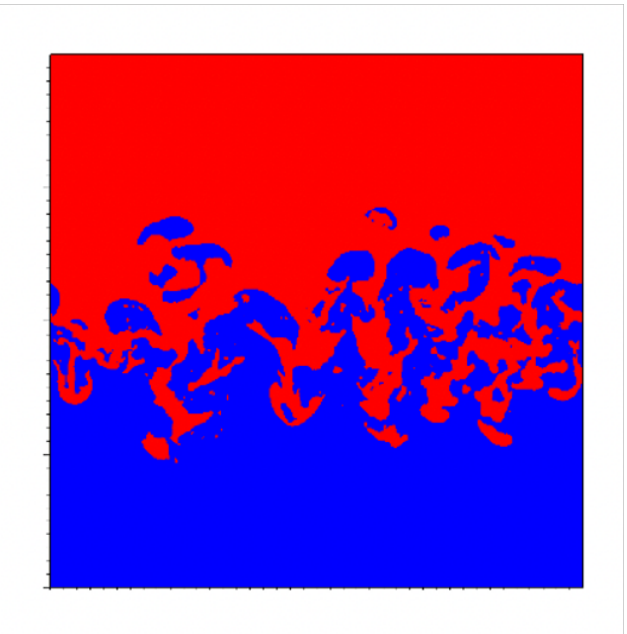


Figure 2.1: Example of a stochastic geometry arising from a Rayleigh-Taylor turbulent instability with surface tension leading to immiscibility [20].

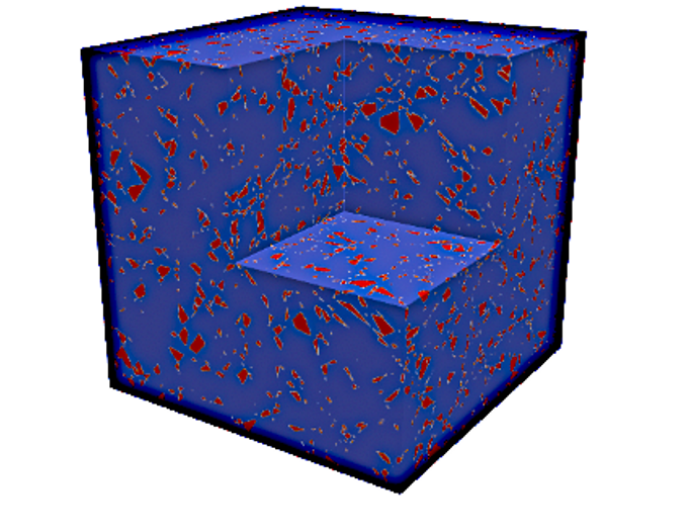


Figure 2.2: Example of a Markovian realization generally used as a benchmark for transport in stochastic media [21].

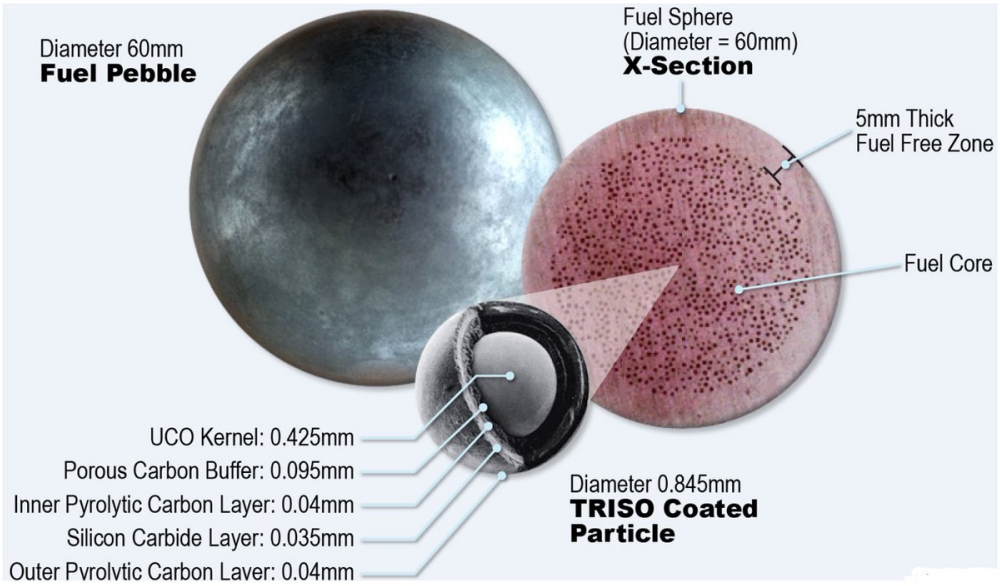


Figure 2.3: Example of a stochastic geometry arising from the inside of a pebble in a pebble bed reactor. The TRISO fuel pellets are randomly dispersed throughout the carbon pebble [22].

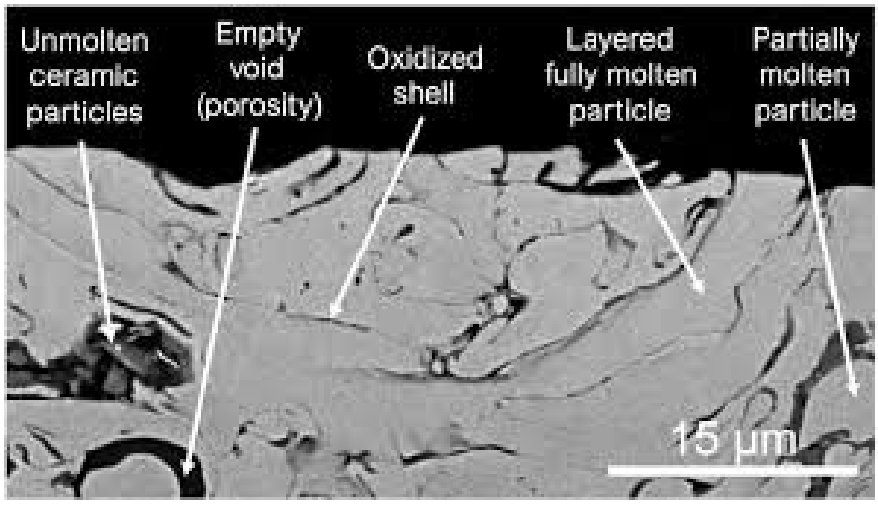


Figure 2.4: Example of a stochastic geometry arising from a thermal spray microstructure. Voids and layers of molten, oxidized, or unmolten material are located randomly throughout [23].

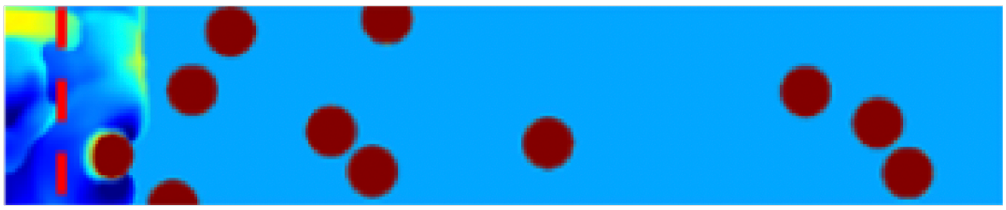


Figure 2.5: Example of a stochastic geometry used for studying thermal radiation flow in stochastic media for the X-ray Flow Over Lumps (XFOL) project at Los Alamos National Laboratory [1].

The scope of the Chapter is as follows. Section 2.2 introduces transport on a fixed realization, first in a general phase-space form and then in the steady-state monoenergetic form used in many stochastic media benchmark studies. Section 2.3 describes the benchmark method based on explicit realization sampling and ensemble averaging. Section 2.4 summarizes the role of realization transport as the foundation for the approximate models developed in later chapters.

2.2 Transport on a Fixed Realization

Consider a random immiscible medium defined on a spatial domain V. A realization of the medium is denoted by ω, and the material occupying position $\mathbf{r}$ in that realization is represented using indicator functions

$$\chi_i(\mathbf{r},\omega) = \begin{cases} 1, & \mathbf{r} \text{ lies in material } i, \\ 0, & \mathbf{r} \text{ does not lie in material } i. \end{cases} \tag{2.1}$$

For a binary mixture, $i = 0, 1$ and

$$\chi_0(\mathbf{r},\omega) + \chi_1(\mathbf{r},\omega) = 1. \tag{2.2}$$

More generally, an M-material immiscible mixture satisfies $\sum_{i=1}^{M} \chi_i = 1$. The essential assumption is that materials occupy disjoint spatial regions; the randomness lies in the shapes, sizes, and locations of those regions.

On a fixed realization, the material fields are deterministic. In a time-dependent, energy-dependent setting with general scattering, the angular flux may be written as

$$\psi = \psi(\mathbf{r}, \mathbf{\Omega}, E, t, \omega), \tag{2.3}$$

where $\mathbf{r}$ is position, $\mathbf{\Omega}$ is direction of flight, E is particle energy, t is time, and ω specifies the material realization. The linear Boltzmann transport equation on that realization may

be written in the form

$$\begin{aligned}\frac{1}{v(E)}\frac{\partial\psi}{\partial t} + \mathbf{\Omega}\cdot\nabla\psi(\mathbf{r},\mathbf{\Omega},E,t,\omega) + \Sigma_t(\mathbf{r},E,t,\omega)\psi(\mathbf{r},\mathbf{\Omega},E,t,\omega)\\ = \int_0^\infty\int_{4\pi}\Sigma_s(\mathbf{r},\mathbf{\Omega}'\cdot\mathbf{\Omega},E'\to E,t,\omega)\psi(\mathbf{r},\mathbf{\Omega}',E',t,\omega)\,d\mathbf{\Omega}'\,dE' + Q(\mathbf{r},\mathbf{\Omega},E,t,\omega).\end{aligned} \tag{2.4}$$

Here $v(E)$ is the particle speed, Q is an external or internal source, Σ_t is the total macroscopic cross section, and Σ_s is the macroscopic differential scattering cross section. In general, the differential scattering cross section may depend on both the incoming and outgoing particle energies and directions. It is often useful to write it in the factored form

$$\Sigma_s(\mathbf{r},\mathbf{\Omega}'\cdot\mathbf{\Omega},E'\to E) = \Sigma_s(\mathbf{r},E')\,p(\mathbf{\Omega}'\cdot\mathbf{\Omega},E'\to E), \tag{2.5}$$

where $\Sigma_s(E')$ is the total macroscopic scattering cross section for particles of incident energy E', and $p(\mathbf{\Omega}'\cdot\mathbf{\Omega},E'\to E)$ is the probability density for scattering from incoming direction $\mathbf{\Omega}'$ and energy E' into outgoing direction $\mathbf{\Omega}$ and energy E.

Boundary and initial conditions complete the deterministic realization problem. For example, an incoming boundary condition may be written as

$$\psi(\mathbf{r},\mathbf{\Omega},E,t,\omega) = \Gamma(\mathbf{r},\mathbf{\Omega},E,t,\omega), \qquad \mathbf{r}\in\partial V, \quad \mathbf{\Omega}\cdot\mathbf{n}<0, \tag{2.6}$$

and an initial condition may be written as

$$\psi(\mathbf{r},\mathbf{\Omega},E,0,\omega) = \psi_0(\mathbf{r},\mathbf{\Omega},E,\omega). \tag{2.7}$$

The realization-dependent material properties may be decomposed using the material indicators. For example,

$$\Sigma_t(\mathbf{r},E,t,\omega) = \sum_i \chi_i(\mathbf{r},\omega)\Sigma_{t,i}(\mathbf{r},E,t), \tag{2.8a}$$

$$\Sigma_s(\mathbf{r},E'\to E,\mathbf{\Omega}'\cdot\mathbf{\Omega},t,\omega) = \sum_i \chi_i(\mathbf{r},\omega)\Sigma_{s,i}(\mathbf{r},E'\to E,\mathbf{\Omega}'\cdot\mathbf{\Omega},t), \tag{2.8b}$$

$$Q(\mathbf{r},\mathbf{\Omega},E,t,\omega) = \sum_i \chi_i(\mathbf{r},\omega)Q_i(\mathbf{r},\mathbf{\Omega},E,t). \tag{2.8c}$$

These equations emphasize an important point: once ω is fixed, Eq. (2.4) is an ordinary deterministic transport problem.

Energy dependence, time dependence, and anisotropic scattering change the phase-space structure of the deterministic transport solve on each fixed realization, but they do not alter the fact that the immiscible geometry is represented statistically by material indicator functions. In deterministic transport calculations, energy dependence is commonly treated using the multigroup approximation, in which the equation for each energy group has the form of a monoenergetic transport equation with additional source terms coupling that

group to the others. Thus, while multigroup, time-dependent, or anisotropically scattering problems introduce additional angular, temporal, and energy variables, the stochastic-media closure problem remains associated with the spatial distribution of material properties. For this reason, many studies of stochastic media transport, including the calculations in this dissertation, use the steady-state, monoenergetic, isotropically scattering limit to isolate the effects of random material geometry [9, 10, 16]. In that setting, the angular flux is $\psi(\mathbf{r}, \mathbf{\Omega}, \omega)$ and the realization transport equation reduces to

$$\mathbf{\Omega} \cdot \nabla \psi(\mathbf{r}, \mathbf{\Omega}, \omega) + \Sigma_t(\mathbf{r}, \omega)\psi(\mathbf{r}, \mathbf{\Omega}, \omega) = \frac{\Sigma_s(\mathbf{r}, \omega)}{4\pi} \int_{4\pi} \psi(\mathbf{r}, \mathbf{\Omega}', \omega)\, d\mathbf{\Omega}' + Q(\mathbf{r}, \mathbf{\Omega}, \omega), \tag{2.9}$$

with incoming boundary condition

$$\psi(\mathbf{r}, \mathbf{\Omega}, \omega) = \Gamma(\mathbf{r}, \mathbf{\Omega}), \qquad \mathbf{r} \in \partial V, \quad \mathbf{\Omega} \cdot \mathbf{n} < 0. \tag{2.10}$$

The binary material decomposition is then

$$\Sigma_t(\mathbf{r}, \omega) = \sum_{i=0}^{1} \chi_i(\mathbf{r}, \omega)\Sigma_{t,i}(\mathbf{r}), \qquad \Sigma_s(\mathbf{r}, \omega) = \sum_{i=0}^{1} \chi_i(\mathbf{r}, \omega)\Sigma_{s,i}(\mathbf{r}), \qquad Q(\mathbf{r}, \mathbf{\Omega}, \omega) = \sum_{i=0}^{1} \chi_i(\mathbf{r}, \omega)Q_i(\mathbf{r}, \mathbf{\Omega}). \tag{2.11}$$

This is the form used as the starting point for the ensemble-averaged and material-conditioned models developed later.

2.3 The Benchmark Method: Realization Sampling and Ensemble Averaging

The most direct method for computing transport in a stochastic medium is to sample the random geometry explicitly. Let $\omega_1, \omega_2, \ldots, \omega_N$ denote N independent realizations sampled from the prescribed material mixing statistics. For each realization, one solves Eq. (2.9), either with deterministic methods like discrete ordinates or with Monte Carlo. If $Q(\omega)$ denotes a scalar quantity of interest, such as transmission, reflection, absorption, or a flux tally in a spatial cell, the benchmark estimator for the ensemble average of said quantity $\overline{Q}_N$ is

$$\overline{Q}_N = \frac{1}{N} \sum_{n=1}^{N} Q(\omega_n). \tag{2.12}$$

For angular flux, this same procedure gives ensemble-average flux $\langle \psi(\mathbf{r}, \mathbf{\Omega}) \rangle$ as

$$\langle \psi(\mathbf{r}, \mathbf{\Omega}) \rangle \approx \frac{1}{N} \sum_{n=1}^{N} \psi(\mathbf{r}, \mathbf{\Omega}, \omega_n). \tag{2.13}$$

The estimator in Eq. (2.12) is unbiased when the realizations are sampled from the correct ensemble and the transport solutions are exact. Its statistical uncertainty is governed by the usual central limit scaling. If variance $\sigma_Q^2 = \mathrm{Var}[Q]$ is finite, then

$$\mathrm{Var}\left[\overline{Q}_N\right] = \frac{\sigma_Q^2}{N}, \tag{2.14}$$

and the standard error of the mean (SEM), which measures the uncertainty in the estimated ensemble mean due to using a finite number of realizations, can be calculated for independent realizations as

$$\mathrm{SEM}\left[\overline{Q}_N\right] = \frac{\sigma_Q}{\sqrt{N}}. \tag{2.15}$$

Thus, the uncertainty associated with the realization ensemble decreases as $1/\sqrt{N}$. This convergence rate is important in practice: reducing the realization-sampling uncertainty by a factor of ten requires roughly one hundred times as many independent realizations.

In Monte Carlo transport calculations on each realization, there is often an additional particle-history uncertainty. The total numerical uncertainty then contains contributions from both the finite number of material realizations and the finite number of particle histories used to solve transport on each realization. Conceptually, however, the benchmark method is defined by the outer ensemble over material configurations. It is the direct numerical representation of the stochastic transport problem and therefore provides the reference solution for approximate ensemble-averaged models.

The benchmark method is conceptually straightforward but computationally expensive. It requires explicit generation, storage, or repeated interrogation of the random geometry, followed by a deterministic or Monte Carlo transport solve on each sampled realization. The cost becomes especially large when the characteristic chord lengths are small compared with the domain size, when optically thick regions require many particle interactions, or when the geometry is multidimensional. These costs motivate the approximate stochastic transport methods discussed in later chapters, which attempt to predict ensemble-averaged quantities without resolving the full random geometry realization by realization, thus saving significant computational expense.

2.4 Summary

Transport in an immiscible random medium is deterministic once the material realization is specified. The random medium can be represented by material indicator functions, and the material-dependent cross sections and sources are obtained by weighting each material property by the corresponding indicator. The resulting realization transport equation may include time dependence, energy dependence, and general anisotropic scattering, but these features do not change the statistical description of the material geometry.

The benchmark method follows directly from this realization viewpoint: sample many geometries, solve transport on each, and average the resulting solutions. This approach

is the most straightforward solution to the stochastic media transport problem, and its realization-sampling uncertainty decreases as $1/\sqrt{N}$ for N independent realizations. Its prohibitive computational cost, however, motivates the development of ensemble-averaged closures and Monte Carlo algorithms that sample geometric features without constructing full realizations. Those classical Markovian methods are reviewed in Chapter 4, after the statistical framework for Markov and renewal media is introduced in Chapter 3.

Chapter 3

Statistics of Markovian and Non-Markovian Random Media

3.1 Introduction

The stochastic media considered in this dissertation are immiscible mixtures: each point in space is occupied by only one material, and neighboring material regions are separated by sharp interfaces. Along a line through such a medium, the material changes at a sequence of random interface locations. The distances between successive interfaces are material chord lengths, and the statistical description of those chord lengths is the starting point for the theory developed in later chapters.

The central statistical model used to represent the medium is the alternating renewal process (ARP). In a binary medium, material segments alternate between materials 0 and 1, with material-dependent chord length distributions dictating the location of interfaces. If the chord length distributions are exponential, then the medium is said to be Markovian because the interfaces are aptly described by a continuous-time Markov process. The ARP may be constructed using any arbitrary chord length distribution, however, which allows for a more accurate description of materials in real applications, such as those in Figures 2.3 and 2.5.

The scope of the Chapter is as follows. Section 3.2 introduces renewal processes as a statistical description of random material interfaces, then specializes the construction to binary alternating renewal media. It defines the chord length densities, survival functions, hazard functions, equilibrium first-chord distributions, and volume-fraction relations used throughout the dissertation. Section 3.3 then identifies Markovian media as the exponential special case of the alternating renewal construction. In that setting, material interfaces form a spatial Poisson process, the material label is a closed Markov state variable, and the Chapman-Kolmogorov and forward master-equation structure provides a deterministic balance description of material-state probabilities. The chapter concludes by showing how general renewal media can be embedded in an augmented Markov state space by retaining

the distance from the previous renewal point, motivating the generalized master equation and renewal Monte Carlo formulations developed in later chapters.

3.2 Renewal Processes and Alternating Renewal Media

Renewal processes provide a natural statistical framework for describing random interface locations in immiscible media. Along a line through such a medium, renewal events correspond to material interfaces and renewal intervals correspond to material chord lengths. When these chord lengths are exponentially distributed, the renewal process reduces to the Poisson process associated with Markovian mixing. More general chord length distributions lead to non-Markovian media in which the probability of encountering an interface depends on the distance already traveled through the current material.

Alternating Renewal Processes for Binary Media

A renewal process is defined by a sequence of independent and identically distributed non-negative random variables

$$X_1, X_2, \ldots, \tag{3.1}$$

where X_n represents the waiting time between the $(n-1)$th and nth event [24]. The renewal time to the nth renewal is

$$S_n = X_1 + X_2 + \cdots + X_n, \tag{3.2}$$

and the associated counting process is

$$N(t) = \max\{n : S_n \leq t\}, \tag{3.3}$$

which gives the number of renewals that have occurred by time t.

In the context of stochastic media, the independent variable is spatial distance rather than time. Renewal events correspond to material interfaces, and the intervals between renewal events correspond to material chord lengths. For a single renewal process, the intervals X_n are identically distributed. The binary media considered in this dissertation, however, are more naturally described by an alternating renewal process (ARP), in which material segments alternate between two material types and the chord length distribution depends on the material.

Let $X_{0,1}, X_{0,2}, \ldots$ denote independent chord lengths in material 0, sampled from the chord length probability density function $f_0(s)$, and let $X_{1,1}, X_{1,2}, \ldots$ denote independent chord lengths in material 1, sampled from the distribution $f_1(s)$. A 1D realization of the binary medium is constructed by alternating these segments. For example, if the realization begins in material 0, the interface locations are generated from partial sums of the sequence

$$X_{0,1},\ X_{1,1},\ X_{0,2},\ X_{1,2}, \ldots. \tag{3.4}$$

Thus,

$$X_{i,n} \longleftrightarrow \text{length of the } n\text{th chord of material } i. \tag{3.5}$$

The Poisson process is recovered as the special case in which the waiting times are exponentially distributed. Similarly, a binary alternating renewal medium becomes Markovian when each material chord length distribution is exponential. In that case, the probability of encountering the next interface depends only on the current material and not on the distance already traveled through the current chord. General alternating renewal media allow arbitrary material-dependent chord length distributions $f_i(s)$, and therefore can represent non-Markovian interface statistics.

Chord Length Distributions

Let $f_i(s)$ denote the chord length probability density function for material i. Then

$$f_i(s)\,ds = \text{probability that a chord of material } i \text{ has length in } (s, s+ds). \tag{3.6}$$

The distribution satisfies the normalization condition

$$\int_0^\infty f_i(s)\,ds = 1. \tag{3.7}$$

The mean chord length λ_i is

$$\lambda_i = \int_0^\infty s f_i(s)\,ds. \tag{3.8}$$

The cumulative distribution function is

$$F_i(s) = \int_0^s f_i(u)\,du, \tag{3.9}$$

and the survival function is

$$S_i(s) = 1 - F_i(s) = \int_s^\infty f_i(u)\,du. \tag{3.10}$$

In reliability and survival analysis, $S_i(s)$ represents the probability that a lifetime exceeds s [25]. In stochastic media, it represents the probability that a material chord extends at least distance s beyond an interface.

Hazard Functions

The hazard function is defined as

$$h_i(s) = \frac{f_i(s)}{S_i(s)} = \frac{f_i(s)}{1 - F_i(s)}. \tag{3.11}$$

Equivalently, since

$$f_i(s) = -\frac{dS_i}{ds}, \tag{3.12}$$

we have

$$h_i(s) = -\frac{1}{S_i(s)}\frac{dS_i}{ds} = -\frac{d}{ds}\ln S_i(s). \tag{3.13}$$

Integrating gives

$$S_i(s) = \exp\left(-\int_0^s h_i(u)\,du\right). \tag{3.14}$$

The hazard function has a direct interpretation in stochastic media. It gives the instantaneous probability per unit distance of encountering an interface, conditional on having already traveled distance s in the current material [26]:

$$P(s < X_i \leq s + ds \mid X_i > s) = h_i(s)\,ds + o(ds). \tag{3.15}$$

Chord Length Distributions Used in This Dissertation

Several chord length distributions are considered throughout this dissertation. The exponential distribution corresponds to Markovian mixing, while the remaining distributions model non-Markovian chord statistics associated with spherical inclusions embedded in an approximately exponential background [5, 19], such as the stochastic geometries shown in Figure 2.5. The ramp distribution describes chords through spherical inclusions of a single fixed radius. The uniformly varying and exponentially varying radius distributions extend this model by allowing the inclusion radius itself to be random, thereby broadening the resulting chord length statistics. Together, these distributions provide a simple hierarchy of inclusion models: constant radius spheres, bounded variable radius spheres, and unbounded variable radius spheres.

For constant radius inclusions, the chord length distribution has finite support and increases linearly with s, reflecting the fact that longer chords correspond to trajectories passing closer to the center of a sphere. When the radius varies uniformly, the chord length distribution remains finite in support because the radius is bounded. When the radius is exponentially distributed, the radius distribution has infinite support, and the resulting chord length distribution also has infinite support. The chord length probability density functions $f_i(s)$, cumulative distribution functions $F_i(s)$, and hazard functions $h_i(s)$ for these cases are shown in Eqs. (3.16) through (3.19).

Markovian media:

$$f_i(s) = \frac{1}{\lambda_i} e^{-s/\lambda_i}, \qquad s \geq 0, \tag{3.16a}$$

$$F_i(s) = 1 - e^{-s/\lambda_i}, \qquad s \geq 0, \tag{3.16b}$$

$$h_i(s) = \frac{1}{\lambda_i}, \qquad s \geq 0. \tag{3.16c}$$

Constant radius spherical inclusions (also known as the ramp distribution) [5, 11, 12, 27]:

$$f_i(s) = \frac{8s}{9\lambda_i^2}, \qquad 0 \leq s \leq \frac{3\lambda_i}{2}, \tag{3.17a}$$

$$F_i(s) = \frac{4s^2}{9\lambda_i^2}, \qquad 0 \leq s \leq \frac{3\lambda_i}{2}, \tag{3.17b}$$

$$h_i(s) = \frac{8s}{9\lambda_i^2 - 4s^2}, \qquad 0 \leq s < \frac{3\lambda_i}{2}. \tag{3.17c}$$

Uniformly varying radius spherical inclusions [5]:

$$f_i(s) = \frac{3s(2\lambda_i - s)}{4\lambda_i^3}, \qquad 0 \leq s \leq 2\lambda_i, \tag{3.18a}$$

$$F_i(s) = \frac{3s^2}{4\lambda_i^2} - \frac{s^3}{4\lambda_i^3}, \qquad 0 \leq s \leq 2\lambda_i, \tag{3.18b}$$

$$h_i(s) = \frac{3s(2\lambda_i - s)}{4\lambda_i^3 - 3\lambda_i s^2 + s^3}, \qquad 0 \leq s < 2\lambda_i. \tag{3.18c}$$

Exponentially varying radius spherical inclusions [5]:

$$f_i(s) = \frac{4s}{\lambda_i^2} e^{-2s/\lambda_i}, \qquad s \geq 0, \tag{3.19a}$$

$$F_i(s) = 1 - e^{-2s/\lambda_i}\left(1 + \frac{2s}{\lambda_i}\right), \qquad s \geq 0, \tag{3.19b}$$

$$h_i(s) = \frac{4s}{\lambda_i(\lambda_i + 2s)}, \qquad s \geq 0. \tag{3.19c}$$

The differences between these chord length distributions are illustrated in Figures 3.1 and 3.2. Figure 3.1 compares the chord length density functions in nondimensional form, while Figure 3.2 compares the corresponding hazard functions. The exponential distribution decreases monotonically from its maximum value at $s = 0$, whereas the spherical inclusion distributions vanish at $s = 0$ because a chord of zero length has zero probability density. The ramp distribution increases linearly up to its maximum allowed chord length, while the uniformly varying and exponentially varying radius distributions are broadened by variation in the inclusion radius.

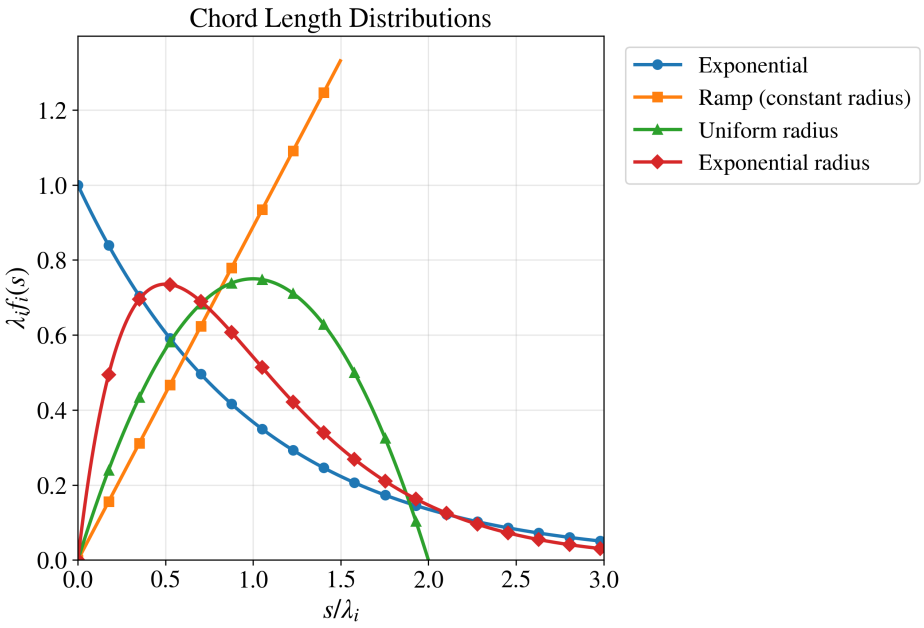


Figure 3.1: Chord length probability density functions/distributions $f_i(s)$ considered in this dissertation, from Eqs. (3.16) through (3.19).

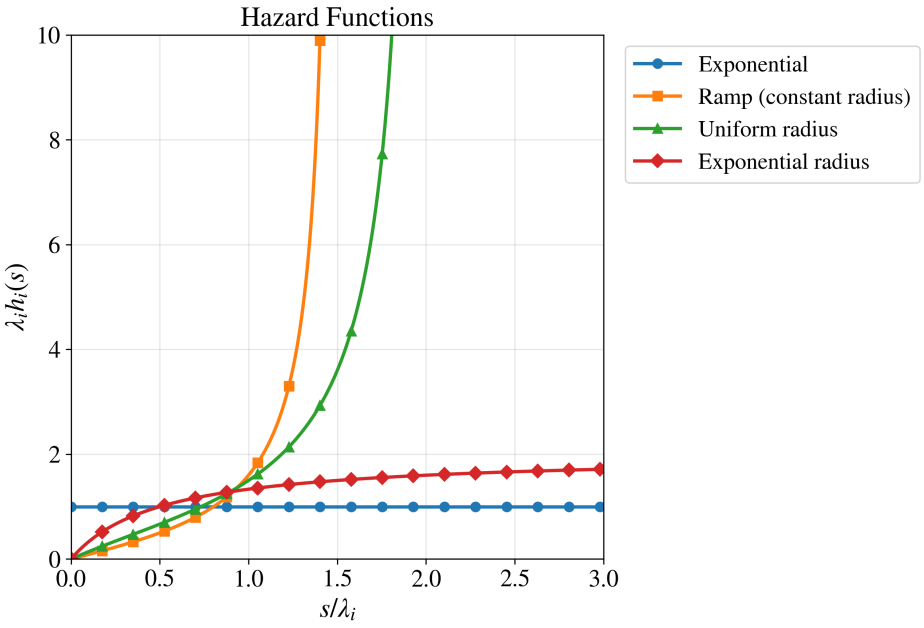


Figure 3.2: Hazard functions $h_i(s)$ considered in this dissertation, from Eqs. (3.16) through (3.19).

The corresponding hazard functions show directly how the different chord length statistics affect the probability of encountering an interface. For the exponential distribution, the hazard function in Eq. (3.16c) is constant and does not depend on the distance since the previous renewal s. This follows from the memoryless nature of the exponential distribution: the probability per unit distance of crossing an interface depends only on the current material state i, not on the distance already traveled through that material. This constant transition rate is the statistical basis for Markovian mixing. In contrast, the spherical-inclusion distributions have age-dependent hazard functions, meaning that the probability of a material transition depends on the current chord age s.

For the ramp distribution and the uniformly varying radius distribution, the chord length distributions have finite support. As s approaches the maximum possible chord length, the survival probability $S_i(s)$ approaches zero, and therefore the hazard function diverges. Specifically, the ramp hazard in Eq. (3.17c) diverges as $s \to 3\lambda_i/2$, while the uniformly varying radius hazard in Eq. (3.18c) diverges as $s \to 2\lambda_i$. This behavior reflects the geometric constraint that a particle cannot remain inside a finite-radius inclusion beyond the maximum possible chord length. As the particle approaches the maximum possible distance through the inclusion (the diameter of said inclusion), the hazard function approaches infinity, and the probability of a material transition approaches 1.

The exponentially varying radius distribution behaves differently. Because the radius distribution has infinite support, the resulting chord length distribution also has infinite support, and the hazard function in Eq. (3.19c) does not diverge at a finite value of s. Instead, it approaches a finite limiting value:

$$h_i(s) = \frac{4s}{\lambda_i(\lambda_i + 2s)} \quad \Longrightarrow \quad \lim_{s\to\infty} h_i(s) = \frac{2}{\lambda_i}. \tag{3.20}$$

Thus, the exponentially varying radius distribution is still non-Markovian, since the hazard depends on the distance since the previous renewal s, but its large-s behavior approaches a constant transition rate rather than diverging.

Stationarity, Homogeneity, and Equilibrium Distributions

For transport calculations in stochastic media, it is usually desirable to construct random geometries that are statistically homogeneous and stationary. Homogeneity means that one-point material statistics, such as volume fractions, do not depend on absolute spatial position; stationarity is the stronger statement that the full statistical description is invariant under translations of the spatial origin [28]. These assumptions are standard in stochastic media transport literature because they allow volume fractions, chord length distributions, and interface densities to be interpreted as intrinsic properties of the random medium rather than artifacts of a particular domain placement [11, 12].

A subtle but important issue arises when constructing a finite domain from a renewal process. If the left boundary of the domain is assumed to coincide with a material interface, then the first chord length in material i may be sampled directly from the chord length

density $f_i(s)$. However, if the domain is interpreted as a finite piece of an infinite statistically stationary medium, then the left boundary will generally lie inside a material chord rather than at an interface. In that case, the distance from the boundary to the next interface is not distributed according to $f_i(s)$. Sampling the first chord directly from $f_i(s)$ would bias the boundary statistics because it would treat the boundary as if it were located at an interface rather than at a random point inside a stationary medium. This is the spatial analog of the inspection paradox in renewal theory [24, 29].

Suppose that a point is chosen uniformly at random in a stationary renewal medium and is found to lie in material i. Let $A_i(s)$ denote the probability density for the forward distance from that point to the next material interface. This distribution is often called the residual life [24], but in our case, we will call it the equilibrium distribution, or the equilibrium age distribution. For chord length density $f_i(s)$, survival function $S_i(s)$, and mean chord length λ_i, the equilibrium distribution is

$$A_i(s) = \frac{1}{\lambda_i} \int_s^\infty f_i(u)\, du = \frac{S_i(s)}{\lambda_i}. \tag{3.21}$$

Equation (3.21) accounts for the fact that a randomly selected point in the medium is more likely to lie in a long chord than in a short chord. If the total chord length is x, then a randomly selected point within that chord has a forward distance to the next interface between 0 and x. Therefore, the probability that the forward distance exceeds s is determined by all chords with total length greater than s. Averaging over the chord length distribution gives a density proportional to the survival function $S_i(s)$, and normalization by the mean chord length λ_i gives Eq. (3.21) [24, 25].

For exponential chord lengths, the equilibrium distribution reduces to the original chord length distribution:

$$A_i(s) = \frac{1}{\lambda_i} e^{-s/\lambda_i} = f_i(s). \tag{3.22}$$

This equality is an expression of the memoryless property of the exponential distribution. For non-exponential renewal media, $A_i(s) \neq f_i(s)$ in general. Thus, in a stationary non-Markovian medium, the distribution of the first chord encountered from a random point differs from the distribution of full material chords generated at interfaces. This distinction must be accounted for when constructing benchmark realizations or sampling initial interface distances in renewal statistical media.

Volume Fractions from Renewal Reward Theory

Renewal reward theory provides a convenient way to relate chord length statistics to spatially averaged properties of an alternating renewal medium. In its simplest form, the renewal reward theorem states that if X_n denotes a sequence of renewal intervals with mean $E[X]$, and R_n denotes a reward accumulated over the nth interval, then the long-run reward per unit distance is [24]

$$\lim_{x\to\infty} \frac{\sum_{n=1}^{N(x)} R_n}{x} = \frac{E[R]}{E[X]}. \tag{3.23}$$

In the stochastic media setting, the renewal reward theorem can be applied directly to an alternating sequence of material chords. Rather than interpreting x as time, we interpret it as distance along a line through the medium. A "cycle" consists of one chord of material 0 followed by one chord of material 1. If X_0 and X_1 denote the corresponding chord lengths, then the mean cycle length is

$$E[X_0 + X_1] = \lambda_0 + \lambda_1. \tag{3.24}$$

The long-run volume fraction of a material is obtained by choosing the reward to be the length of the cycle occupied by that material. For material 0, the reward is $R_0 = X_0$, so

$$p_0 = \frac{E[X_0]}{E[X_0 + X_1]} = \frac{\lambda_0}{\lambda_0 + \lambda_1}. \tag{3.25}$$

Similarly,

$$p_1 = \frac{E[X_1]}{E[X_0 + X_1]} = \frac{\lambda_1}{\lambda_0 + \lambda_1}. \tag{3.26}$$

Thus, for a homogeneous binary alternating renewal medium,

$$p_i = \frac{\lambda_i}{\lambda_0 + \lambda_1}, \qquad i = 0, 1. \tag{3.27}$$

Equation (3.27) shows that, for a homogeneous alternating renewal mixture, the stationary material volume fractions are determined by the mean chord lengths alone. This result is standard in stochastic media transport literature [9, 11, 12, 10]. In more general nonhomogeneous statistical descriptions, including those treated by the generalized master equation formulation introduced later, the material probabilities may vary with position and are not necessarily fixed constants determined only by the mean chord lengths.

For the homogeneous media considered here, Eq. (3.27) is useful because it allows the average material composition of the medium to be specified independently of the detailed shape of the chord length distributions. However, the mean chord lengths do not fully determine the renewal medium. For Markovian media, the mean chord length completely specifies the exponential chord length distribution. For general renewal media, infinitely many chord length distributions can share the same mean while having different variances, survival functions, and hazard functions. Consequently, two media may have the same volume fractions but different interface statistics and different transport behavior.

This distinction is central to the motivation for renewal stochastic transport. The volume fractions p_i describe only the average amount of each material present in the medium. They do not describe how that material is spatially arranged, how long material chords tend to persist, or how the probability of encountering an interface changes with distance traveled

through a chord. Transport observables such as reflection, transmission, absorption, and scalar flux may therefore depend on the full chord length distributions, not only on the volume fractions or mean chord lengths. In particular, the conditional probability of remaining in material i for an additional distance x after already traveling distance s is

$$P(X_i > s + x \mid X_i > s) = \frac{S_i(s + x)}{S_i(s)}. \tag{3.28}$$

This quantity depends on the full survival function, not merely on λ_i. The Markovian approximation represents the geometry using mean chord lengths and constant transition rates, whereas renewal theory retains the distributional information needed to represent geometric memory.

3.3 Markov Processes and Markovian Media

The preceding section described binary stochastic media as alternating renewal processes, in which material interfaces occur after random chord lengths sampled from material-dependent distributions. This formulation is general enough to include non-exponential chord statistics. A particularly important special case occurs when both chord length distributions are exponential. In that case, the renewal process becomes a Poisson process in space, the hazard function is constant, and the material state along a line possesses the Markov property. Markovian random media are therefore not a separate class of stochastic media, but rather the exponential distribution limit of the alternating renewal construction. This section reviews the Markov process concepts needed to make that connection precise.

Markov Processes

A stochastic process is Markovian if the present state contains all information needed to determine the probability law for future states. For a discrete-time process, this means that the conditional distribution of the next state depends only on the current state and not on the full sequence of states visited previously. If $\{X_n\}_{n=0}^{\infty}$ is a discrete-time Markov chain, then

$$P(X_{n+1} = j \mid X_n = i, X_{n-1} = i_{n-1}, \ldots, X_0 = i_0) = P(X_{n+1} = j \mid X_n = i). \tag{3.29}$$

This discrete-time definition is useful for introducing the basic idea of the Markov property, but the stochastic-media models considered in this dissertation are more closely related to continuous-time Markov chains, with spatial distance playing the role of time.

For a continuous-time Markov chain, transitions may occur at arbitrary values of the independent variable. Following the usual definition, it is convenient to state the Markov property by conditioning on a finite set of past observation times. Let $0 \leq s_0 < s_1 < \cdots <$

$s_n < s$ denote previous observation times, and suppose the process is in state i at the present time s. A time-homogeneous continuous-time Markov chain satisfies

$$P(X_{s+t} = j \mid X_s = i, X_{s_n} = i_n, \ldots, X_{s_0} = i_0) = P(X_t = j \mid X_0 = i). \tag{3.30}$$

In words, given the present state $X_s = i$, the rest of the past is irrelevant for predicting the future. Time homogeneity means that the transition probability depends only on the elapsed interval t, not on the absolute time s at which the interval begins [24, 28, 29].

For a continuous-time Markov chain, the transition probability over elapsed time t is denoted

$$P_{ij}(t) = P(X_t = j \mid X_0 = i). \tag{3.31}$$

The matrix $\mathbf{P}(t) = [P_{ij}(t)]$ is the transition probability matrix. Its entries satisfy

$$P_{ij}(t) \geq 0, \qquad \sum_j P_{ij}(t) = 1, \tag{3.32}$$

because the process must occupy one of the possible states at time t.

The infinitesimal behavior of a continuous-time Markov chain is described by transition rates. For $i \neq j$, let q_{ij} denote the rate of transition from state i to state j. Then, for an incremental time dt [29],

$$P_{ij}(dt) = q_{ij}dt + o(dt), \qquad i \neq j, \tag{3.33}$$

while the probability of remaining in state i is

$$P_{ii}(dt) = 1 - \sum_{j \neq i} q_{ij}dt + o(dt). \tag{3.34}$$

The generator matrix $\mathbf{Q} = [q_{ij}]$ is defined by the off-diagonal transition rates q_{ij} and by diagonal entries chosen so that probability is conserved:

$$q_{ii} = -\sum_{j \neq i} q_{ij}. \tag{3.35}$$

Thus, each row of $\mathbf{Q}$ sums to zero. For a binary continuous-time Markov chain with transition rates q_{01} and q_{10}, the generator is

$$\mathbf{Q} = \begin{bmatrix} -q_{01} & q_{01} \\ q_{10} & -q_{10} \end{bmatrix}. \tag{3.36}$$

For the case of binary Markovian medium with mean chord lengths λ_0 and λ_1, the spatial transition rates are

$$q_{01} = \frac{1}{\lambda_0}, \qquad q_{10} = \frac{1}{\lambda_1}. \tag{3.37}$$

Therefore, the generator is

$$\mathbf{Q}_x = \begin{bmatrix} -1/\lambda_0 & 1/\lambda_0 \\ 1/\lambda_1 & -1/\lambda_1 \end{bmatrix}. \tag{3.38}$$

This generator encodes the constant interface-crossing rates implied by exponential chord length statistics and directly connects to the hazard function interpretation in Section 3.2.

Chapman-Kolmogorov Equations

The Chapman-Kolmogorov equation expresses the composition property of Markov transition probabilities. Suppose a time-homogeneous continuous-time Markov chain begins in state i at time 0. The probability of being in state j after elapsed time $t+\tau$ can be computed by conditioning on the intermediate state occupied after time t. Using the transition probabilities defined in Eq. (3.31), this gives

$$P_{ij}(t+\tau) = \sum_k P_{ik}(t) P_{kj}(\tau). \tag{3.39}$$

This is the Chapman-Kolmogorov equation for a discrete state space [28]. The summation accounts for all possible intermediate states k. The Markov property is essential: once the intermediate state is specified, the probability of evolving from k to j over the remaining interval τ is independent of how the process reached k.

For continuous state spaces, the same idea holds with an integral over intermediate states replacing the sum. If $p(x, t \mid x_0, 0)$ is the transition probability density for a continuous-state Markov process, then

$$p(x, t+\tau \mid x_0, 0) = \int p(x, t+\tau \mid y, t)\, p(y, t \mid x_0, 0)\, dy. \tag{3.40}$$

For homogeneous processes, this equation may be written in terms of elapsed intervals rather than absolute times. The binary material process considered in stochastic media has a discrete state space, but this continuous-state form is useful conceptually because later transport formulations involve continuous phase-space variables in addition to the discrete material index.

In the spatial setting, Eq. (3.39) applies with distance replacing time. If $P_{ij}(x)$ is the probability that a line beginning in material i is in material j after distance x, then the probability of being in material j after a total distance $x+x'$ can be decomposed by conditioning on the material state after the intermediate distance x. The spatial Chapman-Kolmogorov equation is

$$P_{ij}(x+x') = \sum_k P_{ik}(x) P_{kj}(x'). \tag{3.41}$$

This equation is valid when the material process is Markovian. For the renewal media considered in this dissertation, that occurs only in the exponential chord length case.

Forward Master Equation

In the stochastic-media setting, the independent variable is spatial distance rather than time. The forward master equation therefore follows from the spatial Chapman-Kolmogorov equation by taking the second spatial interval to be infinitesimal. Starting from Eq. (3.41) and setting $x' = dx$ gives

$$P_{ij}(x+dx) = \sum_k P_{ik}(x) P_{kj}(dx). \tag{3.42}$$

Then, using the spatial analog of Eqs. (3.33) and (3.34), with dt replaced by dx and q_{ij} interpreted as a rate per unit distance, substituting Eqs. (3.33) and (3.34) into Eq. (3.42) gives

$$P_{ij}(x+dx) = P_{ij}(x)\left(1 - \sum_{m\neq j} q_{jm}\,dx\right) + \sum_{k\neq j} P_{ik}(x)q_{kj}\,dx + o(dx). \tag{3.43}$$

Subtracting $P_{ij}(x)$, dividing by dx, and taking the limit $dx \to 0$ yields

$$\frac{dP_{ij}}{dx} = \sum_{k\neq j} P_{ik}(x)q_{kj} - P_{ij}(x)\sum_{m\neq j} q_{jm}. \tag{3.44}$$

Using the diagonal generator entry from Eq. (3.35), Eq. (3.44) may be written compactly as

$$\frac{dP_{ij}}{dx} = \sum_{k} P_{ik}(x)q_{kj}. \tag{3.45}$$

In matrix form,

$$\frac{d\mathbf{P}}{dx} = \mathbf{P}(x)\mathbf{Q}_x. \tag{3.46}$$

This is the forward master equation for the spatial transition probability matrix. It describes how the probability distribution over material states evolves as one moves through a Markovian random medium.

The same gain-loss structure may be written for the unconditional material probability $P_j(x) = P(M(x) = j)$. In component form,

$$\frac{dP_j}{dx} = \sum_{k\neq j} q_{kj}P_k - \sum_{k\neq j} q_{jk}P_j. \tag{3.47}$$

The first term represents probability entering material state j from other material states, while the second term represents probability leaving material state j for other material states. Thus, the forward master equation is a deterministic balance equation for the probabilities associated with a stochastic material switching process.

For the binary Markovian medium with generator given in Eq. (3.38), Eq. (3.47) becomes

$$\frac{dP_0}{dx} = \frac{1}{\lambda_1}P_1 - \frac{1}{\lambda_0}P_0, \tag{3.48}$$

$$\frac{dP_1}{dx} = \frac{1}{\lambda_0}P_0 - \frac{1}{\lambda_1}P_1. \tag{3.49}$$

These equations state that the probability of being in material 0 increases when realizations transition from material 1 to material 0, and decreases when realizations transition from material 0 to material 1.

For a stationary Markov process, $dP_0/dx = dP_1/dx = 0$ with $P_0 + P_1 = 1$, giving

$$p_0 = \frac{\lambda_0}{\lambda_0 + \lambda_1}, \qquad p_1 = \frac{\lambda_1}{\lambda_0 + \lambda_1}. \tag{3.50}$$

This agrees with the volume-fraction result obtained from the alternating renewal construction.

The significance of Eq. (3.47) is that it converts the random material switching process into a closed balance equation for material-state probabilities. In a Markovian medium, the material label is a closed state variable: once $M(x)$ is known, the probability of encountering the next interface is determined by the constant rate $1/\lambda_i$. Equivalently, the material process has a constant hazard in each material, so the future interface statistics depend only on the current material state and not on the distance already traveled through the current chord.

This interpretation is the statistical basis for classical Markovian stochastic transport models. In those models, material interfaces again act as transitions between material states, but the quantities being balanced are material-conditioned transport quantities rather than only material probabilities. The gain and loss terms in the master equation become coupling terms between material-conditioned angular fluxes, representing particles crossing from one material state into another along their trajectories.

For general renewal media, however, Eq. (3.47) is not closed in the material probabilities alone. The transition rate is no longer a constant $1/\lambda_i$, but instead depends on the distance from the previous renewal point through the hazard function $h_i(s)$. Thus, the material label $M(x)$ alone is insufficient to determine the future interface statistics. The generalized master-equation formulation developed later in this dissertation extends the state space from the material label $M(x)$ to an augmented state containing both the material and the distance from the previous interface. In that extended description, the constant Markovian rates are replaced by age-dependent hazard functions, and moments of the resulting equation provide ensemble-averaged transport quantities.

Poisson Processes and Exponential Waiting Times

The Poisson process provides the simplest example of a continuous-time Markov chain with a countably infinite state space. Let $N(t)$ denote the number of events that have occurred by time t. For a homogeneous Poisson process with rate Λ, the state of the process is the event count,

$$N(t) \in \{0, 1, 2, \ldots\}. \tag{3.51}$$

The process is Markovian because, given the current number of events, the distribution of future increments is independent of the past. In the continuous-time Markov-chain interpretation, the Poisson process is a pure birth process: from state n, the only possible transition is to state $n + 1$, and this transition occurs at rate Λ [29]. Thus,

$$q_{n,n+1} = \Lambda, \qquad q_{n,n} = -\Lambda, \qquad q_{n,m} = 0 \quad \text{otherwise.} \tag{3.52}$$

Equivalently, over an infinitesimal interval dt,

$$P(N(t+dt) = n+1 \mid N(t) = n) = \Lambda\, dt + o(dt), \tag{3.53}$$

$$P(N(t+dt) = n \mid N(t) = n) = 1 - \Lambda\, dt + o(dt). \tag{3.54}$$

This is the counting-process analog of the infinitesimal transition-rate description introduced above for continuous-time Markov chains.

The connection to exponential waiting times follows directly from the constant escape rate. Let T denote the waiting time from one event to the next. The probability of no event occurring over an additional interval dt, conditional on no event having occurred up to time t, is $1 - \Lambda dt + o(dt)$. If

$$S(t) = P(T > t) \tag{3.55}$$

is the survival probability for the waiting time, then

$$S(t+dt) = S(t)\,(1 - \Lambda dt) + o(dt). \tag{3.56}$$

Subtracting $S(t)$, dividing by dt, and taking the limit gives

$$\frac{dS}{dt} = -\Lambda S. \tag{3.57}$$

With $S(0) = 1$, this gives

$$S(t) = e^{-\Lambda t}, \tag{3.58}$$

and therefore

$$f(t) = -\frac{dS}{dt} = \Lambda e^{-\Lambda t}. \tag{3.59}$$

Thus, the waiting times between events in a homogeneous Poisson process are exponentially distributed with mean $1/\Lambda$ [29]. This is the probabilistic origin of the memoryless property.

In stochastic media, the same construction is applied with distance replacing time. Let $N_i(x)$ denote the number of material interfaces encountered after traveling distance x through material i under the assumption that interfaces are encountered with constant rate

$$\Lambda_i = \frac{1}{\lambda_i} \tag{3.60}$$

per unit distance. In a Markovian random medium, the interface-counting process is therefore a spatial Poisson process. If X_i denotes the distance to the next interface while in material i, then Eq. (3.59) gives

$$f_i(s) = \Lambda_i e^{-\Lambda_i s} = \frac{1}{\lambda_i} e^{-s/\lambda_i}. \tag{3.61}$$

This is precisely the exponential chord length distribution introduced in Eq. (3.16). The Poisson-process viewpoint therefore gives an equivalent characterization of Markovian mixing: material interfaces occur independently with constant probability per unit distance, and the resulting chord lengths are exponentially distributed.

The memoryless property follows from the exponential survival function. If $S_i(s) = e^{-s/\lambda_i}$, then

$$\begin{aligned} P(X_i > s + x \mid X_i > s) &= \frac{P(X_i > s + x)}{P(X_i > s)} \\ &= \frac{e^{-(s+x)/\lambda_i}}{e^{-s/\lambda_i}} \\ &= e^{-x/\lambda_i} \\ &= P(X_i > x). \end{aligned} \tag{3.62}$$

In words, the remaining distance to the next interface is independent of the distance already traveled through the current material. This memoryless property is the reason the material label alone is a closed Markov state variable in Markovian stochastic media. For renewal media with non-exponential chord length distributions, the interface process is no longer Poisson, the hazard is not constant, and the distance already traveled through the current chord must be retained as part of the state description.

Augmented Markov Description of Renewal Media

The preceding sections show that Markovian random media arise when the material chord lengths are exponentially distributed. In that case, the material label $M(x)$ is a closed Markov state variable: once the current material is known, the distribution of the next interface is determined by the constant transition rate $1/\lambda_i$. For a general renewal medium, this closure is lost because the probability of encountering the next interface depends on the distance already traveled through the current material segment.

A standard way to recover a Markov description for such a non-Markovian process is to augment the state space with supplementary variables. Cox described this approach for continuous-time stochastic processes with non-exponential lifetimes, noting that certain non-Markovian processes can be converted into Markov processes by including sufficient supplementary variables, such as elapsed lifetimes, in the specification of the state [30]. In the present spatial setting, the analogous supplementary variable is the material age s, defined as the distance traveled since the previous material interface.

The augmented material state is therefore

$$(M(x), s)\,. \tag{3.63}$$

Between interfaces, the material label remains fixed and the age increases deterministically:

$$\frac{ds}{dx} = 1. \tag{3.64}$$

At an interface, the material label switches and the age is reset to zero. If the process is currently in material i with age s, then the probability of encountering an interface over the next incremental distance dx is

$$P(M(x + dx) = j \mid M(x) = i, s) = h_i(s)dx + o(dx), \qquad i \neq j. \tag{3.65}$$

Equation (3.65) is the local transition probability for the augmented material process, which fully describes the evolution of the future stochastic material state. Thus, while the material label $M(x)$ alone is not generally Markovian, the alternating renewal process of materials is Markovian on the enlarged state space (M, s). For exponential media, the hazard is constant and this augmented description reduces to the ordinary Poisson material process in Eq. (3.54); for non-exponential renewal statistics, the age variable carries the geometric memory necessary for accurate representation of renewal media. This is the key observation underlying the generalized master equation formulation developed later, where the transport state is augmented by the distance from the previous renewal point s to Markovianize the system.

This Markovianization should be understood as a statement about the material sequence along a specified spatial path. When scattering is introduced, particles may backscatter and revisit regions of space that have already been sampled. As such, the evolution of the joint stochastic process does not depend solely on the current state, but also on future states where particles have backscattered. This means that, even for Markovian media, stochastic media transport descriptions with backscattering particles cannot be exact. This issue, referred to as transport memory, is discussed further in Section 4.3.

3.4 Summary

This Chapter developed the statistical framework used to describe the immiscible random media considered in this dissertation. Along a line through the medium, material interfaces are renewal points and material chord lengths are renewal intervals. For binary mixtures, the appropriate model is an alternating renewal process in which material chords alternate between materials 0 and 1 and are sampled from material-dependent chord length distributions.

The chord length density $f_i(s)$, survival function $S_i(s)$, and hazard function $h_i(s)$ provide equivalent but complementary descriptions of the material statistics. The hazard function is especially important for transport because it gives the conditional interface-crossing rate after a particle has already traveled distance s through the current material. For exponential chord lengths, the hazard function is constant, and the medium is Markovian. For non-exponential renewal statistics, the hazard function depends on the distance from the previous renewal point, so the material state alone does not determine the future interface statistics.

Markovian media were then identified as the exponential-renewal special case. In this limit, material interfaces form a spatial Poisson process, the material label $M(x)$ fully determines the future state of the stochastic process, and the Chapman-Kolmogorov equation leads to a forward master equation for material probabilities. This master equation is a deterministic gain-loss balance over material states, with constant transition rates determined by the inverse mean chord lengths.

For general renewal media, the material label alone is not sufficient to determine future interface statistics. The state must also include the distance s from the previous renewal

point. This state augmentation is the spatial analog of the supplementary-variable method for non-Markovian stochastic processes. It provides the conceptual bridge to the generalized master-equation formulation developed later in the dissertation, where constant Markovian transition rates are replaced by age-dependent hazard functions.

Chapter 4

Transport in Markovian Random Media

4.1 Introduction

This Chapter reviews the classical transport models for binary Markovian random media. In the statistical language of Chapter 3, a Markovian random medium is the exponentially distributed case of an alternating renewal process. The material interfaces along a line occur with constant transition rate $1/\lambda_i$ in material i, and the material state is memoryless. This property underlies the Levermore-Pomraning (LP) closure and its Monte Carlo analogs, Chord Length Sampling (CLS) and Local Realization Preserving (LRP).

The Chapter begins with ensemble averaging of the realization transport equation and the atomic mix approximation. It then derives the LP material-conditioned equations and discusses their connection to Markov process theory. The Monte Carlo algorithms CLS and LRP are then reviewed as stochastic realizations or memory-improved extensions of the same Markovian transition model. Finally, the Chapter discusses attempts to adapt these classical methods to renewal media, including renewal-aware sampling modifications and q-factor corrections. These additions clarify why classical Markovian transport methods are useful foundations but incomplete descriptions of non-Markovian renewal statistical media.

4.2 The Atomic Mix Approximation

The most straightforward approach to modeling particle transport in stochastic media is the atomic mix approximation. Rather than attempting to resolve the random geometry or derive equations for ensemble-averaged quantities, the medium is replaced by a homogeneous material whose properties are obtained by volume fraction averaging.

We return to the realization-dependent transport equation given in Eq. (2.9), where the material properties are expressed in terms of the indicator functions $\chi_i(\mathbf{r}, \omega)$. The primary quantity of interest in stochastic media transport is the ensemble-averaged angular flux $\langle\psi\rangle$,

$$\langle \psi(\mathbf{r}, \mathbf{\Omega}) \rangle = \int \psi(\mathbf{r}, \mathbf{\Omega}, \omega) P(\omega) d\omega = \mathbb{E}_\omega[\psi(\mathbf{r}, \mathbf{\Omega}, \omega)], \tag{4.1}$$

which is obtained by averaging over all realizations of the stochastic medium. For notational convenience, we suppress explicit dependence on the phase-space variables $(\mathbf{r}, \mathbf{\Omega})$ in what follows, except where needed for clarity.

A natural approach is therefore to ensemble-average Eq. (2.9). Substituting the realization-dependent material properties in Eq. (2.8) and averaging yields

$$\mathbf{\Omega} \cdot \nabla \langle \psi \rangle + \sum_{i=0}^{1} \Sigma_{t,i} \langle \chi_i \psi \rangle = \sum_{i=0}^{1} \frac{\Sigma_{s,i}}{4\pi} \int_{4\pi} \langle \chi_i \psi \rangle \, d\mathbf{\Omega}' + \sum_{i=0}^{1} \langle \chi_i \rangle Q_i. \tag{4.2}$$

At this point, a closure problem arises. In order to calculate the ensemble-averaged flux $\langle \psi \rangle$, one must evaluate the mixed moments $\langle \chi_i \psi \rangle$, which couple the random material configuration to the transport solution. These terms represent correlations between the random medium and the angular flux, and their evaluation requires knowledge of the joint statistics of the medium and the transport process. As emphasized in Ref. [8], this cross-correlation is the central obstacle to deriving closed equations for the ensemble-averaged flux.

To make this more explicit, we decompose the random variables into mean and fluctuating components,

$$\chi_i = \langle \chi_i \rangle + \tilde{\chi}_i, \quad \psi = \langle \psi \rangle + \tilde{\psi}, \tag{4.3}$$

where $\langle \tilde{\chi}_i \rangle = 0$ and $\langle \tilde{\psi} \rangle = 0$. Substituting into the mixed moment yields

$$\langle \chi_i \psi \rangle = \langle \chi_i \rangle \langle \psi \rangle + \langle \tilde{\chi}_i \tilde{\psi} \rangle. \tag{4.4}$$

The second term, $\langle \tilde{\chi}_i \tilde{\psi} \rangle$, represents the cross-correlation between fluctuations in the material configuration and fluctuations in the angular flux. It is precisely this term that prevents Eq. (4.2) from being closed in terms of $\langle \psi \rangle$ alone.

The atomic mix approximation is obtained by neglecting the cross-correlation between the random materials and the angular flux. Specifically, we assume

$$\langle \chi_i \psi \rangle \approx \langle \chi_i \rangle \langle \psi \rangle. \tag{4.5}$$

Defining the material probabilities (volume fractions)

$$p_i(\mathbf{r}) = \langle \chi_i(\mathbf{r}, \omega) \rangle, \qquad p_0 + p_1 = 1, \tag{4.6}$$

Eq. (4.2) reduces to

$$\mathbf{\Omega} \cdot \nabla \langle \psi \rangle + \overline{\Sigma}_t \langle \psi \rangle = \frac{\overline{\Sigma}_s}{4\pi} \int_{4\pi} \langle \psi(\mathbf{r}, \mathbf{\Omega}') \rangle \, d\mathbf{\Omega}' + \overline{Q}(\mathbf{r}, \mathbf{\Omega}), \tag{4.7}$$

where the volume fraction averaged material properties are given by

$$\overline{\Sigma}_t = \sum_{i=0}^{1} p_i \Sigma_{t,i}, \quad \overline{\Sigma}_s = \sum_{i=0}^{1} p_i \Sigma_{s,i}, \quad \overline{Q} = \sum_{i=0}^{1} p_i Q_i. \tag{4.8}$$

Eq. (4.7) is simply the classical transport equation in a homogeneous medium with volume fraction averaged material properties. This approximation corresponds to treating the stochastic medium as if it were perfectly mixed at arbitrarily small scales, such that particles experience only the average material properties.

Limitations of Atomic Mix

The atomic mix assumption is only justified when the characteristic length scale of material heterogeneity is much smaller than the particle mean free path. In this limit, particles sample many material regions over a single flight distance, and the medium behaves as though it were homogenized at the microscopic level [8]. Outside of this regime, however, the approximation breaks down.

In particular, neglecting cross-correlations leads to some well-known issues. Most importantly, the atomic mix approximation fails to account for the fact that particles traverse finite material segments rather than an infinitesimally mixed medium. As a result, it cannot accurately capture transport through extended regions of low opacity (low cross section) material interspersed with sparse, highly absorbing inclusions. In these systems, particles may stream through the low opacity regions and avoid the absorbing inclusions, leading to a high probability of transmission. In contrast, the atomic mix model predicts attenuation based on the volume fraction averaged cross section, and therefore severely underestimates transmission [8]. Additionally, because the size of material segments is disregarded, the atomic mix model results in identical transport solutions for problems with the same cross sections but different material segment lengths/distributions [10, 13].

The preceding discussion highlights the central challenge in stochastic media transport: the appearance of cross-correlation terms that arise from ensemble averaging. The atomic mix approximation provides the simplest possible closure by neglecting these terms entirely. However, its deficiencies demonstrate that a more accurate treatment must explicitly account for the interaction between material statistics and particle transport.

Thus, the problem of stochastic transport reduces to the development of models or computational methods capable of approximating or resolving the mixed moments $\langle \chi_i \psi \rangle$. The next section examines the classical closure model from Levermore and Pomraning, which provides a tractable approximation to these terms.

4.3 The Levermore-Pomraning Closure

The discussion in the previous section makes clear that the central difficulty in stochastic transport lies in the evaluation of the mixed moments $\langle \chi_i \psi \rangle$. The atomic mix approxima-

tion provides the simplest possible closure by neglecting the cross-correlation term entirely. However, as discussed previously, this approximation fails to account for the stochastic, heterogeneous nature of the medium. A more refined approach is therefore required to model the interaction between the material statistics and transport.

A classical closure model that addresses this issue is the Levermore-Pomraning (LP) model [8, 9]. Rather than closing the equation for the total ensemble-averaged flux directly, the LP model derives equations for fluxes conditioned on the material present at a point in space. We define the material-conditioned angular fluxes by

$$\langle \chi_i \psi \rangle = p_i \psi_i, \qquad p_i = \langle \chi_i \rangle, \tag{4.9}$$

so that

$$\langle \psi \rangle = \sum_{i=0}^{1} p_i \psi_i. \tag{4.10}$$

To obtain equations for the conditioned fluxes, we multiply the realization-specific transport equation Eq. (2.9) by χ_i and ensemble average. This gives

$$\langle \chi_i \mathbf{\Omega} \cdot \nabla \psi \rangle + \langle \chi_i \Sigma_t \psi \rangle = \frac{1}{4\pi} \left\langle \chi_i \Sigma_s \int_{4\pi} \psi(\mathbf{r}, \mathbf{\Omega}')\, d\mathbf{\Omega}' \right\rangle + \langle \chi_i Q \rangle \,. \tag{4.11}$$

Substituting the realization-dependent material properties from Eq. (2.8) into Eq. (4.11) and using the properties

$$\chi_i \chi_i = \chi_i, \qquad \chi_i \chi_j = 0, \quad i \neq j, \tag{4.12}$$

allows us to simplify the collision, scattering, and source terms in Eq. (4.11) considerably.

For the collision term,

$$\begin{aligned} \langle \chi_i \Sigma_t \psi \rangle &= \langle \chi_i \chi_i \Sigma_{t,i} \psi \rangle + \langle \chi_i \chi_j \Sigma_{t,j} \psi \rangle \\ &= \Sigma_{t,i} \langle \chi_i \psi \rangle \\ &= p_i \Sigma_{t,i} \psi_i, \qquad i \neq j. \end{aligned} \tag{4.13}$$

Similarly, the scattering source term becomes

$$\begin{aligned} \frac{1}{4\pi} \left\langle \chi_i \Sigma_s \int_{4\pi} \psi(\mathbf{r}, \mathbf{\Omega}')\, d\mathbf{\Omega}' \right\rangle &= \frac{1}{4\pi} \left\langle \chi_i \left(\sum_{k=0}^{1} \chi_k \Sigma_{s,k} \right) \int_{4\pi} \psi(\mathbf{r}, \mathbf{\Omega}')\, d\mathbf{\Omega}' \right\rangle \\ &= \frac{\Sigma_{s,i}}{4\pi} \int_{4\pi} \langle \chi_i \psi(\mathbf{r}, \mathbf{\Omega}') \rangle \; d\mathbf{\Omega}' \\ &= \frac{p_i \Sigma_{s,i}}{4\pi} \int_{4\pi} \psi_i(\mathbf{r}, \mathbf{\Omega}')\, d\mathbf{\Omega}'. \end{aligned} \tag{4.14}$$

The source term simply reduces to

$$\langle \chi_i Q \rangle = p_i Q_i. \tag{4.15}$$

Finally, we consider the streaming term, which can be expressed as

$$\begin{aligned}\langle \chi_i \mathbf{\Omega} \cdot \nabla \psi \rangle &= \langle \chi_i \nabla \cdot [\mathbf{\Omega} \psi] \rangle \\ &= \langle \nabla \cdot [\mathbf{\Omega} \chi_i \psi] \rangle - \langle \psi \, \mathbf{\Omega} \cdot \nabla \chi_i \rangle \\ &= \nabla \cdot [\mathbf{\Omega} \langle \chi_i \psi \rangle] - \langle \psi \, \mathbf{\Omega} \cdot \nabla \chi_i \rangle \\ &= \mathbf{\Omega} \cdot \nabla [p_i \psi_i] - \langle \psi \, \mathbf{\Omega} \cdot \nabla \chi_i \rangle . \end{aligned} \tag{4.16}$$

The final term in Eq. (4.16), $\langle \psi \, \mathbf{\Omega} \cdot \nabla \chi_i \rangle$, is called the interface term. Since χ_i is discontinuous across material boundaries, the quantity $\nabla \chi_i$ reduces to a sum of delta functions at material interfaces, with the sign determined by whether the interface corresponds to a transition from material i to material j or vice versa. Consequently, this term represents the net contribution from particles crossing material interfaces. The conditional average of this quantity defines a new average flux, namely the ensemble-averaged angular flux conditioned on the particle position $\mathbf{r}$ lying at a material interface. It can be shown that the interface term may be expressed as [8, 9]

$$\langle \psi(\mathbf{r}, \mathbf{\Omega}) \, \mathbf{\Omega} \cdot \nabla \chi_i(\mathbf{r}) \rangle = \frac{p_j(\mathbf{r})}{\lambda_j(\mathbf{r})} \hat{\psi}_j(\mathbf{r}, \mathbf{\Omega}) - \frac{p_i(\mathbf{r})}{\lambda_i(\mathbf{r})} \hat{\psi}_i(\mathbf{r}, \mathbf{\Omega}), \qquad i, j = 0, 1, \quad i \neq j, \tag{4.17}$$

where $\hat{\psi}_i(\mathbf{r}, \mathbf{\Omega})$ is the ensemble-averaged angular flux conditioned on being located at an interface and approached from material i, and $\lambda_i(\mathbf{r})$ is the mean chord length of material i. Equivalently, $1/\lambda_i(\mathbf{r})$ is the interface crossing rate per unit path length for particles traveling in material i. For the simpler case of spatially homogeneous material statistics, where the material probabilities p_i and mean chord lengths λ_i are independent of position, we can write the interface term as

$$\langle \psi \, \mathbf{\Omega} \cdot \nabla \chi_i \rangle = \frac{p_j}{\lambda_j} \hat{\psi}_j - \frac{p_i}{\lambda_i} \hat{\psi}_i, \qquad i, j = 0, 1, \quad i \neq j. \tag{4.18}$$

Substituting Eqs. (4.13) through (4.18) into Eq. (4.11) gives the exact material-conditioned balance equation

$$\mathbf{\Omega} \cdot \nabla (p_i \psi_i) + p_i \Sigma_{t,i} \psi_i = \frac{p_i \Sigma_{s,i}}{4\pi} \int_{4\pi} \psi_i(\mathbf{r}, \mathbf{\Omega}') \, d\mathbf{\Omega}' + \frac{p_j}{\lambda_j} \hat{\psi}_j - \frac{p_i}{\lambda_i} \hat{\psi}_i + p_i Q_i, \quad i \neq j. \tag{4.19}$$

At this stage, no closure approximation has been introduced. The equation is exact, but it is not closed because it contains the interface-averaged fluxes $\hat{\psi}_i$ rather than only the material-conditioned fluxes ψ_i. This is analogous to the role played by the cross-correlation term $\langle \tilde{\chi}_i \tilde{\psi} \rangle$ in the atomic mix approximation: both terms represent unresolved correlations between the random material configuration and the angular flux that cannot be captured through simple volume-fraction averaging alone.

The LP closure is introduced by assuming that the interface-averaged flux in material i is equal to the material-conditioned flux:

$$\hat{\psi}_i \approx \psi_i. \tag{4.20}$$

With this approximation, Eq. (4.19) becomes

$$\mathbf{\Omega} \cdot \nabla(p_i\psi_i) + p_i\Sigma_{t,i}\psi_i = \frac{p_i\Sigma_{s,i}}{4\pi}\int_{4\pi} \psi_i(\mathbf{r}, \mathbf{\Omega}')\, d\mathbf{\Omega}' + \frac{p_j}{\lambda_j}\psi_j - \frac{p_i}{\lambda_i}\psi_i + p_iQ_i, \quad i \neq j. \tag{4.21}$$

This set of coupled equations for ψ_i and ψ_j Eq. (4.21) can be solved with deterministic methods (namely discrete ordinates) [9, 31], or through Monte Carlo methods [10, 15], as discussed in Section 4.4.

Exactness in the Purely Absorbing Case and Connection to Markov Process Theory

In the absence of scattering, the Levermore-Pomraning (LP) model is exact for Markovian media. Without scattering, particles travel monotonically along straight-line trajectories and do not revisit previously traversed regions. Under these conditions, the sequence of materials encountered along a particle path forms a continuous-time Markov process with transition rates determined by the inverse mean chord lengths $1/\lambda_i$. The terms proportional to $1/\lambda_i$ and $1/\lambda_j$ in Eq. (4.21) therefore represent the Markovian transition rates between materials.

In this setting, the joint process consisting of angular flux and material type, $\{\psi, M_i\}$, is Markovian, and the material-conditioned transport equations may be interpreted as a forward master equation governing the evolution of the process along a particle trajectory [8, 14]. Equivalently, the future evolution depends only on the current state and not on the prior trajectory history, consistent with the Chapman-Kolmogorov framework for Markov processes [28]. This connection has been established through both master equation formulations and direct ensemble averaging [8, 9]. As a result, the LP model provides an exact description of transport in purely absorbing Markovian mixtures.

When scattering is present, however, particles may change direction and revisit previously traversed regions of the geometry. In this case, particles arriving at an interface may carry information about material configurations encountered earlier along the trajectory or at locations further along in the geometry prior to backscattering. We refer to this history dependence of the transport process as *transport memory*. The interface-averaged angular flux $\hat{\psi}_i$ therefore depends on the particle trajectory history, and the approximation $\hat{\psi}_i \approx \psi_i$ becomes inexact. Consequently, the LP model neglects transport memory introduced by particle backscatter and may no longer accurately represent the true transport process.

The loss of exactness in the presence of scattering may therefore be understood as a consequence of the loss of the Markov property. Once particles can reverse direction, the future evolution depends on prior states along the trajectory, and the transport process is no longer Markovian in position and material state alone. The LP model may thus be viewed as a Markovian approximation to an inherently non-Markovian transport process.

Despite this approximation, the LP model has been shown to provide reasonable accuracy in many regimes, particularly when absorption dominates scattering or when material segments are not optically thick [9]. Nevertheless, significant discrepancies can arise in strongly scattering systems where transport memory plays an important role.

In summary, the Levermore-Pomraning model provides a systematic closure for the mixed moments $\langle \chi_i \psi \rangle$ by introducing material-conditioned fluxes and modeling material transitions through Markov statistics. While exact in the purely absorbing case, it becomes approximate in the presence of scattering, where transport memory introduces non-Markovian effects into the transport process. Nevertheless, the LP framework forms the classical foundation for both deterministic and Monte Carlo approaches to stochastic media transport, as discussed in the following section.

4.4 Chord Length Sampling: The Monte Carlo Analog to Levermore-Pomraning

Chord Length Sampling

The classical Chord Length Sampling (CLS) algorithm is the Monte Carlo analog of the LP model for Markovian mixtures [15, 10, 16, 17]. The idea is to sample geometry features on-the-fly rather than constructing a full realization of the stochastic medium in advance. Because Markovian media have exponential chord statistics, the distance to the next interface in material i can be sampled using the mean chord length of material i λ_i from

$$d_i = -\lambda_i \ln \xi, \qquad \xi \sim \text{Uniform}(0, 1), \tag{4.22}$$

independently for each particle segment. The memoryless property of the exponential distribution makes this resampling consistent with the Markov closure [24]. The distance to collision in Monte Carlo particle transport is similarly sampled from an exponential distribution because collision sites are assumed to be Poisson distributed [32]. If Σ_t is the total macroscopic cross section in the current material and $\xi \sim U(0, 1)$ is a pseudo-random number, then the sampled distance to collision along the particle flight path is

$$d_c = -\frac{\ln \xi}{\Sigma_t}. \tag{4.23}$$

This expression follows from the probability that an uncollided neutron/particle at x will have a collision within $x + dx$, $P(x < X < x + dx) = \Sigma_t e^{-\Sigma_t x}$ [32, 31].

It is important to distinguish between the sampled collision distance and its representation in a given geometry. In 3D, Eq. (4.23) is interpreted directly as the physical distance traveled by the particle along its flight path before collision. In 1D planar geometry, however, particle motion is only tracked along x with the direction cosine μ with respect to the x-axis. The collision distance is still sampled along the particle flight path according to Eq. (4.23), but the corresponding projected distance in the x direction is

$$d_{c,x} = |\mu| d_c, \tag{4.24}$$

where $|\mu|$ is used to keep distances positive with respect to the direction of particle movement. When comparing sampled distances in 1D planar geometry, it is therefore common to write the distance to collision in terms of the x coordinate as

$$d_{c,x} = -\frac{\ln \xi}{\Sigma_t} \cdot |\mu|. \tag{4.25}$$

Thus, the sampled free path is the same physical quantity in both 1D planar and 3D transport, but in 1D planar geometry it must be projected onto the transport axis through the factor $|\mu|$.

Algorithm 1 gives the general procedure for CLS, and Figure 4.1 gives an example particle history for CLS.

Algorithm 1 Chord Length Sampling (CLS)

for each particle history **do**
    Initialize particle location x and direction μ
    Sample initial material from volume fractions
    while particle not absorbed or escaped **do**
        Sample distance to interface d_i from Eq. (4.22)
        Sample distance to collision d_c from Eq. (4.23)
        Compute distance to boundary d_b
        $d_{\min} = \min(d_i, d_c, d_b)$
        Move particle distance $d_{\min}$
        if $d_{\min} = d_b$ **then**
            Tally leakage and terminate particle history
        else if $d_{\min} = d_c$ **then**
            if $\xi < \Sigma_a/\Sigma_t$ **then**
                Absorption: terminate particle history
            else
                Scatter: sample new direction μ
            end if
        else if $d_{\min} = d_i$ **then**
            Switch material
        end if
    end while
end for

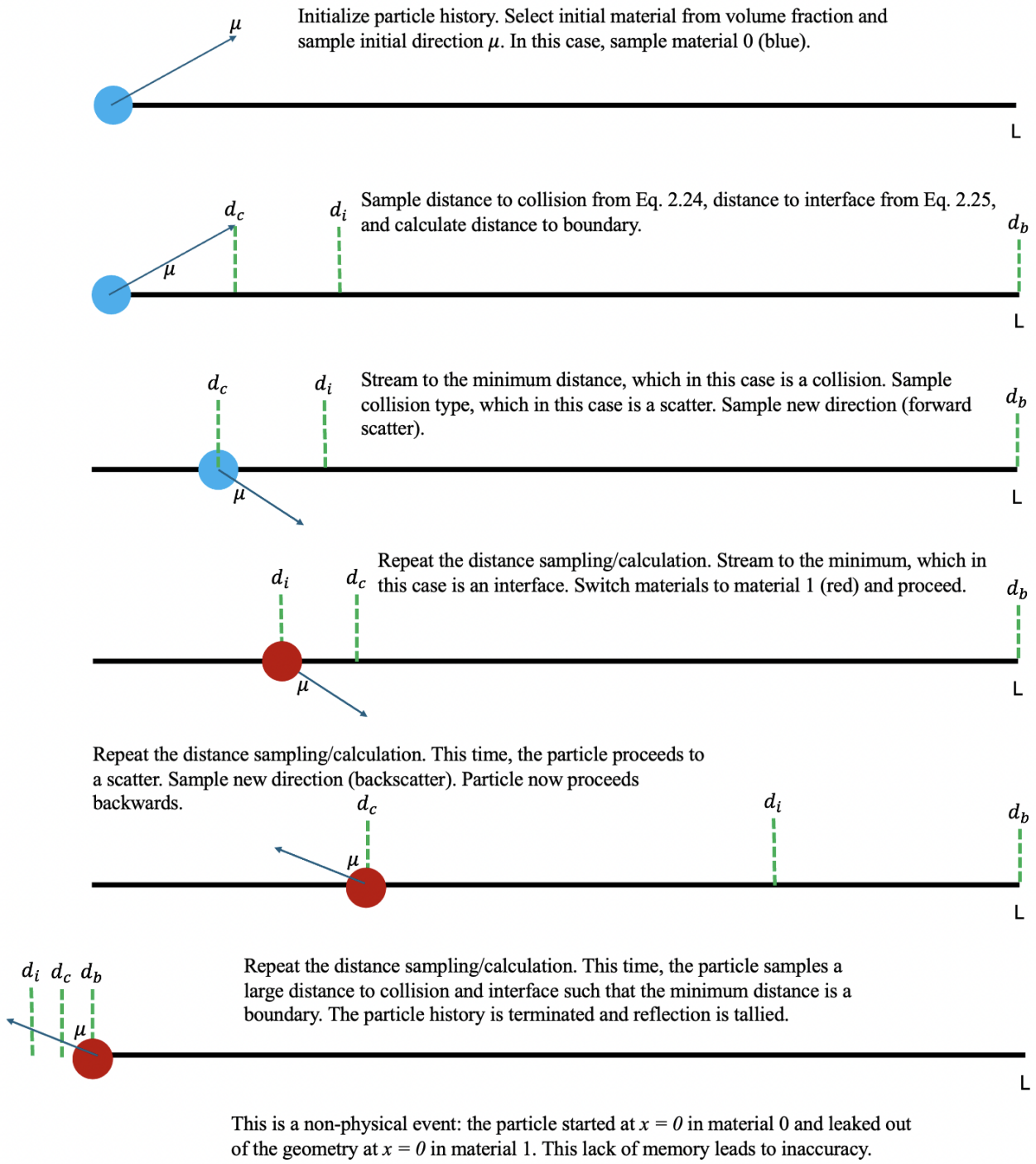


Figure 4.1: Example of a particle history for CLS algorithm.

Because the interface distance is resampled after each event, CLS does not preserve any features of the geometry [27]. That is acceptable when the particle is traveling in the forward direction in Markovian media because exponential chord lengths are memoryless, but the introduction of transport memory via particle backscatter causes inaccuracy relative to benchmark calculations and leads to non-physical events where a particle can experience two different materials at the same spatial location [10, 16]. CLS is exact in purely absorbing media, however, as the lack of particle backscatter means no transport memory is introduced.

Local Realization Preserving

The Local Realization Preserving method (LRP), often called memory-improved CLS and originally referred to as Algorithm B [15, 10], was introduced to improve the accuracy of CLS by retaining some geometric information. The key difference is that with LRP, the distance to the nearest interface in the forward and backward directions relative to the particle are stored in memory. When the particle streams, these stored distances are updated rather than resampled at every particle segment. This retention of the local geometric features around the particle reduces the number of non-physical events that occur with CLS, thereby improving accuracy. Algorithm 2 gives the general procedure for LRP, and Figure 4.2 gives an example particle history for LRP.

Algorithm 2 Local Realization Preserving (LRP)

for each particle history **do**
  Initialize particle location x and direction μ
  Sample initial material from volume fractions
  Sample forward and backward interface distances d_i^+, d_i^- from Eq. (4.22)
  while particle not absorbed or escaped **do**
    Sample distance to collision d_c from Eq. (4.23)
    Compute distance to boundary d_b
    $d_{\min} = \min(d_i^+, d_c, d_b)$
    Move particle distance $d_{\min}$
    $d_i^+ \leftarrow d_i^+ - d_{\min}, \quad d_i^- \leftarrow d_i^- + d_{\min}$
    if $d_{\min} = d_b$ **then**
      Tally leakage and terminate particle history
    else if $d_{\min} = d_c$ **then**
      if $\xi < \Sigma_a/\Sigma_t$ **then**
        Absorption: terminate particle history
      else
        Scatter: sample new direction μ_{new}
        if $\mu_{\text{new}} \cdot \mu_{\text{old}} < 0$ **then**
          Backscatter: swap d_i^+ and d_i^-
        end if
      end if
    else if $d_{\min} = d_i^+$ **then**
      Switch material
      Sample new d_i^+
      $d_i^- \leftarrow 0$
    end if
  end while
end for

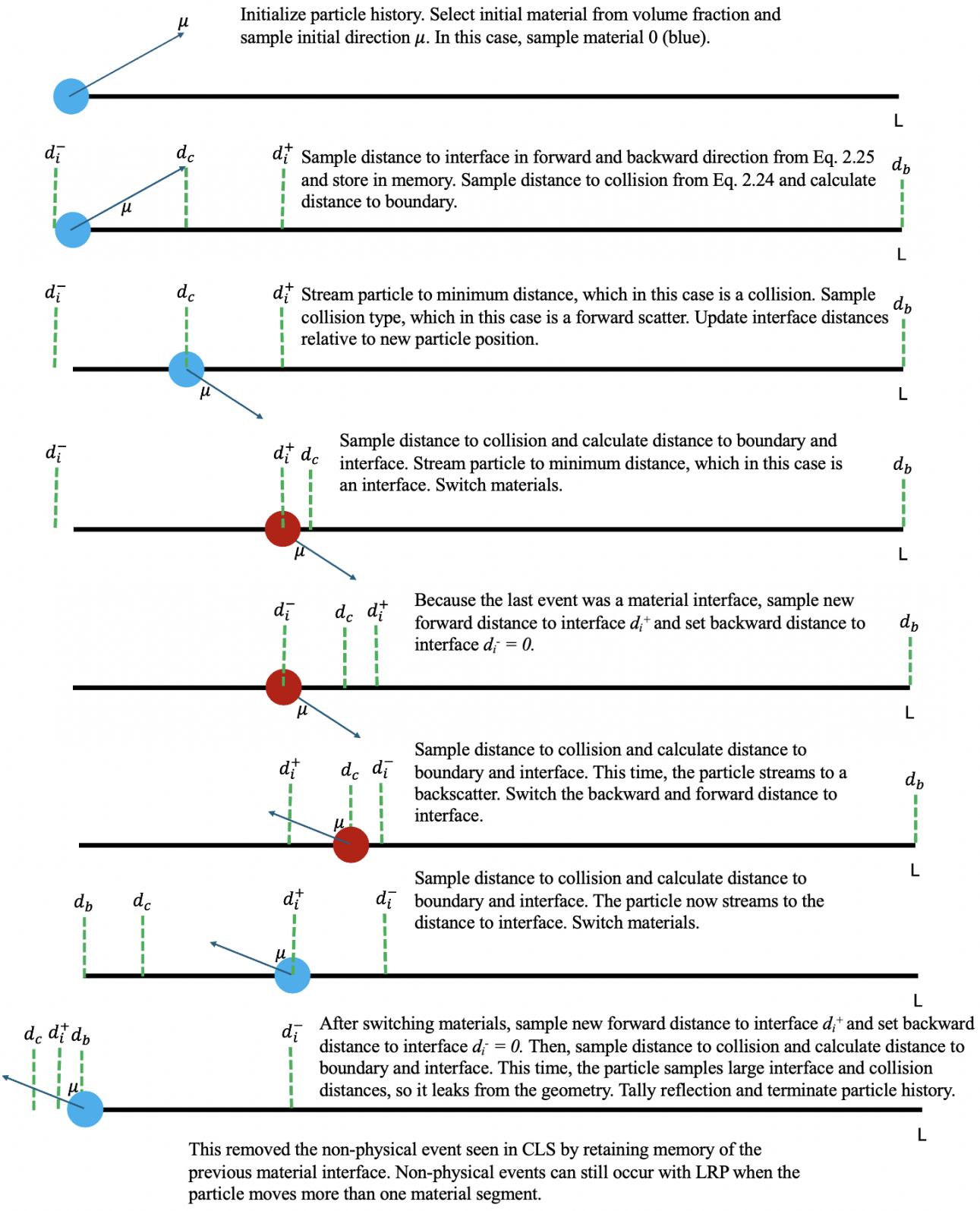


Figure 4.2: Example of a particle history for LRP algorithm.

In Markovian media, LRP reduces the error associated with transport memory in CLS because of the retention of local geometry memory [15, 10, 16]. CLS and LRP have no differences and are both exact in a purely absorbing Markovian medium; the storing of d_i^+ in LRP and the repeated sampling of d_i in CLS are equivalent given the memoryless property of the exponential distribution [24, 27].

4.5 Adapting CLS and LRP to Renewal Statistics

Classical CLS is formulated for Markovian media. In material i, the distance to the next material interface is sampled for every particle segment from Eq. (4.22), which is equivalent to sampling from the exponential chord length distribution. This procedure is consistent with Markovian mixing because the exponential distribution is memoryless. The probability per unit distance of encountering an interface is constant, as given in the hazard function Eq. (3.16c), and does not depend on the distance s traveled since the previous material interface. Therefore, after a collision, scattering event, or change in particle direction, the distance to the next interface may be resampled using only the current material label and its mean chord length.

This property is lost in renewal media. As discussed in Section 3.2, a general renewal medium is characterized by material-dependent chord length distributions $f_i(s)$, survival functions $S_i(s)$, and hazard functions $h_i(s)$. For non-exponential chord statistics, the hazard function generally depends on the current chord age s, where s is the distance from the previous renewal point. Thus, the probability of encountering an interface is not determined by the current material label alone. It also depends on how far the particle has already traveled through the current material segment. A CLS algorithm that repeatedly resamples the distance to the next interface without retaining this information replaces the intended renewal material process with an approximate process that has neglected the geometric memory necessary for accurately reconstructing material statistics.

A second complication arises from the sampling of the first material segment. In a stationary renewal medium, the geometric boundary generally begins inside an existing material chord rather than exactly at a renewal point. As shown in Section 3.2, the forward distance to the next interface from a randomly selected point in material i is distributed according to the equilibrium distribution in Eq. (3.21), not the full chord length density $f_i(s)$. For exponential media, this distinction disappears because $A_i(s) = f_i(s)$. For non-exponential renewal media, however, the first chord and subsequent chords are generally distributed differently, i.e. $A_i(s) \neq f_i(s)$. Any renewal adaptation of CLS must therefore account for both the conditional interface statistics within a chord and the correct first-chord distribution.

These observations show that adapting CLS to renewal media is not simply a matter of replacing the exponential distribution with a non-exponential chord length distribution. The algorithm must retain enough information to determine the relevant conditional distance-to-interface distribution. Equivalently, it must introduce some form of geometric memory, such as the distance from the previous interface, the distance to the next interface, or a

local representation of the current chord. Without this additional information, the method cannot in general reproduce the renewal statistics experienced by particles that scatter or change direction within a material segment.

LRP consequently provides a more natural starting point for renewal media because it already retains local geometric information. Rather than resampling the distance to an interface after every event, LRP stores nearby interface distances and updates them as the particle streams. This local memory is not merely an accuracy improvement in renewal media; it is the information needed to preserve the conditional interface statistics implied by the renewal process. Consequently, LRP can remain accurate for renewal statistics in situations where CLS loses accuracy by repeatedly discarding the chord age or local interface memory.

In this sense, the primary renewal modification to LRP is not a change in the basic philosophy of the method, but a change in how the local geometry is initialized and sampled. In particular, when the particle begins at a random point in a stationary medium, the first forward distance to an interface should be sampled from the equilibrium distribution $A_i(s)$ rather than from $f_i(s)$. Once a local chord geometry has been established, the preservation of local geometric features inherent to LRP allows the method to retain the geometric memory that renewal media require.

The detailed algorithmic choices associated with adapting these classic Monte Carlo methods to account for renewal media are given in more detail in Chapter 6. The purpose of the present discussion is to emphasize the statistical issue: Markovian media permit memoryless interface sampling, whereas renewal media require conditional interface statistics. Classical CLS is therefore not directly transferable to renewal media without adding memory, while LRP is naturally better suited to renewal statistics because it already preserves a local representation of the material realization.

4.6 Previous Heuristic Adaptations to Renewal Media

The preceding sections describe transport models derived for Markovian mixtures, in which the material chord lengths are exponentially distributed. A natural question is whether these Markovian models can be modified in a simple way to approximate transport in non-Markovian renewal media. One of the earliest approaches along these lines was developed by Levermore, Wong, and Pomraning, who used renewal theory to construct effective quantities for transport in binary mixtures with arbitrary chord length distributions [33]. Their analysis showed that, although the full renewal statistics are not retained in the Markovian model, some effects of non-exponential chord statistics can be incorporated through an effective correlation length.

For homogeneous Markovian binary mixtures, the material transition process is characterized by the mean chord lengths λ_0 and λ_1. The corresponding Markovian correlation

length is

$$\frac{1}{\lambda_c} = \frac{1}{\lambda_0} + \frac{1}{\lambda_1}. \tag{4.26}$$

In the Markovian case, λ_i is both the mean chord length in material i and the parameter of the exponential chord length distribution. For renewal statistics, however, the chord length distribution $f_i(s)$ is not generally exponential, and the mean chord length alone does not determine the statistics. Levermore, Wong, and Pomraning proposed an approximate way to use the Markovian transport equations for such non-Markovian media by replacing the Markovian correlation length with an effective correlation length [33, 12]

$$\lambda_{c,\text{eff}} = q\lambda_c. \tag{4.27}$$

Equivalently, in homogeneous binary mixtures this corresponds to replacing the Markovian chord lengths by

$$\lambda_i \longrightarrow q\lambda_i, \qquad i = 0, 1. \tag{4.28}$$

Thus, the transition rates appearing in the Markovian model are modified as

$$\frac{1}{\lambda_i} \longrightarrow \frac{1}{q\lambda_i}. \tag{4.29}$$

It is important to emphasize that this replacement does not change the underlying form of the Markovian model. The material process remains memoryless, and the implied chord length distribution remains exponential. Only the effective exponential mean chord length is changed.

The correction factor q is determined from the renewal chord length statistics. In the notation from Ref. [33], we start by defining

$$Q_i(x) = \int_x^\infty f_i(x')\,dx', \tag{4.30}$$

which is equivalent to the survival function $S_i(s)$, and define its Laplace transform as

$$\widetilde{Q}_i(\sigma) = \int_0^\infty Q_i(x)e^{-\sigma x}\,dx. \tag{4.31}$$

For a purely absorbing binary medium with material cross sections σ_0 and σ_1, the correction factor is

$$q = \frac{1}{\sigma_0}\left[\frac{1}{\widetilde{Q}_0(\sigma_0)} - \frac{1}{\lambda_0}\right] + \frac{1}{\sigma_1}\left[\frac{1}{\widetilde{Q}_1(\sigma_1)} - \frac{1}{\lambda_1}\right] - 1. \tag{4.32}$$

For exponential chord length distributions, one obtains $q = 1$, and the ordinary Markovian model is recovered. For non-exponential renewal statistics, $q \neq 1$.

The q-factor approach should therefore be understood as a heuristic adaptation of Markovian stochastic transport theory, rather than as a renewal transport model. Its purpose was

to retain the structure of existing Markovian equations while modifying the effective chord lengths and correlation length to better reflect selected properties of a non-Markovian mixture. This made the approach attractive for applying Markovian closures to the renewal benchmark problems [11, 12, 34].

This limitation is especially important in the purely absorbing limit. For Markovian media, the classical LP model is exact in purely absorbing media because particles stream through a memoryless material process. For renewal media, the exact pure-absorber solution depends on the actual renewal chord length statistics. A q-modified Markovian model does not retain those statistics. Therefore, even in pure absorption, the q-factor correction does not provide an exact treatment of general renewal media.

This leaves a clear conceptual gap in the existing literature. Previous q-factor approaches recognized that non-Markovian chord length statistics affect transport, but incorporated those effects only through modifications of Markovian chord lengths. As a result, they did not provide a transport formulation that both recovers the exact pure-absorber behavior in renewal media and preserves the intended renewal material statistics. The central objective of this dissertation is to fill this gap. The methods developed here replace effective Markovian length-scale corrections with an augmented renewal-state description, retaining the information needed to accurately describe transport in renewal statistical media.

4.7 Summary

This Chapter reviewed the classical Markovian framework for stochastic media transport. Ensemble averaging of the realization transport equation produces mixed moments $\langle \chi_i \psi \rangle$ that cannot be evaluated from the total ensemble-averaged flux alone. Atomic mix closes the problem by neglecting material-flux correlations entirely, while the Levermore-Pomraning model introduces material-conditioned fluxes and closes the interface terms using Markovian transition rates. In homogeneous Markovian media, those transition rates are determined by the mean chord lengths, and the material process is memoryless.

CLS is the Monte Carlo analog of the Markovian LP transport model. LRP improves on CLS by preserving local interface distances, thereby reducing transport-memory errors associated with backscatter. Both methods rely on exponential chord statistics for their classical justification. When the medium has renewal rather than Markovian statistics, the Markovian assumption inherent to CLS causes inaccuracy, while LRP remains accurate. Additionally, heuristic q-factor corrections were discussed as attempts to extend Markovian closure models to renewal media by modifying the effective transition rates. These models remain limited because they adjust a Markovian length scale rather than representing the renewal statistics directly; a single multiplicative factor cannot capture the conditional non-Markovian interface statistics of general renewal media. These observations motivate the age-dependent transport formulations developed in the following chapters.

Chapter 5

Generalized Master Equation Approach to Transport in Renewal Media

5.1 Introduction

The preceding chapters established the statistical and transport-theoretic setting for particle transport in binary immiscible random media. Chapter 2 introduced transport on fixed material realizations and the benchmark procedure in which transport solutions are averaged over an ensemble of sampled geometries. Chapter 3 developed the alternating renewal process used to describe general non-Markovian mixtures, including the chord length distributions, survival functions, hazard functions, and equilibrium distributions needed to characterize renewal media. Chapter 4 then reviewed classical ensemble-averaged and derivative Monte Carlo approaches, including atomic mix, the Levermore-Pomraning equations, and the Chord Length Sampling class of Monte Carlo stochastic media transport algorithms.

The central limitation identified in Chapter 4 is that classical Markovian models assume a memoryless (exponential) chord length distribution, wherein the material index fully characterizes the future evolution of the stochastic media. For general renewal statistics, however, the material index alone is not sufficient for statistically describing the location of material interfaces: the probability of crossing a material interface also depends on the distance already traveled through the current material segment. Thus, an exact formulation of renewal media must retain some measure of geometric memory.

This Chapter develops an exact formulation for transport in a purely absorbing renewal media. The key idea is to augment the material-conditioned transport description with the material *age* s, defined as the distance from the previous material interface. In a renewal medium, the current material and age together determine the local interface crossing probability through the hazard function. The augmented state, therefore, restores a Markovian description in the expanded stochastic state space, even when the material sequence itself is

non-Markovian. This allows a generalized master equation (GME) to be derived for general renewal media, and the derivation of ensemble-averaged particle flux becomes possible.

The remainder of this Chapter is organized as follows. Section 5.2 summarizes the renewal-statistical and transport definitions needed for the pure absorber derivation. Section 5.3 derives the age-augmented generalized master equation (GME) by formulating a Chapman-Kolmogorov balance for the joint state consisting of flux, material type, and age. Moment equations for material- and age-conditioned flux quantities are then obtained by projection of the joint probability density, and the Markovian limit is recovered when the chord length distributions are exponential. Section 5.4 presents the stochastic numerical implementation of the GME and compares its solutions against analytical solutions to the realization benchmark calculations, showing that the equation is exact. Section 5.5 summarizes the role of the pure absorber GME as the exact renewal statistical media baseline for the later scattering and 3D extensions in Chapters 6 and 7.

5.2 Definitions for Transport in Renewal Media

The general realization-based transport setting was introduced in Chapter 2, and the renewal-statistical description of the random medium was developed in Chapter 3. This section applies the definitions and equations needed to specialize the fixed-realization transport problem to the 1D, purely absorbing renewal media considered in this chapter.

Consider a binary immiscible random medium occupying the slab $0 \leq x \leq L$, with material types denoted by $\mathcal{M}_0$ and $\mathcal{M}_1$. A realization of the medium is denoted by ω. For a fixed realization, each spatial point x lies in one of the two materials, and the cross section ($\Sigma_t = \Sigma_a = \Sigma$ for purely absorbing media) and source take the corresponding material-dependent values:

$$\Sigma(x;\omega) = \Sigma_i, \qquad Q(x;\omega) = Q_i, \qquad \text{when } x \text{ lies in material } \mathcal{M}_i. \tag{5.1}$$

Equivalently, these quantities may be written using the material indicator functions introduced in Chapter 2. Once the realization ω is sampled, the material interface locations are deterministic, and the transport can be solved normally.

Starting from the realization transport equation of Chapter 2, this chapter restricts attention to steady, 1D transport without scattering. In this purely absorbing limit, particles stream monotonically in the positive x direction, such that the realization transport equation reduces to

$$\frac{d\Psi(x;\omega)}{dx} + \Sigma(x;\omega)\Psi(x;\omega) = Q(x;\omega), \qquad 0 \leq x \leq L. \tag{5.2}$$

The incident boundary condition is prescribed at the left boundary,

$$\Psi(0;\omega) = \Gamma_0, \tag{5.3}$$

where Γ_0 is the magnitude of the incident flux. Because particles move only in the positive x direction in the absence of scattering, a boundary condition on the right side of the geometry is unnecessary. Thus, Eq. (5.2) reduces to a stochastic initial-value problem, where for each fixed realization, the transport is deterministic, but the cross section and source vary randomly from one realization to another.

Only a small number of renewal-statistical quantities are needed in this chapter. We use the notation introduced in Chapter 3: the material-dependent chord length density is $f_i(s)$, the survival function is $S_i(s)$, and the hazard function is $h_i(s)$ from Eq. (3.11). The key point is that $h_i(s)$ gives the conditional interface-crossing rate after a particle has already traveled distance s through material $\mathcal{M}_i$. Thus, if the particle is currently in material $\mathcal{M}_i$ with age s, the probability of crossing into the opposite material over an incremental distance dx is

$$P(\mathcal{M}_i \to \mathcal{M}_j \text{ over } dx \mid s) = h_i(s)\,dx + o(dx), \qquad i \neq j. \tag{5.4}$$

Between interfaces, the material type remains fixed and the age increases deterministically with position,

$$\frac{ds}{dx} = 1. \tag{5.5}$$

At a material interface, the material type switches and the age is reset to zero. For exponential chord length distributions, $h_i(s) = 1/\lambda_i$, so the interface-crossing rate is independent of age and the material process is Markovian. For non-exponential renewal statistics, $h_i(s)$ depends on s, so the age carries geometric memory of the current material segment. This information must be retained to develop the generalized master equation derived below.

The incident boundary is treated as a randomly selected point in an infinite statistically stationary renewal medium. Therefore, it is not generally located at a material interface. If the boundary point lies in material $\mathcal{M}_i$, the initial age then must be sampled from the equilibrium age distribution derived in Chapter 3, rather than from the chord length distribution $f_i(s)$. In the notation of Chapter 3, this distribution is $A_i(s)$ from Eq. (3.21). In the GME notation used below, we write the corresponding initial age density as

$$\mathcal{A}_i(s) \equiv A_i(s). \tag{5.6}$$

For exponential chord statistics, $\mathcal{A}_i(s) = f_i(s)$ because of the memoryless property. For general renewal statistics, however, $\mathcal{A}_i(s)$ differs from $f_i(s)$ and must be used to preserve the stationary material statistics at the boundary.

The quantities of interest in this chapter are ensemble-averaged flux moments and leakage quantities associated with Eq. (5.2). Direct benchmark estimates are obtained by sampling many renewal geometries, solving Eq. (5.2) on each realization, and averaging the resulting solutions as described in Chapter 2. The next section replaces this realization-by-realization description with an age-augmented state space, leading to a generalized master equation for renewal media.

5.3 Generalized Master Equation

We now replace the realization-based description of the previous section with an age-augmented state-space formulation. For a fixed realization ω, the flux $\Psi(x;\omega)$ satisfies Eq. (5.2). Across the ensemble of renewal-media realizations, however, the flux, material type, and age at a given position x are random variables. The appropriate stochastic state is therefore defined as

$$\{\psi, i, s\}, \tag{5.7}$$

where ψ is the phase-space value of the particle flux, $i \in \{0, 1\}$ denotes the material index $\mathcal{M}_i$, and s is the age in the current material chord. As discussed in the previous section, the inclusion of s closes the renewal-statistical description because the probability of a material transition over an incremental distance dx is determined by the hazard function $h_i(s)$. Thus, although the material label alone is not a Markovian state variable for general renewal statistics, the augmented state $\{\psi, i, s\}$ is Markovian in the purely absorbing setting considered here.

To characterize the Markov process in the extended state space, we define the joint probability density function $\rho(\psi, s, \mathcal{M}_i, x)d\psi\, ds$ as the probability that material $\mathcal{M}_i, i = 0, 1$, exists at spatial position x and the angular flux and age lie in the ranges $(\psi, \psi + d\psi)$ and $(s, s + ds)$, respectively. This joint probability density function (JPDF) is normalized according to

$$\sum_{i=0}^{1} \int_0^\infty d\psi \int_0^\infty ds\, \rho(\psi, s, \mathcal{M}_i, x) = 1. \tag{5.8}$$

Various useful reduced distribution functions may be defined from this JPDF. Thus, the probability that material $\mathcal{M}_i$ is found at x regardless of the flux and age, in other words the marginal probability for the material type or the volume fraction at x, is given by

$$p_i(x) = \int_0^\infty d\psi \int_0^\infty ds\, \rho(\psi, s, \mathcal{M}_i, x), \tag{5.9}$$

and it follows from Eq. (5.8) that $p_0(x) + p_1(x) = 1$. Factoring out $p_i(x)$ we can decompose the JPDF as

$$\rho(\psi, s, \mathcal{M}_i, x) = p_i(x)\, P_i(\psi, s, x), \tag{5.10}$$

where $P_i(\psi, s, x)d\psi\, ds$ is the joint conditional probability that the angular flux lies in $(\psi, \psi + d\psi)$ and the age lies in $(s, s + ds)$ conditioned on x being in material $\mathcal{M}_i$. From Eq. (5.8), this distribution has the normalization

$$\int_0^\infty d\psi \int_0^\infty ds\, P_i(\psi, s, x) = 1. \tag{5.11}$$

The normalized probability density of the age conditioned on material $\mathcal{M}_i$ at x is defined by

$$\mathcal{A}_i(s,x) = \int_0^\infty P_i(\psi,s,x)d\psi, \tag{5.12}$$

$$\int_0^\infty ds\, \mathcal{A}_i(s,x) = 1. \tag{5.13}$$

Finally, we define the age-dependent flux moments conditioned on material $\mathcal{M}_i$ at x as

$$\psi_i^{(n)}(s,x) = \int_0^\infty d\psi\, \psi^n\, P_i(\psi,s,x), \quad n = 1,2,\ldots, \tag{5.14}$$

which when integrated over the age variable reduce to the conditional flux moments familiar from the Markov case

$$\begin{aligned}\psi_i^{(n)}(x) &= \int_0^\infty ds \int_0^\infty d\psi\, \psi^n\, P_i(\psi,s,x) \\ &= \int_0^\infty ds\, \psi_i^{(n)}(s,x) \quad n = 1,2,\ldots.\end{aligned} \tag{5.15}$$

Our objective is to derive a closed equation for the JPDF $\rho(\ldots)$ from which equations for reduced distributions of interest can be extracted.

Chapman-Kolmogorov Equation

The state of the jointly Markovian system evolves with x due to two distinct events that can occur over an incremental distance dx: (i) event E_1, where the material does not transition from state i within dx; in this case, the flux and age change incrementally by $d\Psi$ and ds respectively; (ii) event E_2, where a material transition into state i from state j, $i \neq j$, occurs within dx; in this case, the age resets to zero while the flux is unchanged. The probability of a material transition occurring simultaneously with a change in flux is $o(dx)$ and is neglected.

From the Markovian property and Law of Total Probability, the JPDF satisfies a Chapman-Kolmogov equation (CKE) [35] which in the present context may be expressed as

$$\begin{aligned}\rho(\psi,s,\mathcal{M}_i,x+dx) = &\int_0^\infty\!\!\!\int \rho(\psi',s',\mathcal{M}_i,x)\, T_{E_1}(\psi'\to\psi, s'\to s, dx)\, d\psi' ds' \\ &+ \int_0^\infty\!\!\!\int \rho(\psi'',s'',\mathcal{M}_j,x)\, T_{E_2}(\psi''\to\psi, s''\to s, dx)\, d\psi'' ds'', \quad i\neq j = 0,1,\end{aligned} \tag{5.16}$$

where $T_{E_1}(\cdots)$ and $T_{E_2}(\cdots)$ are the transition probabilities associated with events E_1 and E_2, respectively. The event E_1 describes the incremental change in the flux over an incremental change in distance conditioned on x and $x + dx$ both being in material $\mathcal{M}_i$. The change in flux is therefore deterministic and can be obtained from the solution to Eq. (5.2). As the $\lim dx \to 0$ will be taken eventually it is necessary to specify the transition probabilities to first order in dx only. Thus, integrating Eq. (5.2) over the elemental volume $\{x, x + dx\}$ in material $\mathcal{M}_i$ we get

$$\Psi(x + dx) - \Psi(x) + \Sigma_i \Psi(x) dx = Q_i dx + o(dx), \tag{5.17}$$

which can be rearranged to give

$$\begin{aligned} \Psi(x) &= [\Psi(x + dx) - Q_i dx] (1 - \Sigma_i dx)^{-1} + o(dx) \\ &= [\Psi(x + dx) - Q_i dx] (1 + \Sigma_i dx) + o(dx), \end{aligned} \tag{5.18}$$

and finally

$$\Psi(x) = \Psi(x + dx)(1 + \Sigma_i dx) - Q_i dx + o(dx). \tag{5.19}$$

The deterministic variation in a fixed material uniquely relates the change in the instantaneous flux and the change in the corresponding state-space flux between x and $x + dx$. We consequently identify the phase point ψ' with $\Psi(x)$ and the phase point ψ with $\Psi(x + dx)$ to obtain from Eq. (5.19)

$$\psi' = \psi + (\Sigma_i \, \psi - Q_i) \; dx. \tag{5.20}$$

Similarly, we identify s' and s with the ages at x and $x + dx$, respectively, and moreover note that $ds = dx$ as the material state does not change. Hence the transition probability for event E_1 may be expressed as

$$\begin{aligned} &T_{E_1}(\psi' \to \psi, s' \to s, dx) = [1 - h_i(s')dx] \times \\ &\times \delta \left[\psi' - \psi - (\Sigma_i \psi - Q_i) \, dx\right] \, \delta \left[s' - (s - dx)\right] + o(dx), \end{aligned} \tag{5.21a}$$

where $[1 - h_i(s')dx]$ is the probability that a material transition does not occur in dx and the delta functions reflect the sharp changes in the state flux and age when the material is fixed.

Similarly, the transition probability for event E_2 may be written as

$$T_{E_2}(\psi'' \to \psi, s'' \to s, dx) = h_j(s'')dx\,\delta(\psi'' - \psi)\,\delta(s) + o(dx), \tag{5.21b}$$

where $h_j(s'')dx$ is the probability of a material state transition in dx and the two delta functions reflect the age resetting to zero and the constancy of the flux as a result of the material change. It follows that to $o(dx)$ these transition probabilities have the normalization

$$\iint_0^\infty d\psi ds\, T_{E_1}(\psi' \to \psi, s' \to s, dx) = [1 - h_i(s')dx] + o(dx), \tag{5.22a}$$

$$\iint_0^\infty d\psi ds\, T_{E_2}(\psi'' \to \psi, s'' \to s, dx) = h_j(s'')dx + o(dx). \tag{5.22b}$$

Reduction to Generalized Master Equation

The goal is the reduction of the CKE to differential form, and as the limit $dx \to 0$ will be taken eventually, contributions of $o(dx)$ will be neglected in the ensuing development. Thus, we begin by expressing the LHS of Eq. (5.16) to first order in dx

$$\rho(\psi, s, \mathcal{M}_i, x) + dx\frac{\partial}{\partial x}\rho(\psi, s, \mathcal{M}_i, x) = \iint_0^\infty \rho(\psi', s', \mathcal{M}_i, x)\, T_{E_1}(\psi' \to \psi, s' \to s, dx)\, d\psi' ds' + \iint_0^\infty \rho(\psi'', s'', \mathcal{M}_j, x)\, T_{E_2}(\psi'' \to \psi, s'' \to s, dx)\, d\psi'' ds'' + o(dx). \tag{5.23}$$

Defining the inner product of two functions $f(\psi, s)$ and $g(\psi, s)$ by

$$\big(f, g\big) = \iint_0^\infty d\psi ds\, f(\psi, s)\, g(\psi, s), \tag{5.24}$$

we take the inner product of Eq. (5.16) with a test function $\chi(\psi, s)$ and rearrange terms to get

$$\int_0^\infty\!\!\int d\psi ds\,\chi(\psi,s)\left\{dx\frac{\partial}{\partial x}\rho(\psi,s,\mathcal{M}_i,x)-\left[\int_0^\infty\!\!\int \rho(\psi',s',\mathcal{M}_i,x)\,T_{E_1}(\psi'\to\psi,s'\to s,dx)\,d\psi' ds'-\rho(\psi,s,\mathcal{M}_i,\right.\right.$$
$$\left.\left.-\int_0^\infty\!\!\int \rho(\psi'',s'',\mathcal{M}_j,x)\,T_{E_2}(\psi''\to\psi,s''\to s,dx)\,d\psi'' ds''+o(dx)\right\}=0. \tag{5.25}$$

Isolating and defining the second line as

$$L_2=\int_0^\infty\!\!\int d\psi ds\,\chi(\psi,s)\left\{\int_0^\infty\!\!\int d\psi' ds'\,\rho(\psi',s')\,T_{E_1}(\psi'\to\psi,s'\to s,dx)\;-\rho(\psi,s)\right\}, \tag{5.26}$$

we proceed by appending the normalization condition given in Eq. (5.22a) to the second $\rho(\cdot)$ term in Eq. (5.26), obtaining

$$L_2=\int_0^\infty\!\!\int d\psi ds\,\chi(\psi,s)\int_0^\infty\!\!\int d\psi' ds'\,\rho(\psi',s')\,T_{E_1}(\psi'\to\psi,s'\to s,dx)$$
$$-\int_0^\infty\!\!\int d\psi ds\,\chi(\psi,s)\,\rho(\psi,s)\int_0^\infty\!\!\int d\psi' ds'\,T_{E_1}(\psi\to\psi',s\to s',dx)\,[1-h_i(s)dx]^{-1}. \tag{5.27}$$

Next, we reverse the order of integration in the first line, interchange the pre- and post-integration variables, and combine the two terms to write

$$L_2=\int_0^\infty\!\!\int d\psi ds\,\rho(\psi,s)\int_0^\infty\!\!\int d\psi' ds'\,T_{E_1}(\psi\to\psi',s\to s',dx)$$
$$\left\{\chi(\psi',s')-\chi(\psi,s)\;[1-h_i(s)dx]^{-1}\right\}. \tag{5.28}$$

Now expanding $[1-h_i(s)dx]^{-1}$ to $o(dx)$, L_2 reduces to

$$L_2=\int_0^\infty\!\!\int d\psi ds\,\rho(\psi,s)\int_0^\infty\!\!\int d\psi' ds'\,T_{E_1}(\psi\to\psi',s\to s',dx)\,\{\chi(\psi',s')-\chi(\psi,s)\;[1+h_i(s)dx+o(dx)]\}$$
$$=\int_0^\infty\!\!\int d\psi ds\,\rho(\psi,s)\int_0^\infty\!\!\int d\psi' ds'\,T_{E_1}(\psi\to\psi',s\to s',dx)\,\{\chi(\psi',s')-\chi(\psi,s)\}$$
$$-\int_0^\infty\!\!\int d\psi ds\,\chi(\psi,s)\,\rho(\psi,s)\,h_i(s)dx+o(dx). \tag{5.29}$$

From Eq.(5.20), ψ' and ψ differ incrementally by $o(dx)$ in event E_1, so we can use the first-order approximation

$$\begin{aligned}\chi(\psi', s') &= \chi\left[\psi - (\psi - \psi'), s - (s - s')\right] \\ &= \chi(\psi, s) - (\psi - \psi')\,\frac{\partial}{\partial \psi}\chi(\psi, s) \\ &\quad - (s - s')\frac{\partial}{\partial s}\chi(\psi, s) + o(dx) + o(ds),\end{aligned} \tag{5.30}$$

to simplify Eq. (5.29) to

$$\begin{aligned}L_2 = &- \int_0^\infty\!\!\int d\psi ds\, \rho(\psi, s)\, \left\{\overline{\Delta\psi}(\psi, s, dx)\,\frac{\partial}{\partial \psi}\chi(\psi, s) + \overline{\Delta s}(\psi, s, dx)\,\frac{\partial}{\partial s}\chi(\psi, s)\right\} \\ &- \int_0^\infty\!\!\int d\psi ds\, \chi(\psi, s)\, \rho(\psi, s, \mathcal{M}_i, x)\, h_i(s)dx + o(dx) + o(ds),\end{aligned} \tag{5.31}$$

where $\overline{\Delta\psi}$ and $\overline{\Delta s}$ are moments defined by

$$\overline{\Delta\psi}(\psi, s, dx) = \int_0^\infty\!\!\int d\psi' ds'\, (\psi - \psi')\, T_{E_1}(\psi \to \psi', s \to s', dx), \tag{5.32}$$

$$\overline{\Delta s}(\psi, s, dx) = \int_0^\infty\!\!\int d\psi' ds'\, (s - s')\, T_{E_1}(\psi \to \psi', s \to s', dx). \tag{5.33}$$

The final step is to use integration by parts in the first term on the RHS of Eq. (5.31) and note that the boundary terms vanish to get

$$\begin{aligned}L_2 = &\int_0^\infty\!\!\int d\psi ds\, \chi(\psi, s)\, \left\{\frac{\partial}{\partial \psi}\left[\,\overline{\Delta\psi}(\psi, s, dx)\,\rho(\psi, s)\right] + \frac{\partial}{\partial s}\left[\,\overline{\Delta\psi}(\psi, s, dx)\,\rho(\psi, s)\right]\right\} \\ &- \int_0^\infty\!\!\int d\psi ds\, \chi(\psi, s)\, \rho(\psi, s, \mathcal{M}_i, x)\, h_i(s)dx + o(dx) + o(ds).\end{aligned} \tag{5.34}$$

Returning to Eq. (5.25) and substituting Eq. (5.34) yields

$$\int_0^\infty\!\!\int d\psi ds\, \chi(\psi,s)\left\{ dx\frac{\partial}{\partial x}\rho(\psi,s,\mathcal{M}_i,x) - \left\{ \frac{\partial}{\partial\psi}\left[\,\overline{\Delta\psi}(\psi,s,dx)\,\rho(\psi,s)\right] + \frac{\partial}{\partial s}\left[\,\overline{\Delta\psi}(\psi,s,dx)\,\rho(\psi,s)\right]\right\}\right.$$
$$+\rho(\psi,s,\mathcal{M}_i,x)\,h_i(s)dx + o(dx) + o(ds)$$
$$\left. - \int\!\!\int_0^\infty \rho(\psi'',s'',\mathcal{M}_j,x)\,T_{E_2}(\psi''\to\psi,s''\to s,dx)\,d\psi''ds'' + o(dx)\right\} = 0. \tag{5.35}$$

Explicit expressions for the moments $\overline{\Delta\psi}(\cdot)$ and $\overline{\Delta s}(\cdot)$ can be obtained by inserting the appropriate transition probabilities. Inserting T_{E_1} from Eq. (5.21a) and expanding we have

$$\begin{aligned}
\overline{\Delta\psi}(\psi,s,dx) &= \int_0^\infty\!\!\int d\psi' ds'\,(\psi-\psi')\,\left[1-h_i(s)dx\right]\,\delta\left[\psi-\psi'-(\Sigma_i\psi'-Q_i)\,dx\right]\,\delta\left[s'-(s+ds)\right]\\
&= \left[1-h_i(s)dx\right]\,(1+\Sigma_i\,dx)^{-1}\int_{-\infty}^{\psi} dy\,y\,\delta\left[y-(\Sigma_i\psi-Q_i)\,dx(1+\Sigma_i\,dx)^{-1}\right]\\
&= \left[1-h_i(s)dx\right]\,(1+\Sigma_i\,dx)^{-2}\,(\Sigma_i\psi-Q_i)\,dx\\
&= (\Sigma_i\psi-Q_i)\,dx+o(dx).
\end{aligned}\tag{5.36}$$

Similarly, inserting T_{E_2} from . (5.21b) gives

$$\begin{aligned}
\overline{\Delta s}(\psi,s,dx) &= \int_0^\infty\!\!\int d\psi' ds'\,(s-s')\,\left[1-h_i(s)dx\right]\,\delta\left[\psi-\psi'-(\Sigma_i\psi'-Q_i)\,dx\right]\,\delta\left[s'-(s+ds)\right]\\
&= (1+\Sigma_i\,dx)^{-1}\int_0^\infty ds'\,(s-s')\,\left[1-h_i(s)dx\right]\,\delta\left[s-(s'-ds)\right]\\
&= -\big(1-\Sigma_i\,dx+o(dx)\big)\,\left[1-h_i(s)dx\right]\,ds\\
&= -ds+o(ds)+o(dx).
\end{aligned}\tag{5.37}$$

Eq. (5.35) with these moment expressions now reads

$$\int_0^\infty\!\!\int d\psi ds\, \chi(\psi,s)\left\{ dx\frac{\partial}{\partial x}\rho(\psi,s,\mathcal{M}_i,x) - \left\{ \frac{\partial}{\partial\psi}\left[(\Sigma_i\psi-Q_i)\,dx\,\rho(\psi,s,\mathcal{M}_i,x)\right] - ds\frac{\partial}{\partial s}\rho(\psi,s,\mathcal{M}_i,x)\right\}\right.$$
$$+\rho(\psi,s,\mathcal{M}_i,x)\,h_i(s)dx + o(dx) + o(ds)$$
$$\left. - \int\!\!\int_0^\infty \rho(\psi'',s'',\mathcal{M}_j,x)\,T_{E_2}(\psi''\to\psi,s''\to s,dx)\,d\psi''ds'' + o(dx)\right\} = 0. \tag{5.38}$$

Similarly, using Eq. (5.21b) for T_{E_2}, the last term in Eq. (5.38) becomes

$$\begin{aligned}\iint_0^\infty \rho(\psi'', s'', \mathcal{M}_j, x)\, T_{E_2}(\psi'' \to \psi, s'' \to s, dx)\, d\psi'' ds'' \\ = \delta(s) \int_0^\infty h_j(s'') dx\, \rho(\psi, s'', \mathcal{M}_j, x)\, ds'',\end{aligned} \tag{5.39}$$

which when inserted into Eq. (5.38) gives

$$\begin{aligned}\int_0^\infty\!\!\int d\psi ds\, \chi(\psi, s) \Bigg\{ dx \frac{\partial}{\partial x}\rho(\psi, s, \mathcal{M}_i, x) - \left\{ \frac{\partial}{\partial \psi}\left[(\Sigma_i \psi - Q_i)\, dx\, \rho(\psi, s, \mathcal{M}_i, x)\right] - ds \frac{\partial}{\partial s}\rho(\psi, s, \mathcal{M}_i, x) \right\} \\ + h_i(s) dx\, \rho(\psi, s, \mathcal{M}_i, x) - \delta(s) \int_0^\infty h_j(s'') dx\, \rho(\psi, s'', \mathcal{M}_j, x)\, ds'' + o(dx) \Bigg\} = 0.\end{aligned} \tag{5.40}$$

As this result holds for any test function, the integrand in braces must vanish, giving

$$\begin{aligned} dx \frac{\partial}{\partial x}\rho(\psi, s, \mathcal{M}_i, x) - dx \frac{\partial}{\partial \psi}\big[\, (\Sigma_i \psi - Q_i)\ \rho(\psi, s, \mathcal{M}_i, x)\big] + ds \frac{\partial}{\partial s}\rho(\psi, s, \mathcal{M}_i, x) \\ = -h_i(s) dx\, \rho(\psi, s, \mathcal{M}_i, x) + dx\, \delta(s) \int_0^\infty h_j(s'')\, \rho(\psi, s'', \mathcal{M}_j, x)\, ds'' + o(dx).\end{aligned} \tag{5.41}$$

Finally, dividing by dx, recalling that $ds = dx$ (the closure condition we referred to earlier) for event E_1, and letting $dx \to 0$, we obtain the integro-differential CKE

$$\begin{aligned} \frac{\partial}{\partial x}\rho(\psi, s, \mathcal{M}_i, x) + \frac{\partial}{\partial s}\rho(\psi, s, \mathcal{M}_i, x) - \frac{\partial}{\partial \psi}\big[\, (\Sigma_i \psi - Q_i)\ \rho(\psi, s, \mathcal{M}_i, x)\big] \\ = -h_i(s)\, \rho(\psi, s, \mathcal{M}_i, x) + \delta(s) \int_0^\infty h_j(s'')\, \rho(\psi, s'', \mathcal{M}_j, x)\, ds'', \quad i \neq j = 0, 1.\end{aligned} \tag{5.42a}$$

The boundary condition at $x = 0$ is given by

$$\rho(\psi, s, \mathcal{M}_i, 0) = p_i(0)\, \mathcal{A}_i(s)\, \delta(\psi - \Psi_0), \tag{5.42b}$$

where $\mathcal{A}_i(s)$ is the intial age distribution. The term with $\delta(s)$ can be eliminated from Eq. (5.42a) and replaced by a constraint or jump condition at zero age as follows. Integrating Eq. (5.42a) over $s \in (-\epsilon, \epsilon)$, the delta function integrates to unity while the second term on the RHS integrates to

$$\begin{aligned}\int_{-\epsilon}^{\epsilon} \frac{\partial}{\partial s}\rho(\psi, s, \mathcal{M}_i, x) ds &= \rho(\psi, \epsilon, \mathcal{M}_i, x) - \rho(\psi, -\epsilon, , \mathcal{M}_i, x) \\ &= \rho(\psi, \epsilon, \mathcal{M}_i, x).\end{aligned} \tag{5.43}$$

Now taking the limit $\epsilon \to 0$ with ρ and h_i presumed continuous in s, the rest of the terms vanish to give the result

$$\rho(\psi, 0, \mathcal{M}_i, x) = \int_0^\infty \rho(\psi, s', \mathcal{M}_j, x)\, h_j(s')\, ds'. \tag{5.44}$$

We can therefore replace Eq. (5.42a) by two equations, one for $s > 0$ and the other a jump condition at $s = 0$, written collectively as

$$\frac{\partial}{\partial \psi}\rho(\psi, s, \mathcal{M}_i, x) + \frac{\partial}{\partial s}\rho(\psi, s, \mathcal{M}_i, x) - \frac{\partial}{\partial \psi}(\Sigma_i \psi - Q_i)\rho(\psi, s, \mathcal{M}_i, x) = -h_i(s)\rho(\psi, s, \mathcal{M}_i, x), \tag{5.45a}$$

$$\rho(\psi, 0, \mathcal{M}_i, x) = \int_0^\infty h_j(s')\, \rho(\psi, s', \mathcal{M}_j, x)\, ds'. \tag{5.45b}$$

Finally, expressing $\rho(\cdot)$ in terms of the distribution conditioned on material type as defined in Eq. (5.10) gives the alternate form

$$\frac{\partial}{\partial x}p_i(x)P_i(\psi, s, x) + \frac{\partial}{\partial s}p_i(x)P_i(\psi, s, x) - \frac{\partial}{\partial \psi}\left[(\Sigma_i \psi - Q_i)\, p_i(x)P_i(\psi, s, x)\right] = -h_i(s, x)\, p_i(x)P_i(\psi, s, x), \tag{5.46a}$$

$$p_i(x)P_i(\psi, 0, x) = \int_0^\infty h_j(s, x)\, p_j(x)\, P_j(\psi, s, x)\, ds, \quad i \neq j = 0, 1, \tag{5.46b}$$

where the x-dependence in the volume fraction and the hazard function has been made explicit to emphasize that the result is valid in general for nonhomogeneous statistics. The corresponding boundary condition is given by

$$P_i(\psi, s, 0) = \mathcal{A}_i(s)\, \delta(\psi - \Psi_0). \tag{5.47}$$

We refer to Eq. (5.42a) or the equivalent forms in Eq. (5.45a) and Eq. (5.45b) and Eq. (5.46a) and Eq. (5.46b) as the *generalized Master equation* or GME, to distinguish it from the Markovian case (see below), and is the central result of this work. A unique feature of the GME is the presence of an auxiliary independent variable, the age, with respect to which the JPDF changes continuously, while the medium type is fixed, and jumps discretely at a material transition. As such it is not a classical Master equation of the type familiar from the Markov case.

The boundary condition given by Eq. (5.47) shows that the age distribution must be specified at the origin. As explained earlier, the problem domain is a segment on the infinite

line on which the ARP is defined and the origin is therefore either coincident with a material interface or lies within a material. In the former case, particles have zero age and the initial age distribution is then simply $\mathcal{A}_i(s,0) = \mathcal{A}_i(s) = \delta(s)$. In the latter case, it is necessary to obtain the age distribution $\mathcal{A}_i(s,x)$ on the infinite line. From its definition in Eq. (5.12), the age distribution satisfies a reduced Master equation which can be obtained by integrating Eq. (5.46a) and Eq. (5.46b) over ψ

$$\frac{\partial}{\partial x} p_i \mathcal{A}_i(s,x) + \frac{\partial}{\partial s} p_i \mathcal{A}_i(s,x) = -h_i(s)\, p_i \mathcal{A}_i(s,x), \quad i = 0,1, \tag{5.48a}$$

$$p_i \mathcal{A}_i(0,x) = \int_0^\infty h_j(s)\, p_j\, \mathcal{A}_j(s,x)\, ds, \quad i \neq j = 0,1. \tag{5.48b}$$

For homogeneous statistics, $\mathcal{A}_i(s,x)$ reduces to the equilibrium distribution $\mathcal{A}_i(s)$ which satisfies the simpler equation pair

$$\frac{d}{ds} p_i \mathcal{A}_i(s) = -h_i(s)\, p_i \mathcal{A}_i(s), \quad i = 0,1, \tag{5.49a}$$

$$p_i \mathcal{A}_i(0) = \int_0^\infty h_j(s)\, p_j\, \mathcal{A}_j(s)\, ds, \quad i \neq j = 0,1. \tag{5.49b}$$

Eq. (5.49) has the elementary solution

$$\mathcal{A}_i(s) = c_i \exp\left[-\int_0^s h_i(s')ds' \right], \quad i \neq j = 1,2, \tag{5.50}$$

where the constant of integration c_i may be obtained by enforcing normalization (see Eq. (5.13))

$$\int_0^\infty \mathcal{A}_i(s)ds = 1, \tag{5.51}$$

to get

$$\frac{1}{c_i} = \int_0^\infty \exp\left[-\int_0^s h_i(s')ds' \right] ds. \tag{5.52}$$

Recalling the definition of the hazard function in terms of the chord length distribution function given in Eq. (3.11), the integral in the exponent can be simplified as follows:

$$\begin{aligned} \int_0^s h_i(s')ds' &= \int_0^s \frac{f_i(s')}{\int_{s'}^\infty f_i(u)du} ds' \\ &= \int_0^s d\left[-\ln\left(\int_{s'}^\infty f_i(u)du \right) \right] \\ &= -\ln\left(\int_s^\infty f_i(u)du \right). \end{aligned} \tag{5.53}$$

Inserting this result in Eq. (5.52) and further simplifying gives

$$\begin{aligned}\frac{1}{c_i} &= \int_0^\infty ds \int_s^\infty f_i(u)du \\ &= \int_0^\infty du\, u\, f_i(u). \end{aligned} \tag{5.54}$$

The integral on the LHS defines the mean chord length for material-i, λ_i, hence it follows that

$$c_i = \frac{1}{\lambda_i}, \quad i = 0, 1. \tag{5.55}$$

Finally, inserting c_i into Eq. (5.50) and using Eq. (5.53) yields the equilibrium age distribution

$$\mathcal{A}_i(s) = \frac{1}{\lambda_i}\int_s^\infty f_i(u)du, \quad i = 0, 1, \tag{5.56}$$

Perhaps not surprisingly, this expression for the equilibrium age distribution is identical to the *modified distribution* used in renewal theory to randomly position the origin in the first interval. [36, 37, 11, 12]. The unconditional equilibrium age distribution, i.e., the distribution regardless of material type, is by definition

$$\begin{aligned}\mathcal{A}(s) &= p_1\mathcal{A}_1(s) + p_2\mathcal{A}_2(s) \\ &= \frac{p_1}{\lambda_1}\int_s^\infty f_1(u)du + \frac{p_2}{\lambda_2}\int_s^\infty f_2(u)du. \end{aligned} \tag{5.57}$$

GME in the Markovian Limit

Recall that the hazard function $h_i(s)$ is constant for exponential statistics, specifically $h_i(s) = \frac{1}{\lambda_i}$ where λ_i is the mean chord length of material type-i. In this case, we now show that the well-known result for Markovian mixing is recovered [14, 8]. Integrating the GME Eq. (5.46a) over all s gives

$$\frac{\partial}{\partial x}p_iP_i(\psi,x) - p_iP_i(\psi,0,x) - \frac{\partial}{\partial\psi}\left[(\Sigma_i\psi - Q_i)\,p_iP_i(\psi,x)\right] = -p_i\int_0^\infty ds\, h_i(s)\,P_i(\psi,s,x), \quad i = 0, 1, \tag{5.58a}$$

$$p_iP_i(\psi,0,x) = p_j\int_0^\infty h_j(s)\,P_j(\psi,s,x)\,ds, \quad i \neq j = 0, 1. \tag{5.58b}$$

Eliminating $P_i(\psi,0,x)$ in 5.58a using 5.58b and rearranging reduces the former to

$$\frac{\partial}{\partial x}p_iP_i(\psi,x) - \frac{\partial}{\partial\psi}\left[(\Sigma_i\psi - Q_i)\,p_iP_i(\psi,x)\right] = p_j\int_0^\infty h_j(s)\,P_j(\psi,s,x)\,ds - p_i\int_0^\infty ds\, h_i(s)\,P_i(\psi,s,x). \tag{5.59}$$

This is not a closed equation because of the presence of the age-dependent distributions in the integrals on the RHS. However, since $h_i(s) = \frac{1}{\lambda_i}$ for exponential statistics, the integrals immediately reduce to age-independent distributions and yield the closed equation pair

$$\frac{\partial}{\partial x} p_i P_i(\psi, x) - \frac{\partial}{\partial \psi} \left[(\Sigma_i \psi - Q_i)\, p_i P_i(\psi, x) \right] = \frac{p_j}{\lambda_j} P_j(\psi, x) - \frac{p_i}{\lambda_i} P_i(\psi, x) \quad i \neq j = 0, 1, \tag{5.60a}$$

with boundary condition

$$P_i(\psi, 0) = \delta(\psi - \Psi_0). \tag{5.60b}$$

Equation Eq. (5.60a) is recognized as the classical Master equation [14, 8] for exponentially distributed material interfaces.

Moment Equations

In practical applications, the quantities of interest are the flux-moments conditioned on material type, as defined by Eq. (5.15), and in particular the mean and standard deviation. As encountered when formulating equations for the reduced JPDF, closed equations can only be obtained for the age-dependent material-conditioned moments $\psi_i^{(n)}(s, x)$ which once solved for must then be integrated over s to obtain the age-indpendent moments $\psi_i^{(n)}(x)$. Proceeding, we multiply Eq. (5.46a) and Eq. (5.46b) by ψ^n and integrate over all ψ to obtain, assuming sufficiently fast decay of the JPDF as $\psi \to \infty$, for $n \geq 1$

$$\begin{aligned} &\frac{\partial}{\partial x} p_i \psi_i^{(n)}(s, x) + \frac{\partial}{\partial s} p_i \psi_i^{(n)}(s, x) + n\, p_i \Sigma_i \psi_i^{(n)}(s, x) + \\ &- h_i(s)\, p_i \psi_i^{(n)}(s, x) + n\, Q_i\, p_i \psi_i^{(n-1)}(s, x), \quad i = 0, 1, \end{aligned} \tag{5.61a}$$

$$p_i \psi_i^{(n)}(0, x) = \int_0^\infty h_j(s)\, p_j\, \psi_j^{(n)}(s, x)\, ds, \quad i \neq j = 0, 1, \tag{5.61b}$$

with boundary condition

$$\psi_i^{(n)}(s, 0) = \Psi_0^n\, \mathcal{A}_i(s). \tag{5.62}$$

We note that in the Markovian case, the constancy of the hazard function allows the age to be integrated out to recover the age-integrated moment equations in the form [8]

$$\begin{aligned} \frac{\partial}{\partial x} p_i \psi_i^{(n)}(x) + n\, \Sigma_i\, p_i \psi_i^{(n)}(x) = \frac{p_j}{\lambda_j}\, \psi_j^{(n)}(x) - \frac{p_i}{\lambda_i}\, \psi_i^{(n)}(x) \\ + n\, p_i Q_i \psi_j^{(n-1)}(x) \quad i \neq j = 0, 1. \end{aligned} \tag{5.63}$$

The special case of $n = 1$ in Eq. (5.61a) and Eq. (5.61b) yields equations for the mean conditional flux for general renewal statistics

$$\frac{\partial}{\partial x}p_i\psi_i(s,x) + \frac{\partial}{\partial s}p_i\psi_i(s,x) + p_i\Sigma_i\psi_i(s,x) = -h_i(s)\,p_i\psi_i(s,x) + Q_i\,p_i\mathcal{A}_i(s,x), \quad i = 0,1, \tag{5.64a}$$

$$p_i\psi_i(0,x) = \int_0^\infty h_j(s)\,p_j\,\psi_j(s,x)\,ds, \quad i \neq j = 0,1, \tag{5.64b}$$

$$\psi_i(s,0) = \Psi_0\,\mathcal{A}_i(s), \tag{5.65}$$

where we have used the definition $\psi_i^{(0)}(s,x) = \mathcal{A}_i(s,x)$. It is interesting that the source contribution on the RHS of Eq. (5.64a) is weighted by the age distribution. This is reasonable as the source particles are independently injected at different spatial points relative to the material interfaces and hence their age distribution is determined by the material statistics. For homogeneous statistics, the source age distribution is just the modified renewal distribution given in Eq. (3.21). Finally, the material-conditioned flux variance and standard deviation follow from the solution for the second moment $\psi_i^{(2)}(s,x)$ which satisfies Eq. (5.61a) and Eq. (5.61b) with $n = 2$. Note that in this case the mean flux appears as an inhomogeneous term.

GLBE Discussion

It will be noted that Eq. (5.64a) and Eq. (5.64b) share a structural similarity with Larsen's Generalized Linear Boltzmann Equation (GLBE) [38] but differ significantly in their foundations and interpretation. In the GLBE framework, an auxiliary variable, analogous in form to our age variable, is introduced to represent the distance since the last *collision*, in order to describe non-exponential free-path distributions in a hypothesized non-Markovian medium. In this formulation, the interaction centers or nuclei are assumed distributed with non-Poisson statistics and an equation for the ensemble-averaged flux, the GLBE, is obtained without requiring an explicit stochastic geometric model of the underlying medium. In contrast, our approach is based on renewal statistics applied to an underlying stochastic material geometry rather than particle interactions or collisions. The auxiliary variable in our formulation represents the distance since the last *material transition* or *interface* between immiscible phases, and our Generalized Master Equation governs the full probability density function of the particle flux conditioned on the material type and age. Thus, while the GLBE presupposes a continuous, homogenized background with a phenomenological path-length distribution, the GME reflects the underlying discontinuous material structure and is consistent with individual realizations of the medium obeying alternating renewal statistics. Although demonstrated here in the absence of scattering, the GME approach is well suited for systematic extension to include additional interaction physics. We emphasize that despite these differences, both formulations give rise to *non-classical* transport equations in which

the standard exponential attenuation law is replaced by more general path-length dependent dynamics, tied to either material geometry (in the GME) or effective path-length statistics (in the GLBE).

The GME approach also differs fundamentally from the previous work of [39, 33] which uses classical renewal theory to derive a coupled system of renewal integral equations for the material- and interface-averaged fluxes. The renewal framework is moreover intrinsically moment-specific: higher moments require the renewal analysis to be repeated and integral equations to be rederived each time [40]. The GME in contrast is a transport equation for the joint probability distribution in the age-augmented state from which moment equations of any order follow directly by projection of the GME, as demonstrated above. Furthermore, the transport-theoretic basis of the GME enables scattering to be incorporated more naturally, albeit phenomenologically due to the resulting loss of Markovianicity.

5.4 Numerical Implementation

Analytical Solution of Benchmark Geometries

Here we derive an exact solution of Eq. (5.2) for any realization of the ARP which, as noted earlier, is comprised of alternating layers of materials with fixed properties. Given a segmentation of the material realization $\{0 = x_0, x_1, \ldots, x_N = X\}$ where the $x_n, n = 1, 2, \ldots N$ are the material interface locations, the random cross section and source can be expressed as (dropping the realization label ω for convenience)

$$\Sigma(x) = \sum_{n=1}^{N} \Sigma^{(n)} \mathcal{I}_{S_n}(x), \tag{5.66}$$

$$Q(x) = \sum_{n=1}^{N} Q^{(n)} \mathcal{I}_{S_n}(x), \tag{5.67}$$

where $\Sigma^{(n)} \in \{\Sigma_0, \Sigma_1\}$ and $Q^{(n)} \in \{Q_0, Q_1\}$ in the n^{th} segment, $S_n = \{x_{n-1}, x_n\}$, and $\mathcal{I}$ is the indicator function defined as

$$\mathcal{I}_{S_n}(x) = \begin{cases} 1, & x \in S_n \\ 0, & \text{otherwise.} \end{cases} \tag{5.68}$$

Restricting Eq. (5.2) to segment n, we obtain

$$\frac{d\Psi^{(n)}(x)}{dx} + \Sigma^{(n)} \Psi(x) = Q^{(n)}, \ x \in S_n, \ n = 1, 2, \ldots N, \tag{5.69}$$

which has the solution

$$\Psi^{(n)}(x) = \Psi^{(n-1)}(x_{n-1}) \exp\left[-\Sigma^{(n)}\,(x - x_{n-1})\right] + \frac{Q^{(n)}}{\Sigma^{(n)}}\left\{1 - \exp\left[-\Sigma^{(n)}\,(x - x_{n-1})\right]\right\}, \tag{5.70}$$

$$\Psi^{(0)}(x_0) = \Psi(0) = \Psi_0, \tag{5.71}$$

where $\Psi^{(n-1)}(x_{n-1})$ is the flux at interface position x_{n-1}. Setting $x = x_n$ in Eq. (5.70) gives a forward recursion for the flux at the material interfaces starting at the boundary

$$\Psi^{(n)}(x_n) = \Psi^{(n-1)}(x_{n-1}) \exp\left[-\Sigma^{(n)}\,(x_n - x_{n-1})\right] + \frac{Q^{(n)}}{\Sigma^{(n)}}\left\{1 - \exp\left[-\Sigma^{(n)}\,(x_n - x_{n-1})\right]\right\}, \tag{5.72}$$

$$\Psi^{(0)}(x_0) = \Psi_0, \tag{5.73}$$

or with $\Delta_n = (x_n - x_{n-1})$ and $T_n = \Psi^{(n)}(x_n)$

$$T_n = T_{n-1} \exp\left[-\Sigma^{(n)}\,\Delta_n\right] + \frac{Q^{(n)}}{\Sigma^{(n)}}\left\{1 - \exp\left[-\Sigma^{(n)}\,\Delta_n\right]\right\}, \quad n = 1, 2, \ldots N, \tag{5.74}$$

$$T_0 = \Psi_0. \tag{5.75}$$

Eq. (5.74) is equivalent to the inhomogeneous difference equation with a non-constant coefficient

$$T_n = A_n\, T_{n-1} + B_n, \tag{5.76}$$

where

$$A_n = \exp\left[-\Sigma^{(n)}\,\Delta_n\right], \tag{5.77}$$

$$B_n = \frac{Q^{(n)}}{\Sigma^{(n)}}\left\{1 - \exp\left[-\Sigma^{(n)}\,\Delta_n\right]\right\}. \tag{5.78}$$

The difference equation has the closed form solution

$$T_n(\omega) = T_0 \prod_{k=1}^{n} A_k(\omega) + \sum_{j=1}^{n-1} B_j(\omega) \left(\prod_{k=j+1}^{n} A_k(\omega)\right) + B_n(\omega), \tag{5.79}$$

where the index ω has been restored as a reminder that the solution is realization dependent. The first term on the RHS of Eq. (5.79) is simply the solution to the homogeneous equation, i.e., the solution with $Q(x) = 0$, which we express as

$$\begin{aligned} T_n^{(H)}(\omega) &= T_0 \prod_{k=1}^{n} A_k(\omega) \\ &= \Psi_0 \exp\left(-\tau_n(\omega)\right), \quad n = 1, 2, \dots N, \end{aligned} \tag{5.80}$$

where

$$\tau_n(\omega) = \sum_{j=1}^{n} \Sigma^{(j)}(\omega)\, \Delta_j, \tag{5.81}$$

is the optical thickness of the medium through the n^{th} interface. Eq. (5.79) then becomes

$$T_n(\omega) = T_n^{(H)}(\omega) + \sum_{j=1}^{n-1} B_j(\omega) \left(\prod_{k=j+1}^{n} A_k(\omega) \right) + B_n(\omega). \tag{5.82}$$

Setting $n = N$ gives the transmittance at the right boundary for any realization

$$T_N(\omega) = T_N^{(H)}(\omega) + \sum_{j=1}^{N-1} B_j(\omega) \left(\prod_{k=j+1}^{N} A_k(\omega) \right) + B_N(\omega), \tag{5.83}$$

which when combined with Eq. (5.70) gives the interior solution for $x \in S_n$ and $n = 1, 2, \dots N$

$$\begin{aligned} \Psi^{(n)}(x, \omega) &= T_{n-1}(\omega) \exp\left[-\Sigma^{(n)}(\omega)\left(x - x_{n-1}\right)\right] \\ &\quad + \frac{Q^{(n)}}{\Sigma^{(n)}} \left\{1 - \exp\left[-\Sigma^{(n)}\left(x - x_{n-1}\right)\right]\right\}. \end{aligned} \tag{5.84}$$

The unconditional, i.e., regardless of material type, k^{th}-moment of the transmittance and interior flux distribution are obtained by computing averages over an ensemble of size Ω, as

$$\left\langle T^{(k)} \right\rangle = \frac{1}{\Omega} \sum_{\omega} \left[T_N(\omega)\right]^k, \tag{5.85}$$

$$\left\langle \Psi^{(k)}(x) \right\rangle = \frac{1}{\Omega} \sum_{\omega} \left[\Psi^{(n)}(x, \omega)\right]^k. \tag{5.86}$$

Moments conditioned on material type may be computed as restricted averages defined by

$$\left\langle T_i^{(k)} \right\rangle = \frac{1}{\Omega} \sum_{\omega} \left[T_N(\omega)\right]^k \mathcal{I}_i(X), \tag{5.87}$$

$$\left\langle \Psi_i^{(k)}(x) \right\rangle = \frac{1}{\Omega} \sum_{\omega} \left[\Psi^{(n)}(x, \omega)\right]^k \mathcal{I}_i(x), \tag{5.88}$$

where the indicator function $\mathcal{I}_i(x)$ is unity when x is in material-i and zero otherwise. The following relationships between the unconditional and conditional averages are easily established from the properties of the indicator function:

$$\left\langle T^{(k)} \right\rangle = \left\langle T_i^{(k)} \right\rangle + \left\langle T_j^{(k)} \right\rangle \tag{5.89}$$

$$\left\langle \Psi^{(k)}(x) \right\rangle = \left\langle \Psi_i^{(k)}(x) \right\rangle + \left\langle \Psi_j^{(k)}(x) \right\rangle . \tag{5.90}$$

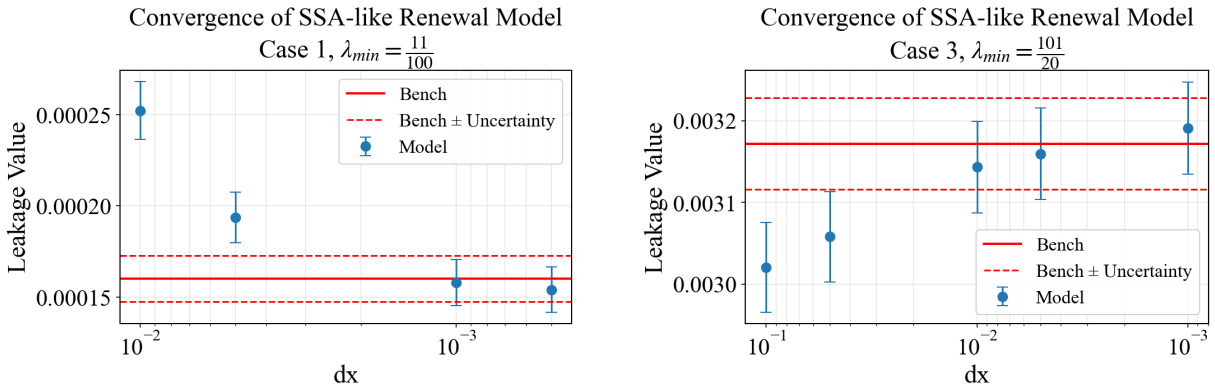
Stochastic Simulation Algorithm for GME

The Markovian formulation lends itself to the construction of a stochastic simulation algorithm that updates the state of the system over short spatial steps Δx through transition rates determined by the transition probabilities. Given the system state at position x, namely, $\{\psi, i, s\}$, the state after an incremental spatial step Δx changes in two mutually exclusive steps, as described earlier. With probability $1-h_i(s)\Delta x$ the material does not switch but the flux and age are changed by an incremental amount. With probability $h_i(s)\Delta x$ the material switches to type $j \neq i$, the age resets to zero but the flux remains unchanged. Thus, given an initial state $\{\psi^*, i^*, s^*\}$ at $x = 0$ and increment Δx, a trajectory of ψ and s can be constructed by marching across the problem domain. When repeated for a large number of trajectories or histories, averages conditioned on material type at any spatial location may then be obtained. The details can be seen in Algorithm 1.

Algorithm 3 SSA-like GME Algorithm

```
Initialize realization
Sample initial material i from volume fractions
Sample initial age s from A_i(s)
for each realization do
    for each spatial cell do
        s = s + Δx
        P_switch = h_i(s) Δx
        Generate random number ξ ~ U(0,1)
        if ξ < P_switch then
            Switch material i → j
            Reset age s → 0
            ψ_j(x + Δx) = ψ_i(x)
        else
            ψ_i(x + Δx) = ψ_i(x)(1 − Σ_{t,i} Δx) + q_i Δx
        end if
    end for
end for
```

For numerical illustration, we consider a selection of renewal distributions previously analyzed in the literature [11, 12, 41], specifically the ramp-ramp, exponential-ramp, and



(a) Convergence case 1

(b) Convergence case 3

Figure 5.1: Convergence of cases 1 and 3 as a function of step size Δx for ramp-ramp mixing.

exponential-exponential (Markov) material distributions. Additionally, simulations were conducted with the distributions corresponding to spherical inclusions with both uniformly distributed radii and exponentially distributed radii [5]. The chord length distributions used to produce the numerical results are those defined in Chapter 3, specifically Eqs. (3.16) through (3.19). Similarly, cross sections $\Sigma_{t,i}$ (cm^{-1}) and mean layer thicknesses or mean chord lengths λ_i (cm) for materials $i = 0, 1$ were taken from a standard binary stochastic media transport benchmark set [9, 10], reproduced in Table 5.1.

Case	$\Sigma_{t,0}$	$\Sigma_{t,1}$	λ_0	λ_1
1	10/99	100/11	99/100	11/100
2			99/10	11/10
3	2/101	200/101	101/20	101/20

Table 5.1: Material parameters

The domain size was taken to be $L = 10$ (cm), to ensure statistically well represented realizations, and 10^6 realizations of the geometry were sufficient to give statistically converged results for the analytical benchmark. Similarly, 10^6 histories provided statistically converged averages in the stochastic simulation. Convergence of the transmittance as a function of the step-size Δx and $\lambda_{min}/\Delta x$, where λ_{min} is the smaller of the two mean chord lengths, for cases 1 and 3 with ramp-ramp mixing is provided in Figure 5.1. To ensure convergence across all cases in this work, a conservative value of $\Delta x = 0.001$ was used.

Numerical Results

An important test of the model and algorithm is if the equilibrium age distribution $\mathcal{A}_i(s)$ is reproduced at the right boundary of the geometry. The material-conditioned equilibrium age distributions are constructed in the simulation by sampling material realizations and averaging the age at the right boundary for each material segment. The distributions for the last segment being materials $\mathcal{M}_0$ and $\mathcal{M}_1$ are shown Figure 5.2, confirming that the stochastic simulation reproduces the analytic equilibrium age distribution in each case. The distribution when the last segment is $\mathcal{M}_1$ is noisier because the mean chord length is an almost an order of magnitude smaller than $\mathcal{M}_0$ which leads to rarer occurrences of $\mathcal{M}_1$. The statistical error is reduced by averaging over a larger ensemble of realizations.

Simulation results with particle transport were compared against the analytic benchmark for problems with an incident boundary source $\Psi(0) = \Gamma_0 = 1$. Mean leakage values ($\langle T \rangle$) for transmittance and second moments ($\langle T_2 \rangle$) are summarized in Table 5.2, while ensemble-averaged material-conditioned interior fluxes and material-conditioned relative standard deviations for case 3 for each material distribution are shown in Figures 5.3–5.7. The leakage values in Table 5.2 are displayed with the statistical uncertainty in the last digit shown in parentheses (i.e., 0.123(4) denotes 0.123 ± 0.004). In general, the model agrees with the benchmark for leakage values within statistical uncertainty for almost all cases. The only exception is the second moment for case 1, which shows a small absolute discrepancy between the model and benchmark for both Markov and ramp-ramp mixing. This discrepancy is attributed to Δx not being small enough in the simulation. The ensemble average flux distributions and relative standard deviations are also subject to this discretization error, but the model and the benchmark show good agreement regardless of the three selected renewal material distribution combinations.

The SSA model was also evaluated against the analytic benchmark for problems with a random interior particle source and no incident boundary flux. Two different source configurations were considered. Figure 5.8 presents the material-conditioned ensemble-average flux distribution and material-conditioned relative standard deviation of the flux for case $q_0 = 0.1,\ q_1 = 1.0$ with ramp-ramp material distributions, while Figure 5.9 shows the corresponding results for $q_0 = 1.0,\ q_1 = 0.1$. For both source configurations, the simulation results are in agreement with the benchmark across all tested material distributions and cases, but only ramp-ramp mixing with case 3 is presented here for brevity. A table of leakage values is also omitted for these interior source problems for brevity; the demonstrated agreement in interior flux is sufficient to validate the model.

Finally, in Figures 5.10 and 5.11, we show the probability density function (PDF) of the transmission both in total and conditioned on the last segment material type, respectively. Once again, excellent agreement with the analytical benchmark is observed. Although the PDF for Case 2 only is shown, the agreement is uniform across the spectrum of material distributions and cross sections. The displayed case is highlighted here because of the spike observed at the upper end (maximum transmittance) of the PDF which represents the contribution from particles that traverse the medium without colliding. This is dominant in

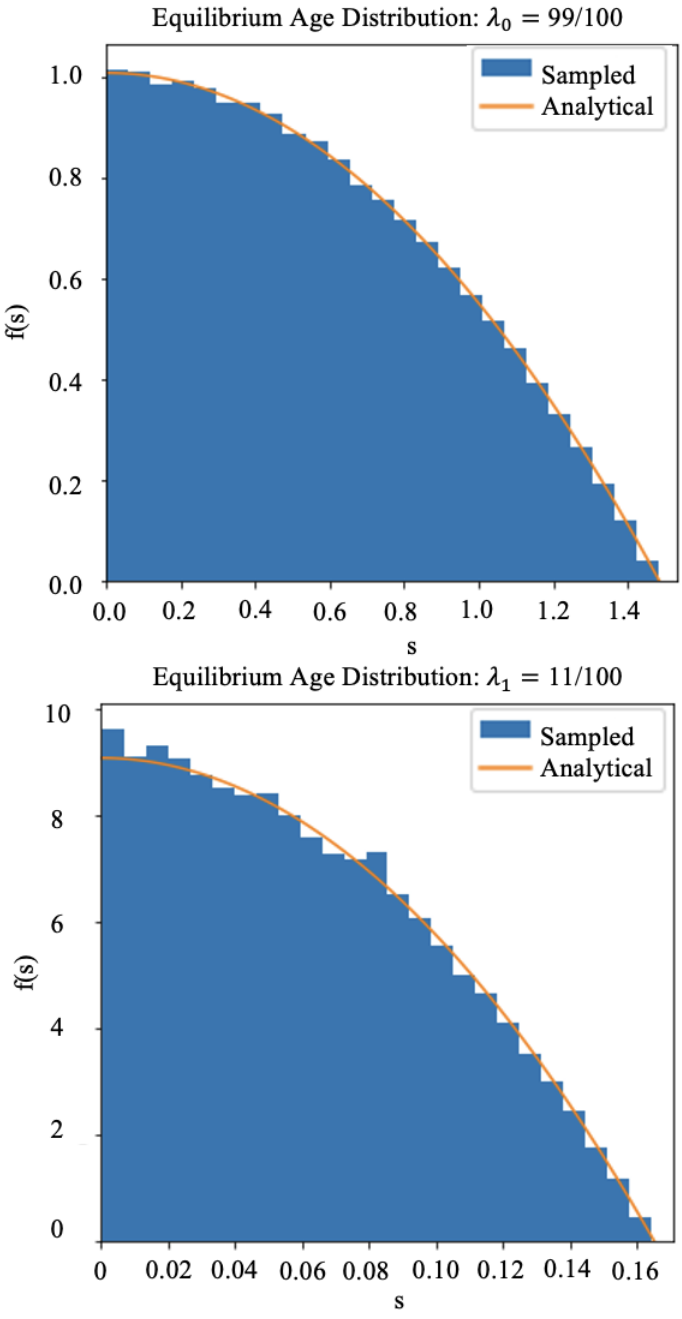
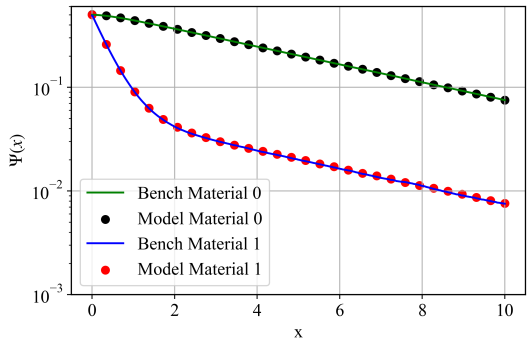


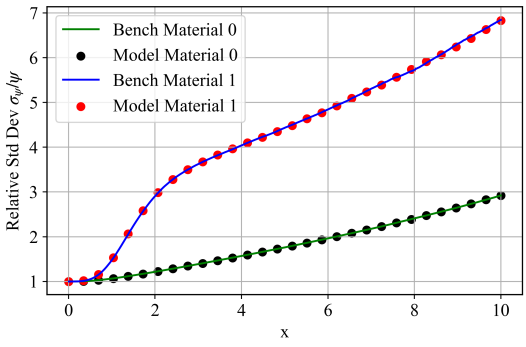
Figure 5.2: Sampled equilibrium age distribution from model compared with analytic solution for ramp distribution.

		$\langle T \rangle$		$\langle T_2 \rangle$	
Distributions (Mat 0, Mat 1)	Case	Bench	Model	Bench	Model
Exp., Exp.	1	0.00270(2)	0.00277(5)	0.0001696(7)	0.000178(2)
	2	0.1336(1)	0.1338(3)	0.04609(2)	0.04616(6)
	3	0.08264(9)	0.0827(3)	0.05644(6)	0.0564(2)
Ramp, Ramp	1	0.000111(3)	0.00012(1)	5.92(2)e-8	6.67(8)e-8
	2	0.05290(7)	0.0532(2)	0.01793(1)	0.01804(4)
	3	0.00213(1)	0.00211(5)	0.000261(2)	0.000256(6)
Exp., Ramp	1	0.00103(1)	0.00105(3)	3.77(4)e-5	3.8(1)e-5
	2	0.1232(1)	0.1233(3)	0.04408(2)	0.04409(6)
	3	0.07127(8)	0.0711(3)	0.05175(6)	0.0516(2)
Exp., Exp. Radii	1	0.00163(4)	0.00170(4)	7.6(2)e-5	8.0(2)e-5
	2	0.1256(3)	0.1256(3)	0.04437(6)	0.04436(6)
	3	0.0736(3)	0.0736(3)	0.0522(2)	0.0522(2)
Exp., Unif. Radii	1	0.00114(3)	0.00119(3)	4.5(1)e-5	4.7(1)e-5
	2	0.1238(3)	0.1238(3)	0.04413(6)	0.04415(6)
	3	0.0723(3)	0.0718(3)	0.0522(2)	0.0518(2)

Table 5.2: Numerical results for leakage values.

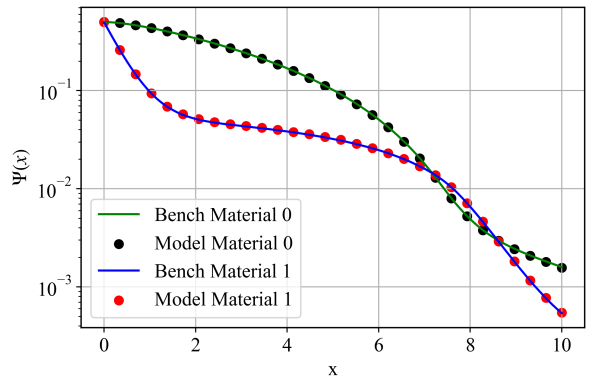


(a) Material conditional ensemble average flux distribution: benchmark vs. model, exponential-exponential (Markov) mixing.

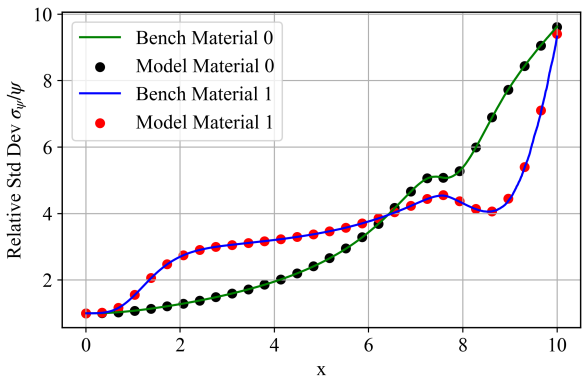


(b) Material conditional relative standard deviation of flux distribution: benchmark vs. model, exponential-exponential (Markov) mixing.

Figure 5.3: Comparison of interior flux quantities for SSA model vs. analytic benchmark for case 3 with exponential-exponential (Markov) mixing.

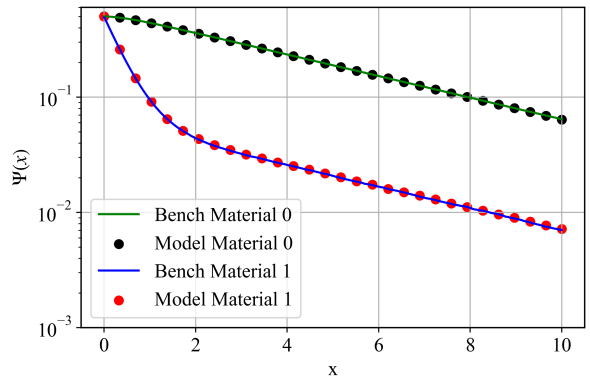


(a) Material conditional ensemble average flux distribution: benchmark vs. model, ramp-ramp mixing.

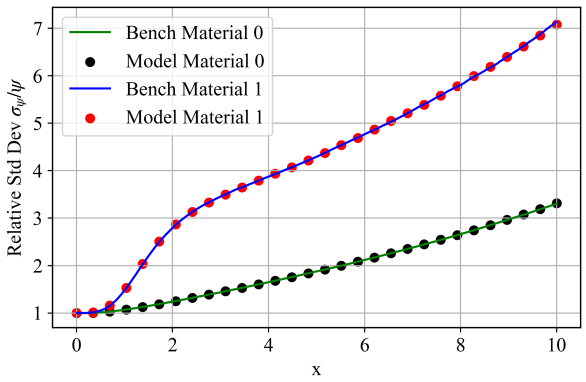


(b) Material conditional relative standard deviation of flux distribution: benchmark vs. model, ramp-ramp mixing.

Figure 5.4: Comparison of interior flux quantities for SSA model vs. analytic benchmark for case 3 with ramp-ramp mixing and a boundary source of particles at $x = 0$.

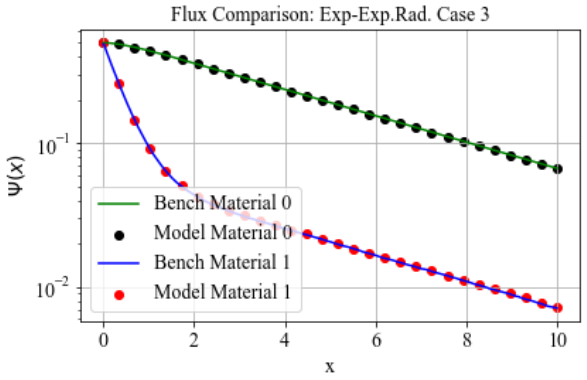


(a) Material conditional ensemble average flux distribution: benchmark vs. model, exponential-ramp mixing.

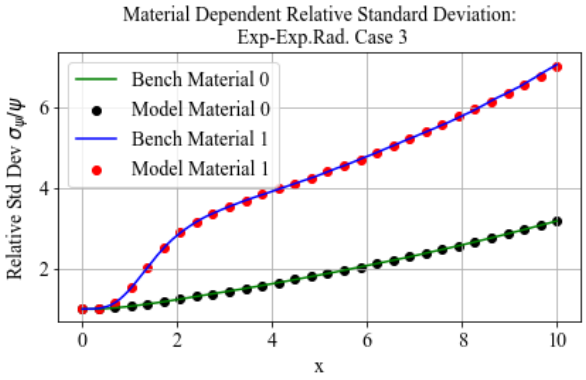


(b) Material conditional relative standard deviation of flux distribution: benchmark vs. model, exponential-ramp mixing.

Figure 5.5: Comparison of interior flux quantities for SSA model vs. analytic benchmark for case 3 with exponential-ramp mixing and a boundary source of particles at $x = 0$.

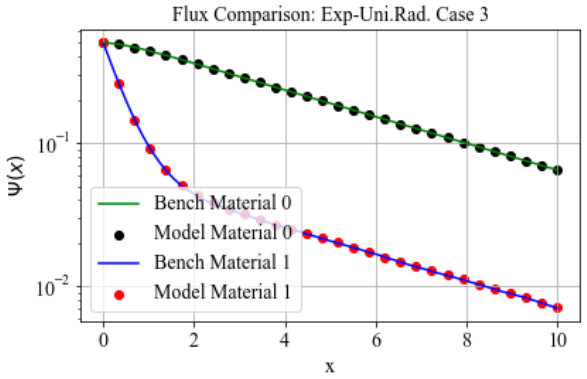


(a) Material conditional ensemble average flux distribution: benchmark vs. model, exponential-exponential radii mixing.

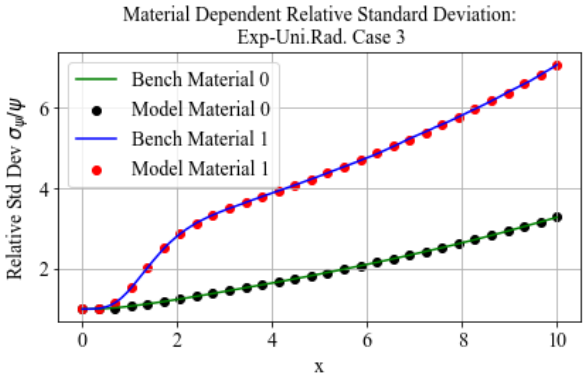


(b) Material conditional relative standard deviation of flux distribution: benchmark vs. model, exponential-exponential radii mixing.

Figure 5.6: Comparison of interior flux quantities for SSA model vs. analytic benchmark for case 3 with exponential-exponential radii mixing and a boundary source of particles at $x = 0$.

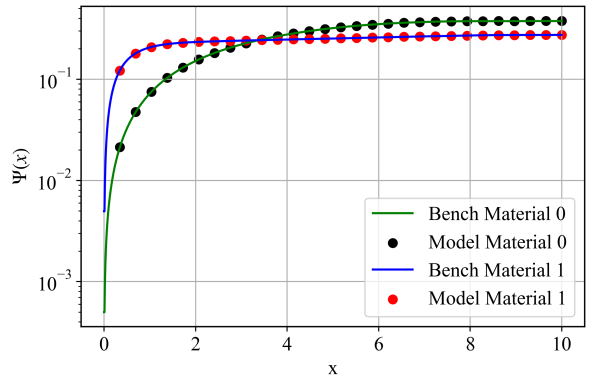


(a) Material conditional ensemble average flux distribution: benchmark vs. model, exponential-uniform radii mixing.

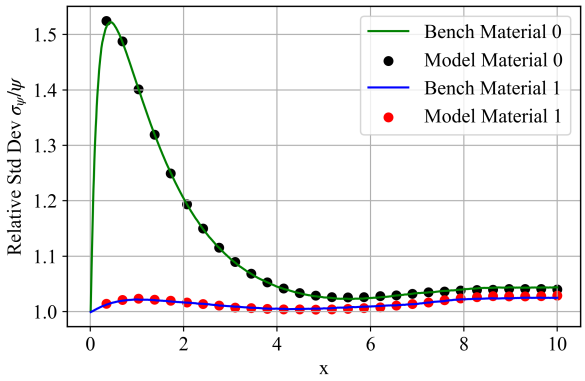


(b) Material conditional relative standard deviation of flux distribution: benchmark vs. model, exponential-uniform radii mixing.

Figure 5.7: Comparison of interior flux quantities for SSA model vs. analytic benchmark for case 3 with exponential-uniform radii mixing and a boundary source of particles at $x = 0$.

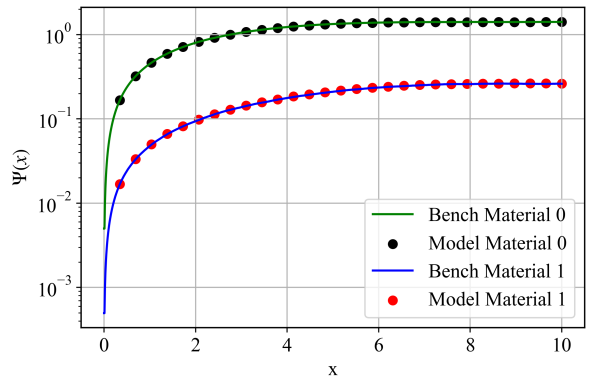


(a) Material conditional ensemble average flux distribution: benchmark vs. model, ramp-ramp mixing.

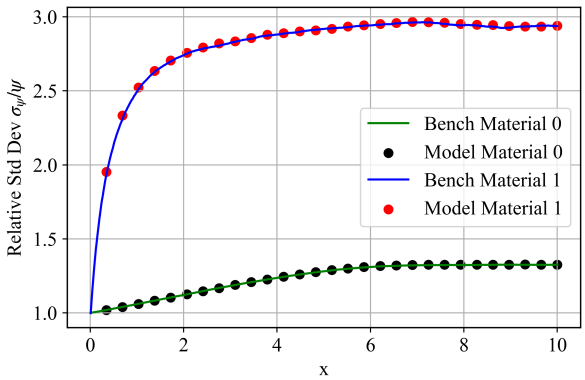


(b) Material conditional relative standard deviation of flux distribution: benchmark vs. model, ramp-ramp mixing.

Figure 5.8: Comparison of interior flux quantities for SSA model vs. analytic benchmark for case 3 with ramp-ramp mixing and a random interior source of particles with $q_0 = 0.1,\ q_1 = 1.0$.



(a) Material conditional ensemble average flux distribution: benchmark vs. model, ramp-ramp mixing.



(b) Material conditional relative standard deviation of flux distribution: benchmark vs. model, ramp-ramp mixing.

Figure 5.9: Comparison of interior flux quantities for SSA model vs. analytic benchmark for case 3 with ramp-ramp mixing and a random interior source of particles with $q_0 = 1.0,\ q_1 = 0.1$.

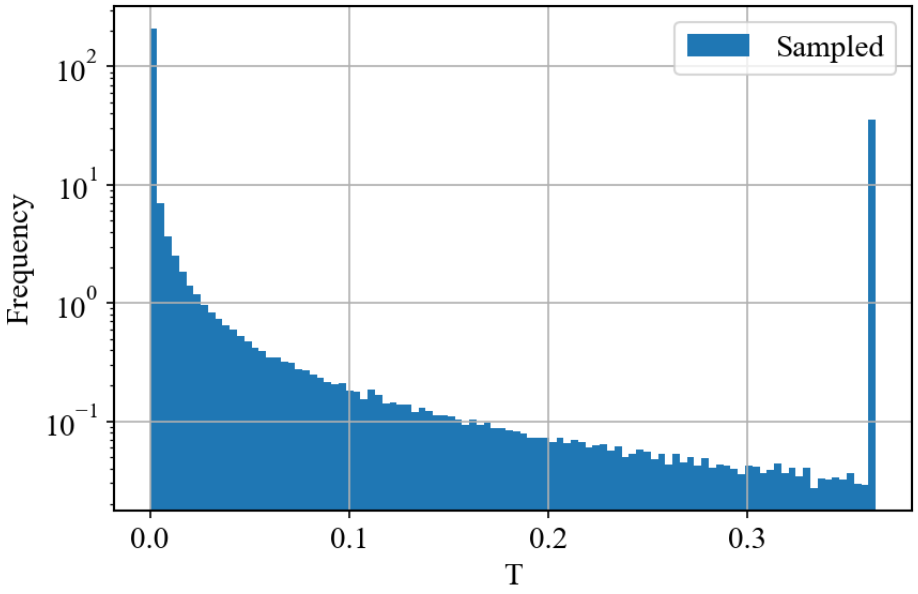
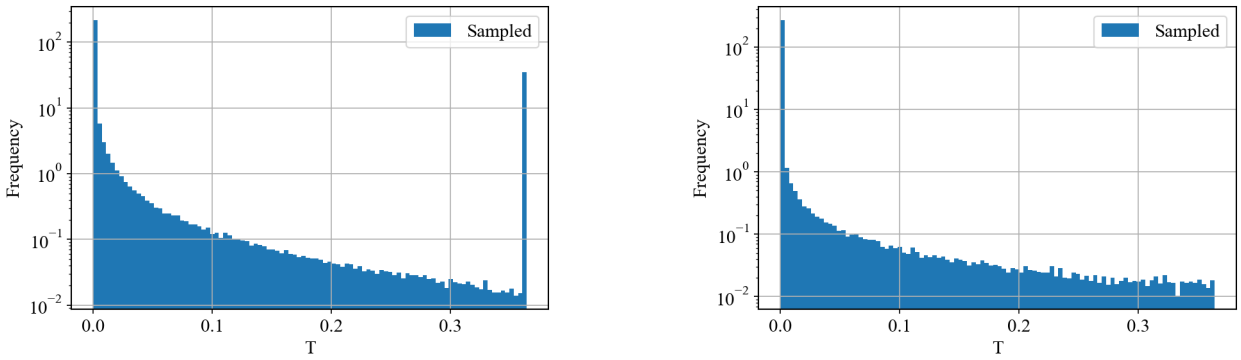


Figure 5.10: Distribution of transmission values for case 2 with ramp-ramp mixing and incident boundary flux.

Case 2 because the mean chord length of $\mathcal{M}_0$ ($\lambda_0 = 99/10$) is on the order of the medium thickness (10 cm), which results in a preponderance of realizations of a single material. However, as the associated particle mean free path ($1/\Sigma_0 = 99/10$) is also of the order of the medium thickness, particle transmittance is significant in these realizations, more so than in other cases. Distributions for interior source problems as well as incident boundary source problems with different material distributions are omitted for brevity, but similarly strong agreement with the benchmark is observed across the board.

Beyond validating the GME for non-Markovian ARP media, these simulations show that applying a Markov (exponential) approximation to binary mixtures with non-exponential segment statistics can produce large errors in both transmittance and interior flux. A physically relevant example is a background medium containing randomly distributed spherical inclusions of fixed radius (e.g., [1, 5]); in this case, the inclusion chord lengths follow a ramp distribution while the background chords are exponential. For nonscattering materials, the GME yields an exact description of transport in such mixtures. Figure 5.12 contrasts GME predictions with those obtained by replacing the true inclusion distribution by an exponential for all three cases, where material index 1 denotes the spherical inclusions. We observe that while the discrepancy between the Markov approximation and the exact renewal description in Case 3 increases monotonically to $\sim 15\%$ at the transmission boundary, the maximum discrepancy can be almost an order of magnitude larger in Case 1. Thus, the Markov approximation seems significantly less accurate for small inclusions with a large cross section relative to the background material. A representative scenario is provided by



(a) Material 0

(b) Material 1

Figure 5.11: Material dependent transmittance PDFs with incident boundary flux.

Rayleigh-Taylor unstable mixtures in ICF pellets.

Additionally, the proper representation of the spherical inclusions is important to the interior flux distributions and leakage quantities. The assumption that spherical inclusions have a constant radius can lead to inaccurate flux solutions if the spheres have a random distribution of radii. Figure 5.13 shows the relative difference in particle flux depending on the distribution of sphere radii for case 1, where the discrepancy between fixed radii and exponentially distributed radii reaches roughly 60%, and the discrepancy between fixed radii and uniformly distributed radii reaches roughly 13%.

5.5 Conclusions

This Chapter developed an age-based generalized master equation formulation for particle transport in purely absorbing binary random media governed by alternating renewal statistics. The central idea was to augment the joint stochastic state space with the age s, defined as the distance since the previous material interface. By including the age variable, the renewal material process is made Markovian in the expanded state space, and deriving the GME becomes possible.

The resulting GME provides an exact formulation for the purely absorbing renewal-media problem considered here. The monotonic relationship between position and age in a pure absorber is the key property that makes the age-augmented state sufficient. Moment equations for material-conditioned flux quantities were obtained by projection of the joint probability density, and the classical Markovian result was recovered in the exponential chord length limit, where the hazard functions are constant and the age dependence can be integrated out.

A stochastic state algorithm based on the GME was then used to simulate the evolution of the particle flux and age through the medium. Comparisons against benchmark

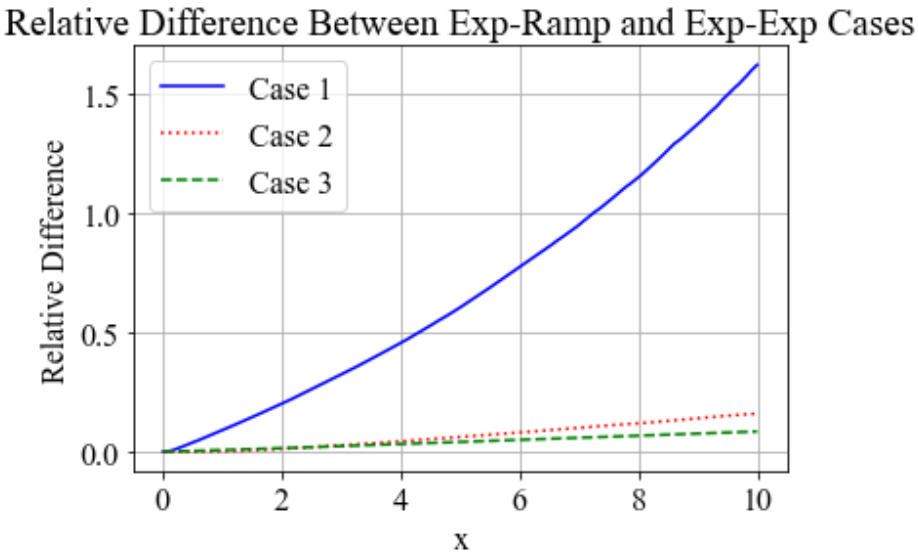


Figure 5.12: Relative difference between benchmark interior fluxes for Markov (exponential-exponential) and exponential-ramp media.

ensemble-averaged calculations validated the GME formulation for nonscattering renewal media. The equilibrium age distribution, interior flux moments, and boundary transmittance were all reproduced accurately. The numerical results also demonstrated that replacing non-exponential renewal statistics with a Markovian approximation can produce significant discrepancies in both transmittance and interior flux profiles, even when the mean chord lengths and volume fractions are preserved. This confirms that the full chord length statistics, not only their means, can be important for transport in non-Markovian random media.

The exactness of the formulation derived in this chapter relies on the absence of scattering. When scattering is introduced, particles may reverse direction and revisit regions of the material realization that have already been sampled. In that case, the current material type and age no longer fully determine the future material sequence seen by the particle. Scattering, therefore, introduces the transport memory effect that makes the model approximate. Chapter 6 builds on the purely absorbing GME model by introducing and testing age-based Monte Carlo extensions for scattering renewal media, including several possible treatments of the post-scatter age.

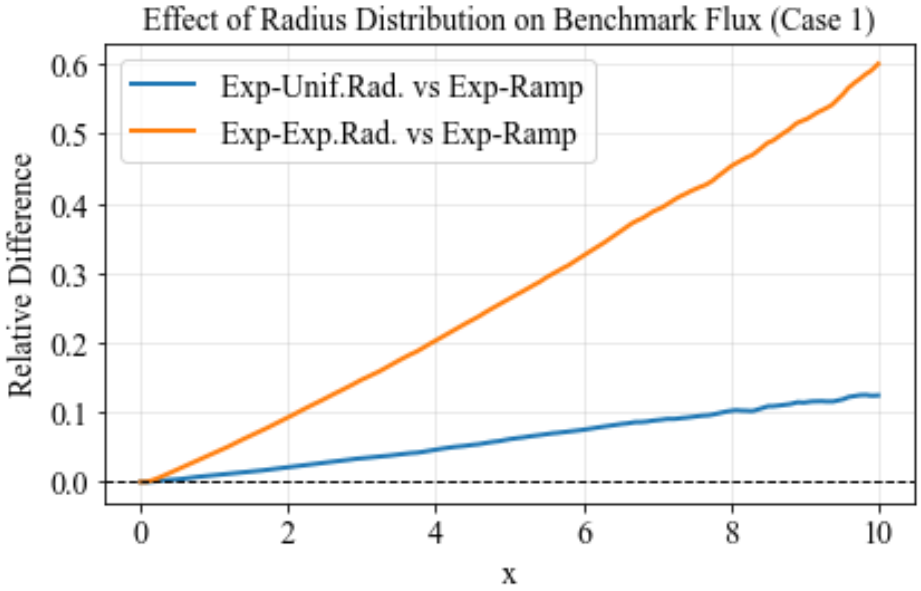


Figure 5.13: Relative difference between benchmark interior fluxes for spherical inclusion geometries with constant radii (exponential-ramp) and spherical inclusion geometries with randomly distributed radii (exponential-uniform radii and exponential-exponential radii) for case 1.

Chapter 6

Extension of Age-Based Transport in Renewal Statistical Media to Include Particle Scatter

6.1 Introduction

The preceding chapters developed the statistical and transport-theoretic setting for particle transport in random media. Chapter 3 introduced the alternating renewal process used to describe non-Markovian binary mixtures, and Chapter 5 derived an age-based generalized Master equation (GME) for renewal statistical media in the purely absorbing limit. In that setting, extending the joint stochastic state space by the age s, defined as the distance from the previous material interface, is sufficient to recover a Markovian description of the problem. The probability of encountering the next material interface is then fully determined by the current material and the current age through the hazard function.

The purpose of this Chapter is to extend the age-based framework to include particle scattering in 1D planar geometry. This extension is complicated by the same transport memory mechanism discussed in Chapter 4 for the Levermore–Pomraning (LP) equations and the associated Monte Carlo methods. In purely absorbing problems, particles stream monotonically along a fixed direction until absorption or leakage, so a particle never revisits a previously sampled portion of the material realization. With scattering, however, particles may reverse direction, meaning the particle flux at point x can depend on the flux at points beyond x in space. Thus, the next state of the joint stochastic process is no longer determined only by the current state, and therefore the process is no longer Markovian. Because of this transport memory, both the LP model and the age-based GME extension become approximate when particle scattering is introduced.

Extending the age-based model to scattering additionally requires specifying how the material age is treated at scattering events. In the purely absorbing limit, the age increases monotonically with distance until a material interface is reached. With scattering, particles

may move back towards an interface, which invalidates the monotonicity of the age variable. This Chapter considers several approximate treatments of age at scattering events, including always resampling the age from the equilibrium age distribution, never resampling the age, resampling only after backscatter, and allowing the age to decrease when the particle reverses direction. Transport equations and equivalent Monte Carlo methods are discussed for these treatments. This chapter also discusses renewal-statistical extensions of existing Monte Carlo methods introduced in Chapter 4, including CLS and LRP.

The Chapter proceeds as follows. Section 6.2 states the age-based transport equations with scattering and introduces the age-redistribution models. Section 6.2 presents the Monte Carlo algorithms, including renewal-statistical extensions of CLS, FLRP, and LRP. Section 6.3 compares the methods against benchmark calculations for boundary-source and interior-source test suites. Section 6.4 summarizes the implications of the results for age-based transport modeling in scattering renewal media.

6.2 Theory and Methods

Statistical Quantities Considered in This Chapter

Only a small number of renewal-statistical quantities are needed in this chapter. To avoid repeating the statistical development from Chapter 3, we use the notation already introduced there. The material-dependent chord length density is $f_i(s)$, the survival function is $S_i(s)$, the hazard function is $h_i(s)$ from Eq. (3.11), and the equilibrium age distribution is $A_i(s)$ from Eq. (3.21). The key point is that $h_i(s)$ gives the conditional interface-crossing rate after a particle has already traveled distance s through material i. For exponential chord statistics, $h_i(s) = 1/\lambda_i$, so the material process is Markovian and the age carries no additional information. For non-exponential renewal statistics, $h_i(s)$ depends on s, so the age carries geometric memory of the current chord.

The Monte Carlo algorithms below repeatedly require a distance to the next material interface conditional on the current age. This distance is obtained from the conditional survival probability introduced in Chapter 3. In practice, a random number $\xi \sim U(0,1)$ is drawn and the interface distance d_i is found from

$$-\ln \xi = \int_s^{s+d_i} h_i(u)\, du. \tag{6.1}$$

Equation (6.1) is included here because it is the operational sampling rule used by the algorithms in this chapter. The chord distributions themselves, including the exponential, ramp, uniformly distributed radius, and exponentially distributed radius cases, are defined in Eqs. (3.16)-(3.19).

For Markovian media, the constant nature of the hazard function yields the familiar

sampling scheme for distance to interface:

$$-\ln\xi = \int_s^{s+d_i} h_i(s'), ds' = \int_s^{s+d_i} \frac{1}{\lambda_i}, ds' = \frac{d_i}{\lambda_i}, \implies d_i = -\lambda_i \ln\xi. \tag{6.2}$$

This is the same sampling scheme used in standard CLS algorithms [15, 10, 16, 6], and is notably independent of the current age s. This independence follows from the memoryless property of the exponential chord length distribution.

To contrast this with a non-Markovian renewal medium, consider the ramp distribution, which describes chord lengths through spheres of uniform radius [5, 11, 12, 27, 26]. As given in Eq (3.17), the ramp chord length distribution is

$$f_i(s) = \frac{8s}{9\lambda_i^2}, \qquad 0 \le s \le \frac{3\lambda_i}{2}, \tag{6.3}$$

with hazard function

$$h_i(s) = \frac{8s}{9\lambda_i^2 - 4s^2}, \qquad 0 \le s < \frac{3\lambda_i}{2}. \tag{6.4}$$

The distance to the next material interface is then sampled by solving

$$-\ln\xi = \int_s^{s+d_i} h_i(s'), ds' = \int_s^{s+d_i} \frac{8s'}{9\lambda_i^2 - 4s'^2}, ds' = \ln\left(\frac{9\lambda_i^2 - 4s^2}{9\lambda_i^2 - 4(s+d_i)^2}\right). \tag{6.5}$$

Solving for d_i gives

$$d_i = -s + \frac{1}{2}\sqrt{4s^2 - (\xi - 1)\,(9\lambda_i^2 - 4s^2)}. \tag{6.6}$$

Unlike the Markovian case, the sampled distance to the next interface depends explicitly on the current age s. This new sampling scheme, however, gives us a way to sample geometric features on-the-fly for any arbitrary chord length distribution.

Age-Based Transport Equation with Scattering

We consider the standard binary, immiscible, statistically homogeneous renewal medium in 1D planar geometry. Let $\psi_i(s, x, \mu)$ denote the material-conditioned angular flux in material $i = 0, 1$, weighted by the material volume fraction p_i, with age s, position x, and direction cosine μ. The purely absorbing GME-derived equation for the ensemble-averaged material-conditioned flux Eq. (5.64) can be extended to scatter by heuristically introducing the standard scattering source term for 1D planar geometry [32]. The resulting equation is

$$\begin{aligned}&\mu\frac{\partial}{\partial x}p_i\psi_i(s,x,\mu) + \frac{\partial}{\partial s}p_i\psi_i(s,x,\mu) + \Sigma_i p_i\psi_i(s,x,\mu) = \\ &\int_0^\infty ds' \int_{-1}^1 d\mu' \Sigma_s(\mu_0) p_i\psi_i(s',x,\mu')K(s,s') - |\mu| h_i(s) p_i\psi_i(s,x,\mu) + Q_i p_i A_i(s), \quad i = 0,1,\end{aligned} \tag{6.7a}$$

with the jump condition, or zero-age boundary condition,

$$p_i\psi_i(0,x,\mu) = \int_0^\infty |\mu| h_j(s) p_j \psi_j(s,x,\mu) ds, \quad i \neq j = 0,1. \tag{6.7b}$$

Here $\Sigma_{t,i}$ and $\Sigma_{s,i}$ are the total and scattering cross sections of material i, respectively, and $\mu_0 = \mu \cdot \mu'$ denotes the cosine of the scattering angle. The term $|\mu| h_i(s)$ is the interface crossing rate (with interfaces only existing perpendicular to the x-axis), and the jump condition places particles that cross from material j into material i at zero age.

The variability in the model comes from the treatment of the age at a scattering event, manifesting in the scattering kernel $K_i(s,s')$. The kernel specifies how the age after a scattering collision is related to the incoming age s'. There are several choices of varying complexity for said kernel, three of which are discussed in the following section.

Age Redistribution Kernels

Always Resample

One simplistic approach is to ignore the incoming age at every scattering event and resample the outgoing age from the equilibrium age distribution:

$$K_i(s,s') = A_i(s). \tag{6.8}$$

This model treats a scattered particle as though it has been reinserted at a random point in material i, where the equilibrium age distribution gives us the distribution of the age at any random point in the infinite alternating renewal process. It is simple and allows for solving the transport equation, but it erases all local geometric information at every scattering collision.

Never Resample

The opposite approach is to always retain the age at each scattering event:

$$K_i(s,s') = \delta(s-s'). \tag{6.9}$$

In this model, scattering changes only the particle direction. The material age continues to evolve as the particle streams. This preserves age information, but it does not distinguish between forward scatter and backscatter. Consequently, it accurately represents the age for forward-streaming particles but misrepresents the age after a backscatter.

Backscatter Resample

A more refined approach combines the two approaches, retaining the age for forward scattering and resampling it only when the scattering event reverses the particle direction. In this

case, the scattering source in Eq. (6.7) may be interpreted as the sum of a forward-scattering contribution, for which $\mu_0 > 0$, and a backscattering contribution, for which $\mu_0 < 0$. This is represented with the kernel

$$K(s, s') = \delta(s - s')\mathbb{1}_{\mu_0>0} + A_i(s)\mathbb{1}_{\mu_0<0}, \tag{6.10}$$

This kernel is motivated by the observation that forward scattering does not change the particle's direction of traversal through the current material chord, so the age remains a meaningful measure of the distance from the previous interface. After backscatter, however, the particle begins moving toward previously encountered interface, and the distance to the interface behind the particle is not known. The Backscatter-Resample model therefore replaces the outgoing age with a new sample from the equilibrium age distribution. This is not an exact reconstruction of the local geometry, but it provides a kernel that partially accounts for the loss of geometric memory caused by direction reversal.

For Markovian chord length statistics, all three kernels reduce to the same Levermore-Pomraning scattering model from Eq. (4.21) after integration over s. The integrals of both $A_i(s)$ and $\delta(s - s')$ over outgoing age are unity, so the kernel choice disappears. Differences between the kernels therefore arise only for non-Markovian renewal statistics, where the age dependence of $h_i(s)$ matters.

Transport with Forward Scatter Only

Before considering full scattering, it is useful to isolate the role of backscatter. If particles are constrained to move forward only with $\mu \in (0, 1]$, the age-based equation is exact because particles never return to previously sampled portions of the realization. The augmentation of the state space with age remains sufficient: age increases monotonically along each history, and the interface statistics conditioned on s are completely determined by Eq. (6.1). Numerical results for the transport with particles only moving forward with $\mu \in (0, 1]$ and isotropic scatter confirm exactness for the Ramp-Ramp case, as shown in Fig. 6.1 and Table 6.1. The agreement in this limiting case supports the interpretation that the only source of approximation in the age-based transport model is transport memory, just as in the Markovian model.

Table 6.1: Leakage Comparison Between GME Model and Benchmark for forward moving particles only with Ramp-Ramp mixing.

Case	GME Model T	Benchmark T
1a	0.1919(1)	0.1919(3)
1b	0.000040(2)	0.000039(4)
1c	0.1497(1)	0.1498(3)
2a	0.2362(1)	0.2362(3)
2b	0.1385(1)	0.1384(2)
2c	0.2509(1)	0.2510(3)
3a	0.8339(1)	0.8343(1)
3b	0.00104(1)	0.00101(1)
3c	0.1716(1)	0.1715(1)

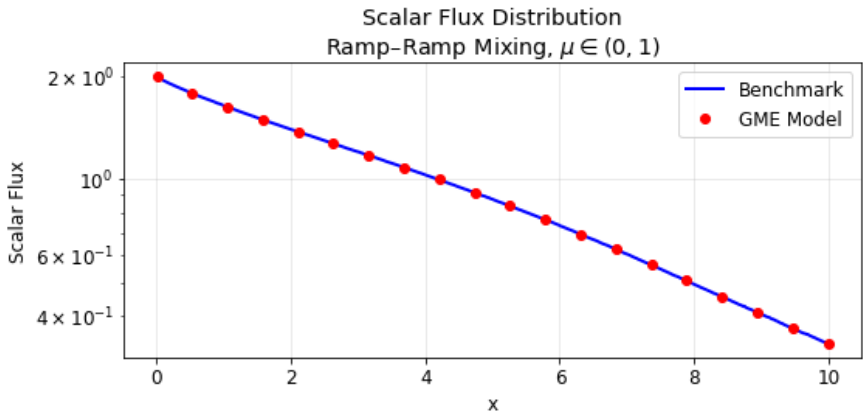


Figure 6.1: Scalar flux for the GME method and the benchmark in Case 3c with Ramp-Ramp mixing, considering particles moving only in the forward direction.

Monte Carlo Algorithms

Age-Based Monte Carlo

The kernels in Section 6.2 correspond to a straightforward Monte Carlo algorithm. The distance to the next interface is sampled conditionally on the current age using Eq. (6.1). The distance to collision is sampled from the usual exponential collision distribution and projected onto the x-axis in 1D planar geometry, as discussed in the classical Monte Carlo methods CLS and LRP discussed in Section 4.4. The only difference between the age-kernel methods is the age update applied after a scattering event. The general procedure for these

methods is seen in Algorithm 4. An example particle history for the Backscatter-Resample method is also given in Figure 6.2.

Algorithm 4 Age-Based Monte Carlo Algorithms with Scattering

Initialize particle position x and direction μ according to source specifications
Select initial material i according to volume fractions
Sample initial age s from the equilibrium age distribution Eq. (3.21)
while particle is alive **do**
    Sample distance to next material interface d_i by solving Eq. (6.1) for d_i
    Sample distance to collision as $d_c = \frac{-\ln \xi}{\Sigma_{t,i}} \cdot |\mu|$
    Compute distance to domain boundary d_b in current direction of travel
    Stream particle distance = $\min\{d_i, d_c, d_b\}$
    Update position x and age s according to distance moved
    if distance = d_c: collision **then**
        if $\xi < \Sigma_{s,i}/\Sigma_{t,i}$ **then**
            Scattering event:
            Sample new direction $\mu \sim$ Uniform$(-1, 1)$
            Update age s using Eq. (6.8), (6.9), or (6.10)
        else
            Tally absorption and terminate particle history
        end if
    else if distance = d_i: material interface **then**
        Switch material $i \leftarrow j$ and set age $s = 0$
    else if distance = d_b: boundary **then**
        Tally leakage and terminate particle history
    end if
end while

Forward Local Realization Preserving

The Backscatter-Resample method also provides a natural place to introduce Forward Local Realization Preserving (FLRP). FLRP was developed in Ref. [27] as a heuristic renewal-statistical extension of CLS. Its purpose is to preserve the forward interface distance in memory to avoid the additional approximation that regular CLS resampling would introduce, as discussed in Section 4.5. In the 1D planar problems considered here, FLRP is equivalent to the Backscatter-Resample model: it retains the current forward distance to material interface while the particle continues in the same direction, and it resamples the distance to material interface from the equilibrium age distribution after a backscatter. Both methods retain one interface in memory, but in opposite directions. In this way, the Backscatter-Resample method provides a transport-theoretic basis to the heuristic FLRP method developed in Ref. [27]. The detailed FLRP algorithm is given in Algorithm 5.

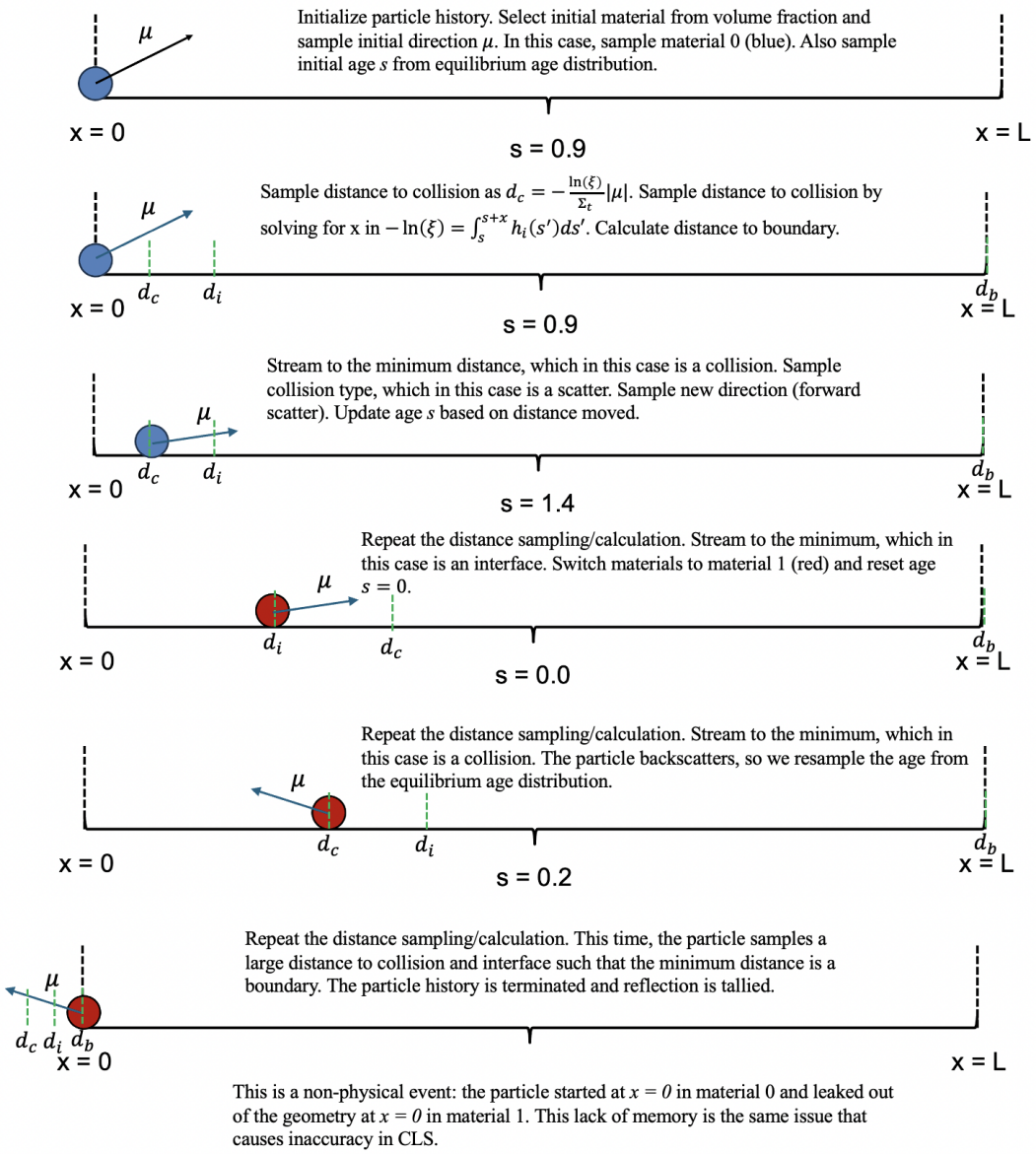


Figure 6.2: Example of a particle history for the Backscatter-Resample method.

Algorithm 5 Forward Local Realization Preserving (FLRP) Algorithm [27]

for each particle history **do**
  Initialize x, μ, and material i from the source and volume fractions
  Sample the initial age s from $A_i(s)$
  while particle is alive **do**
    Sample the forward distance to interface d_i conditional on age s using Eq. (6.1)
    Sample projected distance to collision $d_c = -|\mu| \ln \xi / \Sigma_{t,i}$
    Compute distance to boundary d_b
    Move the particle by $d_{\min} = \min\{d_i, d_c, d_b\}$ and update x and s
    if $d_{\min} = d_b$ **then**
      Tally leakage and terminate the history
    else if $d_{\min} = d_i$ **then**
      Switch material and reset $s = 0$
    else if $d_{\min} = d_c$ **then**
      if collision is absorption **then**
        Tally absorption and terminate the history
      else
        Sample new direction μ
        if the scatter is a backscatter, $\mu\mu' < 0$ **then**
          Reinitialize the forward renewal description by sampling $s \sim A_i(s)$
        else
          Retain the current age s
        end if
      end if
    end if
  end while
end for

Age-Decreasing Method and LRP

The Backscatter-Resample and FLRP methods retain only one-sided geometric memory, as is necessary for accurately representing renewal material distributions. A simple way to make the age-based model more accurate is to allow the age to decrease after a backscatter, so that a particle traveling back toward the most recently sampled interface retains said interface in memory. This method is not represented by a simple monotone-age transport equation because the age derivative changes sign after direction reversal. The development of a transport equation that allows the age to decrease is a subject of ongoing research. Nevertheless, it is useful as a way to improve accuracy for the age-based models by incorporating more geometric memory. Dubbed the Age-Decreasing method, the algorithm is presented in Algorithm 6. An example particle history for the Age-Decreasing method is given in Figure 6.3.

Algorithm 6 Age-Decreasing Monte Carlo Algorithm with Scattering

Initialize particle position x and direction μ according to source specifications
Select initial material i according to volume fractions
Sample initial age s from the equilibrium age distribution Eq. (3.21)
Set age modifier $m_s = 1$
while particle is alive **do**
    if $m_s = 1$ **then**
        Sample distance to next material interface d_i by solving Eq. (6.1) for d_i
    else
        Set distance to next material interface $d_i = s$
    end if
    Sample distance to collision as $d_c = \frac{-\ln \xi}{\Sigma_{t,i}} \cdot |\mu|$
    Compute distance to domain boundary d_b in current direction of travel
    Stream particle distance $= \min\{d_i, d_c, d_b\}$
    Update position x according to distance moved
    Update age $s \leftarrow s + m_s$ distance
    if distance $= d_c$: collision **then**
        if $\xi < \Sigma_{s,i}/\Sigma_{t,i}$ **then**
            Scattering event:
            Store incoming direction $\mu' \leftarrow \mu$
            Sample new direction $\mu \sim \text{Uniform}(-1, 1)$
            if $\mu\mu' < 0$ **then**
                Reverse age modifier $m_s \leftarrow -m_s$
            end if
        else
            Tally absorption and terminate particle history
        end if
    else if distance $= d_i$: material interface **then**
        Switch material $i \leftarrow j$, set age $s = 0$, and set age modifier $m_s = 1$
    else if distance $= d_b$: boundary **then**
        Tally leakage and terminate particle history
    end if
end while

The Age-Decreasing method is closer to LRP than to FLRP because it retains information about an interface behind the particle after a backscatter. It is not identical to LRP, however. LRP stores the distances to the nearest material interfaces on both sides of the particle and updates those distances as the particle streams. The Age-Decreasing model stores only the distance to the previous interface. As a result, after multiple backscatters within the same material segment, the Age-Decreasing model can sample a material interface before the particle returns to a location where it previously backscattered. This is non-physical because

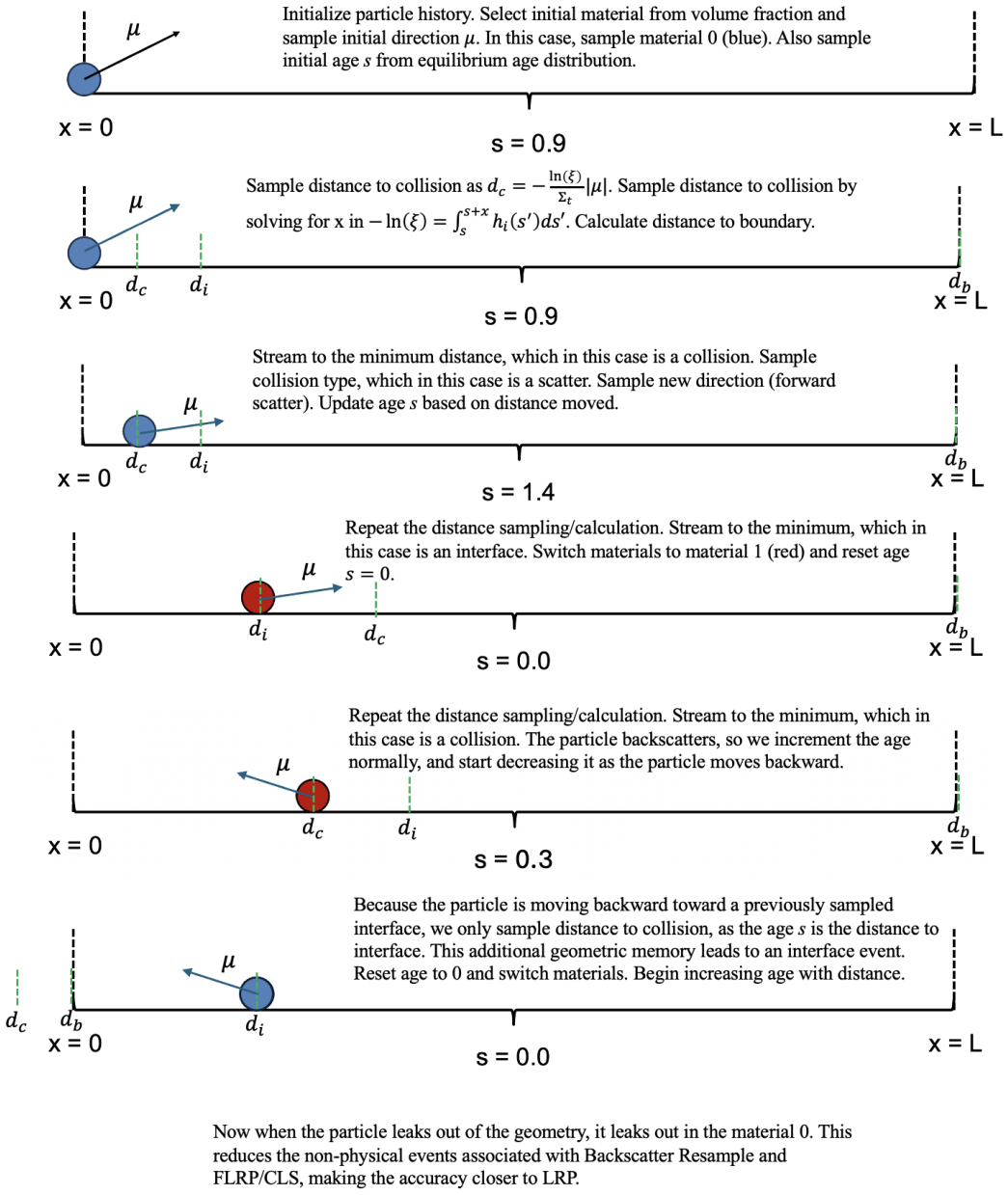


Figure 6.3: Example of a particle history for the Age-Decreasing method.

that location was already known to be in the original material segment. This inconsistency does not occur in LRP because of the enhanced geometric memory. However, unlike LRP, the Age-Decreasing model is motivated by the age-based transport formulation and can be viewed as a transport-theoretic algorithm rather than a purely heuristic algorithm.

6.3 Results

This section compares the Monte Carlo methods from Section 6.2 against benchmark calculations that explicitly sample material realizations. The test problems use the standard material property combinations from Ref. [9], summarized in Table 6.2. Each problem is monoenergetic and time independent in a 1D slab of thickness $L = 10$ cm with vacuum boundaries. The methods are compared for five mixing-statistics combinations: Exponential-Exponential, Ramp-Ramp, Exponential-Ramp, Exponential-Uniform-Radii, and Exponential-Exponential-Radii. The corresponding chord distributions are defined in Chapter 3, Eqs. (3.16)-(3.19).

The primary quantities of interest are reflection R and transmission T, interpreted as the exiting partial currents at $x = 0$ and $x = L$. In the notation of the angular flux, these are

$$R = \int_{-1}^{0} |\mu|\psi(0,\mu)\,d\mu, \qquad T = \int_{0}^{1} \mu\psi(L,\mu)\,d\mu. \tag{6.11}$$

Scalar flux profiles are also used to diagnose where the methods differ from the benchmark in the interior of the slab. Each approximate method used 10^7 particle histories. The benchmark used 2 particles on each of 5×10^6 realizations, giving the same total number of 10^7 particle histories. This choice reflects the two distinct sources of statistical uncertainty in Monte Carlo stochastic media benchmark calculations: uncertainty from sampling a finite number of material realizations and uncertainty from using a finite number of particle histories to solve transport on each realization. Following the optimal-cost Monte Carlo analysis of Ref. [42], the optimal number of particle histories per realization may be estimated as

$$N_{\text{opt}} = \frac{\sigma_{\text{MC}}}{\sigma_{\text{RS}}} \left(\frac{C_{\text{RS}}}{C_{\text{MC}}} \right)^{1/2}, \tag{6.12}$$

where σ_{RS} and σ_{MC} characterize the realization-sampling and particle-transport standard deviations, respectively, and C_{RS} and C_{MC} are the corresponding costs of sampling a realization and transporting one particle history. For the benchmark implementation used here, scoping calculations indicated that a small number of histories per realization was near optimal, so two histories per realization were used for the benchmark calculations.

Boundary Source: Suite I

Suite I uses an incident boundary source at $x = 0$ and no interior source:

$$\psi(0,\mu) = 2, \quad \mu > 0, \qquad \psi(L,\mu) = 0, \quad \mu < 0, \qquad Q_i(x) = 0. \tag{6.13}$$

Table 6.2: Material Properties for the Standard Benchmark Cases [9]

Case	$\Sigma_{t,0}$	$\Sigma_{t,1}$	λ_0	λ_1	Case	c_0	c_1
1	10/99	100/11	99/100	11/100	a	0	1
2			99/10	11/10	b	1	0
3	2/101	200/101	101/20	101/20	c	0.9	0.9

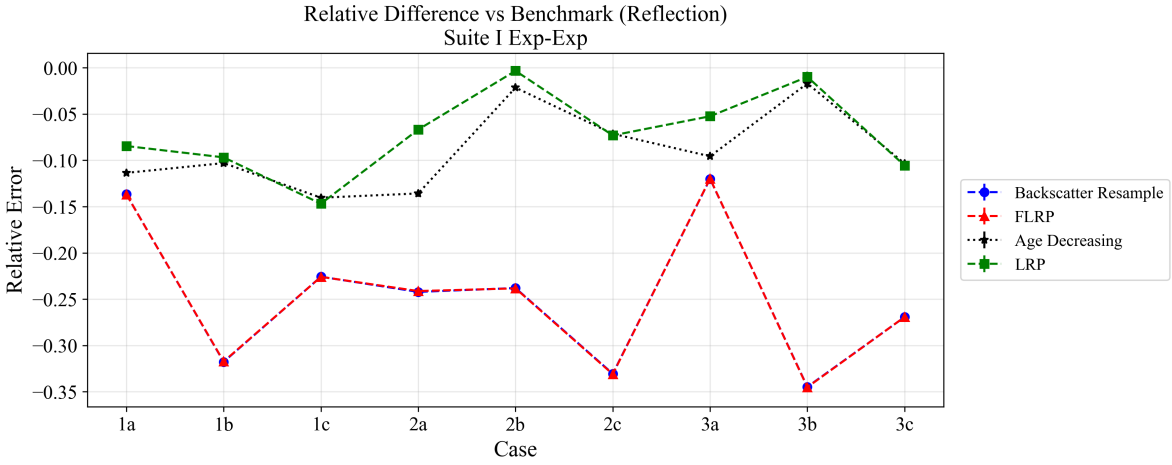
Tables 6.3-6.7 list the leakage results for the five material statistics combinations. Figures 6.4-6.8 show the signed relative leakage errors, and Table 6.8 summarizes the leakage errors using the root mean square error:

$$\text{RMSE} = \sqrt{\frac{1}{N}\sum_{n=1}^{N}(x_n - x_n^{\text{bench}})^2}. \tag{6.14}$$

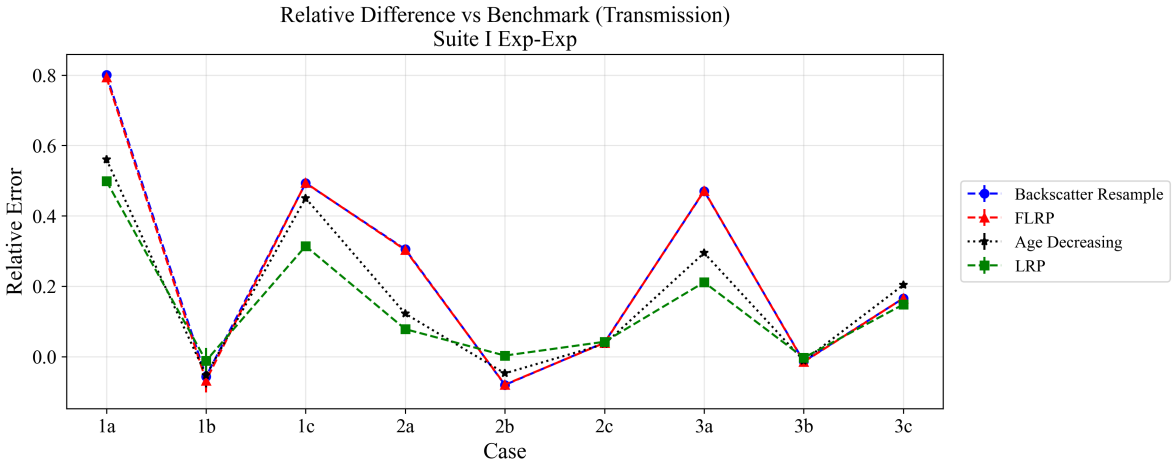
The most consistent trend in Suite I is that methods retaining more geometric memory are more accurate. Backscatter Resample and FLRP are statistically identical across all distributions, which is expected from the algorithmic connection discussed in Section 6.2. Both methods serve as an analog to CLS for renewal statistical media, as they provide statistically equivalent answers to CLS/LP for Markovian mixing [27], and in the case of the Backscatter-Resample method, reduce directly to LP in equation form. The Age-Decreasing method reduces the error significantly by allowing particles to move back toward a remembered interface. LRP is generally the most accurate method because it stores local interface distances on both sides of the particle, but the accuracy of the Age-Decreasing model is very close to that of LRP.

For Suite I leakage, the improvement from Age-Decreasing and LRP is especially visible for the non-Markovian distributions. For Ramp-Ramp, for example, the RMSE in reflection decreases from about 8.7×10^{-2} for FLRP/Backscatter Resample to 1.9×10^{-2} for Age Decreasing and 1.4×10^{-2} for LRP. The same ordering appears in transmission. This trend also carries over to the spherical inclusion mixing geometries, but to a lesser extent because the background material is still exponentially distributed.

The scalar flux comparisons in Figs. 6.9-6.14 give the same qualitative message. The largest errors occur in cases with large amounts of particle scatter. Methods that lose geometric memory after backscatter tend to distort the spatial flux shape, while the Age-Decreasing method and LRP better preserve the benchmark flux profile. In several cases, the scalar flux plots exhibit isolated one-cell spikes, where the flux is artificially higher or lower than the surrounding cells. These spikes are understood to be numerical artifacts rather than physical features of the solution. For this reason, the interpretation of the flux results emphasizes broad spatial trends and systematic differences between methods and the benchmark rather than isolated single-bin deviations. 1000 cells were used for binning the flux with track-length tallies.

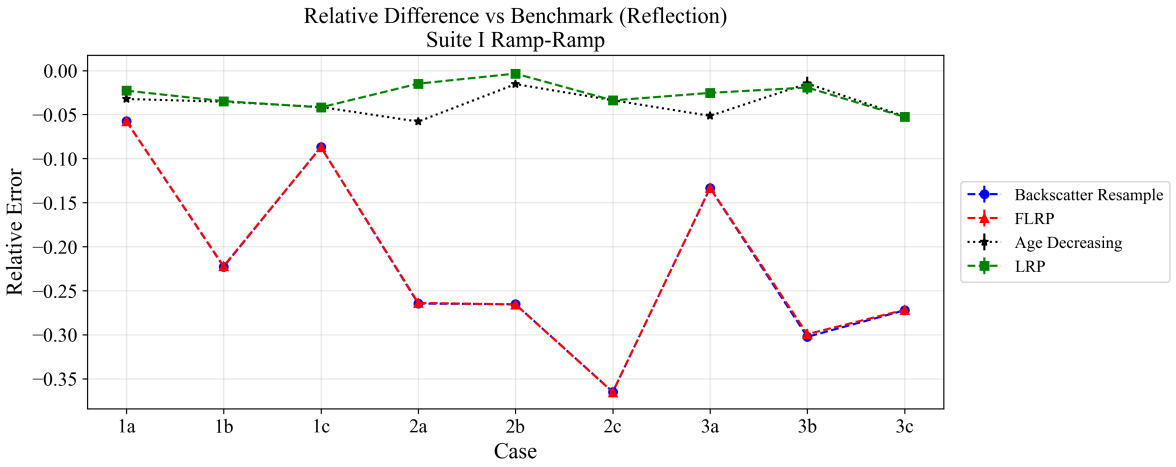


(a) Exponential-Exponential: Reflection (R)

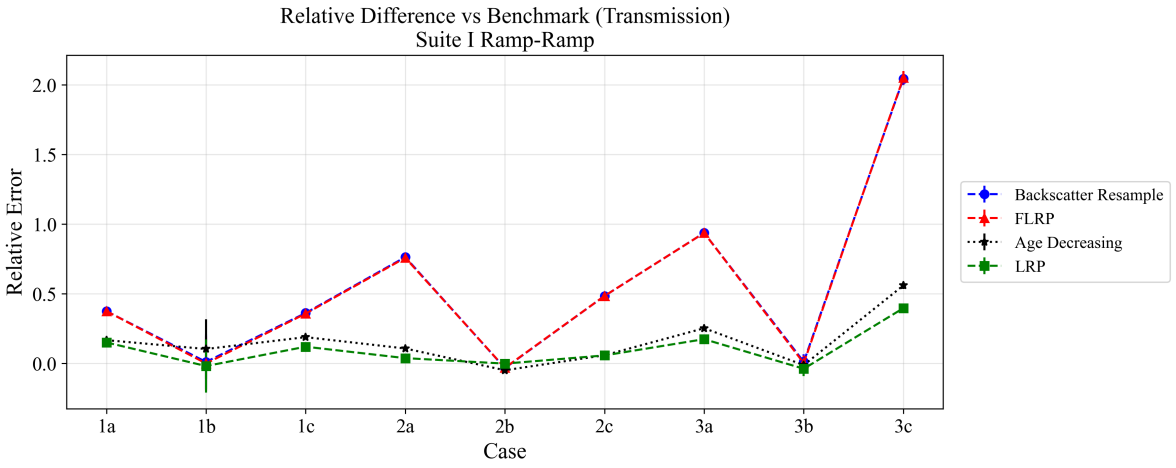


(b) Exponential-Exponential: Transmission (T)

Figure 6.4: Relative error of leakage quantities for Suite I, Exponential-Exponential distributions.

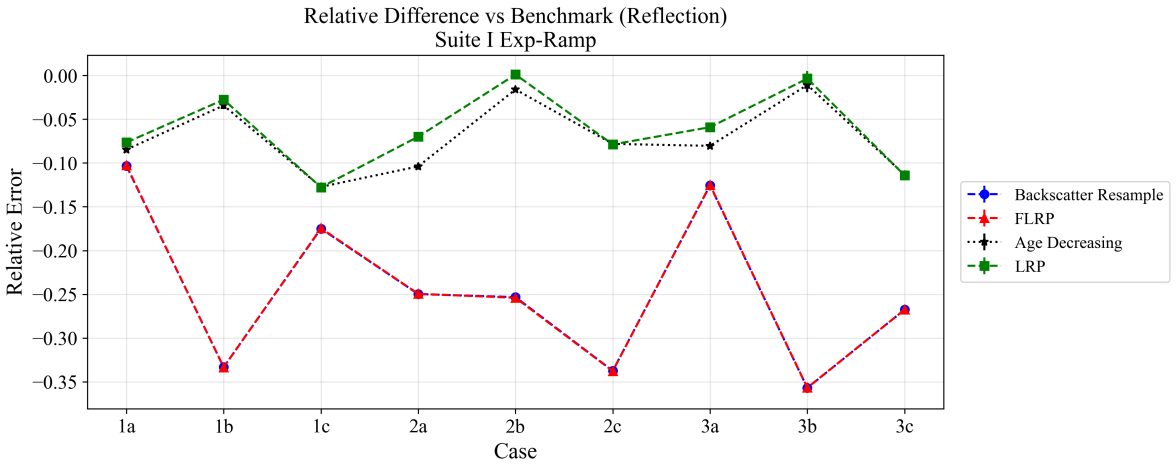


(a) Ramp-Ramp: Reflection (R)

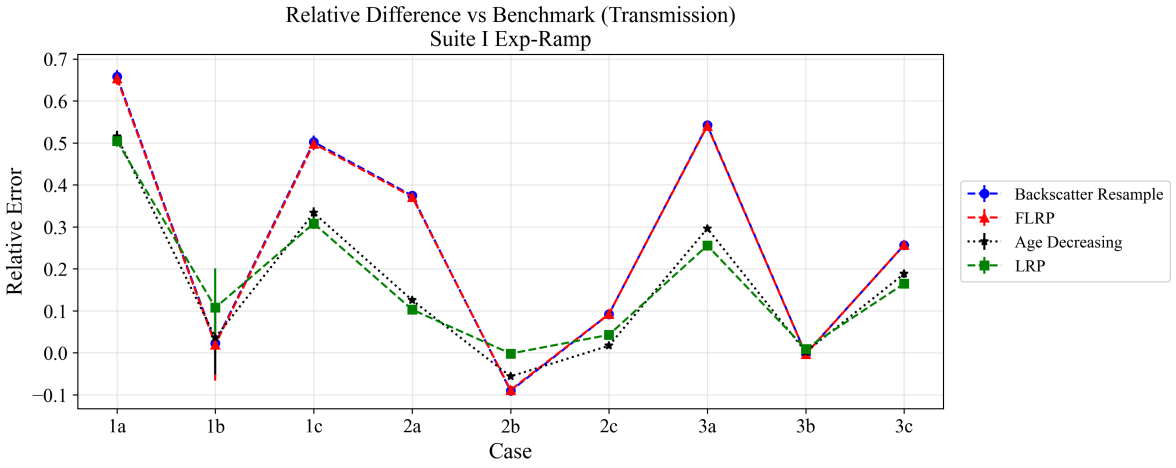


(b) Ramp-Ramp: Transmission (T)

Figure 6.5: Relative error of leakage quantities for Suite I, Ramp-Ramp distributions.

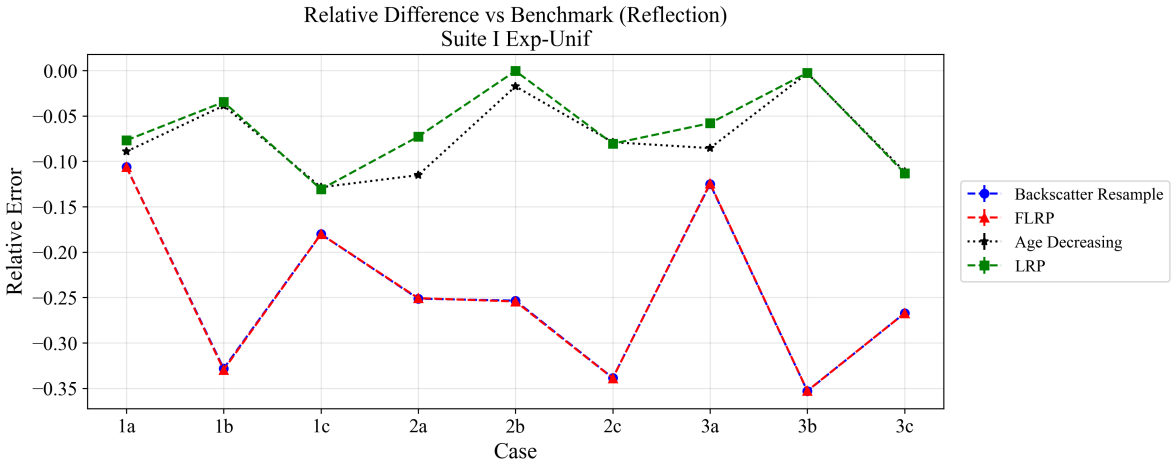


(a) Exponential-Ramp: Reflection (R)

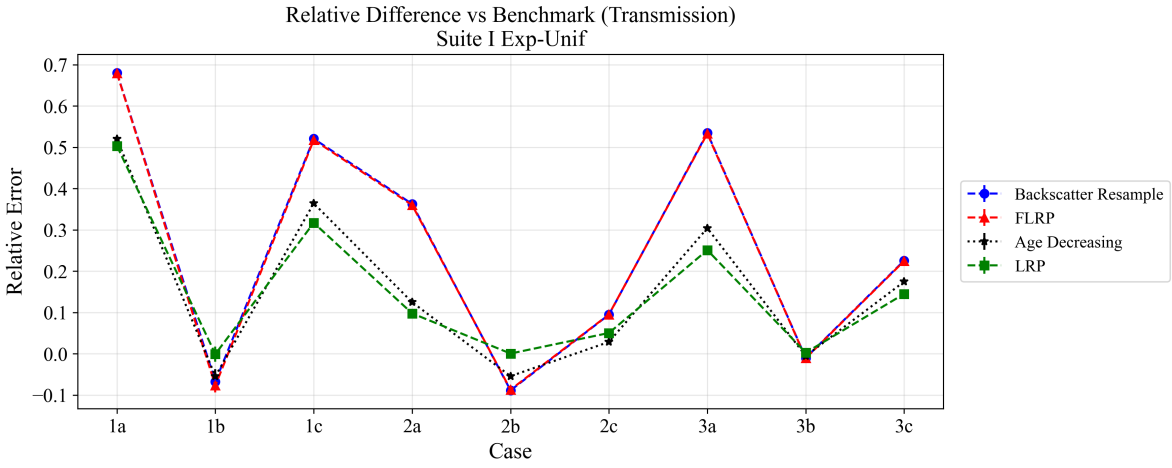


(b) Exponential-Ramp: Transmission (T)

Figure 6.6: Relative error of leakage quantities for Suite I, Exponential-Ramp distributions.

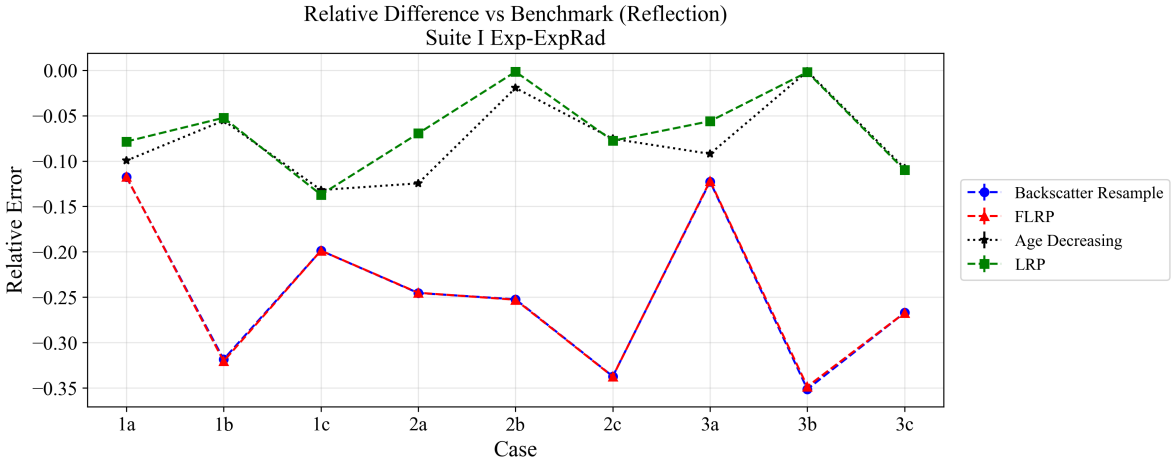


(a) Exponential-Uniform-Radii: Reflection (R)

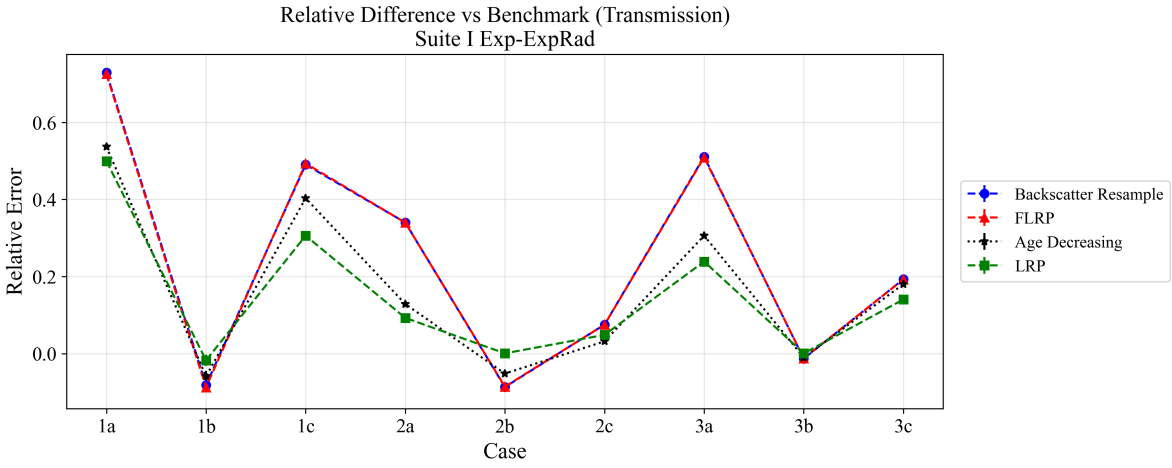


(b) Exponential-Uniform-Radii: Transmission (T)

Figure 6.7: Relative error of leakage quantities for Suite I, Exponential-Uniform-Radii distributions.



(a) Exponential-Exponential-Radii: Reflection (R)



(b) Exponential-Exponential-Radii: Transmission (T)

Figure 6.8: Relative error of leakage quantities for Suite I, Exponential-Exponential-Radii distributions.

Table 6.3: Methods Comparison for Exp-Exp Distributions (Suite I).

Case		Quantity	Bench	Backscatter Resample	FLRP	Age Decreasing	LRP
1	a	R	0.4378(7)	0.3779(2)	0.3779(2)	0.3881(2)	0.4008(2)
		T	0.0147(1)	0.02647(5)	0.02637(5)	0.02294(5)	0.02203(5)
	b	R	0.0859(3)	0.05860(7)	0.05864(7)	0.07705(8)	0.07758(8)
		T	0.00167(6)	0.00157(1)	0.00156(1)	0.00158(1)	0.00165(1)
	c	R	0.4774(5)	0.3696(2)	0.3695(2)	0.4104(2)	0.4073(2)
		T	0.0159(1)	0.02374(5)	0.02375(5)	0.02306(5)	0.02089(5)
2	a	R	0.238(1)	0.1804(1)	0.1806(1)	0.2057(1)	0.2221(1)
		T	0.0985(4)	0.1285(1)	0.1284(1)	0.1105(1)	0.1062(1)
	b	R	0.2864(5)	0.2182(1)	0.2181(1)	0.2802(1)	0.2854(1)
		T	0.1949(9)	0.1792(1)	0.1793(1)	0.1856(1)	0.1954(1)
	c	R	0.4326(4)	0.2896(1)	0.2894(1)	0.4017(2)	0.4010(2)
		T	0.1877(7)	0.1952(1)	0.1950(1)	0.1944(1)	0.1956(1)
3	a	R	0.6903(9)	0.6074(2)	0.6076(2)	0.6243(2)	0.6541(2)
		T	0.1634(6)	0.2403(1)	0.2404(1)	0.2115(1)	0.1979(1)
	b	R	0.0366(2)	0.02398(5)	0.02397(5)	0.03598(6)	0.03624(6)
		T	0.0768(7)	0.07573(8)	0.07563(8)	0.07589(8)	0.07653(8)
	c	R	0.4461(6)	0.3260(1)	0.3260(1)	0.4000(2)	0.3990(2)
		T	0.1026(7)	0.1196(1)	0.1196(1)	0.1235(1)	0.1178(1)

Table 6.4: Methods Comparison for Ramp-Ramp Distributions (Suite I).

Case		Quantity	Bench	Backscatter Resample	FLRP	Age Decreasing	LRP
1	a	R	0.4863(7)	0.4583(2)	0.4583(2)	0.4706(2)	0.4752(2)
		T	0.00705(8)	0.00969(3)	0.00970(3)	0.00823(3)	0.00811(3)
	b	R	0.0504(2)	0.03917(6)	0.03920(6)	0.04861(7)	0.04865(7)
		T	0.000027(5)	0.000027(2)	0.000027(2)	0.000030(2)	0.000027(2)
	c	R	0.4776(5)	0.4360(2)	0.4361(2)	0.4578(2)	0.4576(2)
		T	0.00495(7)	0.00674(3)	0.00672(3)	0.00589(2)	0.00554(2)
2	a	R	0.2826(9)	0.2078(1)	0.2080(1)	0.2662(1)	0.2784(1)
		T	0.0594(3)	0.1047(1)	0.1044(1)	0.06578(8)	0.06167(8)
	b	R	0.2582(7)	0.1897(1)	0.1896(1)	0.2542(1)	0.2573(1)
		T	0.0768(5)	0.07424(8)	0.07440(8)	0.07305(8)	0.07672(8)
	c	R	0.4600(4)	0.2921(1)	0.2920(1)	0.4445(2)	0.4444(2)
		T	0.0796(5)	0.1182(1)	0.1182(1)	0.08429(9)	0.08420(9)
3	a	R	0.7605(5)	0.6590(1)	0.6591(1)	0.7213(1)	0.7412(1)
		T	0.0974(3)	0.1887(1)	0.1887(1)	0.1220(1)	0.1144(1)
	b	R	0.0259(2)	0.01807(4)	0.01815(4)	0.02552(5)	0.02540(5)
		T	0.00095(5)	0.00096(1)	0.00095(1)	0.00094(1)	0.00091(1)
	c	R	0.4775(6)	0.3475(2)	0.3477(2)	0.4527(2)	0.4523(2)
		T	0.0128(2)	0.03896(6)	0.03904(6)	0.01997(4)	0.01788(4)

Table 6.5: Methods Comparison for Exp-Ramp Distributions (Suite I).

Case		Quantity	Bench	Backscatter Resample	FLRP	Age Decreasing	LRP
1	a	R	0.4582(6)	0.4109(2)	0.4112(2)	0.4194(2)	0.4231(2)
		T	0.0112(1)	0.01857(4)	0.01852(4)	0.01697(4)	0.01685(4)
	b	R	0.0755(3)	0.05033(7)	0.05033(7)	0.07291(8)	0.07341(8)
		T	0.00048(4)	0.000491(7)	0.000490(7)	0.000498(7)	0.000532(7)
	c	R	0.4780(5)	0.3943(2)	0.3946(2)	0.4171(2)	0.4169(2)
		T	0.0103(1)	0.01547(4)	0.01543(4)	0.01373(4)	0.01347(4)
2	a	R	0.251(1)	0.1883(1)	0.1884(1)	0.2249(1)	0.2334(1)
		T	0.0897(4)	0.1233(1)	0.1230(1)	0.1009(1)	0.09894(9)
	b	R	0.2847(6)	0.2126(1)	0.2124(1)	0.2801(1)	0.2850(1)
		T	0.1847(8)	0.1679(1)	0.1683(1)	0.1743(1)	0.1844(1)
	c	R	0.4354(4)	0.2885(1)	0.2883(1)	0.4014(2)	0.4011(2)
		T	0.1673(9)	0.1827(1)	0.1827(1)	0.1701(1)	0.1745(1)
3	a	R	0.7046(9)	0.6161(2)	0.6164(2)	0.6479(2)	0.6630(1)
		T	0.1504(7)	0.2319(1)	0.2317(1)	0.1949(1)	0.1889(1)
	b	R	0.0361(3)	0.02321(5)	0.02322(5)	0.03571(6)	0.03597(6)
		T	0.0678(7)	0.06763(8)	0.06758(8)	0.06796(8)	0.06845(8)
	c	R	0.4493(4)	0.3291(1)	0.3291(1)	0.3983(2)	0.3980(2)
		T	0.0857(7)	0.1077(1)	0.1077(1)	0.1018(1)	0.09982(9)

Table 6.6: Methods Comparison for Exp-Unif Rad Distributions (Suite I).

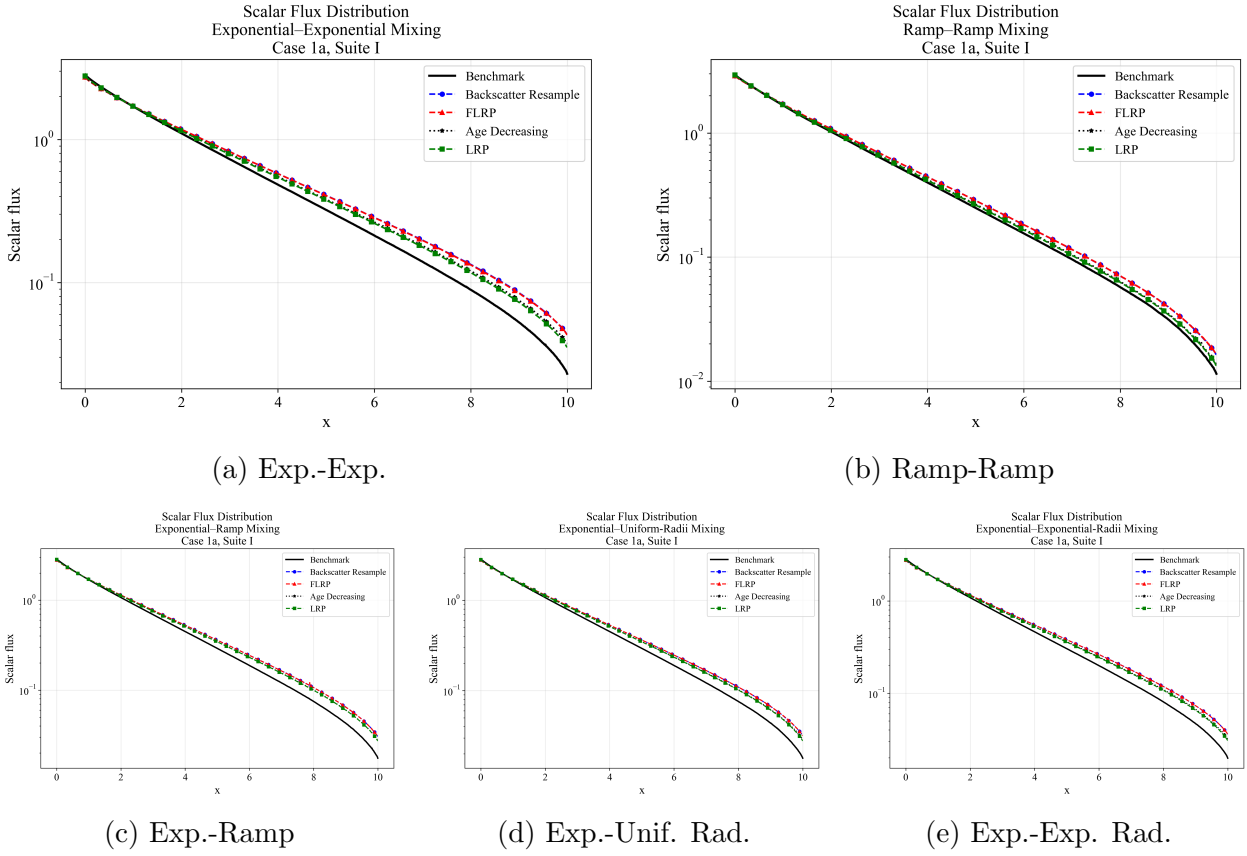
Case		Quantity	Bench	Backscatter Resample	FLRP	Age Decreasing	LRP
1	a	R	0.4558(2)	0.4074(2)	0.4073(2)	0.4151(2)	0.4207(2)
		T	0.01153(3)	0.01937(4)	0.01936(4)	0.01752(4)	0.01733(4)
	b	R	0.07628(8)	0.05124(7)	0.05113(7)	0.07333(8)	0.07364(8)
		T	0.000609(8)	0.000568(8)	0.000562(8)	0.000576(8)	0.000608(8)
	c	R	0.4777(2)	0.3916(2)	0.3916(2)	0.4162(2)	0.4152(2)
		T	0.01072(3)	0.01630(4)	0.01627(4)	0.01462(4)	0.01412(4)
2	a	R	0.2508(1)	0.1877(1)	0.1879(1)	0.2219(1)	0.2325(1)
		T	0.09072(9)	0.1236(1)	0.1234(1)	0.1020(1)	0.09957(9)
	b	R	0.2851(1)	0.2128(1)	0.2126(1)	0.2801(1)	0.2850(1)
		T	0.1849(1)	0.1685(1)	0.1688(1)	0.1749(1)	0.1850(1)
	c	R	0.4363(2)	0.2885(1)	0.2884(1)	0.4018(2)	0.4011(2)
		T	0.1676(1)	0.1835(1)	0.1836(1)	0.1724(1)	0.1760(1)
3	a	R	0.7035(1)	0.6154(2)	0.6159(2)	0.6433(2)	0.6627(1)
		T	0.1515(1)	0.2324(1)	0.2322(1)	0.1975(1)	0.1895(1)
	b	R	0.03593(6)	0.02324(5)	0.02325(5)	0.03582(6)	0.03584(6)
		T	0.06864(8)	0.06794(8)	0.06789(8)	0.06826(8)	0.06882(8)
	c	R	0.4489(2)	0.3289(1)	0.3289(1)	0.3989(2)	0.3981(2)
		T	0.08854(9)	0.1085(1)	0.1084(1)	0.1040(1)	0.1014(1)

Table 6.7: Methods Comparison for Exp-Exp Rad Distributions (Suite I).

Case		Quantity	Bench	Backscatter Resample	FLRP	Age Decreasing	LRP
1	a	R	0.4484(2)	0.3957(2)	0.3958(2)	0.4038(2)	0.4132(2)
		T	0.01271(4)	0.02197(5)	0.02193(5)	0.01953(4)	0.01906(4)
	b	R	0.07885(9)	0.05374(7)	0.05358(7)	0.07449(8)	0.07472(8)
		T	0.00092(1)	0.000843(9)	0.000838(9)	0.000864(9)	0.000902(9)
	c	R	0.4778(2)	0.3828(2)	0.3828(2)	0.4147(2)	0.4123(2)
		T	0.01267(4)	0.01889(4)	0.01892(4)	0.01778(4)	0.01655(4)
2	a	R	0.2469(1)	0.1863(1)	0.1864(1)	0.2162(1)	0.2297(1)
		T	0.09288(9)	0.1245(1)	0.1244(1)	0.1048(1)	0.1015(1)
	b	R	0.2855(1)	0.2135(1)	0.2133(1)	0.2799(1)	0.2850(1)
		T	0.1863(1)	0.1701(1)	0.1703(1)	0.1766(1)	0.1864(1)
	c	R	0.4355(2)	0.2887(1)	0.2886(1)	0.4026(2)	0.4017(2)
		T	0.1729(1)	0.1858(1)	0.1858(1)	0.1783(1)	0.1812(1)
3	a	R	0.6998(1)	0.6139(2)	0.6145(2)	0.6353(2)	0.6606(1)
		T	0.1548(1)	0.2339(1)	0.2336(1)	0.2022(1)	0.1918(1)
	b	R	0.03592(6)	0.02330(5)	0.02340(5)	0.03587(6)	0.03584(6)
		T	0.06997(8)	0.06904(8)	0.06909(8)	0.06924(8)	0.07001(8)
	c	R	0.4481(2)	0.3284(1)	0.3284(1)	0.3997(2)	0.3988(2)
		T	0.09275(9)	0.1106(1)	0.1106(1)	0.1094(1)	0.1058(1)

Table 6.8: RMSE Comparison (Suite I).

Distribution	Qty	Backscatter Resample	FLRP	Age Decreasing	LRP
Exp-Exp	R	0.0855	0.0855	0.0416	0.0352
	T	0.0291	0.0291	0.0187	0.0134
Ramp-Ramp	R	0.0877	0.0871	0.0192	0.0140
	T	0.0381	0.0374	0.0091	0.0061
Exp-Ramp	R	0.0837	0.0837	0.0378	0.0347
	T	0.0314	0.0313	0.0168	0.0144
Exp-Unif Rad	R	0.0841	0.0841	0.0389	0.0349
	T	0.0310	0.0309	0.0172	0.0142
Exp-Exp Rad	R	0.0848	0.0848	0.0402	0.0349
	T	0.0301	0.0300	0.0178	0.0139



(a) Exp.-Exp.

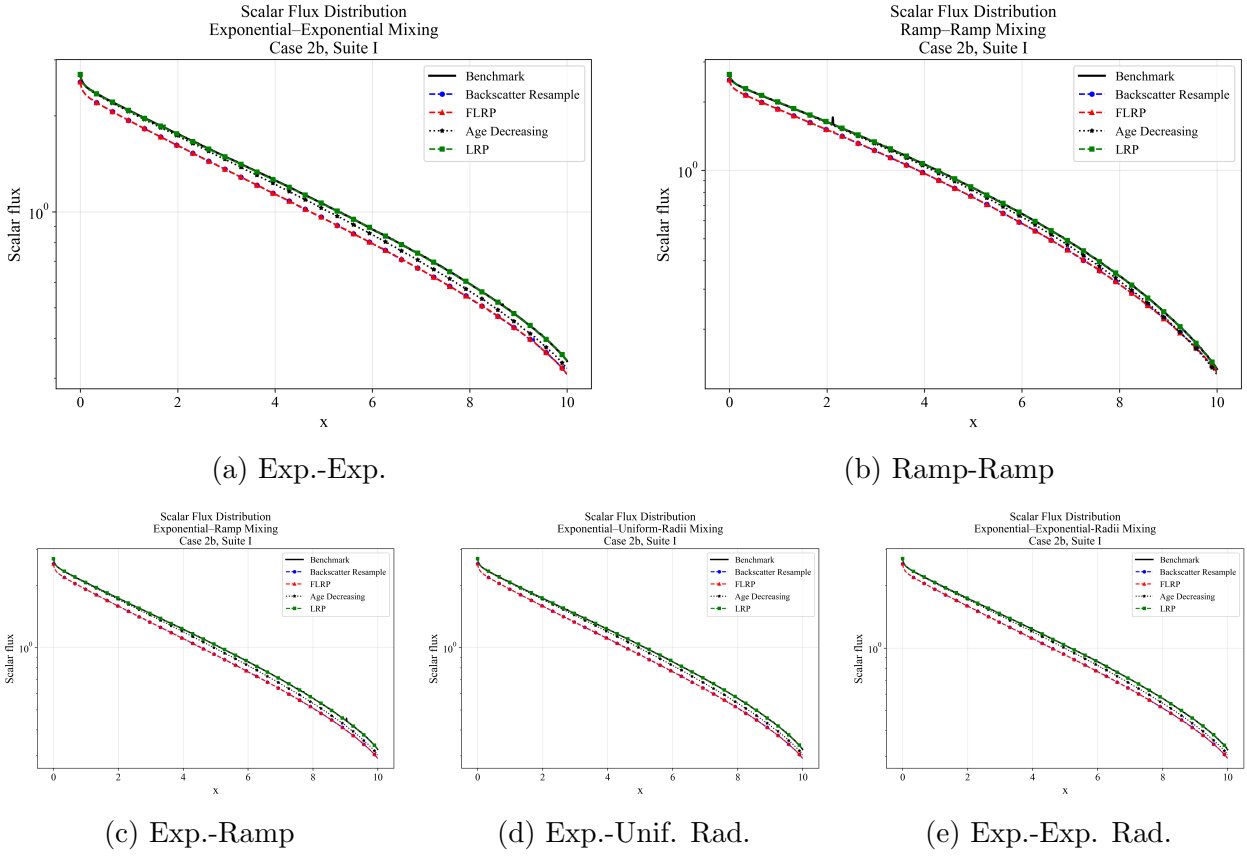
(b) Ramp-Ramp

(c) Exp.-Ramp

(d) Exp.-Unif. Rad.

(e) Exp.-Exp. Rad.

Figure 6.9: Scalar flux distributions for Case 1a (Suite I) comparing five material mixing statistics: Exponential-Exponential, Ramp-Ramp, Exponential-Ramp, Exponential-Uniform-Radii, and Exponential-Exponential-Radii.



(a) Exp.-Exp.

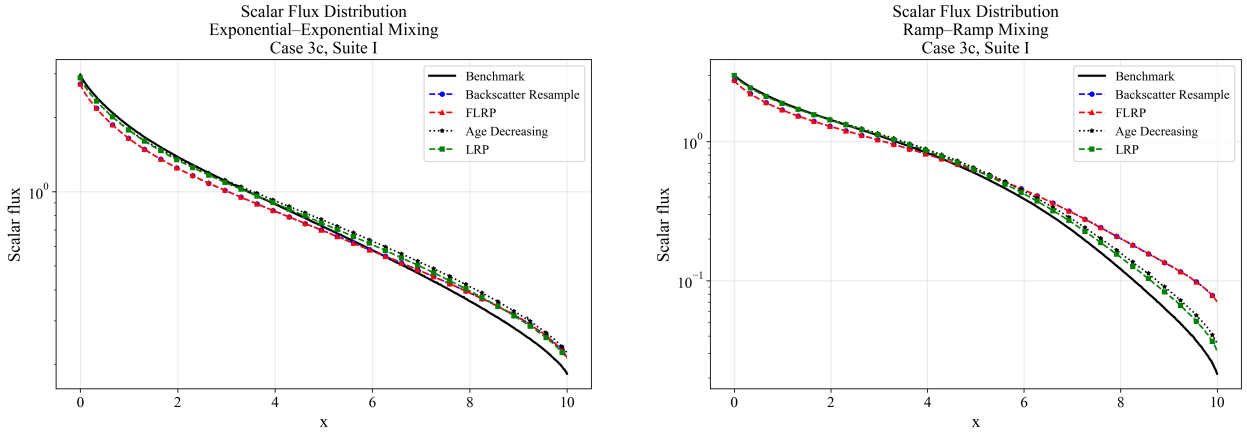
(b) Ramp-Ramp

(c) Exp.-Ramp

(d) Exp.-Unif. Rad.

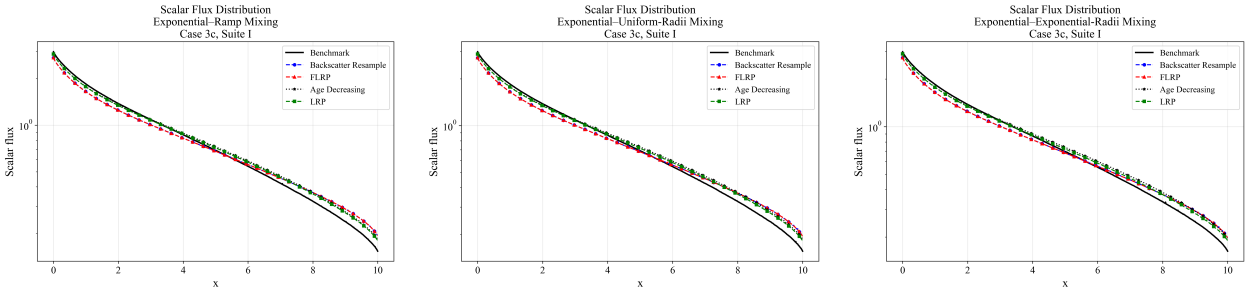
(e) Exp.-Exp. Rad.

Figure 6.10: Scalar flux distributions for Case 2b (Suite I) comparing five material mixing statistics: Exponential-Exponential, Ramp-Ramp, Exponential-Ramp, Exponential-Uniform-Radii, and Exponential-Exponential-Radii.



(a) Exp.-Exp.

(b) Ramp-Ramp

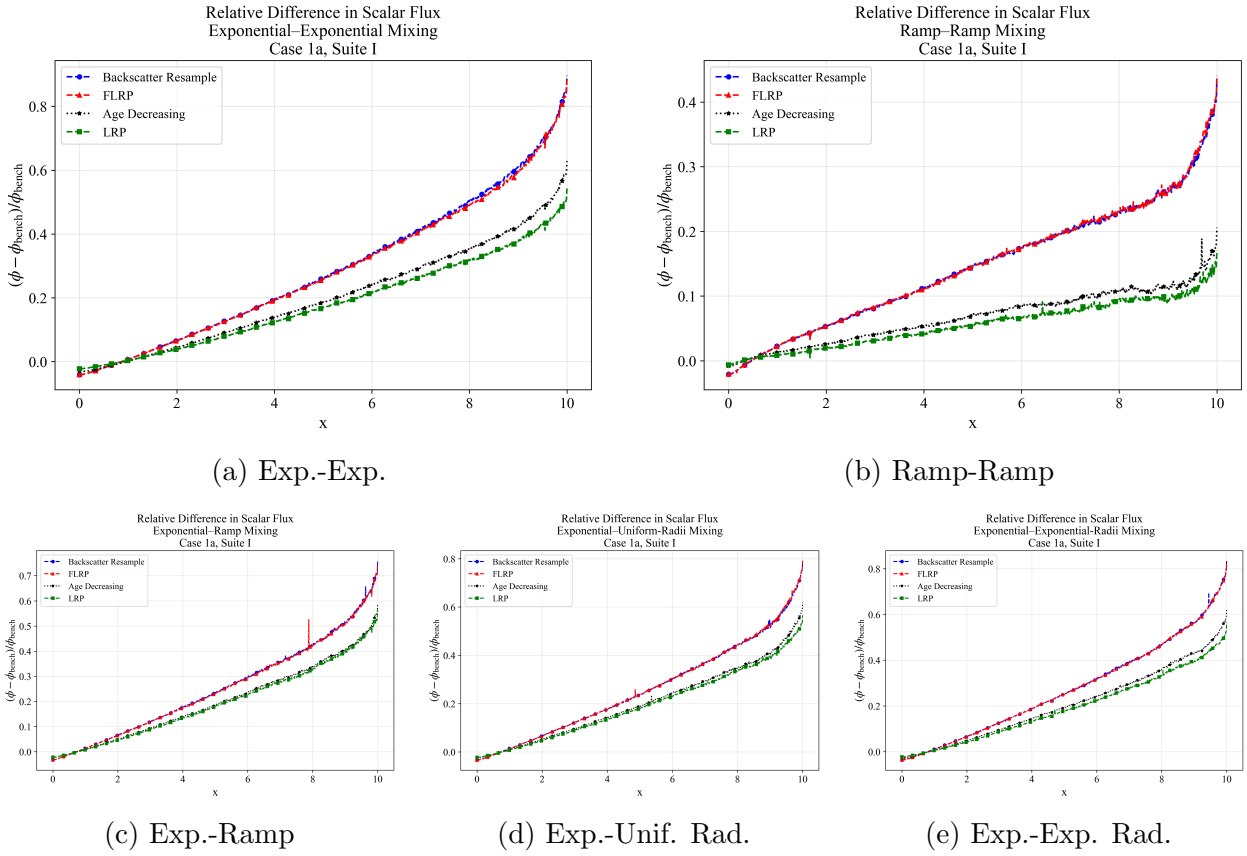


(c) Exp.-Ramp

(d) Exp.-Unif. Rad.

(e) Exp.-Exp. Rad.

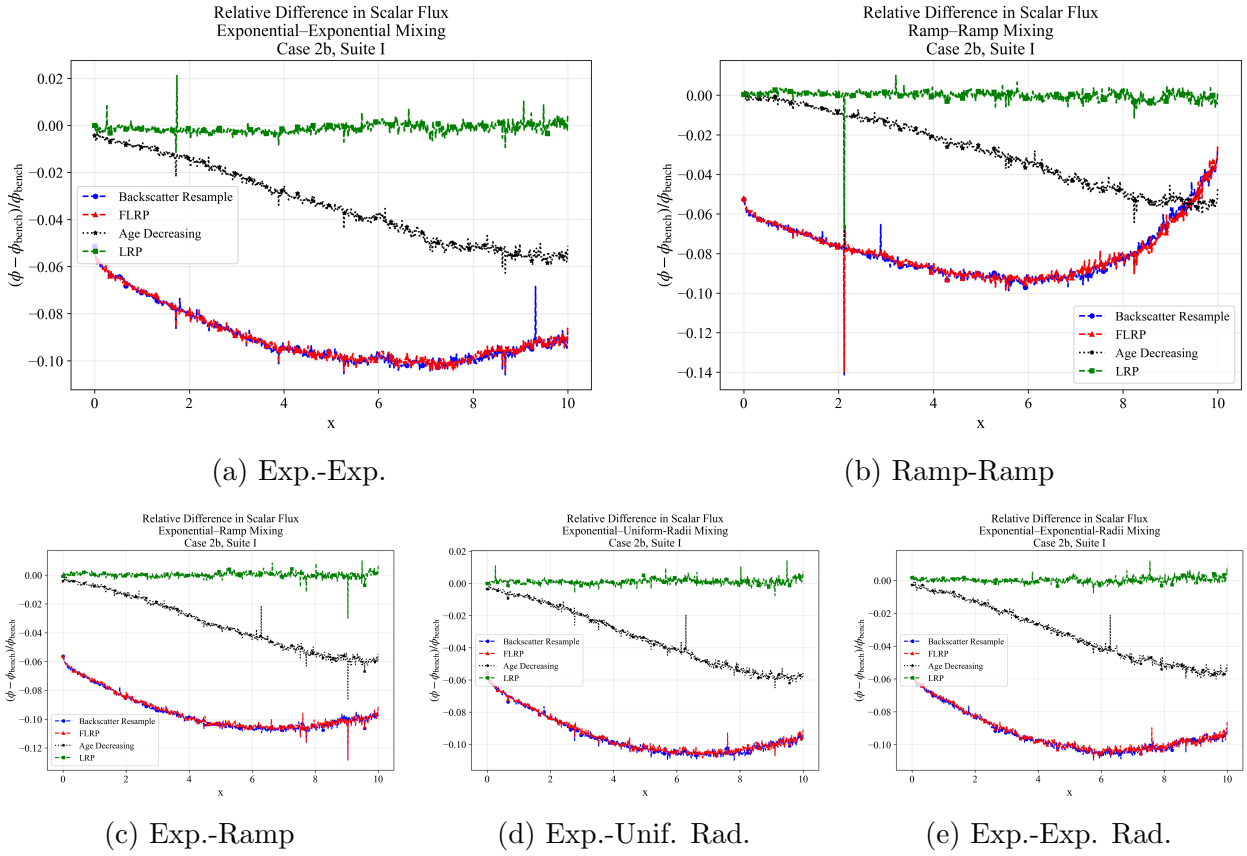
Figure 6.11: Scalar flux distributions for Case 3c (Suite I) comparing five material mixing statistics: Exponential-Exponential, Ramp-Ramp, Exponential-Ramp, Exponential-Uniform-Radii, and Exponential-Exponential-Radii.



(a) Exp.-Exp. (b) Ramp-Ramp

(c) Exp.-Ramp (d) Exp.-Unif. Rad. (e) Exp.-Exp. Rad.

Figure 6.12: Relative error of the scalar flux for Case 1a (Suite I), comparing five material mixing statistics: Exponential-Exponential, Ramp-Ramp, Exponential-Ramp, Exponential-Uniform-Radii, and Exponential-Exponential-Radii. All methods are shown relative to the benchmark solution.



(a) Exp.-Exp.

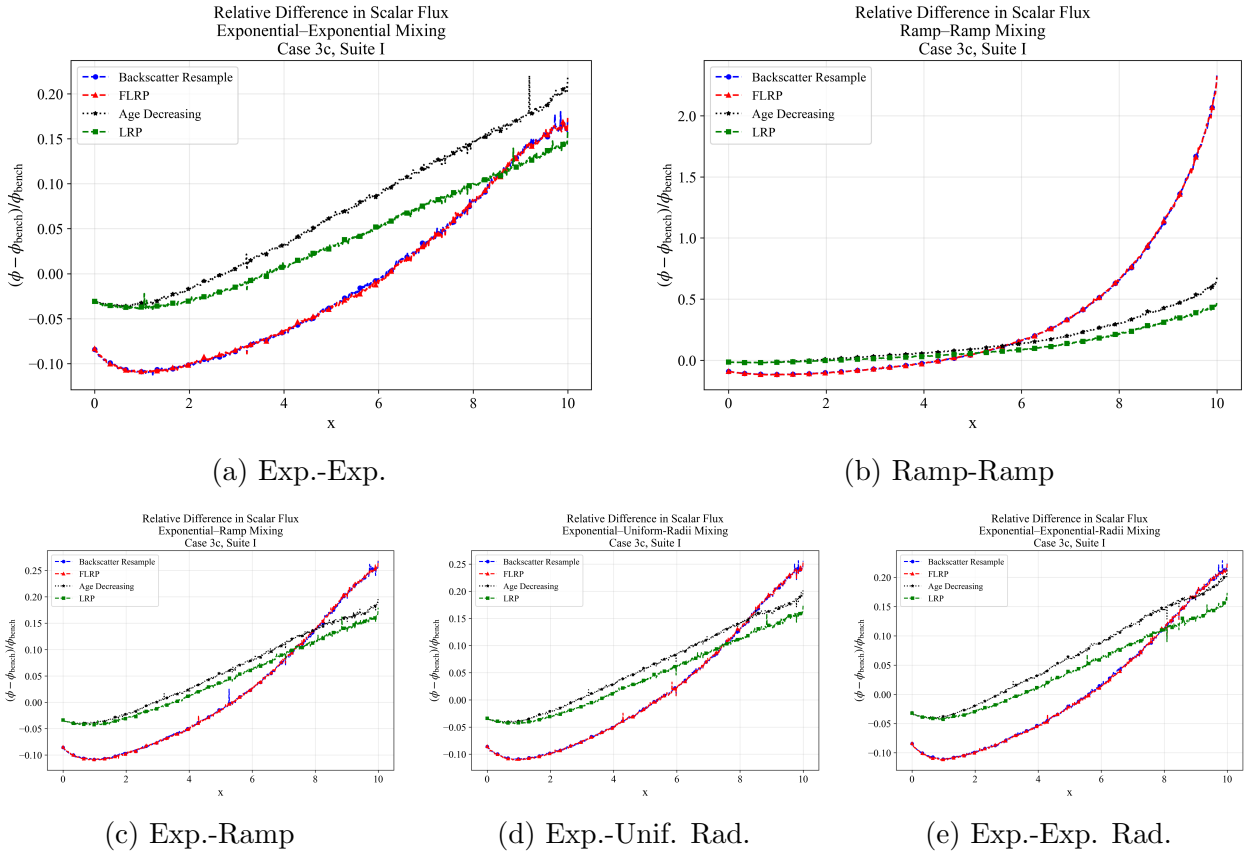
(b) Ramp-Ramp

(c) Exp.-Ramp

(d) Exp.-Unif. Rad.

(e) Exp.-Exp. Rad.

Figure 6.13: Relative error of the scalar flux for Case 2b (Suite I), comparing five material mixing statistics: Exponential-Exponential, Ramp-Ramp, Exponential-Ramp, Exponential-Uniform-Radii, and Exponential-Exponential-Radii. All methods are shown relative to the benchmark solution.



(a) Exp.-Exp. (b) Ramp-Ramp

(c) Exp.-Ramp (d) Exp.-Unif. Rad. (e) Exp.-Exp. Rad.

Figure 6.14: Relative error of the scalar flux for Case 3c (Suite I), comparing five material mixing statistics: Exponential-Exponential, Ramp-Ramp, Exponential-Ramp, Exponential-Uniform-Radii, and Exponential-Exponential-Radii. All methods are shown relative to the benchmark solution.

Interior Source: Suite II

Suite II uses a uniform interior source and no incoming boundary source:

$$\psi(0,\mu) = 0, \quad \mu > 0, \qquad \psi(L,\mu) = 0, \quad \mu < 0, \qquad Q_i(x) = \frac{1}{L}. \tag{6.15}$$

This source produces nearly symmetric reflection and transmission values, so Suite II is a useful check on whether a method introduces directional bias. Tables 6.9-6.13 list the leakage results, and Table 6.14 summarizes the leakage RMSE. Because of the symmetry in leakage values, only the relative error of transmission is presented in the relative error plots Figures 6.15-6.19.

Compared with Suite I, the absolute leakage errors in Suite II are smaller for all methods. The ranking of methods, however, is similar. Backscatter Resample and FLRP remain statistically identical. The Age-Decreasing method improves the results by retaining limited backward memory. LRP is again generally the most accurate method, though the difference between Age-Decreasing and LRP is smaller than it is in Suite I.

The Suite II RMSE values sharpen the interpretation of the methods. Across the five distributions, FLRP/Backscatter Resample produces reflection and transmission RMSE values of roughly 1.2×10^{-2} to 1.5×10^{-2}. The Age-Decreasing method reduces these errors to roughly 3.6×10^{-3} to 6.3×10^{-3}, while LRP is typically near 3.3×10^{-3} to 3.9×10^{-3}. Thus, most of the improvement comes from retaining some memory of the interface behind the particle after backscatter, with the remaining improvement obtained by retaining the full two sided interface memory.

The scalar flux results in Figs. 6.20-6.25 display similar results, where the FLRP and Backscatter-Resample methods are less accurate than the Age-Decreasing and LRP methods.

Table 6.9: Methods Comparison for Exp-Exp Distributions (Suite II).

Case		Quantity	Bench	Backscatter Resample	FLRP	Age Decreasing	LRP
1	a	R	0.1525(1)	0.1655(1)	0.1658(1)	0.1607(1)	0.1610(1)
		T	0.1526(1)	0.1658(1)	0.1658(1)	0.1605(1)	0.1610(1)
	b	R	0.07318(8)	0.06934(8)	0.06935(8)	0.07126(8)	0.07226(8)
		T	0.07298(8)	0.06953(8)	0.06927(8)	0.07154(8)	0.07220(8)
	c	R	0.1748(1)	0.1729(1)	0.1729(1)	0.1796(1)	0.1745(1)
		T	0.1749(1)	0.1729(1)	0.1729(1)	0.1795(1)	0.1744(1)
2	a	R	0.1909(1)	0.1955(1)	0.1955(1)	0.1903(1)	0.1937(1)
		T	0.1908(1)	0.1954(1)	0.1954(1)	0.1905(1)	0.1934(1)
	b	R	0.2928(1)	0.2677(1)	0.2678(1)	0.2829(1)	0.2923(1)
		T	0.2928(1)	0.2677(1)	0.2679(1)	0.2828(1)	0.2923(1)
	c	R	0.3130(1)	0.2834(1)	0.2838(1)	0.3120(1)	0.3117(1)
		T	0.3132(1)	0.2837(1)	0.2835(1)	0.3122(1)	0.3120(1)
3	a	R	0.4112(2)	0.4091(2)	0.4093(2)	0.4017(2)	0.4157(2)
		T	0.4113(2)	0.4094(2)	0.4092(2)	0.4017(2)	0.4153(2)
	b	R	0.1295(1)	0.1258(1)	0.1257(1)	0.1289(1)	0.1296(1)
		T	0.1295(1)	0.1256(1)	0.1257(1)	0.1288(1)	0.1294(1)
	c	R	0.2255(1)	0.2117(1)	0.2119(1)	0.2342(1)	0.2258(1)
		T	0.2254(1)	0.2117(1)	0.2117(1)	0.2340(1)	0.2257(1)

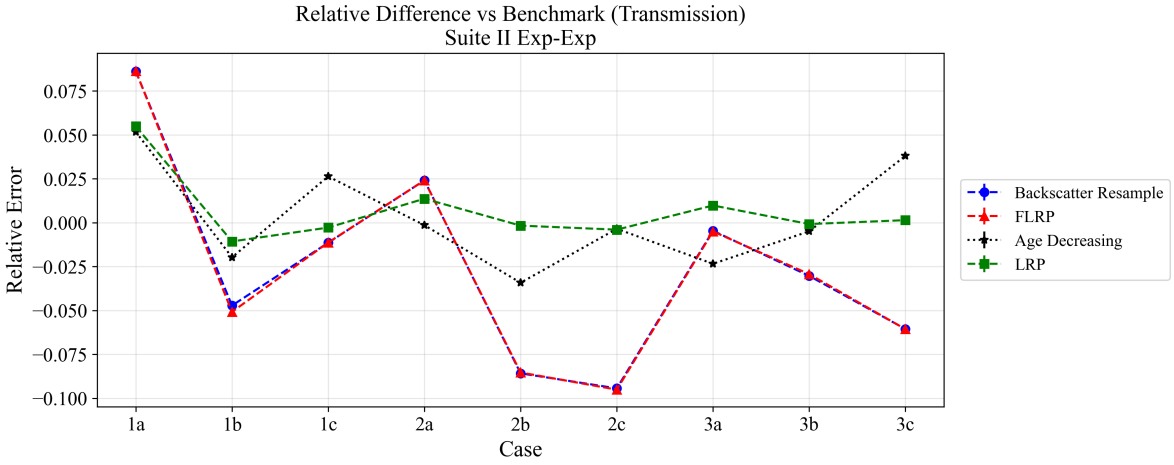


Figure 6.15: Relative error of transmission (T) for Suite II, Exponential-Exponential distributions.

Table 6.10: Methods Comparison for Ramp-Ramp Distributions (Suite II).

Case		Quantity	Bench	Backscatter Resample	FLRP	Age Decreasing	LRP
1	a	R	0.1407(1)	0.1480(1)	0.1478(1)	0.1437(1)	0.1437(1)
		T	0.1406(1)	0.1475(1)	0.1476(1)	0.1434(1)	0.1436(1)
	b	R	0.04212(6)	0.04150(6)	0.04139(6)	0.04198(6)	0.04245(6)
		T	0.04212(6)	0.04152(6)	0.04154(6)	0.04196(6)	0.04254(6)
	c	R	0.1397(1)	0.1433(1)	0.1434(1)	0.1424(1)	0.1411(1)
		T	0.1393(1)	0.1435(1)	0.1434(1)	0.1425(1)	0.1410(1)
2	a	R	0.1891(1)	0.1953(1)	0.1953(1)	0.1890(1)	0.1905(1)
		T	0.1890(1)	0.1954(1)	0.1953(1)	0.1891(1)	0.1906(1)
	b	R	0.2451(1)	0.2261(1)	0.2260(1)	0.2402(1)	0.2512(1)
		T	0.2449(1)	0.2262(1)	0.2260(1)	0.2401(1)	0.2511(1)
	c	R	0.2898(1)	0.2629(1)	0.2629(1)	0.2903(1)	0.2927(1)
		T	0.2894(1)	0.2631(1)	0.2632(1)	0.2905(1)	0.2927(1)
3	a	R	0.3981(2)	0.4070(2)	0.4071(2)	0.3967(2)	0.4055(2)
		T	0.3982(2)	0.4072(2)	0.4072(2)	0.3965(2)	0.4058(2)
	b	R	0.09048(9)	0.08927(9)	0.08909(9)	0.09045(9)	0.09198(9)
		T	0.09059(9)	0.08923(9)	0.08932(9)	0.09053(9)	0.09204(9)
	c	R	0.2004(1)	0.1940(1)	0.1936(1)	0.2090(1)	0.2034(1)
		T	0.2003(1)	0.1942(1)	0.1939(1)	0.2088(1)	0.2036(1)

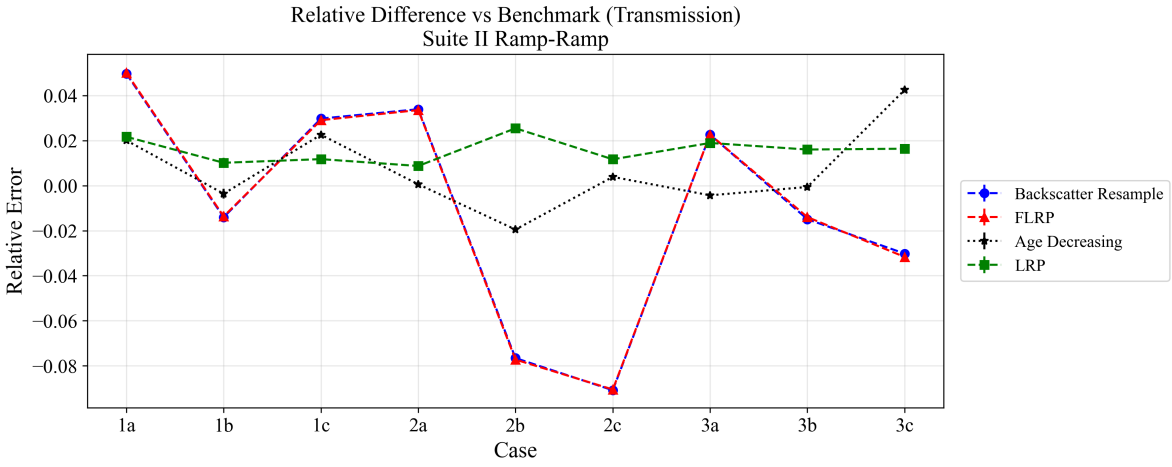


Figure 6.16: Relative error of transmission (T) for Suite II, Ramp-Ramp distributions.

Table 6.11: Methods Comparison for Exp-Ramp Distributions (Suite II).

Case		Quantity	Bench	Backscatter Resample	FLRP	Age Decreasing	LRP
1	a	R	0.1476(1)	0.1586(1)	0.1585(1)	0.1557(1)	0.1560(1)
		T	0.1473(1)	0.1587(1)	0.1584(1)	0.1555(1)	0.1559(1)
	b	R	0.06159(8)	0.05867(7)	0.05879(7)	0.06062(8)	0.06148(8)
		T	0.06176(8)	0.05879(7)	0.05866(7)	0.06080(8)	0.06165(8)
	c	R	0.1592(1)	0.1611(1)	0.1611(1)	0.1607(1)	0.1598(1)
		T	0.1592(1)	0.1613(1)	0.1611(1)	0.1609(1)	0.1599(1)
2	a	R	0.1870(1)	0.1947(1)	0.1948(1)	0.1895(1)	0.1910(1)
		T	0.1867(1)	0.1948(1)	0.1946(1)	0.1899(1)	0.1910(1)
	b	R	0.2871(1)	0.2613(1)	0.2614(1)	0.2776(1)	0.2871(1)
		T	0.2870(1)	0.2613(1)	0.2614(1)	0.2772(1)	0.2870(1)
	c	R	0.3031(1)	0.2783(1)	0.2780(1)	0.2994(1)	0.3016(1)
		T	0.3030(1)	0.2783(1)	0.2785(1)	0.2994(1)	0.3017(1)
3	a	R	0.4048(2)	0.4084(2)	0.4088(2)	0.4037(2)	0.4119(2)
		T	0.4047(2)	0.4089(2)	0.4087(2)	0.4036(2)	0.4114(2)
	b	R	0.1262(1)	0.1225(1)	0.1224(1)	0.1257(1)	0.1263(1)
		T	0.1262(1)	0.1223(1)	0.1225(1)	0.1256(1)	0.1261(1)
	c	R	0.2195(1)	0.2090(1)	0.2091(1)	0.2248(1)	0.2193(1)
		T	0.2200(1)	0.2093(1)	0.2093(1)	0.2246(1)	0.2194(1)

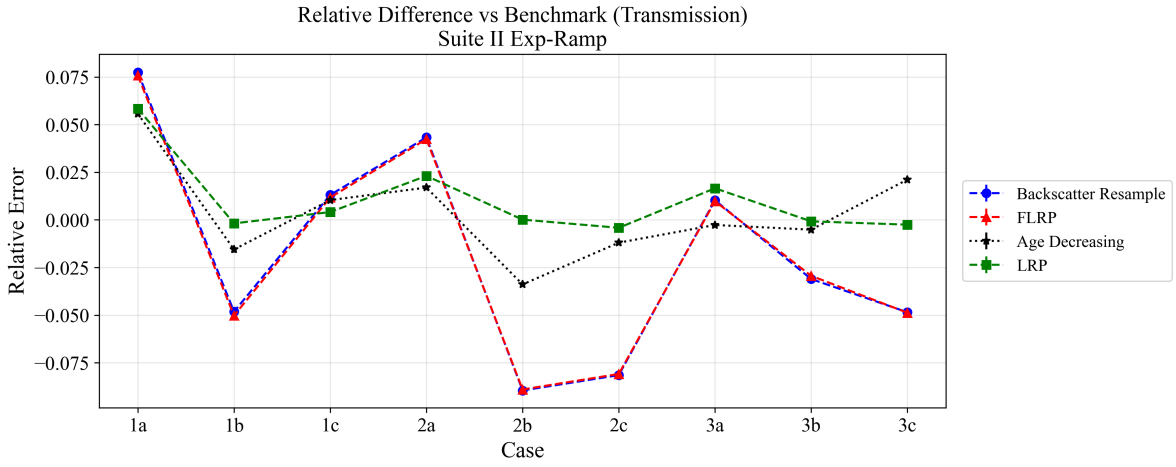


Figure 6.17: Relative error of transmission (T) for Suite II, Exponential-Ramp distributions.

Table 6.12: Methods Comparison for Exp-Unif Rad Distributions (Suite II).

Case		Quantity	Bench	Backscatter Resample	FLRP	Age Decreasing	LRP
1	a	R	0.1479(1)	0.1593(1)	0.1593(1)	0.1561(1)	0.1563(1)
		T	0.1482(1)	0.1595(1)	0.1592(1)	0.1560(1)	0.1564(1)
	b	R	0.06287(8)	0.05970(7)	0.05976(7)	0.06176(8)	0.06271(8)
		T	0.06295(8)	0.05981(7)	0.05978(7)	0.06188(8)	0.06281(8)
	c	R	0.1606(1)	0.1625(1)	0.1625(1)	0.1629(1)	0.1614(1)
		T	0.1608(1)	0.1626(1)	0.1624(1)	0.1630(1)	0.1613(1)
2	a	R	0.1872(1)	0.1947(1)	0.1948(1)	0.1895(1)	0.1911(1)
		T	0.1871(1)	0.1948(1)	0.1946(1)	0.1897(1)	0.1911(1)
	b	R	0.2874(1)	0.2616(1)	0.2616(1)	0.2779(1)	0.2870(1)
		T	0.2871(1)	0.2615(1)	0.2617(1)	0.2776(1)	0.2872(1)
	c	R	0.3039(1)	0.2785(1)	0.2784(1)	0.3008(1)	0.3026(1)
		T	0.3043(1)	0.2786(1)	0.2788(1)	0.3009(1)	0.3024(1)
3	a	R	0.4055(2)	0.4084(2)	0.4088(2)	0.4025(2)	0.4117(2)
		T	0.4056(2)	0.4090(2)	0.4087(2)	0.4028(2)	0.4123(2)
	b	R	0.1263(1)	0.1226(1)	0.1226(1)	0.1258(1)	0.1263(1)
		T	0.1264(1)	0.1224(1)	0.1227(1)	0.1258(1)	0.1263(1)
	c	R	0.2204(1)	0.2091(1)	0.2097(1)	0.2265(1)	0.2199(1)
		T	0.2204(1)	0.2096(1)	0.2092(1)	0.2263(1)	0.2200(1)

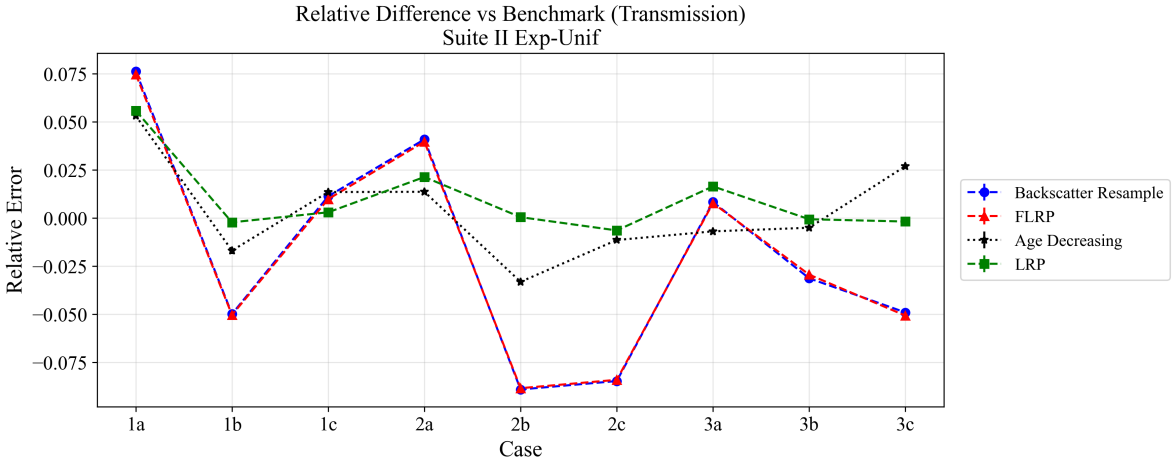


Figure 6.18: Relative error of transmission (T) for Suite II, Exponential-Uniform-Radii distributions.

Table 6.13: Methods Comparison for Exp-Exp Rad Distributions (Suite II).

Case		Quantity	Bench	Backscatter Resample	FLRP	Age Decreasing	LRP
1	a	R	0.1498(1)	0.1620(1)	0.1620(1)	0.1578(1)	0.1583(1)
		T	0.1499(1)	0.1622(1)	0.1620(1)	0.1578(1)	0.1582(1)
	b	R	0.06626(8)	0.06300(8)	0.06289(8)	0.06510(8)	0.06600(8)
		T	0.06613(8)	0.06300(8)	0.06312(8)	0.06522(8)	0.06610(8)
	c	R	0.1663(1)	0.1663(1)	0.1666(1)	0.1698(1)	0.1664(1)
		T	0.1661(1)	0.1666(1)	0.1665(1)	0.1697(1)	0.1661(1)
2	a	R	0.1882(1)	0.1950(1)	0.1950(1)	0.1897(1)	0.1920(1)
		T	0.1883(1)	0.1949(1)	0.1945(1)	0.1896(1)	0.1920(1)
	b	R	0.2878(1)	0.2625(1)	0.2624(1)	0.2784(1)	0.2879(1)
		T	0.2879(1)	0.2624(1)	0.2626(1)	0.2784(1)	0.2878(1)
	c	R	0.3069(1)	0.2794(1)	0.2793(1)	0.3043(1)	0.3052(1)
		T	0.3068(1)	0.2795(1)	0.2798(1)	0.3043(1)	0.3049(1)
3	a	R	0.4075(2)	0.4086(2)	0.4089(2)	0.4011(2)	0.4132(2)
		T	0.4081(2)	0.4090(2)	0.4088(2)	0.4014(2)	0.4135(2)
	b	R	0.1270(1)	0.1230(1)	0.1230(1)	0.1263(1)	0.1268(1)
		T	0.1268(1)	0.1228(1)	0.1231(1)	0.1261(1)	0.1268(1)
	c	R	0.2215(1)	0.2095(1)	0.2101(1)	0.2290(1)	0.2214(1)
		T	0.2215(1)	0.2098(1)	0.2096(1)	0.2292(1)	0.2213(1)

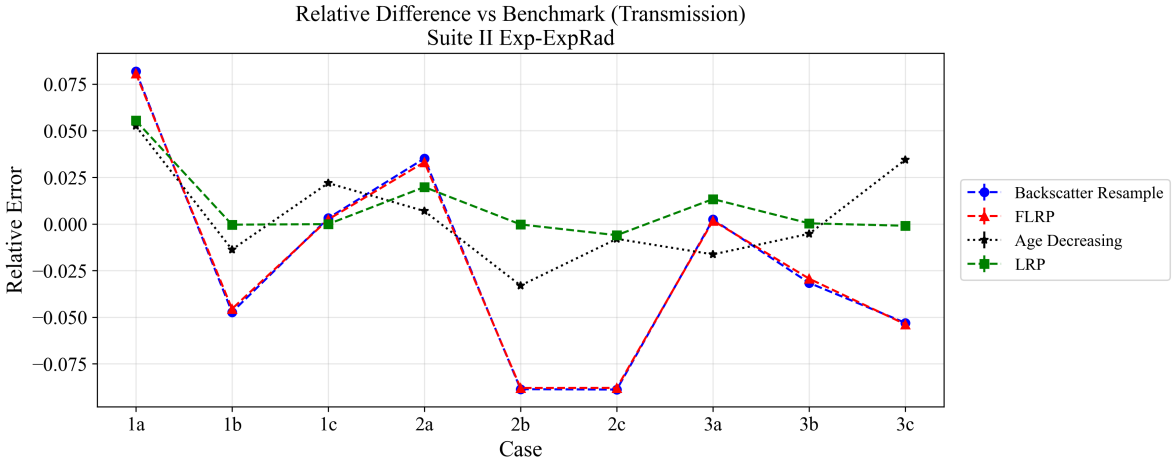
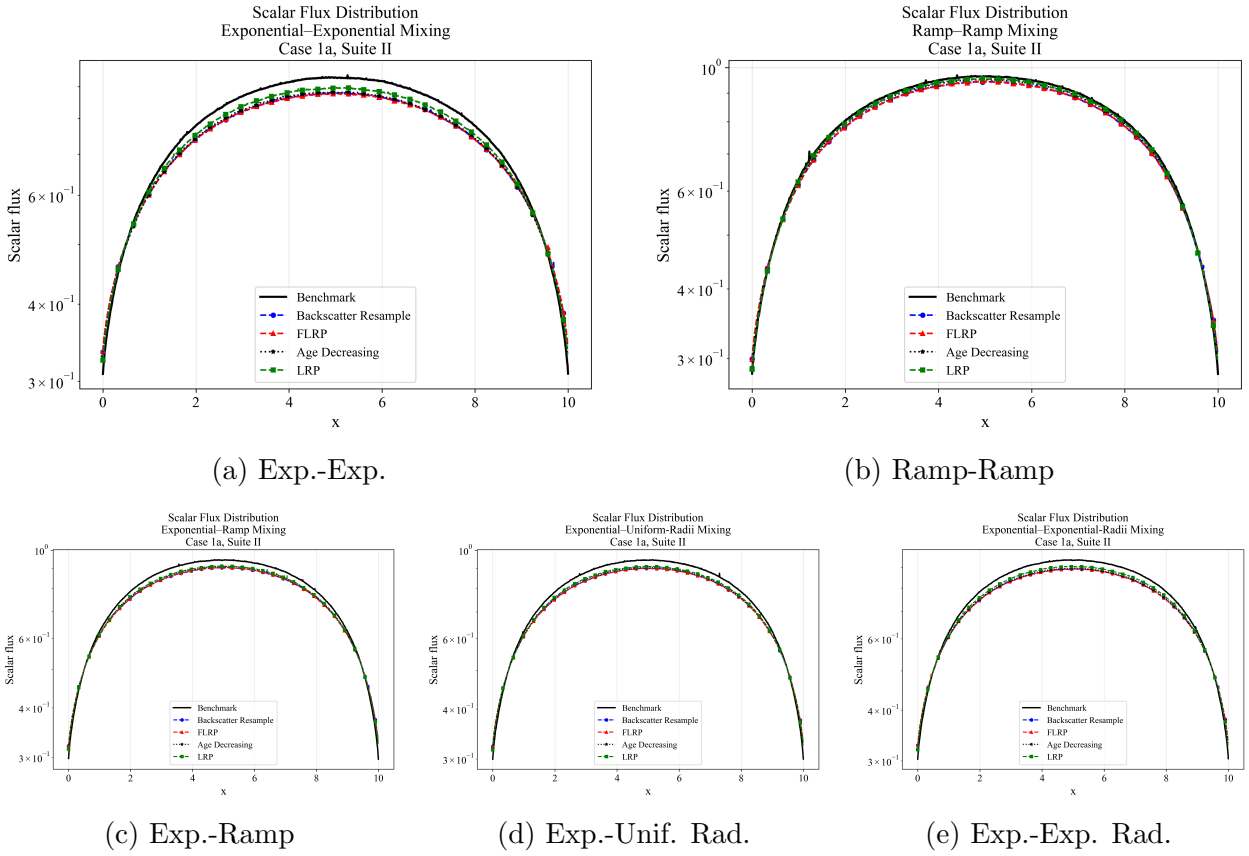


Figure 6.19: Relative error of transmission (T) for Suite II, Exponential-Exponential-Radii distributions.



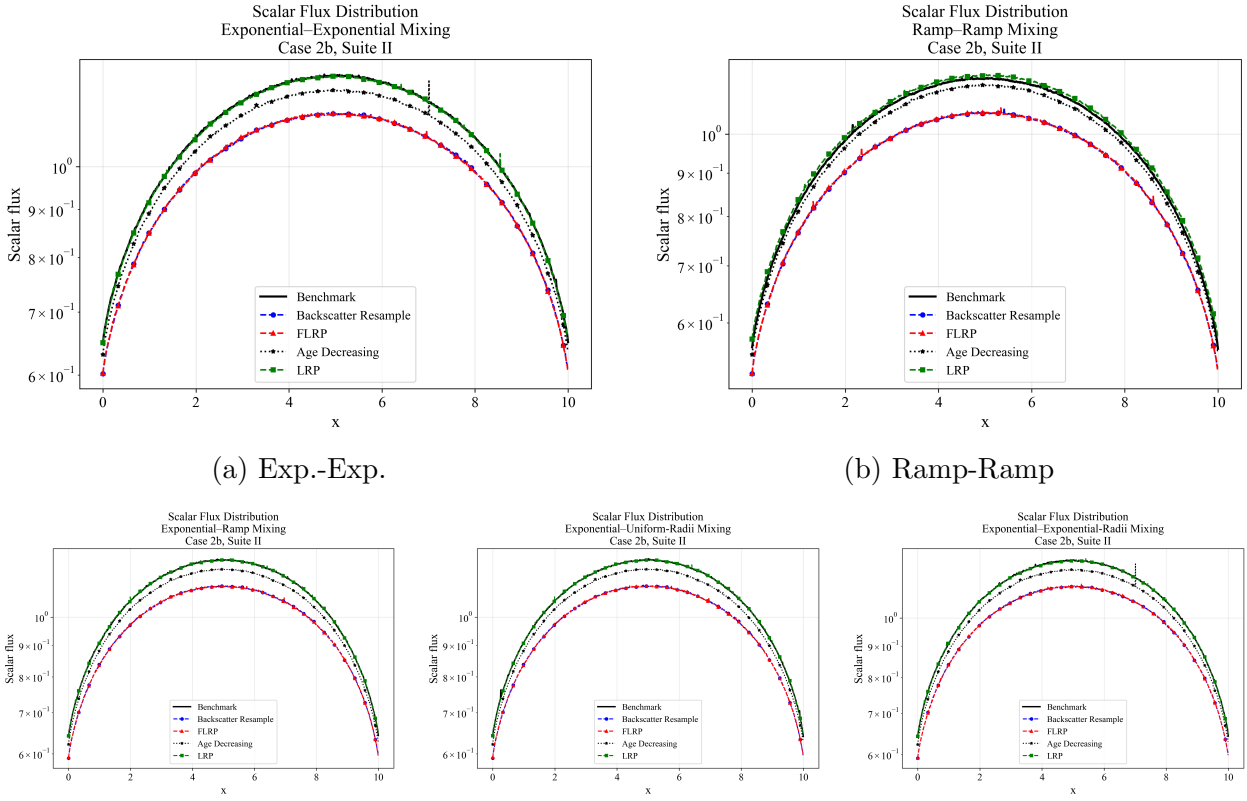
(a) Exp.-Exp. (b) Ramp-Ramp

(c) Exp.-Ramp (d) Exp.-Unif. Rad. (e) Exp.-Exp. Rad.

Figure 6.20: Scalar flux distributions for Case 1a (Suite II) comparing five material mixing statistics: Exponential-Exponential, Ramp-Ramp, Exponential-Ramp, Exponential-Uniform-Radii, and Exponential-Exponential-Radii.

Table 6.14: RMSE Comparison (Suite II).

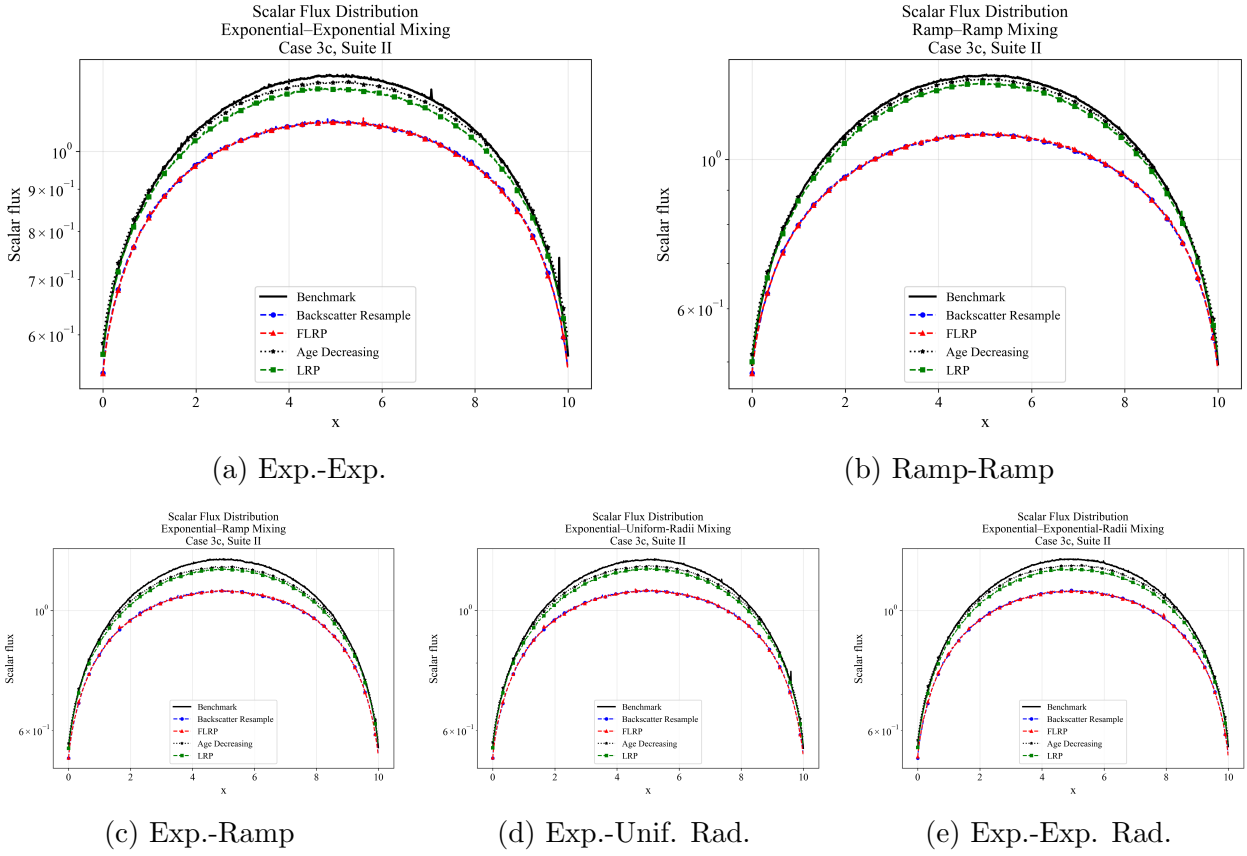
Distribution	Qty	Backscatter Resample	FLRP	Age Decreasing	LRP
Exp-Exp	R	0.0146	0.0145	0.0063	0.0034
	T	0.0146	0.0146	0.0063	0.0033
Ramp-Ramp	R	0.0121	0.0121	0.0036	0.0037
	T	0.0119	0.0119	0.0036	0.0039
Exp-Ramp	R	0.0134	0.0134	0.0048	0.0039
	T	0.0134	0.0133	0.0049	0.0039
Exp-Unif Rad	R	0.0136	0.0136	0.0050	0.0037
	T	0.0136	0.0135	0.0049	0.0038
Exp-Exp Rad	R	0.0140	0.0140	0.0055	0.0037
	T	0.0140	0.0138	0.0055	0.0036



(a) Exp.-Exp. (b) Ramp-Ramp

(c) Exp.-Ramp (d) Exp.-Unif. Rad. (e) Exp.-Exp. Rad.

Figure 6.21: Scalar flux distributions for Case 2b (Suite II) comparing five material mixing statistics: Exponential-Exponential, Ramp-Ramp, Exponential-Ramp, Exponential-Uniform-Radii, and Exponential-Exponential-Radii.



(a) Exp.-Exp.

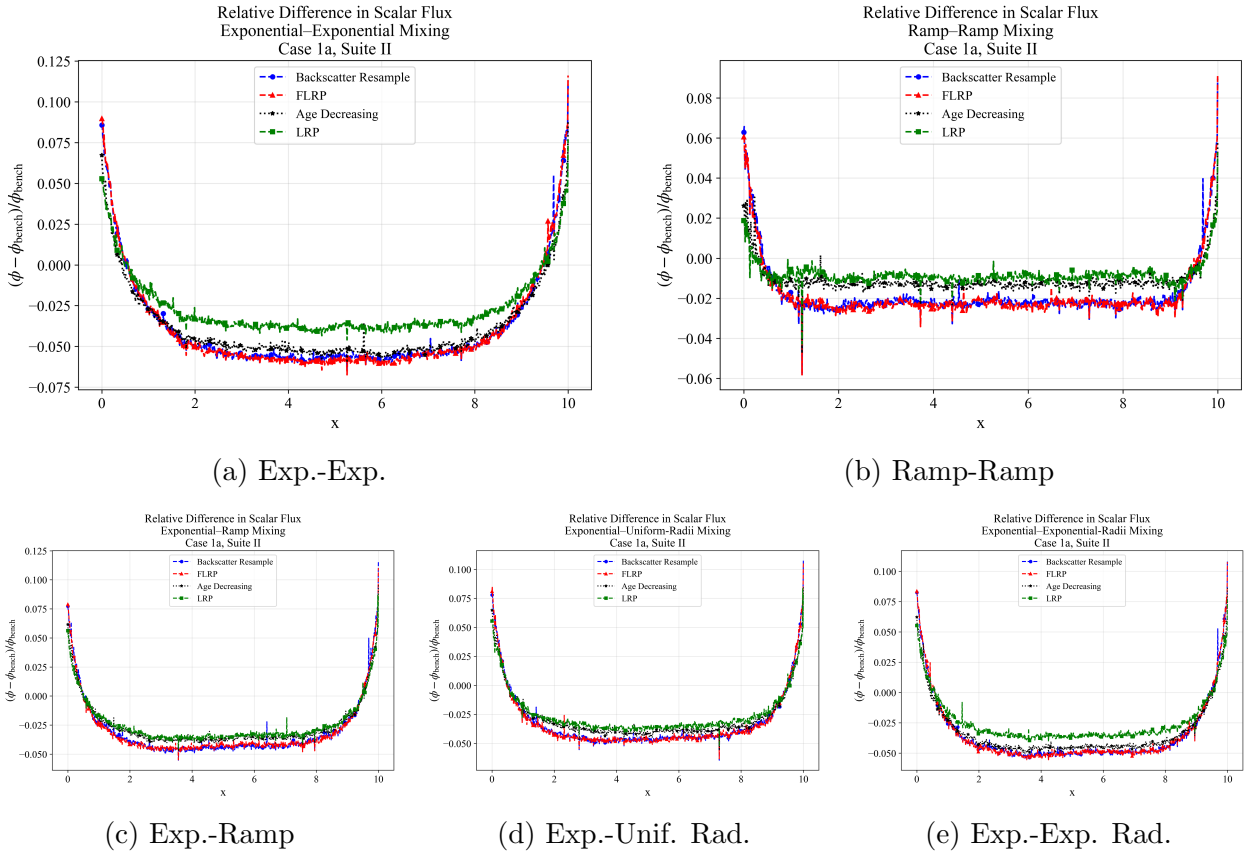
(b) Ramp-Ramp

(c) Exp.-Ramp

(d) Exp.-Unif. Rad.

(e) Exp.-Exp. Rad.

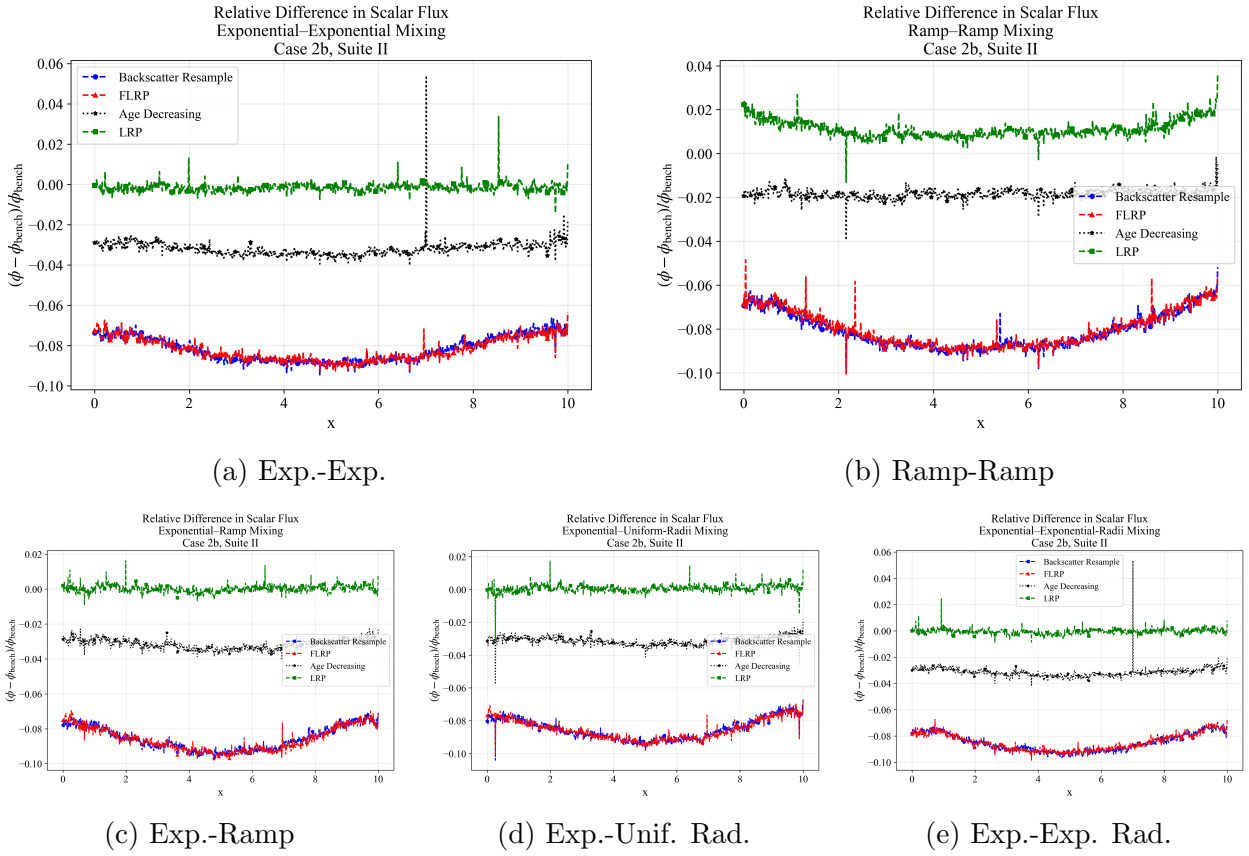
Figure 6.22: Scalar flux distributions for Case 3c (Suite II) comparing five material mixing statistics: Exponential-Exponential, Ramp-Ramp, Exponential-Ramp, Exponential-Uniform-Radii, and Exponential-Exponential-Radii.



(a) Exp.-Exp. (b) Ramp-Ramp

(c) Exp.-Ramp (d) Exp.-Unif. Rad. (e) Exp.-Exp. Rad.

Figure 6.23: Relative error of the scalar flux for Case 1a (Suite II), comparing five material mixing statistics: Exponential-Exponential, Ramp-Ramp, Exponential-Ramp, Exponential-Uniform-Radii, and Exponential-Exponential-Radii. All methods are shown relative to the benchmark solution.



(a) Exp.-Exp.

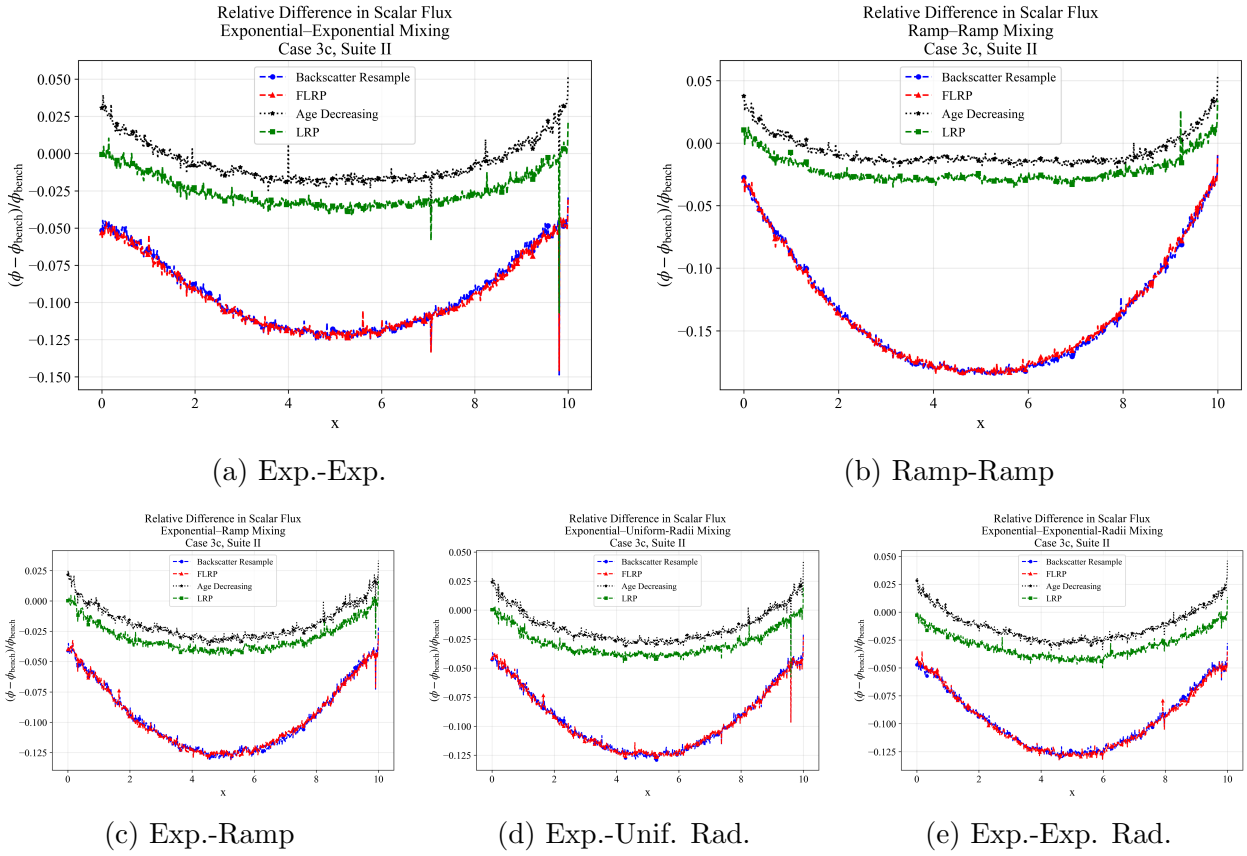
(b) Ramp-Ramp

(c) Exp.-Ramp

(d) Exp.-Unif. Rad.

(e) Exp.-Exp. Rad.

Figure 6.24: Relative error of the scalar flux for Case 2b (Suite II), comparing five material mixing statistics: Exponential-Exponential, Ramp-Ramp, Exponential-Ramp, Exponential-Uniform-Radii, and Exponential-Exponential-Radii. All methods are shown relative to the benchmark solution.



(a) Exp.-Exp.

(b) Ramp-Ramp

(c) Exp.-Ramp

(d) Exp.-Unif. Rad.

(e) Exp.-Exp. Rad.

Figure 6.25: Relative error of the scalar flux for Case 3c (Suite II), comparing five material mixing statistics: Exponential-Exponential, Ramp-Ramp, Exponential-Ramp, Exponential-Uniform-Radii, and Exponential-Exponential-Radii. All methods are shown relative to the benchmark solution.

Effect of Radius Distributions on Scalar Flux in 1D Planar Geometries

The previous results compared the accuracy of the various stochastic media transport methods for a fixed choice of material mixing statistics. It is also useful to isolate the effect of the mixing statistics themselves. In this section, the scalar flux from Exponential-Uniform-Radii and Exponential-Exponential-Radii mixing is compared against the scalar flux from Exponential-Ramp mixing. These comparisons are intended to show how strongly the distribution of the radius in spherical inclusion stochastic geometries affects the scalar flux profile.

Figures 6.26-6.31 show the relative difference in scalar flux between the variable radius distributions and the Exponential-Ramp distribution (constant radius) for Cases 1a, 2b, and 3c in both Suite I and Suite II benchmark problems. The relative difference is computed as

$$\frac{|\phi_{\text{other}}(x) - \phi_{\text{Exp-Ramp}}(x)|}{\phi_{\text{Exp-Ramp}}(x)}, \tag{6.16}$$

where ϕ_{other} denotes either the Exponential-Uniform-Radii or Exponential-Exponential-Radii scalar flux.

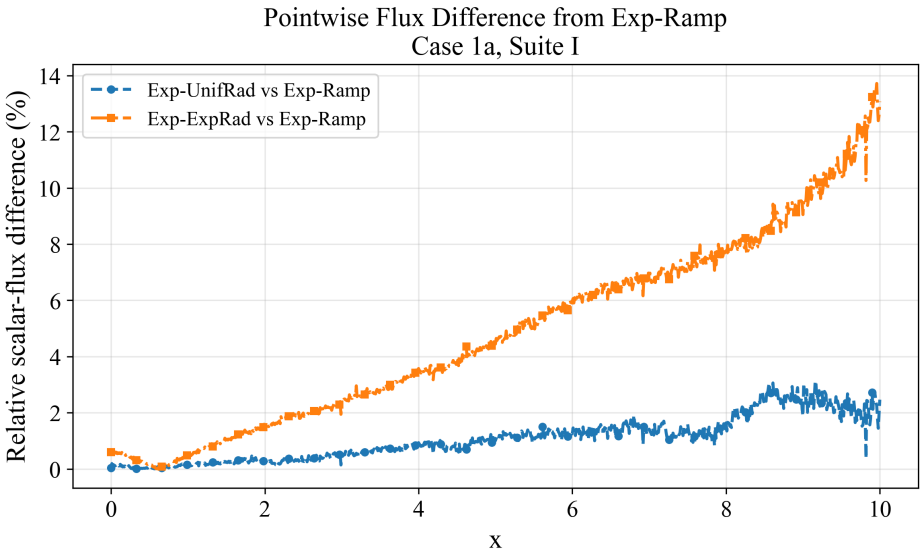


Figure 6.26: Pointwise relative scalar-flux difference from Exponential-Ramp mixing for Case 1a, Suite I.

The most prominent trend is that the Exponential-Exponential-Radii distribution produces a larger deviation from Exponential-Ramp than the Exponential-Uniform-Radii distribution. This is expected because the exponentially distributed radius model permits a

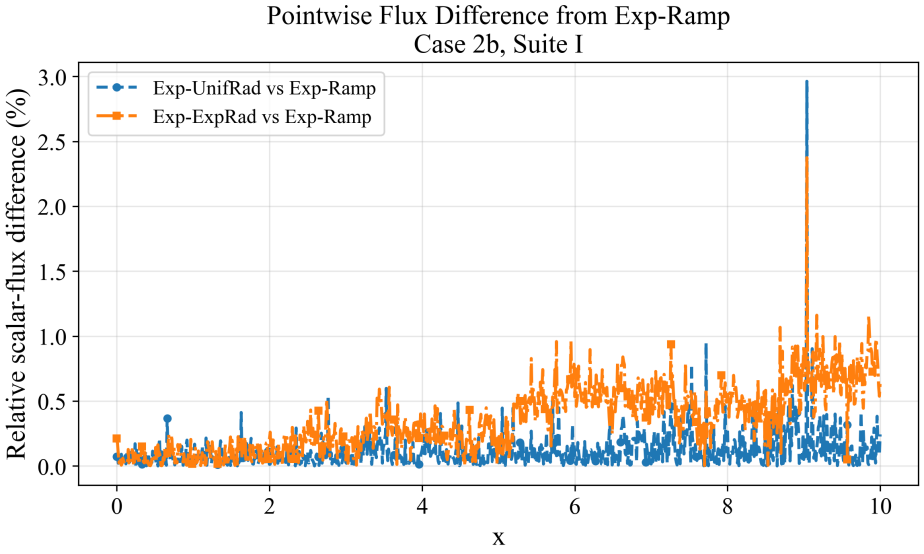


Figure 6.27: Pointwise relative scalar-flux difference from Exponential-Ramp mixing for Case 2b, Suite I.

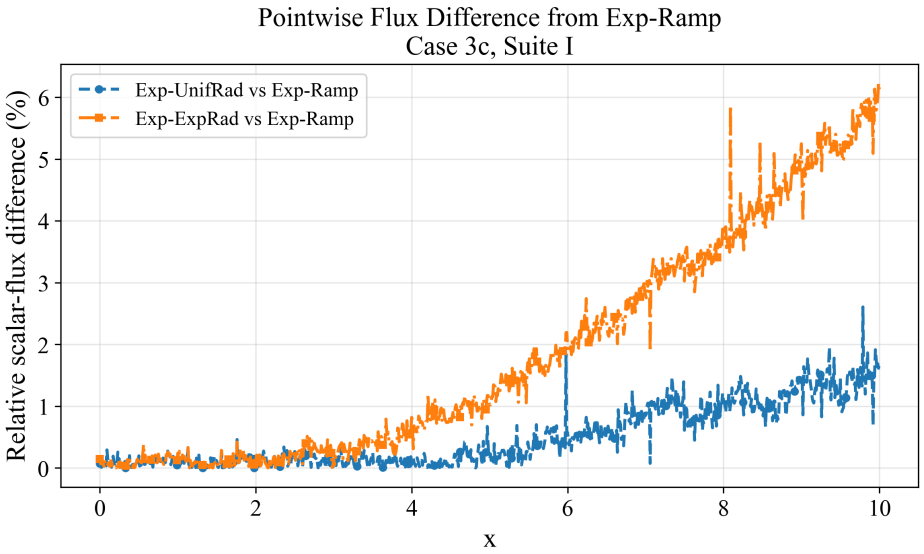


Figure 6.28: Pointwise relative scalar-flux difference from Exponential-Ramp mixing for Case 3c, Suite I.

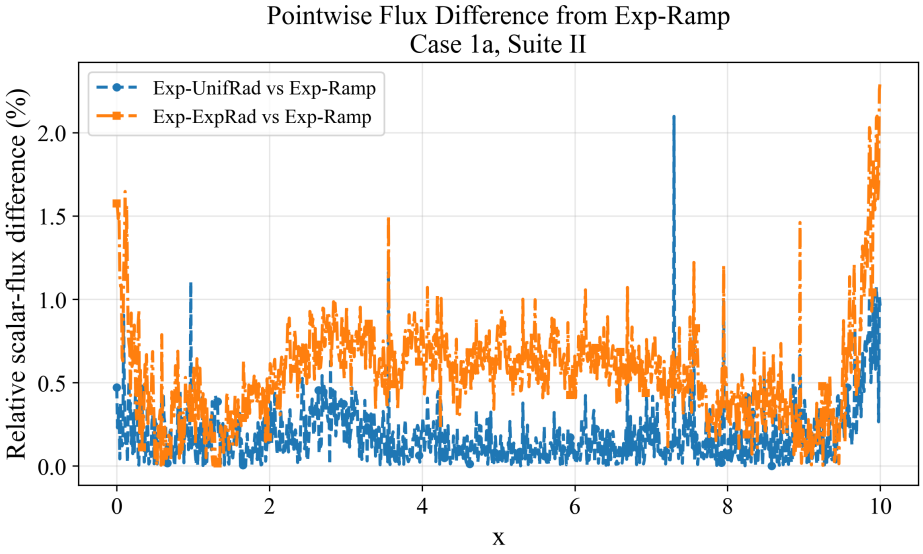


Figure 6.29: Pointwise relative scalar-flux difference from Exponential-Ramp mixing for Case 1a, Suite II.

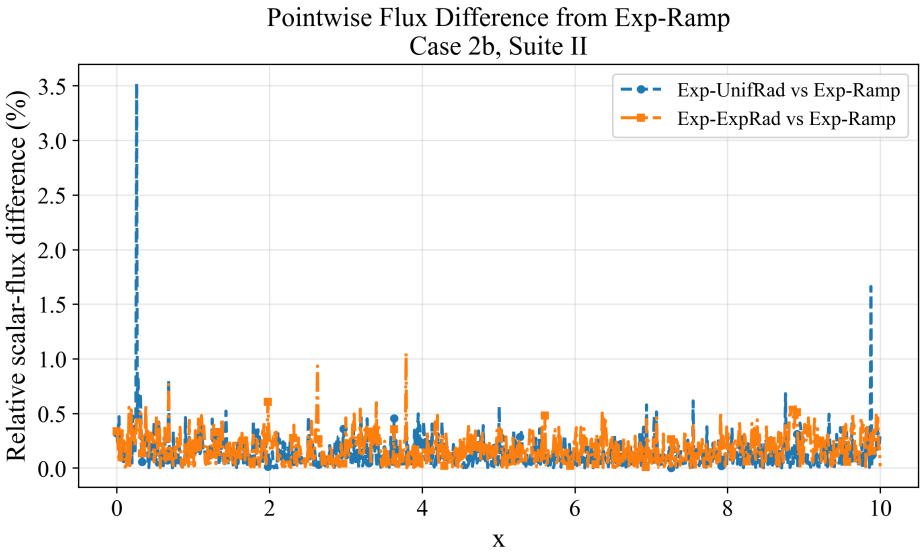


Figure 6.30: Pointwise relative scalar-flux difference from Exponential-Ramp mixing for Case 2b, Suite II.

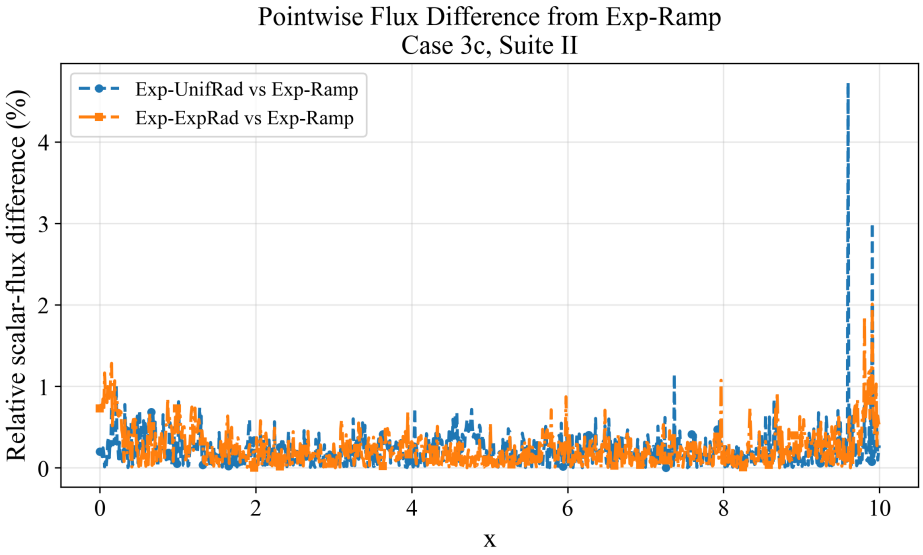


Figure 6.31: Pointwise relative scalar-flux difference from Exponential-Ramp mixing for Case 3c, Suite II.

broader range of inclusion sizes, including longer chords, while the uniform radius distribution remains more tightly constrained. As a result, the Exponential-Exponential-Radii case differs more strongly from the constant radius ramp distribution.

For Suite I, the relative differences generally grow with distance into the slab. This trend is clearest in Cases 1a and 3c, where the largest differences occur near the downstream boundary. In these boundary source problems, particles enter at $x = 0$ and the influence of the material chord length statistics accumulates as particles stream across the domain.

The Suite II behavior shows that the radius distribution has a nearly negligible effect on the scalar flux. This is likely because the source particles are distributed uniformly throughout the geometry, leading to a much more similar flux profile, and less accumulation of differences from the influence of chord length statistics. Any discrepancies larger than 2% are the effect of statistical noise from Monte Carlo.

The Figure 6.32 shows the maximum relative difference in the scalar flux between the exponential radius distribution and the constant radius ramp distribution as a function of scattering for Suite I. The chord lengths and cross sections are from Case 1, with the scattering fraction c of both materials being the same. Generally, as the amount of scatter increases and the material becomes diffusive, the mixing statistics become less relevant.

Overall, these comparisons demonstrate that the detailed renewal chord length distribution can affect the ensemble-averaged scalar flux, even when the mean chord lengths and background statistics are similar. The effect is most visible in boundary source problems and for the Exponential-Exponential-Radii distribution, whose broader chord length statistics differ most strongly from the constant radius ramp distribution. However, increased

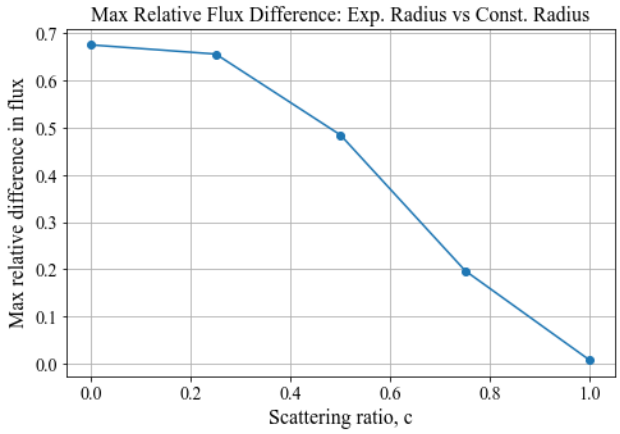


Figure 6.32: Maximum relative difference in scalar flux as a function of scattering fraction for Exponential Radius Distribution and Constant Radius.

scattering reduces the impact of these differences.

6.4 Summary

This Chapter extended the age-based renewal transport framework to include particle scattering in 1D planar geometry. The main theoretical result is the scattering form of the age-based transport equation, Eq. (6.7), together with age-redistribution kernels that define different treatments for how material age changes at scattering events. In the Markovian limit, the kernel choice disappears and the equations reduce to the familiar Levermore-Pomraning scattering model. For non-Markovian renewal media, however, the kernel matters because the hazard function depends on age.

Additionally, Monte Carlo methods for age-based models were developed. Specifically, the Backscatter-Resample model provides a transport-theoretic equivalent to the heuristic FLRP method, and the Age-Decreasing method improves on accuracy and approaches the accuracy of LRP. The Backscatter-Resample model and FLRP also reduce to CLS/LP in the case of Markovian mixing.

The numerical results show that the methods with improved geometric memory are more accurate. Backscatter Resample and FLRP are statistically identical because both retain memory of one material interface, with backscatter events resampling said material interface. They provide a useful renewal-statistical extension of CLS, but their errors remain significant in scattering problems. The Age-Decreasing method improves the results by allowing particles to move back toward the most recently sampled interface. LRP is generally the most accurate method because it preserves interface distances on both sides of the particle and therefore retains the most geometric memory.

Finally, the effect of radius distribution on spherical inclusion geometries was investigated, and it was shown that exponentially distributed radii can lead to significantly different flux profiles for some problems in comparison to constant radii. A uniform interior source and increased scatter decrease the relative difference between different radius distributions.

Chapter 7

Extension of Age-Based Transport in Renewal Statistical Media to 3D

7.1 Introduction

The preceding chapters developed an age-based description of particle transport in renewal statistical media. Chapter 3 introduced the renewal-statistical quantities used throughout this dissertation, and Chapter 5 showed that the age variable provides the geometric memory needed to obtain an exact generalized Master equation for purely absorbing renewal media. Chapter 6 then extended the same framework to include particle scattering in 1D planar geometry and developed several methods that consider different treatment of the age at backscatter events. Particle backscatter was shown to make the methods approximate transport memory because particles may reverse direction and move back toward previously sampled material. As a result, the methods that preserve more local geometric memory, the Age-Decreasing and LRP methods, are generally more accurate.

The purpose of this Chapter is to extend the methods of Chapter 6 to 3D stochastic media and analyze how the methods adapt in the context of transport through spherical inclusion geometries, such as those in Figure 2.5 or 2.3. The benchmark problems considered here retain the slab leakage interpretation used in the previous chapters, with reflection and transmission measured through the left and right faces, but the stochastic geometry is now generated from non-overlapping spheres embedded in a background material.

One difficulty in adapting the age-based methods to 3D is the treatment of local geometric memory after scattering. In 1D planar transport, the treatment of geometric memory after scattering is relatively straightforward because all material interfaces are perpendicular to the single spatial coordinate x. If the sign of μ changes, the particle begins moving back toward the previously sampled material interface, so the age or stored interface distances can be updated consistently with that reversal. In 3D, however, the stored age or local interface memory is an approximation of the surrounding geometry. After a scattering event, the particle generally travels along a new ray through the medium, and the previously

sampled interface information is not sufficient to determine the material geometry along that new direction. Thus, the difficulty in 3D is that any update of the age variable or LRP interface memory after scattering is necessarily approximate unless the local 3D realization is explicitly resolved. Previous implementations of 3D LRP used a probabilistic treatment of local geometric memory when a particle scatters to compensate for this approximate geometric memory [18]. This Chapter compares deterministic and probabilistic approaches to the treatment of the age variable in the event of a scatter in order to determine which is more appropriate for the spherical inclusion benchmark problems.

The rest of this Chapter is organized as follows. Section 7.2 describes the benchmark generation procedure, which uses the existing tools in Sandia National Laboratories' research code PlaybookMC [43]. Section 7.3 describes the adaptation of the Chapter 6 methods to 3D transport, including analysis of geometric memory updates at scattering events. Section 7.4 presents the Suite I leakage and scalar-flux results, including comparisons between the different radius distributions. Section 7.5 summarizes the main conclusions of the 3D extension.

7.2 3D Benchmark Generation Procedure

Spherical Inclusion Geometries in PlaybookMC

The benchmark calculations in this chapter are generated using the spherical inclusion geometry capability in PlaybookMC [43]. The geometry is a binary mixture consisting of a background material and randomly placed spherical inclusions [5, 19, 44, 1]. For the binary benchmark problems considered here, the geometry input specifies the target sphere volume fraction, the sphere-radius distribution and its parameters, and the boundary treatment used when checking sphere placement. The generated spheres are assigned to material 1 and embedded in a material 0 background. The size distribution options used here are constant, uniform, and exponential radii, which correspond to the distributions shown in Section 3.2. Figure 7.1 shows representative 2D versions of the 3D spherical inclusion geometries used for these calculations.

The benchmark geometry generation procedure can be summarized as follows. First, sphere radii are sampled from the specified radius distribution until the cumulative sphere volume reaches the target inclusion volume fraction. For the uniform and exponential radius distributions, the final sampled radius may be adjusted so that the remaining target sphere volume is filled more closely. The target radii are then sorted from largest to smallest before placement. This ordering improves the likelihood that large spheres are placed while sufficient free volume remains.

After the target radii have been selected, PlaybookMC attempts to place the spheres in the domain. A candidate center is sampled uniformly from the region in which the sphere can fit without crossing the boundaries of the domain. The candidate sphere is then checked against previously placed spheres and is accepted only if it does not overlap with

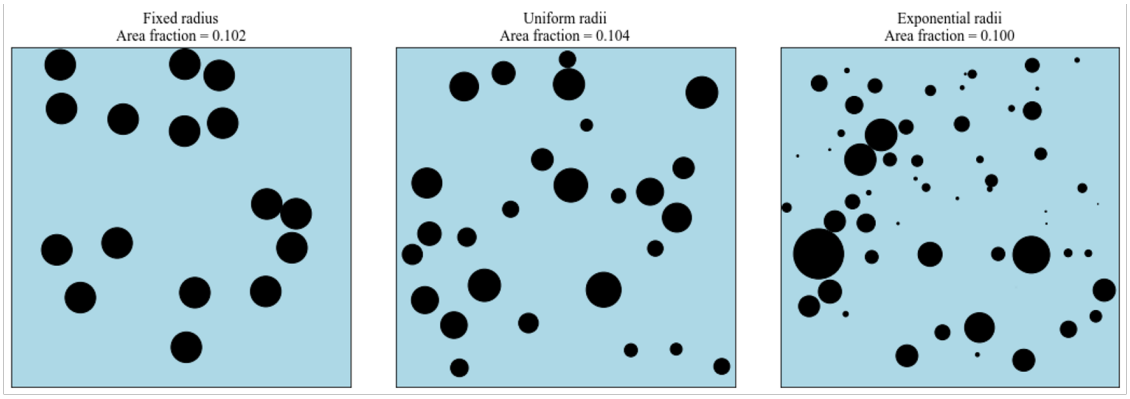


Figure 7.1: 2D representations of various spherical inclusion geometries used for 3D benchmarks.

any previously placed sphere. If the placement is successful, the sphere center and radius are stored. If the sphere cannot be placed after the prescribed maximum number of attempts, geometry generation fails.

Once all spheres are placed, each sphere is assigned a material index according to the user-specified material probabilities for the inclusion material. Points outside all spheres are assigned to the background material. During transport, the benchmark solver determines the material at a particle position by checking whether the point lies inside any sphere, transporting the particles through an explicitly sampled 3D material realization. This procedure uses the Monte Carlo method to effectively solve Eq. (2.9) for a given spherical inclusion geometry ω.

Failure of Some High-Volume-Fraction Constant Radius Benchmarks

One practical limitation encountered in the benchmark generation is that some constant radius geometries cannot be generated with a high volume fraction. This issue occurs most prominently for the case 3 constant radius benchmark at a 30% inclusion volume fraction (the specific material properties for case 3 and other cases can be found in Table 7.2). The PlaybookMC spherical inclusion generator places non-overlapping spheres that also do not overlap the domain boundaries. For a constant radius distribution, every sphere has the same size. As the target volume fraction increases, the remaining void spaces between already placed spheres become smaller. Eventually, the algorithm may be unable to find a valid location for the next sphere, even though the target volume fraction has not been reached. When this happens, the attempted realization is rejected even after millions of placement attempts.

Uniform and exponential radius distributions are less prone to this failure because smaller

spheres can be sampled. These smaller spheres can fit into gaps that are inaccessible to a constant radius sphere. In addition, the final radius can be reduced in the random-radius cases to fill the remaining target sphere volume. Therefore, random-radius cases are able to create benchmark realizations with the same 30% volume fraction even when the corresponding constant radius case cannot be packed by the random sequential placement algorithm.

For this reason, any missing constant radius case 3 results at 30% volume fraction should be treated as a limitation of the explicit benchmark geometry generation procedure, not as a failure of any transport methods. Case 3 is particularly limited because the inclusions are larger and therefore harder to fit in the gaps between the existing spheres. In the results shown in Section 7.4, the corresponding leakage values are labeled as N/A, and the flux plots and relative flux plots are not provided.

7.3 Adapting the Methods to 3D Media

Particle Tracking in a 3D Slab

The methods considered in this chapter use the same basic particle state as in Chapter 6, augmented by the full 3D position and direction. A particle state consists of position $\mathbf{r} = (x, y, z)$, direction $\mathbf{\Omega} = (\Omega_x, \Omega_y, \Omega_z)$, current material i, and whatever age or local-interface information is required by the selected method. The methods still sample material interfaces on the fly along the particle trajectory using the conditional interface-sampling procedure already developed in Chapter 6 rather than building physical geometries.

Only the geometric interpretation of a transport step changes. In the 1D algorithms, the sampled distance to collision and sampled distance to material interface were projected onto the x coordinate through the particle direction cosine. In 3D, distances are sampled and compared as physical path lengths along the current particle direction

$$\mathbf{\Omega} = (\Omega_x, \Omega_y, \Omega_z) = \left(\mu, \sqrt{1-\mu^2}\cos\varphi, \sqrt{1-\mu^2}\sin\varphi\right), \tag{7.1}$$

where $\mu = \Omega_x = \cos\theta$, θ is the polar angle measured from the positive x axis, and φ is the azimuthal angle about the x axis. The methods otherwise function identically in 1D and 3D.

Geometric Memory in 3D

In Chapter 6, the treatment of geometric memory variables relied on the 1D planar structure of the material realization. Scattering events were classified according to the sign of $\mu\mu'$, and this classification determined how the age variable or stored interface distances were updated. This procedure is natural in 1D planar geometry because the only spatial direction relevant to material memory is the x direction. If the sign of μ changes, the particle is moving back toward the material interface it most recently crossed.

In 3D, this same memory updating procedure is no longer an exact representation of the local realization memory. One possible procedure for considering a switch in the relative position of the local geometric memory is to use the sign of $\mathbf{\Omega} \cdot \mathbf{\Omega}'$. This rule switches the relative position of the geometric memory when the outgoing direction lies in the forward or backward half-space relative to the incoming direction. For isotropic scattering, the probability that $\mathbf{\Omega} \cdot \mathbf{\Omega}' < 0$ is one half. However, the methods used here do not store the actual local 3D interface geometry: as a result, the interface locations stored in memory in the Age-Decreasing method and LRP may inaccurately represent the boundaries of the spheres.

The existing literature that extended LRP to 3D uses a probabilistic determination of local geometric memory updating [18]. For LRP, the probability of switching distances is taken to be

$$P_{\text{switch}} = \frac{1}{2}(1 - \mathbf{\Omega} \cdot \mathbf{\Omega}'), \tag{7.2}$$

such that the interface distances in either direction are switched if pseudorandom number $\xi \in \mathrm{U}(0, 1)$

$$\xi < \frac{1}{2}\left(1 - \mathbf{\Omega} \cdot \mathbf{\Omega}'\right). \tag{7.3}$$

In the interest of finding the most accurate way to update the local geometric memory upon scattering events for the methods, the probabilistic approach was compared with the $\mathbf{\Omega} \cdot \mathbf{\Omega}' < 0$ deterministic approach relative to the benchmark for leakage values. The RMSE for the leakage values as calculated in Eq. (6.14) is presented in Table 7.1 for each method for each type of spherical inclusion geometry with a sphere volume fraction of 0.1.

Table 7.1: Leakage RMSE comparison by geometric memory treatment for volume fraction 0.10.

Memory Treatment	Distribution	Qty	Backscatter Resample	FLRP	Age Decreasing	LRP
Prob.	Exp-Const Rad	R	0.0298	0.0296	0.0124	0.0129
		T	0.0061	0.0062	0.0046	0.0064
	Exp-Unif Rad	R	0.0311	0.0311	0.0134	0.0139
		T	0.0065	0.0068	0.0043	0.0060
	Exp-Exp Rad	R	0.0315	0.0317	0.0110	0.0131
		T	0.0064	0.0062	0.0094	0.0111
Deter.	Exp-Const Rad	R	0.0291	0.0295	0.0154	0.0162
		T	0.0062	0.0060	0.0020	0.0039
	Exp-Unif Rad	R	0.0306	0.0311	0.0157	0.0169
		T	0.0065	0.0066	0.0018	0.0037
	Exp-Exp Rad	R	0.0318	0.0317	0.0145	0.0159
		T	0.0062	0.0063	0.0072	0.0091

For the Backscatter-Resample method and FLRP, the two treatments produce nearly identical accuracy within the statistical uncertainty of the calculations. For the Age-Decreasing method and LRP, however, the treatment of the age at scattering events has a more visible effect. Across the radius distributions considered, the probabilistic treatment gives lower RMSE values for reflection, while the deterministic treatment gives lower RMSE values for transmission.

One possible explanation is that reflection and transmission are sensitive to different aspects of the particle history. Transmission is dominated by particles that continue to make progress across the slab without backscattering, so a probabilistic classification can occasionally modify the interface memory after scattering events that do not strongly reverse the particle trajectory. This can degrade the representation of the local geometry for particles that ultimately transmit. Reflection, on the other hand, can result from a sequence of scattering events that gradually redirect a particle back toward the incident boundary, even if no single collision satisfies the deterministic condition $\mathbf{\Omega} \cdot \mathbf{\Omega}' < 0$. In that case, the probabilistic treatment can represent some of this accumulated directional reversal more effectively.

For consistency with previous 3D LRP implementations, the remainder of this chapter uses the probabilistic treatment of geometric memory switching. The deterministic condition $\mathbf{\Omega} \cdot \mathbf{\Omega}' < 0$ may also be reasonable, particularly for problems with forward-peaked scattering. For the isotropic scattering problems considered here, both treatments have merit, but the probabilistic treatment is adopted as the baseline convention.

Exactness in Purely Absorbing Case

The age-based renewal model remains exact in 3D for purely absorbing transport, provided that the material statistics along each particle trajectory are described by the prescribed renewal chord length distributions. In the absence of scattering, a particle travels along a fixed direction $\mathbf{\Omega}$ until it is absorbed or leaks from the domain. The particle therefore never changes direction and never revisits a portion of the material realization that was previously sampled. Along this fixed ray, the 3D problem reduces to a 1D rod problem along $\mathbf{\Omega}$, which is the exact model described in Chapter 5.

7.4 Results

Problem Definition and Material Properties

All results in this chapter are computed in a 3D Cartesian geometry. Particles move in three spatial dimensions, but the leakage quantities are defined with respect to the x direction. The left and right faces of the domain are vacuum boundaries. Particles crossing the left face are tallied as reflection R, and particles crossing the right face are tallied as transmission T. The y and z faces are reflecting boundaries, which allow for more statistically significant leakage

tallies and approximate an infinite stochastic geometry in the y and z directions. Retaining the same reflection and transmission leakage values is also valuable so that the 3D results can be compared with the 1D renewal media trends. All calculations are monoenergetic and time independent.

Scalar fluxes are also tallied as functions of x only. Although the particles move in 3D and flux tallies could be constructed in the transverse directions, the present comparisons focus on the x-dependent scalar flux because this is the direction of net transport and leakage. This choice also makes the flux profiles directly comparable to the 1D scalar flux results from Chapter 6.

Only Suite I boundary source problems are considered in this chapter. In these problems, particles are incident from the left side of the slab, and the primary quantities of interest are the reflection, transmission, and scalar flux profiles. Suite II interior-source calculations are not included because the explicit 3D benchmark calculations are computationally expensive (with some calculations taking more than 2 days to run), and based on the 1D results of Chapter 6, we do not expect that the interior-source suite would provide substantially different conclusions about the relative accuracy of the methods. The Suite I problems therefore provide the most direct and computationally practical test of the 3D extensions developed in this chapter.

The material properties used in this chapter are based on the 3D spherical inclusion benchmark problems of Brantley [44]. In these problems, material 0 is the optically thin background matrix material and material 1 is the optically thick spherical inclusion material. The case numbers correspond to different spherical inclusion mean chord lengths. Unlike the 1D benchmark cases used in Chapter 6, the background mean chord length is not specified independently of the inclusion volume fraction. Instead, for a prescribed sphere volume fraction p_1 and inclusion mean chord length λ_1, the background mean chord length is computed, neglecting finite-domain boundary effects, as

$$\lambda_0 = \left(\frac{1}{p_1} - 1\right)\lambda_1. \tag{7.4}$$

The value λ_0^* shown in Table 7.2 denotes the background mean chord length for the reference volume fraction $p_1 = 0.10$.

Brantley's original 3D spherical inclusion comparisons used scattering ratio $c = \Sigma_s/\Sigma_t = 0.9$ in both materials. In this chapter, the same material cases are used, but the scattering cases from Chapter 6 are also considered. Case a corresponds to an absorbing background and scattering inclusions, case b corresponds to a scattering background and absorbing inclusions, and case c corresponds to the uniformly scattering case used in the original Brantley calculations. The numerical case labels and scattering case labels are independent; thus, each material case is run with each scattering case considered in this chapter, giving cases 1a through 3c.

The benchmark calculations were produced using PlaybookMC and utilized 5000 particles on each of 200 realizations for a total of 10^6 particles per case. The results for each method

Table 7.2: Material properties for the 3D spherical inclusion benchmark cases [44]. The material case numbers correspond to the Brantley spherical inclusion mean chord length cases. The quantity λ_0^* denotes the background mean chord length for sphere volume fraction $p_1 = 0.10$, with λ_0 at other volume fractions computed using Eq. (7.4). The scattering cases a and b are added in this chapter, while case c corresponds to the scattering ratio used in the original 3D spherical inclusion calculations.

Case	$\Sigma_{t,0}$	λ_0^*	$\Sigma_{t,0}\lambda_0^*$	$\Sigma_{t,1}$	λ_1	$\Sigma_{t,1}\lambda_1$	Case	c_0	c_1
1	10/99	99/40	0.25	100/11	11/40	2.5	a	0	1
2		99/20	0.5		11/20	5.0	b	1	0
3		99/10	1.0		11/10	10.0	c	0.9	0.9

were produced in independent codes and used 10^6 particles per case. The scalar flux was binned over 100 cells in the geometry.

As a verification step, the independently developed codes were checked for Markovian media against published 3D leakage results in Refs. [16] and [21]. This verification ensures that, in the Markovian limit, the implementation produces the expected CLS behavior before being applied to non-exponential spherical inclusion statistics.

Results and Discussion

This subsection gives the leakage and flux results for the 3D spherical inclusion problems. The leakage values are included in Tables 7.3 through 7.11. The RMSE for each radius distribution and volume fraction is provided in Table 7.12. The scalar flux plots are provided in Figures 7.2 through 7.10, with the relative error on said flux values for each method provided in Figures 7.11 through 7.19. It is also noted that case 3 constant radius leakage values and flux plots are not provided for the reasons described in Section 7.2.

Across the volume fractions and radius distributions considered, the Backscatter-Resample and FLRP methods produce nearly identical leakage RMSE values. This agreement is expected because both methods retain the same memory of the renewal media in different directions, and aligns with prior 1D results in Chapter 6. The Age-Decreasing and LRP methods generally provide a substantial improvement in reflection accuracy. In particular, the reflection RMSE values for the Age-Decreasing method and LRP are much smaller than those of the Backscatter-Resample method and FLRP for every radius distribution and volume fraction considered. For transmission RMSE values, the Age-Decreasing method and LRP remain more accurate than the Backscatter-Resample method and FLRP in all cases except for the exponentially distributed radii with 10% volume fraction. Another interesting takeaway is that the Age-Decreasing method is often slightly more accurate than LRP for 3D leakage values, even though LRP retains more local geometric information. This suggests that retaining more memory is not always beneficial when the memory itself is approximate: the probabilistic treatment of local memory can sometimes modify the stored interface infor-

mation after scattering events that do not correspond to a true reversal of the particle path through the renewal geometry. In such cases, the geometric memory retained by LRP can misrepresent the spherical inclusions, leading to relatively inaccurate leakage values. Because the Age-Decreasing method only retains one interface in memory, there is seemingly less of this effect, though still present in cases such as the exponentially distributed radii with 10% volume fraction.

Overall, the 3D RMSE values are smaller than the corresponding 1D Suite I RMSE values. This is most apparent for the Backscatter-Resample and FLRP methods, where the 1D reflection RMSE values are approximately 0.084–0.088, while the 3D reflection RMSE values are generally closer to 0.03 for the spherical-inclusion cases. The same trend is observed for transmission, where the 3D RMSE values are typically well below the 1D values. This improvement is consistent with the reduced importance of direct transport memory in 3D. In 1D, a scattering event can only send the particle forward or backward along the slab direction, so backscatter directly causes the particle to revisit previously sampled material. In 3D, scattering redistributes the particle direction over both polar and azimuthal angles, so particles are less likely to reverse along the same path. As a result, the memory errors associated with resampling or incompletely preserving nearby interfaces are less severe. The flux relative error plots show the same general behavior: the method errors are still visible and retain the same ordering, but their magnitudes are generally smaller than in the 1D flux comparisons. This is also consistent with the increase in accuracy for CLS and LRP observed in 3D Markovian media [16].

The flux relative-error curves show additional spatial structure that is not captured by the leakage RMSE alone. Near the incident boundary, the relative errors are often initially larger, then decrease over the first few spatial bins before increasing more gradually through the interior of the slab. Near the transmitted boundary, the errors often peak and then decrease again in the final few bins. This behavior is likely related to a difference in problem setup between the benchmark calculation and the methods. In the benchmark calculations, spherical inclusions are not allowed to overlap the boundary of the domain. In the approximate methods, however, material chord lengths are sampled statistically and material 1 can be sampled at or near the boundary without enforcing this geometric exclusion. This mismatch is evident near the domain boundaries, but is not likely to impact the flux solutions in the interior of the domain significantly.

There are also significant oscillations between adjacent bins in the flux relative error plots, which has a simple explanation. The explicit 3D benchmark calculations are computationally expensive, and the current PlaybookMC implementation requires collision tallies for the scalar flux in these calculations. These tallies have significantly higher relative standard deviations than track length tallies [31], especially in low-flux regions near the transmission boundary. Increasing the number of benchmark particle histories or realizations would reduce the statistical variation, but doing so is computationally prohibitive for the full set of 3D spherical-inclusion cases. Therefore, the overall trends in the flux relative error plots are more meaningful than small local fluctuations.

Table 7.3: Methods comparison for Exp-Constant Radius distributions, volume fraction 0.10.

Case		Quantity	Bench	Backscatter Resample	FLRP	Age Decreasing	LRP
1	a	R	0.3449(7)	0.3555(5)	0.3554(5)	0.3594(5)	0.3604(5)
		T	0.0270(2)	0.0294(2)	0.0293(2)	0.0282(2)	0.0280(2)
	b	R	0.0655(2)	0.0502(2)	0.0502(2)	0.0631(2)	0.0649(2)
		T	0.00476(4)	0.00435(7)	0.00425(7)	0.00528(7)	0.00549(7)
	c	R	0.3738(3)	0.3574(5)	0.3575(5)	0.3745(5)	0.3727(5)
		T	0.0294(1)	0.0306(2)	0.0305(2)	0.0313(2)	0.0310(2)
2	a	R	0.268(1)	0.2793(4)	0.2795(4)	0.2863(5)	0.2882(5)
		T	0.05181(9)	0.0587(2)	0.0592(2)	0.0557(2)	0.0557(2)
	b	R	0.1097(3)	0.0818(3)	0.0817(3)	0.1036(3)	0.1077(3)
		T	0.0305(1)	0.0279(2)	0.0282(2)	0.0331(2)	0.0357(2)
	c	R	0.3399(4)	0.3045(5)	0.3058(5)	0.3402(5)	0.3384(5)
		T	0.0694(2)	0.0704(3)	0.0701(3)	0.0742(3)	0.0745(3)
3	a	R	0.190(1)	0.2084(4)	0.2094(4)	0.2160(4)	0.2186(4)
		T	0.0879(3)	0.0997(3)	0.1000(3)	0.0951(3)	0.0959(3)
	b	R	0.1734(8)	0.1342(3)	0.1347(3)	0.1633(4)	0.1709(4)
		T	0.1054(7)	0.0979(3)	0.0978(3)	0.1110(3)	0.1175(3)
	c	R	0.3329(5)	0.2751(4)	0.2753(4)	0.3288(5)	0.3287(5)
		T	0.1458(5)	0.1370(3)	0.1370(3)	0.1530(4)	0.1554(4)

Table 7.4: Methods comparison for Exp-Uniform Radius distributions, volume fraction 0.10.

Case		Quantity	Bench	Backscatter Resample	FLRP	Age Decreasing	LRP
1	a	R	0.3423(5)	0.3511(5)	0.3517(5)	0.3567(5)	0.3572(5)
		T	0.0276(1)	0.0303(2)	0.0304(2)	0.0285(2)	0.0291(2)
	b	R	0.0669(4)	0.0506(2)	0.0512(2)	0.0639(2)	0.0652(2)
		T	0.00510(8)	0.00453(7)	0.00471(7)	0.00565(7)	0.00603(8)
	c	R	0.3739(4)	0.3556(5)	0.3556(5)	0.3754(5)	0.3708(5)
		T	0.0308(2)	0.0321(2)	0.0324(2)	0.0328(2)	0.0324(2)
2	a	R	0.264(1)	0.2775(4)	0.2777(4)	0.2851(5)	0.2867(5)
		T	0.0526(1)	0.0600(2)	0.0597(2)	0.0565(2)	0.0571(2)
	b	R	0.1093(3)	0.0827(3)	0.0826(3)	0.1042(3)	0.1082(3)
		T	0.0317(1)	0.0286(2)	0.0288(2)	0.0343(2)	0.0371(2)
	c	R	0.3426(2)	0.3053(5)	0.3051(5)	0.3437(5)	0.3401(5)
		T	0.0721(3)	0.0715(3)	0.0714(3)	0.0774(3)	0.0769(3)
3	a	R	0.1875(9)	0.2086(4)	0.2082(4)	0.2157(4)	0.2183(4)
		T	0.0889(3)	0.0996(3)	0.1002(3)	0.0953(3)	0.0957(3)
	b	R	0.176(1)	0.1349(3)	0.1342(3)	0.1646(4)	0.1716(4)
		T	0.1067(5)	0.0979(3)	0.0978(3)	0.1109(3)	0.1180(3)
	c	R	0.3350(8)	0.2751(4)	0.2758(4)	0.3318(5)	0.3309(5)
		T	0.1493(6)	0.1384(3)	0.1375(3)	0.1563(4)	0.1578(4)

Table 7.5: Methods comparison for Exp-Exp Radius distributions, volume fraction 0.10.

Case		Quantity	Bench	Backscatter Resample	FLRP	Age Decreasing	LRP
1	a	R	0.3315(6)	0.3423(5)	0.3419(5)	0.3471(5)	0.3496(5)
		T	0.0304(2)	0.0331(2)	0.0336(2)	0.0320(2)	0.0317(2)
	b	R	0.0699(3)	0.0540(2)	0.0539(2)	0.0653(2)	0.0672(3)
		T	0.0066(1)	0.00593(8)	0.00606(8)	0.00695(8)	0.00757(9)
	c	R	0.3747(4)	0.3500(5)	0.3489(5)	0.3780(5)	0.3709(5)
		T	0.0357(1)	0.0358(2)	0.0360(2)	0.0387(2)	0.0369(2)
2	a	R	0.2561(8)	0.2728(4)	0.2728(4)	0.2785(4)	0.2821(5)
		T	0.0556(3)	0.0624(2)	0.0624(2)	0.0587(2)	0.0590(2)
	b	R	0.1114(7)	0.0848(3)	0.0849(3)	0.1058(3)	0.1096(3)
		T	0.0350(5)	0.0317(2)	0.0315(2)	0.0370(2)	0.0395(2)
	c	R	0.3484(4)	0.3035(5)	0.3030(5)	0.3513(5)	0.3450(5)
		T	0.0810(6)	0.0762(3)	0.0765(3)	0.0859(3)	0.0847(3)
3	a	R	0.196(2)	0.2064(4)	0.2069(4)	0.2122(4)	0.2169(4)
		T	0.0856(5)	0.1012(3)	0.1006(3)	0.0973(3)	0.0969(3)
	b	R	0.166(2)	0.1360(3)	0.1365(3)	0.1650(4)	0.1728(4)
		T	0.096(1)	0.1006(3)	0.0999(3)	0.1133(3)	0.1200(3)
	c	R	0.3397(5)	0.2769(4)	0.2768(4)	0.3400(5)	0.3372(5)
		T	0.144(1)	0.1407(3)	0.1408(3)	0.1620(4)	0.1632(4)

Table 7.6: Methods comparison for Exp-Constant Radius distributions, volume fraction 0.20.

Case		Quantity	Bench	Backscatter Resample	FLRP	Age Decreasing	LRP
1	a	R	0.4991(6)	0.5111(5)	0.5131(5)	0.5157(5)	0.5177(5)
		T	0.00614(7)	0.00715(8)	0.00700(8)	0.00656(8)	0.00651(8)
	b	R	0.0362(3)	0.0225(1)	0.0228(1)	0.0284(2)	0.0290(2)
		T	0.00021(1)	0.000034(6)	0.000029(5)	0.000048(7)	0.000048(7)
	c	R	0.3829(3)	0.3689(5)	0.3692(5)	0.3838(5)	0.3809(5)
		T	0.00148(2)	0.00132(4)	0.00132(4)	0.00142(4)	0.00134(4)
2	a	R	0.4211(3)	0.4421(5)	0.4426(5)	0.4476(5)	0.4509(5)
		T	0.0161(1)	0.0196(1)	0.0196(1)	0.0181(1)	0.0180(1)
	b	R	0.0633(6)	0.0375(2)	0.0374(2)	0.0488(2)	0.0499(2)
		T	0.00266(6)	0.00141(4)	0.00144(4)	0.00184(4)	0.00203(5)
	c	R	0.3453(5)	0.3139(5)	0.3135(5)	0.3442(5)	0.3402(5)
		T	0.0086(1)	0.00769(9)	0.00767(9)	0.00875(9)	0.00867(9)
3	a	R	0.333(1)	0.3644(5)	0.3633(5)	0.3707(5)	0.3762(5)
		T	0.0376(2)	0.0471(2)	0.0472(2)	0.0433(2)	0.0435(2)
	b	R	0.1078(8)	0.0653(2)	0.0651(2)	0.0840(3)	0.0866(3)
		T	0.0220(1)	0.0168(1)	0.0169(1)	0.0206(1)	0.0224(1)
	c	R	0.3311(3)	0.2719(4)	0.2721(4)	0.3262(5)	0.3234(5)
		T	0.0385(3)	0.0333(2)	0.0335(2)	0.0413(2)	0.0419(2)

Table 7.7: Methods comparison for Exp-Uniform Radius distributions, volume fraction 0.20.

Case		Quantity	Bench	Backscatter Resample	FLRP	Age Decreasing	LRP
1	a	R	0.4957(7)	0.5098(5)	0.5097(5)	0.5127(5)	0.5142(5)
		T	0.00648(8)	0.00740(9)	0.00736(9)	0.00669(8)	0.00675(8)
	b	R	0.0369(2)	0.0230(1)	0.0230(1)	0.0287(2)	0.0292(2)
		T	0.000222(9)	0.000040(6)	0.000044(7)	0.000050(7)	0.000063(8)
	c	R	0.3827(2)	0.3659(5)	0.3661(5)	0.3835(5)	0.3783(5)
		T	0.00168(5)	0.00145(4)	0.00152(4)	0.00158(4)	0.00148(4)
2	a	R	0.4177(9)	0.4409(5)	0.4392(5)	0.4450(5)	0.4492(5)
		T	0.0165(1)	0.0200(1)	0.0202(1)	0.0186(1)	0.0185(1)
	b	R	0.0637(5)	0.0377(2)	0.0377(2)	0.0492(2)	0.0504(2)
		T	0.00255(4)	0.00146(4)	0.00153(4)	0.00197(4)	0.00222(5)
	c	R	0.3468(3)	0.3124(5)	0.3121(5)	0.3476(5)	0.3416(5)
		T	0.00901(4)	0.00811(9)	0.00820(9)	0.0095(1)	0.0093(1)
3	a	R	0.3280(7)	0.3634(5)	0.3643(5)	0.3694(5)	0.3756(5)
		T	0.0390(2)	0.0470(2)	0.0471(2)	0.0439(2)	0.0434(2)
	b	R	0.1084(6)	0.0647(2)	0.0649(2)	0.0836(3)	0.0872(3)
		T	0.0224(3)	0.0171(1)	0.0174(1)	0.0208(1)	0.0228(1)
	c	R	0.3342(4)	0.2717(4)	0.2712(4)	0.3293(5)	0.3257(5)
		T	0.0411(1)	0.0340(2)	0.0340(2)	0.0427(2)	0.0428(2)

Table 7.8: Methods comparison for Exp-Exp Radius distributions, volume fraction 0.20.

Case		Quantity	Bench	Backscatter Resample	FLRP	Age Decreasing	LRP
1	a	R	0.4838(4)	0.5019(5)	0.5014(5)	0.5046(5)	0.5071(5)
		T	0.00725(9)	0.00851(9)	0.00846(9)	0.00783(9)	0.00771(9)
	b	R	0.0385(2)	0.0242(2)	0.0242(2)	0.0301(2)	0.0302(2)
		T	0.00023(2)	0.000067(8)	0.000056(7)	0.000079(9)	0.000089(9)
	c	R	0.3832(4)	0.3614(5)	0.3605(5)	0.3855(5)	0.3783(5)
		T	0.00220(6)	0.00189(4)	0.00186(4)	0.00222(5)	0.00198(4)
2	a	R	0.408(1)	0.4355(5)	0.4344(5)	0.4391(5)	0.4439(5)
		T	0.0177(1)	0.0213(1)	0.0217(1)	0.0195(1)	0.0197(1)
	b	R	0.06456(9)	0.0392(2)	0.0392(2)	0.0500(2)	0.0510(2)
		T	0.00291(7)	0.00174(4)	0.00177(4)	0.00241(5)	0.00247(5)
	c	R	0.3532(7)	0.3115(5)	0.3099(5)	0.3554(5)	0.3453(5)
		T	0.0113(2)	0.0092(1)	0.0093(1)	0.0118(1)	0.0112(1)
3	a	R	0.332(1)	0.3616(5)	0.3626(5)	0.3669(5)	0.3741(5)
		T	0.0365(2)	0.0482(2)	0.0477(2)	0.0445(2)	0.0442(2)
	b	R	0.1015(3)	0.0655(2)	0.0660(2)	0.0840(3)	0.0879(3)
		T	0.0187(3)	0.0179(1)	0.0179(1)	0.0214(1)	0.0235(2)
	c	R	0.3394(7)	0.2717(4)	0.2718(4)	0.3383(5)	0.3314(5)
		T	0.0373(3)	0.0352(2)	0.0353(2)	0.0470(2)	0.0465(2)

Table 7.9: Methods comparison for Exp-Constant Radius distributions, volume fraction 0.30.

Case		Quantity	Bench	Backscatter Resample	FLRP	Age Decreasing	LRP
1	a	R	0.6029(7)	0.6155(5)	0.6164(5)	0.6168(5)	0.6191(5)
		T	0.00195(5)	0.00230(5)	0.00218(5)	0.00207(5)	0.00212(5)
	b	R	0.0238(1)	0.0130(1)	0.0129(1)	0.0158(1)	0.0160(1)
		T	0.000052(4)	0.0000(0)	0.0000(0)	0.0000(0)	0.0000(0)
	c	R	0.3983(5)	0.3863(5)	0.3873(5)	0.3982(5)	0.3958(5)
		T	0.000134(5)	0.000030(5)	0.000030(5)	0.000036(6)	0.000041(6)
2	a	R	0.5372(6)	0.5572(5)	0.5580(5)	0.5619(5)	0.5656(5)
		T	0.0057(1)	0.00725(8)	0.00715(8)	0.00644(8)	0.00643(8)
	b	R	0.0427(2)	0.0212(1)	0.0211(1)	0.0274(2)	0.0276(2)
		T	0.000437(8)	0.000028(5)	0.000040(6)	0.000080(9)	0.000087(9)
	c	R	0.3609(6)	0.3352(5)	0.3354(5)	0.3614(5)	0.3571(5)
		T	0.00114(3)	0.00054(2)	0.00051(2)	0.00068(3)	0.00065(3)
3	a	R	N/A	0.4878(5)	0.4882(5)	0.4934(5)	0.4994(5)
		T	N/A	0.0219(1)	0.0218(1)	0.0194(1)	0.0196(1)
	b	R	N/A	0.0363(2)	0.0363(2)	0.0478(2)	0.0494(2)
		T	N/A	0.00215(5)	0.00222(5)	0.00288(5)	0.00331(6)
	c	R	N/A	0.2918(5)	0.2913(5)	0.3377(5)	0.3346(5)
		T	N/A	0.00599(8)	0.00602(8)	0.00849(9)	0.00857(9)

Table 7.10: Methods comparison for Exp-Uniform Radius distributions, volume fraction 0.30.

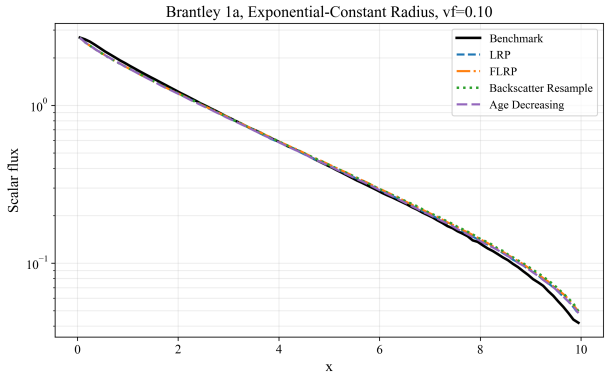
Case		Quantity	Bench	Backscatter Resample	FLRP	Age Decreasing	LRP
1	a	R	0.5982(2)	0.6142(5)	0.6133(5)	0.6141(5)	0.6179(5)
		T	0.00213(6)	0.00229(5)	0.00233(5)	0.00203(4)	0.00217(5)
	b	R	0.0244(2)	0.0131(1)	0.0131(1)	0.0161(1)	0.0161(1)
		T	0.000056(9)	0.0000(0)	0.0000(0)	0.0000(0)	0.000001(1)
	c	R	0.3982(3)	0.3842(5)	0.3854(5)	0.3989(5)	0.3941(5)
		T	0.000151(9)	0.000043(7)	0.000048(7)	0.000053(7)	0.000057(8)
2	a	R	0.5307(7)	0.5565(5)	0.5557(5)	0.5594(5)	0.5646(5)
		T	0.00605(5)	0.00740(9)	0.00768(9)	0.00649(8)	0.00651(8)
	b	R	0.0428(3)	0.0210(1)	0.0211(1)	0.0272(2)	0.0279(2)
		T	0.00046(2)	0.000033(6)	0.000050(7)	0.000071(8)	0.00009(1)
	c	R	0.3625(2)	0.3348(5)	0.3345(5)	0.3645(5)	0.3573(5)
		T	0.00126(5)	0.00062(2)	0.00059(2)	0.00079(3)	0.00070(3)
3	a	R	0.4431(5)	0.4871(5)	0.4883(5)	0.4915(5)	0.4994(5)
		T	0.0177(2)	0.0223(1)	0.0217(1)	0.0193(1)	0.0200(1)
	b	R	0.0748(5)	0.0367(2)	0.0366(2)	0.0481(2)	0.0493(2)
		T	0.00499(4)	0.00224(5)	0.00222(5)	0.00286(5)	0.00346(6)
	c	R	0.3428(6)	0.2915(5)	0.2911(5)	0.3413(5)	0.3361(5)
		T	0.0100(1)	0.00619(8)	0.00617(8)	0.00887(9)	0.00900(9)

Table 7.11: Methods comparison for Exp-Exp Radius distributions, volume fraction 0.30.

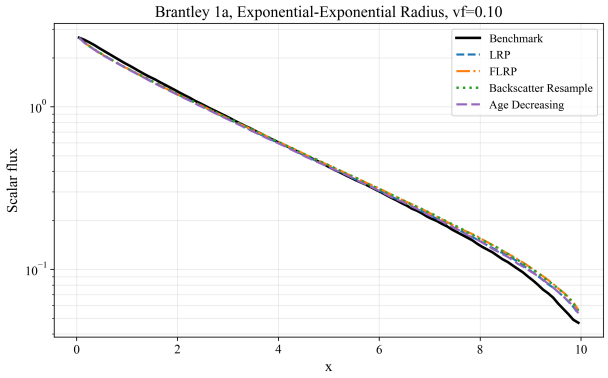
Case		Quantity	Bench	Backscatter Resample	FLRP	Age Decreasing	LRP
1	a	R	0.5877(4)	0.6069(5)	0.6068(5)	0.6069(5)	0.6120(5)
		T	0.00231(4)	0.00269(5)	0.00264(5)	0.00245(5)	0.00245(5)
	b	R	0.0252(1)	0.0136(1)	0.0136(1)	0.0164(1)	0.0167(1)
		T	0.000052(6)	0.0000(0)	0.0000(0)	0.0000(0)	0.000001(1)
	c	R	0.3980(7)	0.3812(5)	0.3799(5)	0.4011(5)	0.3935(5)
		T	0.00014(1)	0.000050(7)	0.000049(7)	0.000070(8)	0.000054(7)
2	a	R	0.5210(8)	0.5523(5)	0.5525(5)	0.5539(5)	0.5604(5)
		T	0.00644(9)	0.00802(9)	0.00811(9)	0.00695(8)	0.00712(8)
	b	R	0.0432(3)	0.0219(1)	0.0218(1)	0.0280(2)	0.0283(2)
		T	0.00046(3)	0.000063(8)	0.000065(8)	0.000089(9)	0.00011(1)
	c	R	0.3677(5)	0.3322(5)	0.3329(5)	0.3709(5)	0.3624(5)
		T	0.00151(3)	0.00065(3)	0.00070(3)	0.00107(3)	0.00093(3)
3	a	R	0.448(1)	0.4862(5)	0.4866(5)	0.4879(5)	0.4975(5)
		T	0.0160(2)	0.0225(1)	0.0227(1)	0.0201(1)	0.0201(1)
	b	R	0.0693(3)	0.0364(2)	0.0371(2)	0.0481(2)	0.0496(2)
		T	0.00371(7)	0.00245(5)	0.00242(5)	0.00310(6)	0.00346(6)
	c	R	0.3483(4)	0.2922(5)	0.2916(5)	0.3494(5)	0.3422(5)
		T	0.00861(3)	0.00665(8)	0.00655(8)	0.0104(1)	0.0101(1)

Table 7.12: Leakage RMSE comparison by volume fraction.

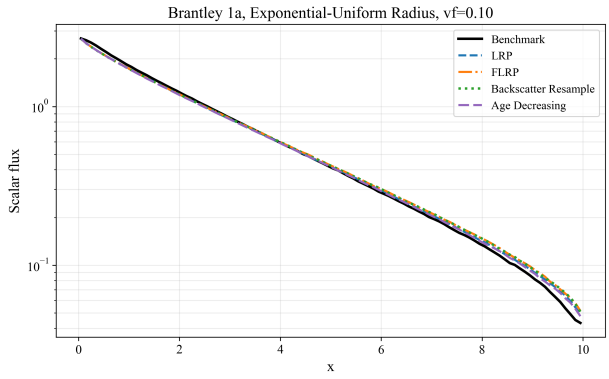
Volume Fraction	Distribution	Qty	Backscatter Resample	FLRP	Age Decreasing	LRP
0.10	Exp-Const Rad	R	0.0298	0.0296	0.0124	0.0129
		T	0.0061	0.0062	0.0046	0.0064
	Exp-Unif Rad	R	0.0311	0.0311	0.0134	0.0139
		T	0.0065	0.0068	0.0043	0.0060
	Exp-Exp Rad	R	0.0315	0.0317	0.0110	0.0131
		T	0.0064	0.0062	0.0094	0.0111
0.20	Exp-Const Rad	R	0.0314	0.0315	0.0190	0.0207
		T	0.0042	0.0042	0.0023	0.0024
	Exp-Unif Rad	R	0.0336	0.0336	0.0202	0.0221
		T	0.0042	0.0042	0.0019	0.0017
	Exp-Exp Rad	R	0.0348	0.0349	0.0189	0.0215
		T	0.0043	0.0041	0.0043	0.0044
0.30	Exp-Const Rad	R	0.0180	0.0181	0.0136	0.0152
		T	0.0007	0.0007	0.0004	0.0004
	Exp-Unif Rad	R	0.0308	0.0309	0.0223	0.0253
		T	0.0023	0.0022	0.0010	0.0010
	Exp-Exp Rad	R	0.0318	0.0320	0.0205	0.0243
		T	0.0024	0.0025	0.0015	0.0015



(a) Constant radius

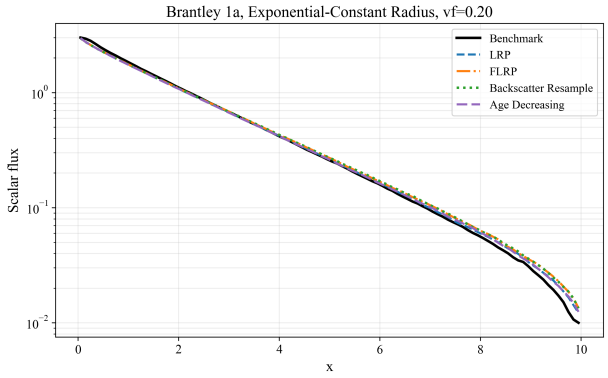


(b) Exponential radius

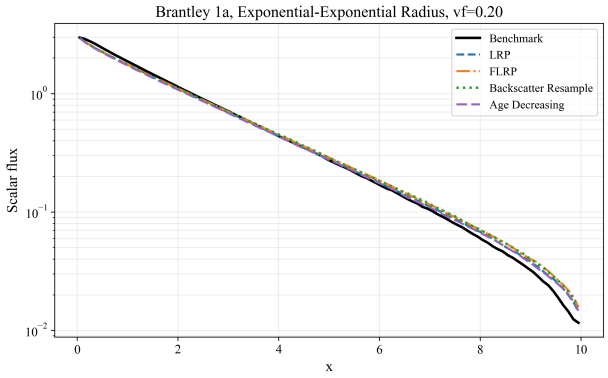


(c) Uniform radius

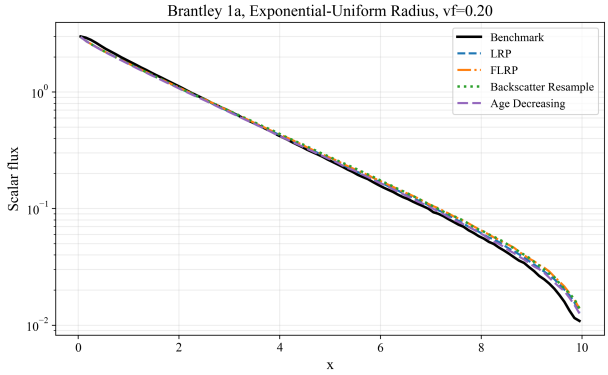
Figure 7.2: Scalar flux distributions for Case 1a with sphere volume fraction $p_1 = 0.10$, comparing constant, exponential, and uniform spherical inclusion radius distributions.



(a) Constant radius

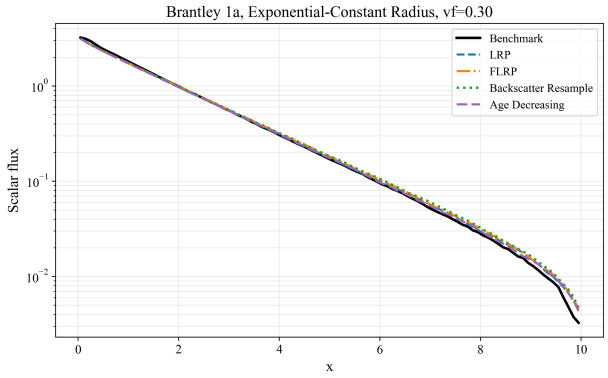


(b) Exponential radius

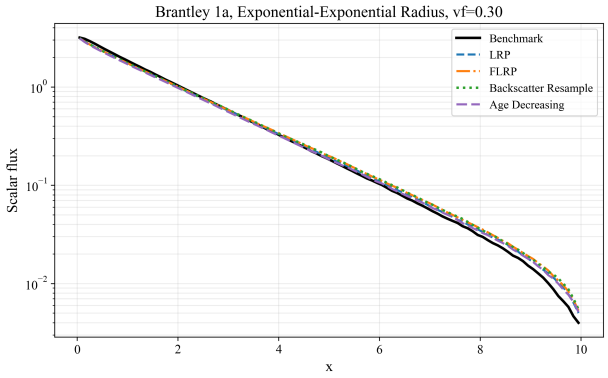


(c) Uniform radius

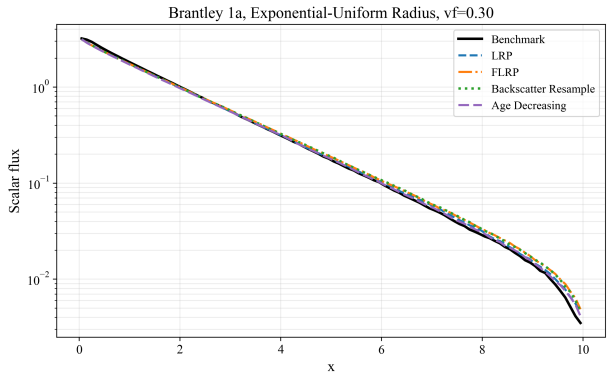
Figure 7.3: Scalar flux distributions for Case 1a with sphere volume fraction $p_1 = 0.20$, comparing constant, exponential, and uniform spherical inclusion radius distributions.



(a) Constant radius

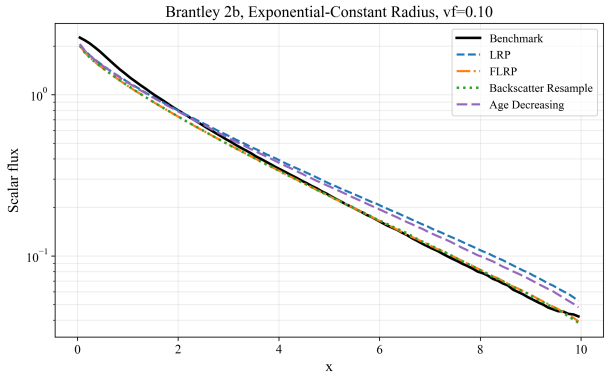


(b) Exponential radius

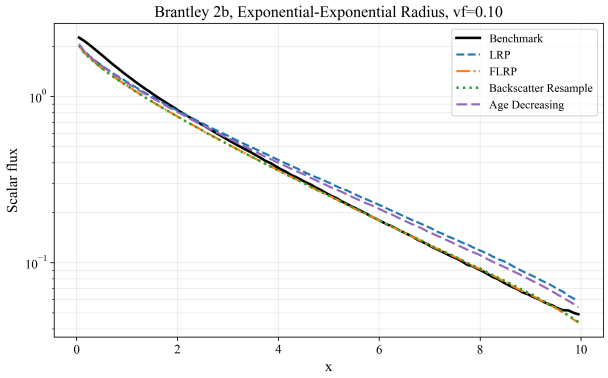


(c) Uniform radius

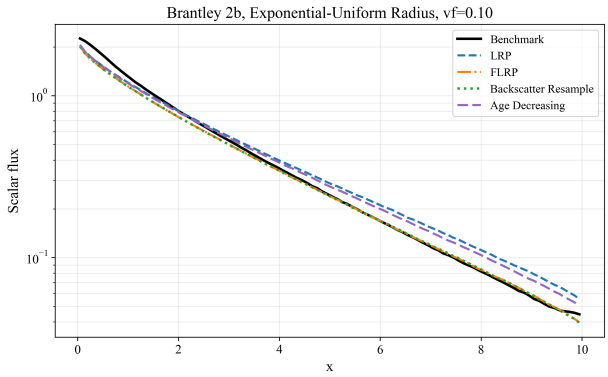
Figure 7.4: Scalar flux distributions for Case 1a with sphere volume fraction $p_1 = 0.30$, comparing constant, exponential, and uniform spherical inclusion radius distributions.



(a) Constant radius

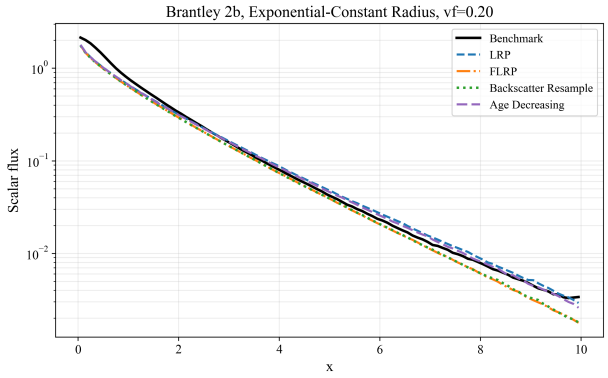


(b) Exponential radius

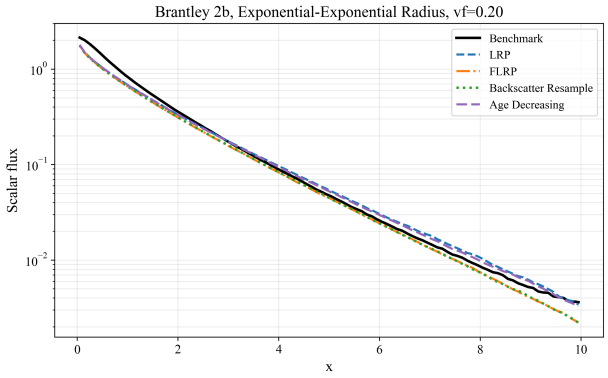


(c) Uniform radius

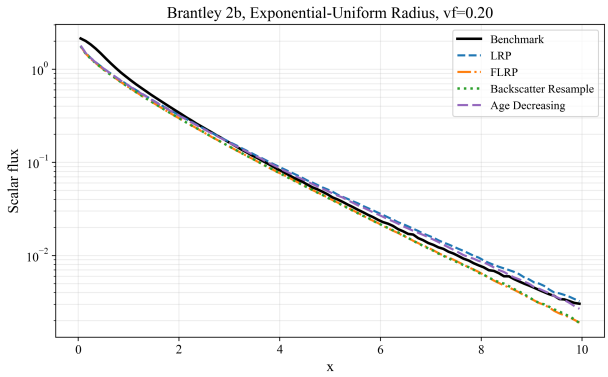
Figure 7.5: Scalar flux distributions for Case 2b with sphere volume fraction $p_1 = 0.10$, comparing constant, exponential, and uniform spherical inclusion radius distributions.



(a) Constant radius

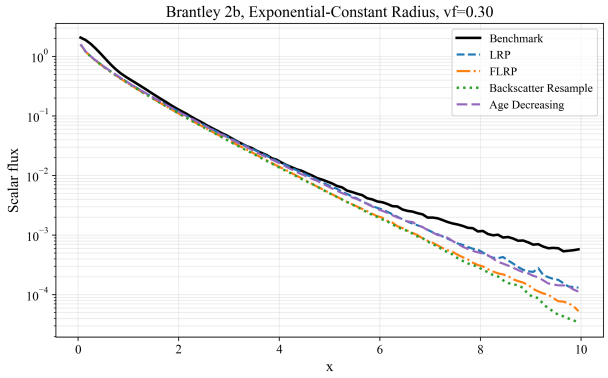


(b) Exponential radius

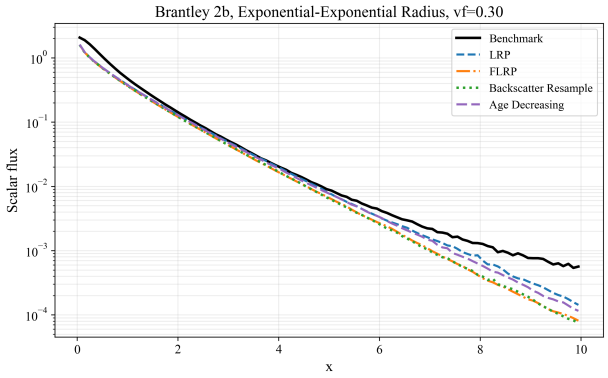


(c) Uniform radius

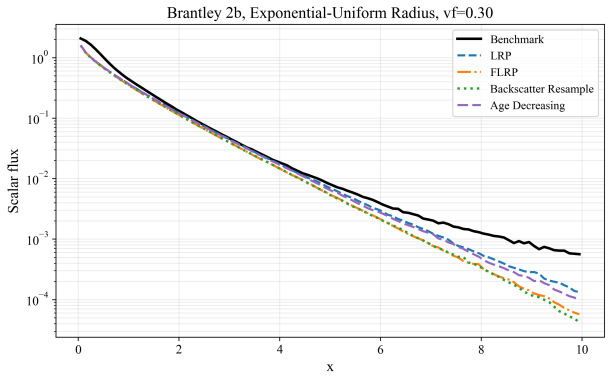
Figure 7.6: Scalar flux distributions for Case 2b with sphere volume fraction $p_1 = 0.20$, comparing constant, exponential, and uniform spherical inclusion radius distributions.



(a) Constant radius

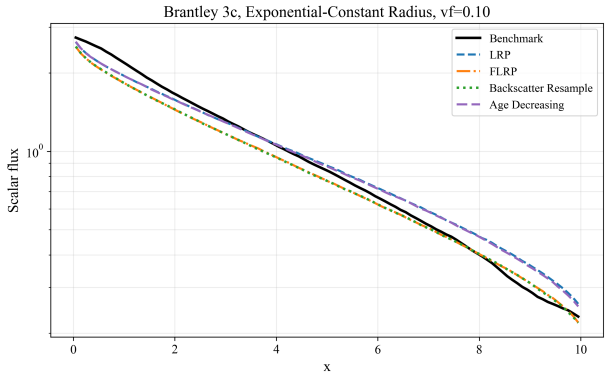


(b) Exponential radius

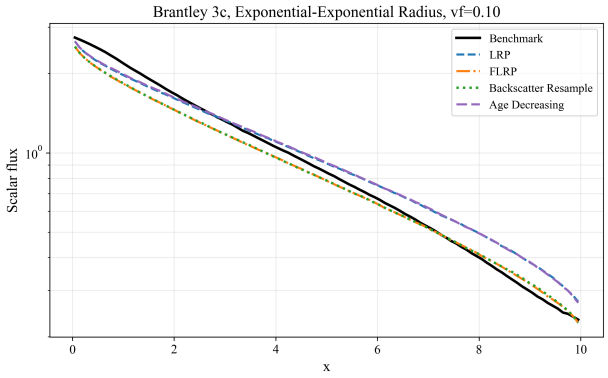


(c) Uniform radius

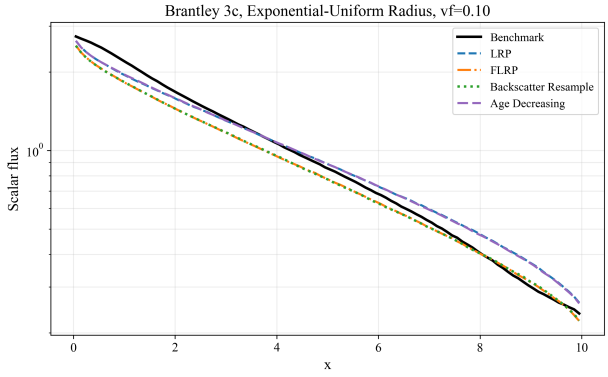
Figure 7.7: Scalar flux distributions for Case 2b with sphere volume fraction $p_1 = 0.30$, comparing constant, exponential, and uniform spherical inclusion radius distributions.



(a) Constant radius

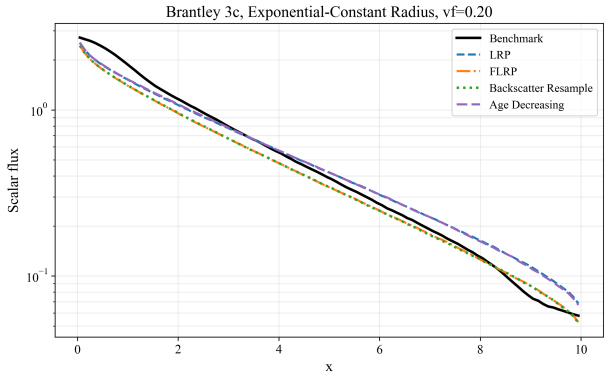


(b) Exponential radius

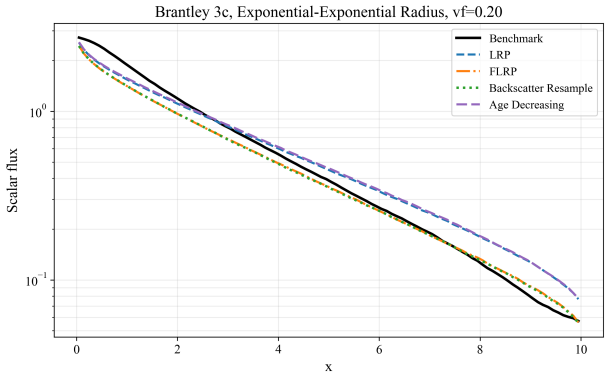


(c) Uniform radius

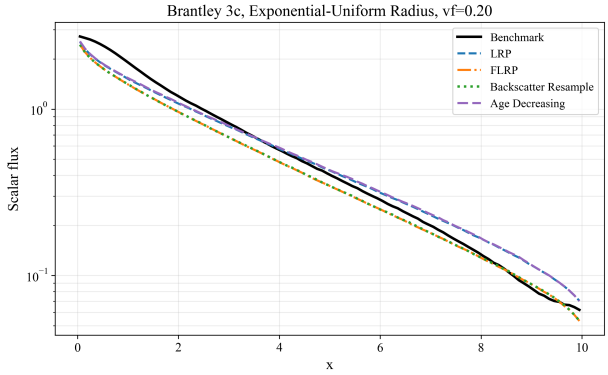
Figure 7.8: Scalar flux distributions for Case 3c with sphere volume fraction $p_1 = 0.10$, comparing constant, exponential, and uniform spherical inclusion radius distributions.



(a) Constant radius

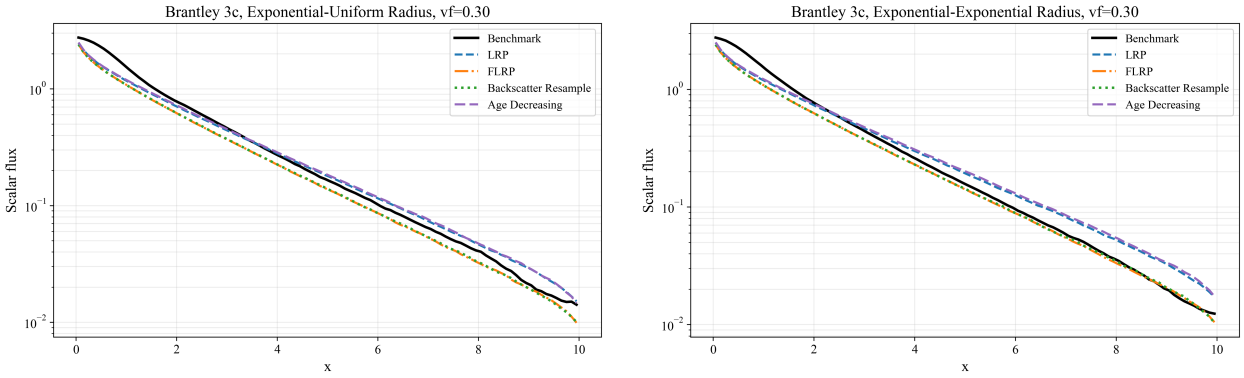


(b) Exponential radius



(c) Uniform radius

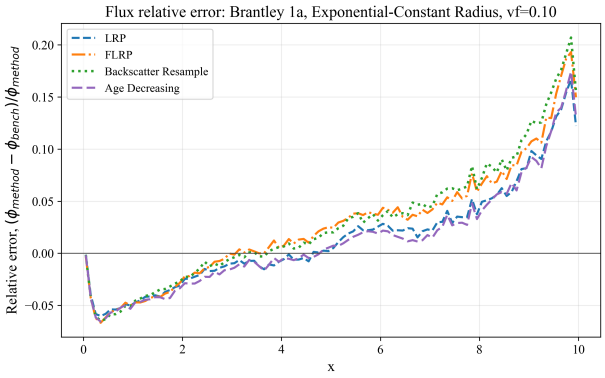
Figure 7.9: Scalar flux distributions for Case 3c with sphere volume fraction $p_1 = 0.20$, comparing constant, exponential, and uniform spherical inclusion radius distributions.



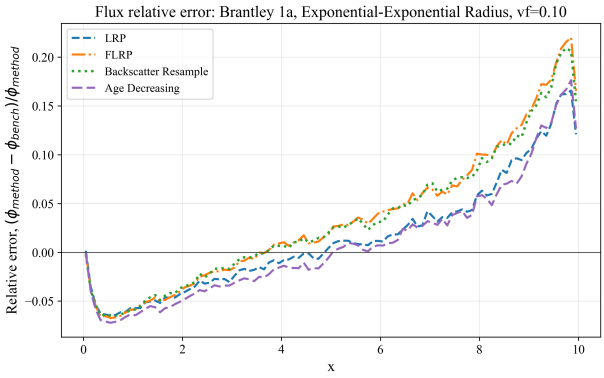
(a) Uniform radius

(b) Exponential radius

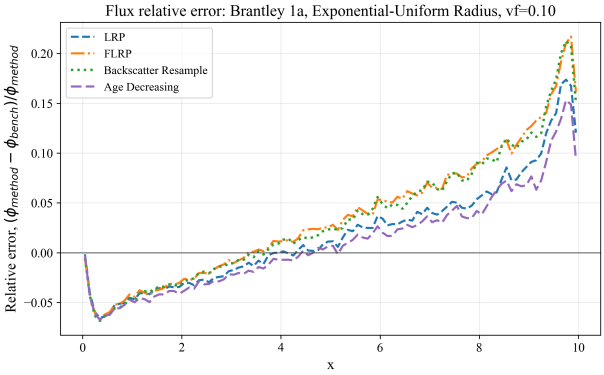
Figure 7.10: Scalar flux distributions for Case 3c with sphere volume fraction $p_1 = 0.30$, comparing exponential and uniform spherical inclusion radius distributions. Constant radius not included, see Section 7.2.



(a) Constant radius

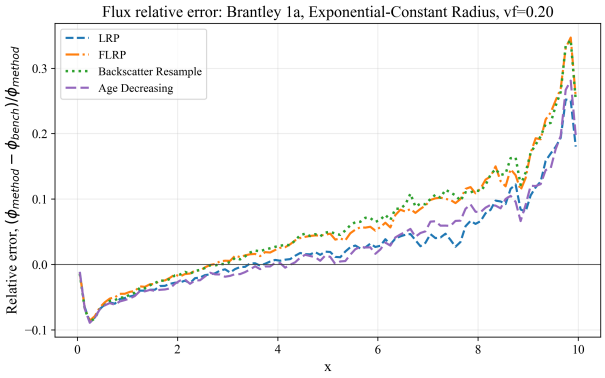


(b) Exponential radius

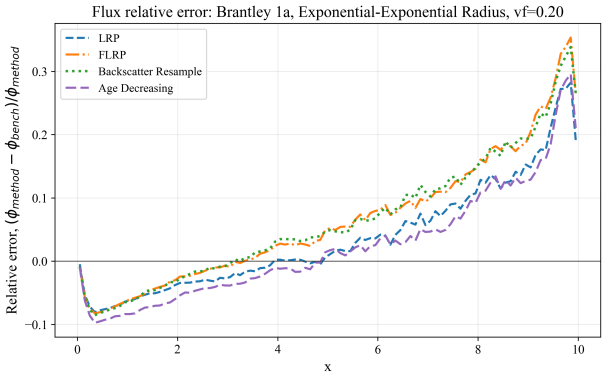


(c) Uniform radius

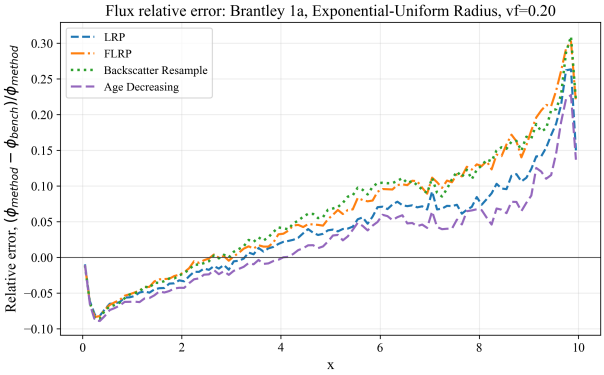
Figure 7.11: Relative scalar flux error for Case 1a with sphere volume fraction $p_1 = 0.10$, comparing constant, exponential, and uniform spherical inclusion radius distributions.



(a) Constant radius

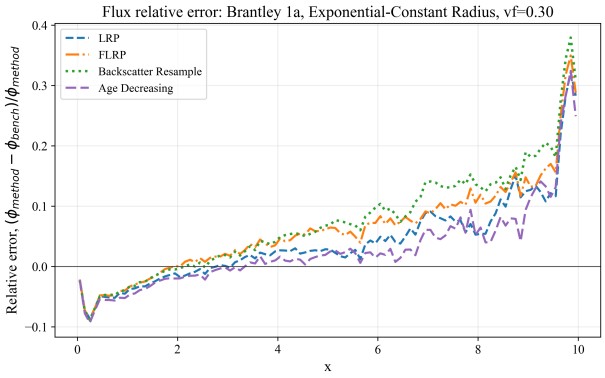


(b) Exponential radius

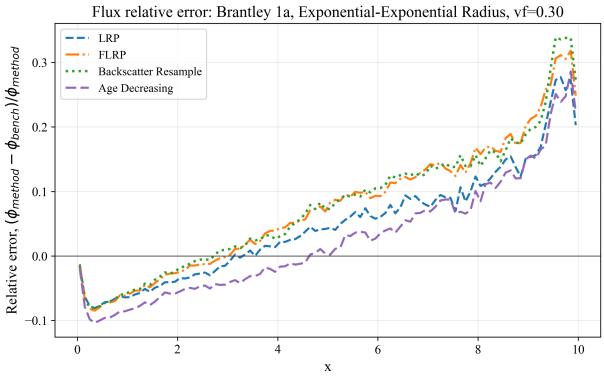


(c) Uniform radius

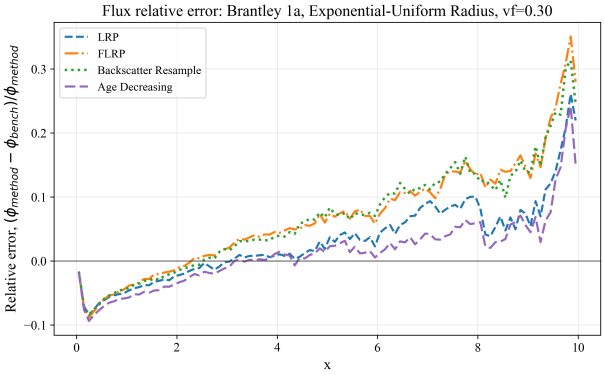
Figure 7.12: Relative scalar flux error for Case 1a with sphere volume fraction $p_1 = 0.20$, comparing constant, exponential, and uniform spherical inclusion radius distributions.



(a) Constant radius

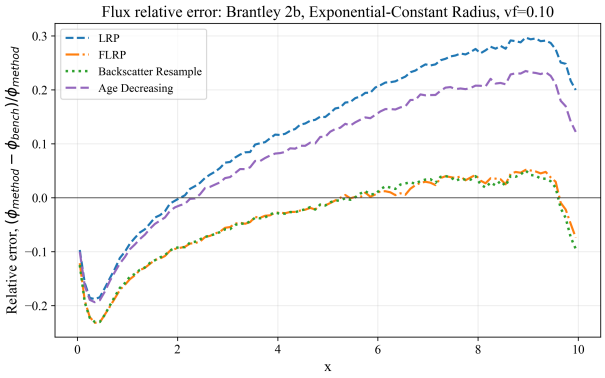


(b) Exponential radius

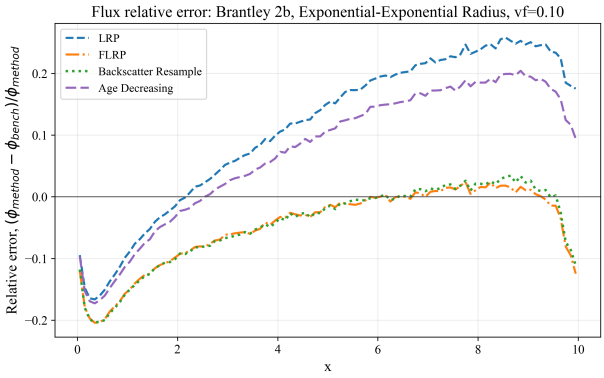


(c) Uniform radius

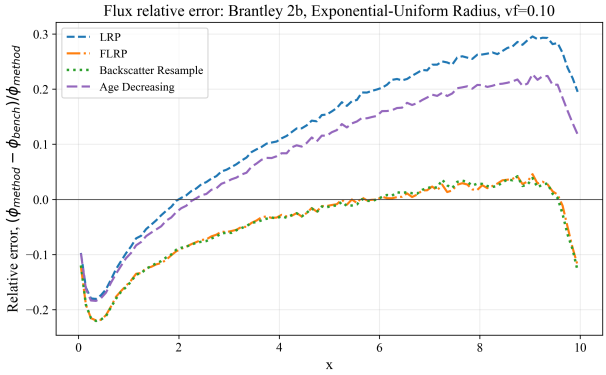
Figure 7.13: Relative scalar flux error for Case 1a with sphere volume fraction $p_1 = 0.30$, comparing constant, exponential, and uniform spherical inclusion radius distributions.



(a) Constant radius

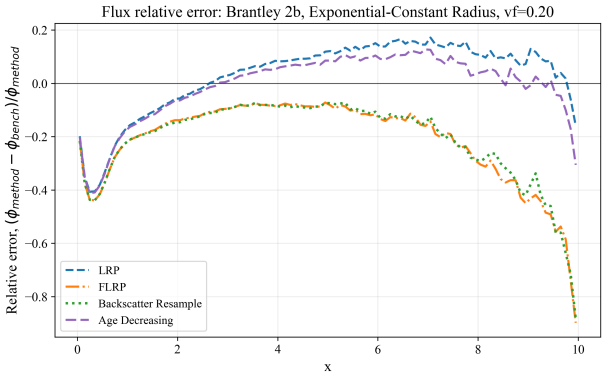


(b) Exponential radius

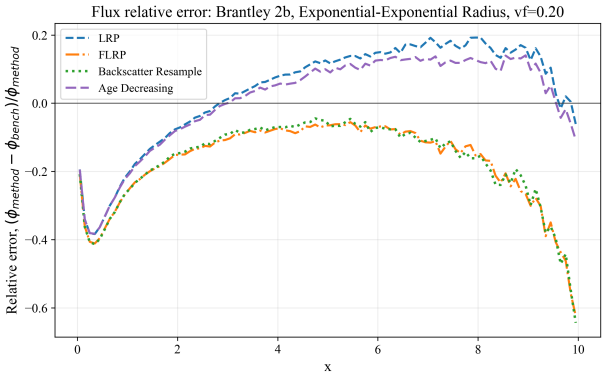


(c) Uniform radius

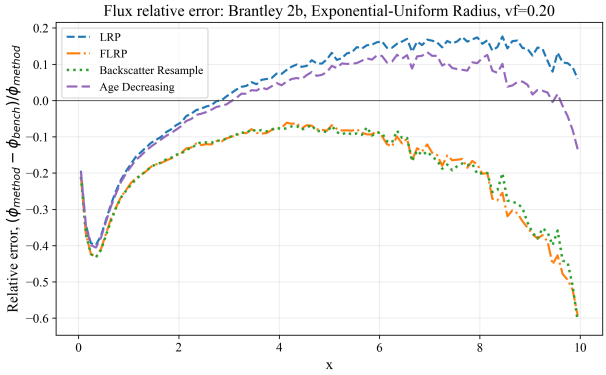
Figure 7.14: Relative scalar flux error for Case 2b with sphere volume fraction $p_1 = 0.10$, comparing constant, exponential, and uniform spherical inclusion radius distributions.



(a) Constant radius

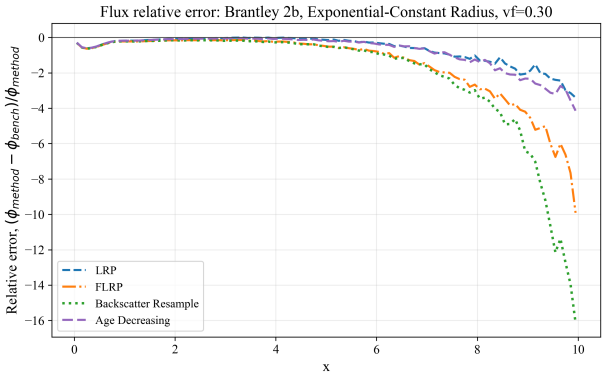


(b) Exponential radius

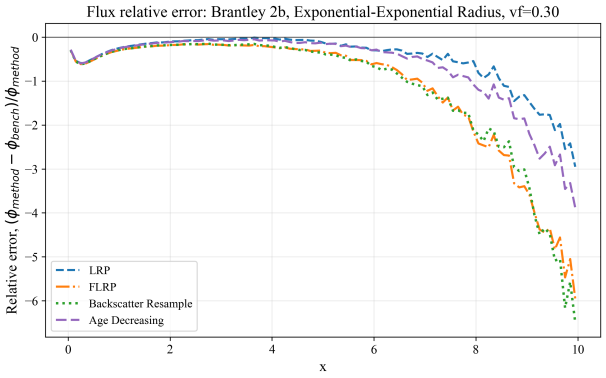


(c) Uniform radius

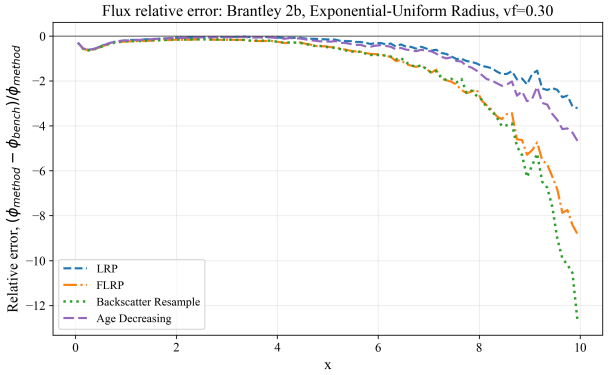
Figure 7.15: Relative scalar flux error for Case 2b with sphere volume fraction $p_1 = 0.20$, comparing constant, exponential, and uniform spherical inclusion radius distributions.



(a) Constant radius

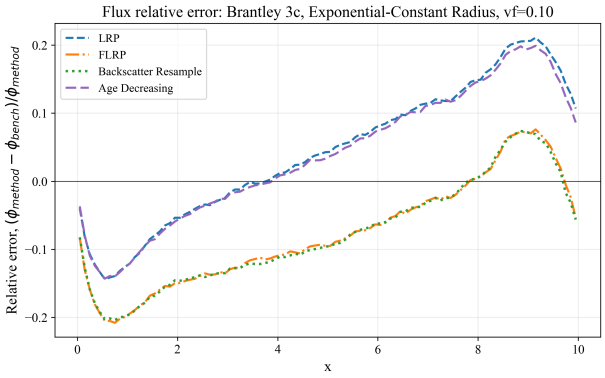


(b) Exponential radius

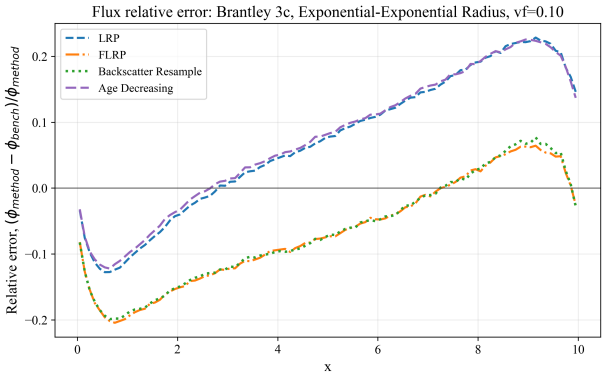


(c) Uniform radius

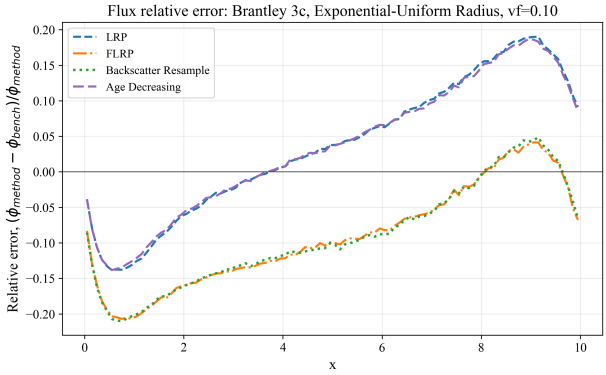
Figure 7.16: Relative scalar flux error for Case 2b with sphere volume fraction $p_1 = 0.30$, comparing constant, exponential, and uniform spherical inclusion radius distributions.



(a) Constant radius

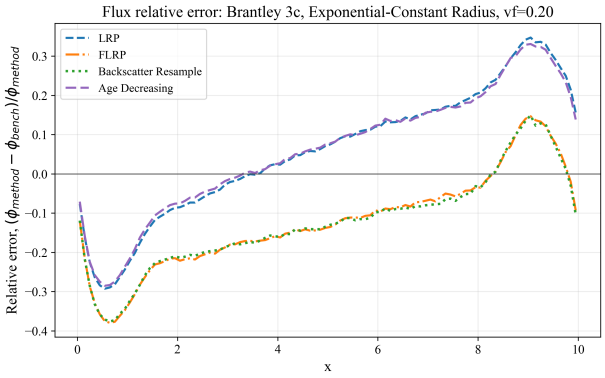


(b) Exponential radius

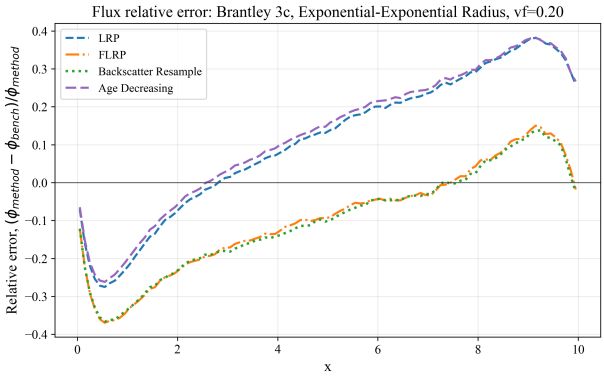


(c) Uniform radius

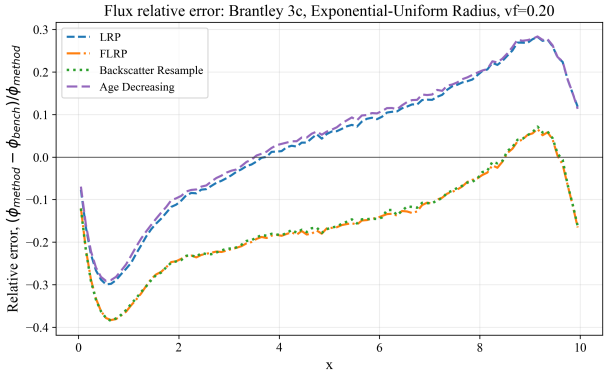
Figure 7.17: Relative scalar flux error for Case 3c with sphere volume fraction $p_1 = 0.10$, comparing constant, exponential, and uniform spherical inclusion radius distributions.



(a) Constant radius

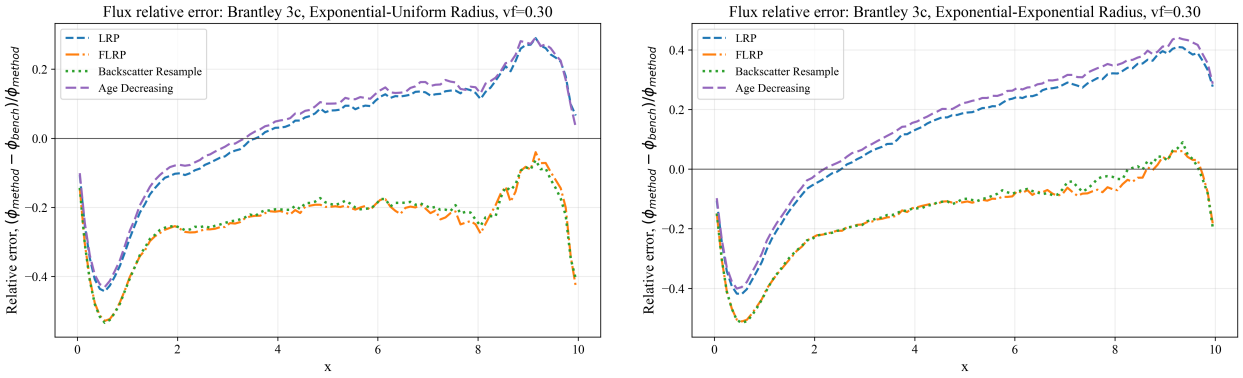


(b) Exponential radius



(c) Uniform radius

Figure 7.18: Relative scalar flux error for Case 3c with sphere volume fraction $p_1 = 0.20$, comparing constant, exponential, and uniform spherical inclusion radius distributions.



(a) Uniform radius

(b) Exponential radius

Figure 7.19: Relative scalar flux error for Case 3c with sphere volume fraction $p_1 = 0.30$, comparing exponential and uniform spherical inclusion radius distributions. Constant radius not included, see Section 7.2.

Effect of Sphere Radius Distribution on Scalar Flux in 3D Geometries

Similar to Section 6.3, it is useful to investigate the effect of the radius distribution itself on the benchmark scalar flux in a more realistic 3D setting. The constant radius case (or equivalently ramp chord length distribution) is used as the reference distribution, and the pointwise signed relative difference is computed with Eq. (6.16). Case 3 at $p_1 = 0.30$ is omitted from this comparison again as discussed in Section 7.2.

Figures 7.20 through 7.23 show representative radius-distribution comparisons. The most consistent trend is that the exponentially distributed radius model produces a larger deviation from the constant radius benchmark than the uniformly distributed radius model, as was shown in Section 6.3. This is expected because the exponential radius distribution permits a broader range of inclusion sizes, including relatively large spheres that generate longer inclusion chords. The uniform radius distribution is more tightly constrained and therefore remains closer to the constant radius case.

The effect of radius distribution generally grows with distance into the slab as the influence of the inclusion size statistics accumulates along particle paths. The relative difference peaks somewhere near the transmission boundary for all cases. These relative discrepancies also grow significantly as the flux values become very small.

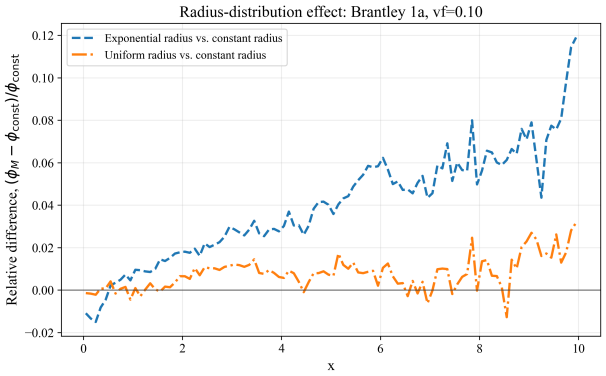
Increasing the sphere volume fraction changes both the amount of inclusion material and the background mean chord length through Eq. (7.4). Thus, increasing p_1 also shortens the background chord length and changes the spatial packing of inclusions. In most cases, the radius distribution effect becomes more noticeable as the volume fraction increases from $p_1 = 0.10$ to $p_1 = 0.30$, although the trend is subject to small bin-to-bin fluctuations because of Monte Carlo noise and the small transmitted flux.

The material properties strongly affect whether the sphere radius distribution is visible in the scalar flux, but the trend differs from the 1D renewal comparisons in Chapter 6. In the 1D calculations, increasing scattering generally reduced the sensitivity to the mixing statistics. In the 3D spherical inclusion benchmarks, however, changing the radius distribution modifies more than just the chord length distribution. It also changes the number of spheres, their sizes, and the packing structure. As a result, highly scattering cases can remain sensitive to the radius distribution because particles spend more time in the geometry and sample those differences in the inclusion structure. This helps explain why the radius distribution effect is relatively weak in case a, where the absorbing background removes many particles before they sample much of the inclusion geometry, but remains noticeable in cases b and c. In case b, the sizes of the optically thick absorbing inclusions directly affect the surviving particle population, while in case c the particles spend more time in the geometry, allowing the differences in structure between geometries with varying inclusion radii to influence the cumulative scalar flux.

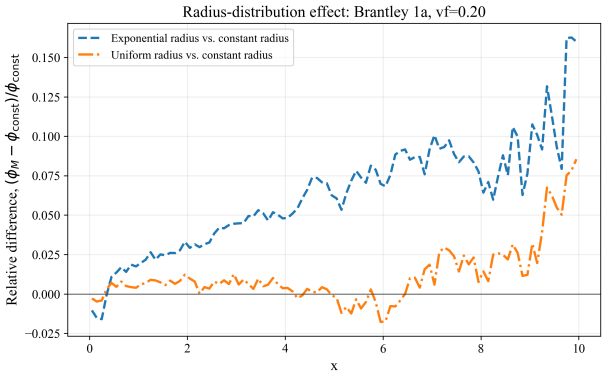
Overall, these comparisons show that the sphere radius distribution can have a measurable effect on the ensemble-averaged scalar flux, even when the material cross sections, volume fraction, and mean inclusion chord length are fixed. The effect is strongest for the

exponential radius distribution and for material cases in which particles survive long enough to sample a substantial portion of the stochastic geometry.

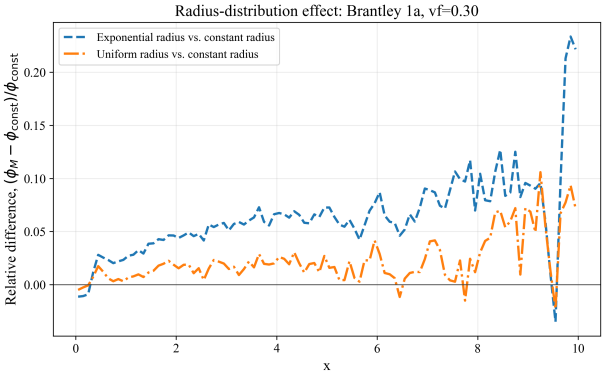
One additional source of potential discrepancy is the treatment of the background material. The methods used here approximate the background chord length distribution as exponential, using the infinite medium mean chord length relation [5]. This approximation is expected to be reasonable at low sphere volume fractions, but becomes less reasonable as the sphere volume fraction increases and is not exact for explicit non-overlapping sphere packing. The work in this dissertation does not investigate this effect because there is no defined analytical background chord length distribution, but in future work, one could use empirically measured background chord length distributions for each case of material properties and use those distributions directly in the renewal statistical methods.



(a) $p_1 = 0.10$

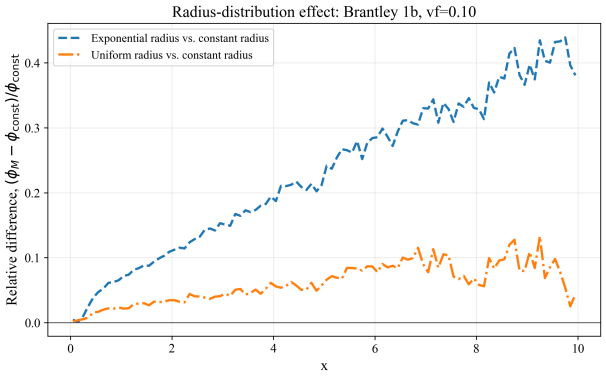


(b) $p_1 = 0.20$

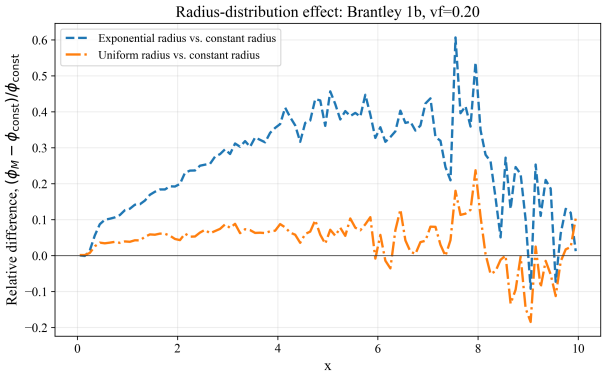


(c) $p_1 = 0.30$

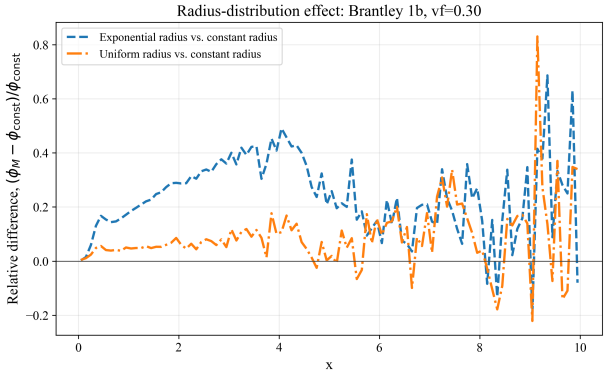
Figure 7.20: Effect of spherical inclusion radius distribution on the benchmark scalar flux for Case 1a. The signed relative difference is computed relative to the constant radius benchmark.



(a) $p_1 = 0.10$

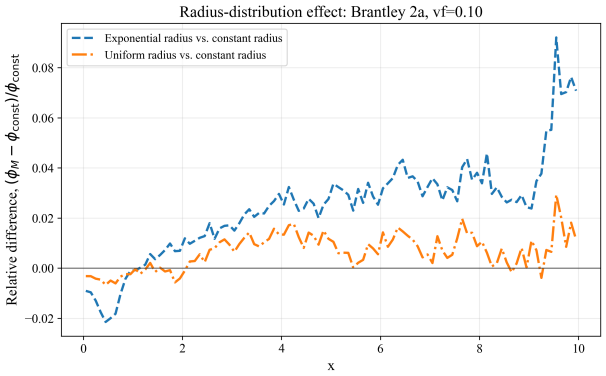


(b) $p_1 = 0.20$

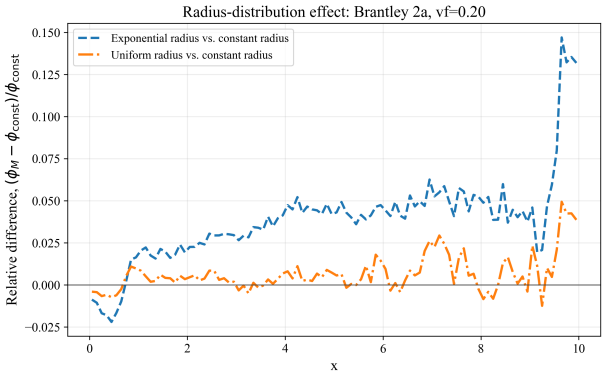


(c) $p_1 = 0.30$

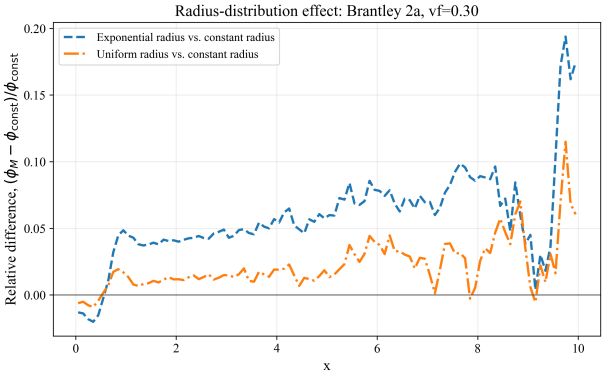
Figure 7.21: Effect of spherical inclusion radius distribution on the benchmark scalar flux for Case 1b. The sensitivity is larger than in Case 1a because the optically thick inclusion material is absorbing while the background material is scattering.



(a) $p_1 = 0.10$

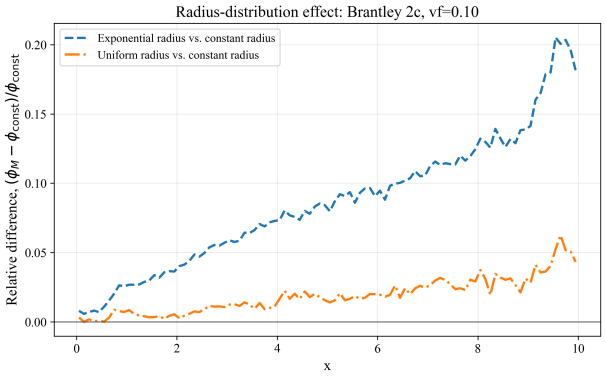


(b) $p_1 = 0.20$

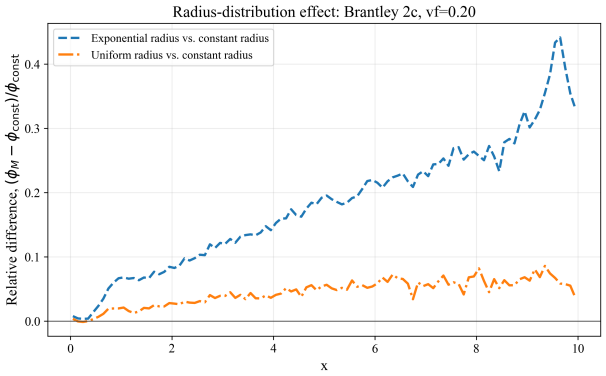


(c) $p_1 = 0.30$

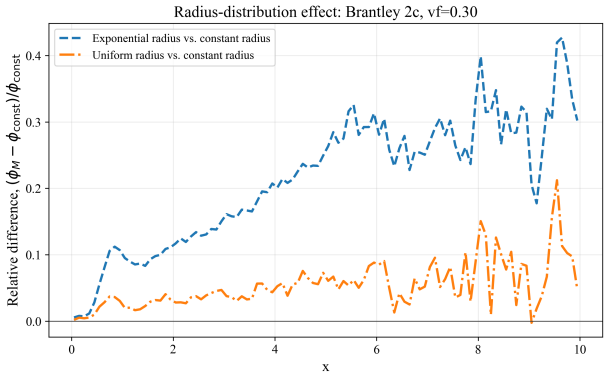
Figure 7.22: Effect of spherical inclusion radius distribution on the benchmark scalar flux for Case 2a. The radius-distribution effect remains relatively modest compared with the absorbing-inclusion and uniformly scattering cases.



(a) $p_1 = 0.10$



(b) $p_1 = 0.20$



(c) $p_1 = 0.30$

Figure 7.23: Effect of spherical inclusion radius distribution on the benchmark scalar flux for Case 2c. The uniformly scattering case shows that radius-distribution effects can remain significant when particles undergo many collisions before leakage or absorption.

7.5 Summary

This chapter extended the age-based renewal transport methods from Chapter 6 to 3D stochastic media. The methods were adapted to sample material interfaces along 3D particle trajectories and were tested against PlaybookMC spherical inclusion benchmark calculations. The implementations were also checked in the Markovian limit against published 3D CLS and LRP leakage results, providing verification that the methods reproduce established results for Markovian media.

The treatment of interface memory at scattering events in 3D was investigated by comparing deterministic and probabilistic approaches to updating the memory. Both treatments were shown to have merit. The probabilistic treatment generally improved reflection accuracy, while the deterministic treatment was often more favorable for transmission. For consistency with previous 3D LRP implementations, the probabilistic treatment was used for the remainder of the chapter.

The 3D leakage and scalar-flux results showed the same broad accuracy ordering observed in Chapter 6. The Backscatter-Resample method and FLRP produced nearly identical results, while the Age-Decreasing method and LRP generally gave lower leakage RMSE values and improved scalar-flux accuracy. The 3D errors were generally smaller than the corresponding 1D errors, which is consistent with the reduced importance of direct backscatter memory in 3D. Since particles scatter into a continuum of directions, they are less likely to reverse along the same previously sampled path than in 1D planar geometry.

The explicit spherical inclusion benchmarks also showed that the sphere radius distribution can have a significant effect on the scalar flux. This effect was especially noticeable in cases with absorbing inclusions or highly scattering materials, where particles either strongly sample the absorbing inclusion structure or remain in the medium long enough for 3D geometric correlations to matter. This differs somewhat from the 1D renewal results, where increased scattering tended to reduce sensitivity to the mixing statistics. In 3D, changing the radius distribution changes not only the chord length distribution, but also the number of spheres and packing structure of the medium.

Chapter 8

Conclusions and Future Work

8.1 Conclusions

This dissertation developed and tested age-based particle transport methods for non-Markovian stochastic media with renewal statistics. The central motivation was that many physically relevant stochastic media cannot be accurately described by Markovian mixing statistics alone. In Markovian media, material chord lengths are exponentially distributed and the material label is sufficient to determine the probability of encountering the next material interface. In renewal statistical media, the chord length distributions can be non-exponential, so the probability of encountering a material interface depends on the distance already traveled through the current material. This additional geometric memory is the main difficulty addressed in this work.

The main contribution of this dissertation is the use of the age variable, defined as the distance from the previous material interface, to represent this memory. By augmenting the stochastic state with the age, the joint stochastic process becomes Markovian, allowing for the derivation of a generalized master equation for purely absorbing binary renewal media. In the purely absorbing case, particles stream monotonically until absorption or leakage, so the age variable contains the required geometric information. The resulting stochastic simulation model was shown to reproduce benchmark leakage values, scalar fluxes, and relative standard deviations of the flux for several renewal material distributions.

The age-based framework was then extended to include particle scattering in 1D planar geometry. Scattering introduces transport memory, which causes the model to be approximate because particles can reverse direction and move back toward previously sampled material. Specifically, the treatment of age at scattering events becomes approximate and multiple treatments for the age after scattering are possible. Several Monte Carlo methods with different treatments of the age were developed and compared, including the Backscatter Resample and Age Decreasing methods, and those were compared to the heuristic extension of prior Monte Carlo stochastic media methods FLRP and LRP. The results showed that methods retaining more local geometric memory generally improve accuracy relative to

methods that resample the renewal geometry after backscatter. In particular, Age Decreasing produced accuracy comparable to LRP while retaining a simpler memory structure.

The methods were also extended to 3D spherical inclusion geometries. This extension required adapting interface sampling to full 3D particle trajectories and investigating how interface memory should be updated at scattering events in 3D. In 1D, the treatment of geometric memory after scattering is straightforward because material interfaces are defined only along the x direction. When the particle direction cosine changes sign, the particle begins moving back toward a previously sampled material interface, so the age variable or stored interface distances can be updated consistently with that reversal. In 3D, however, scattering generally places the particle on a new ray through the medium. A scalar age variable or limited LRP interface memory does not fully describe the surrounding 3D interface geometry, so any memory update after scattering is necessarily approximate unless the local realization is explicitly resolved. Both deterministic and probabilistic geometric-memory update treatments were investigated and shown to have merit. The probabilistic treatment was used as the default 3D convention because of its consistency with previous 3D LRP implementations.

The 3D results showed that the overall method hierarchy remained similar to the 1D results. Backscatter Resample and FLRP produced nearly identical leakage values, while Age Decreasing and LRP generally gave lower leakage RMSE values and improved scalar flux accuracy. The 3D errors were generally smaller than the corresponding 1D errors, which is consistent with the reduced importance of direct backscatter memory in 3D. Since particles scatter into a continuum of directions, they are less likely to reverse along the same previously sampled path than in 1D planar geometry.

The explicit spherical inclusion benchmarks also showed that the sphere radius distribution can affect scalar flux and leakage values. This effect is not fully captured by mean chord length alone. In 3D, changing the radius distribution changes the chord length distribution in the inclusion material, the number of spheres, packing structure, and spatial correlations of the inclusion field. This was especially apparent in cases with absorbing inclusions or highly scattering materials, where particles either strongly sample the absorbing inclusion structure or remain in the medium long enough for geometric correlations to affect the accumulated transport history.

Overall, the results demonstrate that age-based renewal methods provide a useful framework for extending stochastic media transport beyond the Markovian assumption. The methods developed here preserve the prescribed chord length distributions more directly than previous heuristic adaptations of Markovian models while retaining much of the computational advantage of on-the-fly stochastic media Monte Carlo methods. The work also shows that accurate treatment of renewal statistics can be very important for accurately applying stochastic media models to real-world problems depending on material properties.

8.2 Future Work

Several directions remain open for future work. The most immediate next step would be to compare the 3D renewal methods developed in this dissertation with the LCLS methods of Donovan and Danon [19]. The renewal methods developed here represent both materials stochastically, while LCLS explicitly models transport through spherical inclusions while modeling the background with CLS. A direct comparison would help determine how much accuracy is gained by explicitly resolving the inclusion geometry and how much extra computational cost that incurs.

A similar investigation could be done with the background chord length distribution in 3D spherical inclusion geometries. The calculations in Chapter 7 approximate the background material with an exponential chord length distribution whose mean is determined from the inclusion volume fraction and the inclusion mean chord length. This approximation is reasonable for a lower sphere volume fraction, but it is not exact for non-overlapping spheres and becomes increasingly inaccurate with higher sphere volume fractions. Future work could measure empirical background chord length distributions directly from generated spherical inclusion geometries and use those measured distributions in the renewal statistical methods. This comparison could introduce even larger discrepancies between a Markovian approximation and the more accurate renewal approximation, and it could also show potentially larger differences between geometries with different radius distributions due to the different background material distributions.

The dimensional emulation approach of Ref. [21] could also be applied to the methods developed in this dissertation for transport in renewal media. Dimensional emulation was previously shown to reproduce 3D stochastic media results using modified 1D transport algorithms. Since the renewal methods developed here function similar to the classic Markovian models studied in Ref. [21], adapting them to function with dimensional emulation should be relatively straightforward.

Another natural extension is to solve the age-based transport equations deterministically. This dissertation focused on Monte Carlo implementations of the age-based methods, but the generalized master equation and the scattering extensions in Chapter 6 could be solved deterministically. An equivalent discrete ordinates solver would provide an independent verification of the Monte Carlo methods and could be useful for problems that are particularly inefficient for Monte Carlo methods due to their relative optical thickness. This could also allow for numerical studies on the asymptotic limits of the age-based transport models.

A related theoretical direction is to derive transport equations corresponding to the Age Decreasing method. In this dissertation, Age Decreasing was introduced as a Monte Carlo algorithm that retains memory of the previous interface after backscatter. The method performed well in both 1D and 3D, sometimes even outperforming LRP despite retaining less explicit interface information. However, it was developed heuristically without a direct transport equation interpretation. A corresponding equation may require an additional memory variable representing the distance to a previously sampled interface. Unlike the ordinary age variable, this memory variable would decrease as a particle moves back toward the re-

membered interface. Deriving such an equation would clarify the mathematical relationship between Age Decreasing, LRP, and the generalized master equation, and could provide a path toward deterministic solvers for memory improved renewal methods. Such an equation could be similar to those recently developed for Markovian media in Refs. [45, 46].

The methods could also be investigated within the context of fissile systems. The present work considered fixed-source, non-multiplying transport, but many advanced reactor applications involve stochastic arrangements of fuel, coolant, moderator, or absorber regions. Pebble bed reactors are a particularly relevant example because they contain multiple levels of stochastic structure: TRISO particles are randomly distributed within pebbles, and pebbles are randomly distributed within the core. Such an extension would make it possible to study how non-Markovian stochastic structure affects quantities such as k_{eff}, fission-source convergence, and flux distributions in randomly structured fissile systems.

The age-based methods should also be investigated for thermal radiative transfer and Implicit Monte Carlo. Recent work has already applied the stochastic media algorithms FLRP and LRP to 3D IMC calculations with Markovian and renewal material statistics [47]. The methods developed in this dissertation provide another possible way to incorporate renewal material statistics into IMC. Applying the Backscatter-Resample method, the Age-Decreasing method, or future age-based methods to IMC would test whether the improved behavior observed in linear transport carries over to thermal radiative transfer problems with material-energy coupling and effective scatter introduced by the Fleck factor [48, 49, 50, 51].

The largest open problem is the extension of stochastic media transport methods to turbulent media that are neither purely immiscible nor purely miscible. Most stochastic media methods assume immiscible mixtures, where each point in space is occupied by one material and particles encounter sharp interfaces. Many high-energy-density physics problems do not fit this assumption cleanly. In inertial confinement fusion experiments and simulations, for example, chunks of ablator material may act as optically thin inclusions in an optically thin background plasma, but the plasma itself also mixes together continuously through hydrodynamic instabilities. An example of the continuous mixture is shown in Figure 8.1.

Bridging the gap between immiscible and miscible stochastic media is likely one of the central future challenges in stochastic media transport. Immiscible stochastic media methods, including the renewal methods developed in this dissertation, are well suited to problems with identifiable material interfaces and chord length statistics. Miscible or partially mixed media may instead be better described by randomly varying volume fractions. A realistic HEDP mixing model likely requires both approaches to be accurate. Future work could therefore seek to develop accurate methods for continuous miscible media, and extend to hybrid stochastic media models that combine immiscible renewal statistics with continuous random volume fraction profiles. Developing a unified framework for stochastic media transport in this setting could greatly improve the accuracy of simulation of HEDP experiments.

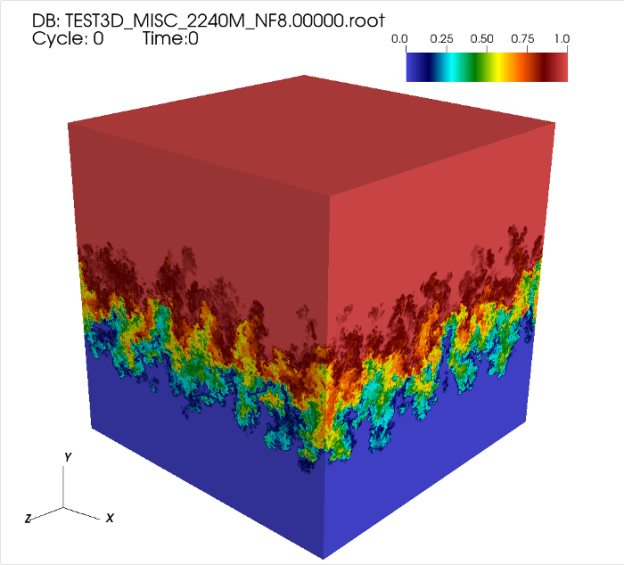


Figure 8.1: Example Rayleigh-Taylor mixing problem with miscible materials from Ref. [20].

Bibliography

[1] T. Byvank, S. X. Coffing, D. A. Lioce, et al. "Design of Experiments to Spectroscopically Characterize Radiation Flow in Stochastic Media". In: *Physics of Plasmas* 31.4 (2024), p. 042702. DOI: https://doi.org/10.1063/5.0198139.

[2] K. P. Driver et al. "Radiation-Mix Interaction at a Hydrodynamically Evolving Interface". In: *Bulletin of the American Physical Society, 65th Annual Meeting of the APS Division of Plasma Physics*. American Physical Society. Denver, CO, Oct. 2023. URL: https://meetings.aps.org/Meeting/DPP23/Session/AP01.29.

[3] A. B. Kostinski. "On the Extinction of Radiation by a Homogeneous but Spatially Correlated Random Medium". In: *Journal of the Optical Society of America A* 18.8 (2001), pp. 1929–1933. DOI: https://doi.org/10.1364/JOSAA.18.001929.

[4] C. Larmier et al. "Monte Carlo particle transport in random media: The effects of mixing statistics". In: *Journal of Quantitative Spectroscopy and Radiative Transfer* 196 (2017), pp. 270–286. DOI: https://doi.org/10.1016/j.jqsrt.2017.04.006.

[5] G. L. Olson et al. "Chord Length Distributions in Binary Stochastic Media in Two and Three Dimensions". In: *Journal of Quantitative Spectroscopy and Radiative Transfer* 101 (2006), pp. 269–283. DOI: https://doi.org/10.1016/j.jqsrt.2005.11.070.

[6] E. H. Vu and A. J. Olson. "Conditional Point Sampling: A stochastic media transport algorithm with full geometric sampling memory". In: *Journal of Quantitative Spectroscopy and Radiative Transfer* 272 (2021), p. 107767. DOI: https://doi.org/10.1016/j.jqsrt.2021.107767.

[7] C. D. Levermore et al. "Linear transport theory in a random medium". In: *Journal of Mathematical Physics* 27.10 (1986), pp. 2526–2536. DOI: https://doi.org/10.1063/1.527320.

[8] G. C. Pomraning. *Linear Kinetic Theory and Particle Transport in Stochastic Mixtures*. 1st ed. River Edge, NJ: World Scientific Publishing Co., 1991.

[9] M. L. Adams, E. W. Larsen, and G. C. Pomraning. "Benchmark Results for Particle Transport in a Binary Markov Statistical Medium". In: *Journal of Quantitative Spectroscopy and Radiative Transfer* 42.4 (1989), pp. 253–266. DOI: https://doi.org/10.1016/0022-4073(89)90072-1.

[10] P. S. Brantley. "A benchmark comparison of Monte Carlo particle transport algorithms for binary stochastic mixtures". In: *Journal of Quantitative Spectroscopy and Radiative Transfer* 112.4 (2011), pp. 599–618. DOI: https://doi.org/10.1016/j.jqsrt.2010.06.007.

[11] B. Su and G. C. Pomraning. "Benchmark results for particle transport in binary non-markovian mixtures". In: *Journal of Quantitative Spectroscopy and Radiative Transfer* 50 (1993), pp. 211–226. DOI: https://doi.org/10.1016/0022-4073(93)90119-3.

[12] O. Zuchuat et al. "Transport in renewal statistical media: Benchmarking and comparison with models". In: *Journal of Quantitative Spectroscopy and Radiative Transfer* 51 (1994), pp. 689–722. DOI: https://doi.org/10.1016/0022-4073(94)90125-2.

[13] C. Larmier et al. "Benchmark solutions for transport in d-dimensional Markov binary mixtures". In: *Journal of Quantitative Spectroscopy and Radiative Transfer* 189 (2017), pp. 133–148. DOI: https://doi.org/10.1016/j.jqsrt.2016.11.015.

[14] D. Vanderhaegen. "Radiative transfer in statistically heterogeneous mixtures". In: *Journal of Quantitative Spectroscopy and Radiative Transfer* 36.6 (1986), pp. 557–561. DOI: https://doi.org/10.1016/0022-4073(86)90128-7.

[15] G. B. Zimmerman and M. L. Adams. "Algorithms for Monte-Carlo particle transport in binary statistical mixtures". In: *Transactions of the American Nuclear Society* 63 (1991), p. 287.

[16] C. Larmier et al. "Monte Carlo Chord Length Sampling for d-dimensional Markov binary mixtures". In: *Journal of Quantitative Spectroscopy and Radiative Transfer* 204 (2018), pp. 256–271. DOI: https://doi.org/10.1016/j.jqsrt.2017.09.014.

[17] D. C. Sahni. "Equivalence of generic equation method and the phenomenological model for linear transport problems in a two-state random scattering medium". In: *Journal of Mathematical Physics* 30.7 (1989), pp. 1554–1559. DOI: https://doi.org/10.1063/1.528288.

[18] P. S. Brantley and G. B. Zimmerman. "Benchmark comparison of Monte Carlo algorithms for three-dimensional binary stochastic media". In: *Transactions of the American Nuclear Society* 117 (2017), pp. 765–768.

[19] T. J. Donovan and Y. Danon. "Application of Monte Carlo chord-length sampling algorithms to transport through a two-dimensional binary stochastic mixture". In: *Nuclear Science and Engineering* 143.3 (2003), pp. 226–239. DOI: https://doi.org/10.13182/NSE03-A2332.

[20] B. E. Morgan. *Thermal Radiative Transport Through Turbulent Media*. Presentation. LLNL-PRES-2004484. 2025.

[21] D. Lioce, A. J. Olson, and A. K. Prinja. "Emulation of Radiation Transport in 3D Stochastic Media Using 1D Planar Monte Carlo Stochastic Media Radiation Transport Algorithms". In: *Journal of Quantitative Spectroscopy and Radiative Transfer* 345 (2025), p. 109507. DOI: https://doi.org/10.1016/j.jqsrt.2025.109507.

[22] A. Oung. *What's So Hot About TRISO?* Elemental. Oct. 17, 2024. URL: https://elementalenergy.substack.com/p/whats-so-hot-about-triso (visited on 06/03/2026).

[23] A. Dudás et al. "Wear Behaviour of Ceramic Particle Reinforced Atmospheric Plasma Spray Coatings on the Cylinder Running Surface of Internal Combustion Engines". In: *Wear* 502–503 (2022), p. 204373. DOI: https://doi.org/10.1016/j.wear.2022.204373.

[24] R. Durrett. *Essentials of Stochastic Processes*. 1st ed. New York: Springer, 1999.

[25] J. F. Lawless. *Statistical Models and Methods for Lifetime Data*. 2nd ed. Hoboken, NJ: John Wiley & Sons, 2003.

[26] A. K. Prinja and D. A. Lioce. "Generalized Master Equation for Particle Transport in Binary Random Media with Renewal Statistics". In: *Physical Review E* 113 (2026), p. 044111. DOI: https://doi.org/10.1103/r23t-h3lv.

[27] D. A. Lioce, P. S. Brantley, and A. K. Prinja. "Monte Carlo Particle Transport in Renewal Statistical Media". Manuscript submitted to Journal of Quantitative Spectroscopy and Radiative Transfer. Apr. 2026.

[28] N. G. van Kampen. *Stochastic Processes in Physics and Chemistry*. 3rd ed. Amsterdam: North-Holland, 2007.

[29] S. M. Ross. *Introduction to Probability Models*. 10th ed. Burlington, MA: Academic Press, 2010.

[30] D. R. Cox. "The Analysis of Non-Markovian Stochastic Processes by the Inclusion of Supplementary Variables". In: *Mathematical Proceedings of the Cambridge Philosophical Society* 51.3 (1955), pp. 433–441. DOI: https://doi.org/10.1017/S0305004100030437.

[31] E. E. Lewis and W. F. Miller Jr. *Computational Methods of Neutron Transport*. 2nd ed. La Grange Park, IL: American Nuclear Society, 1993.

[32] A. K. Prinja and E. W. Larsen. "General Principles of Neutron Transport". In: *Handbook of Nuclear Engineering*. Ed. by D. G. Cacuci. New York, NY: Springer, 2010, pp. 427–542. DOI: https://doi.org/10.1007/978-0-387-98149-9_5.

[33] C. D. Levermore, J. Wong, and G. C. Pomraning. "Renewal theory for transport processes in binary statistical mixtures". In: *Journal of Mathematical Physics* 29.4 (1988), pp. 995–1004. DOI: https://doi.org/10.1063/1.527997.

[34] B. Su and G. C. Pomraning. "Modification to a Previous Higher Order Model for Particle Transport in Binary Stochastic Media". In: *Journal of Quantitative Spectroscopy and Radiative Transfer* 54.5 (1995), pp. 779–801. DOI: https://doi.org/10.1016/0022-4073(95)00110-7.

[35] C. W. Gardiner. *Handbook of Stochastic Methods: for Physics, Chemistry and the Natural Sciences*. 3rd ed. Springer Series in Synergetics. Heidelberg: Springer, 2004.

[36] D. R. Cox and H. D. Miller. *The Theory of Stochastic Processes*. London: Methuen, 1965.

[37] G. C. Pomraning. "Statistics, renewal theory, and particle transport". In: *Journal of Quantitative Spectroscopy and Radiative Transfer* 42.4 (1989), pp. 279–293. DOI: https://doi.org/10.1016/0022-4073(89)90074-5.

[38] E. W. Larsen and R. Vasques. "A generalized linear Boltzmann equation for non-classical particle transport". In: *Journal of Quantitative Spectroscopy and Radiative Transfer* 112.4 (2011), pp. 619–631. DOI: https://doi.org/10.1016/j.jqsrt.2010.07.003.

[39] D. Vanderhaegen. "Impact of a Mixing Structure on Radiative Transfer in Random Media". In: *Journal of Quantitative Spectroscopy and Radiative Transfer* 39.4 (1988), pp. 337–337. DOI: https://doi.org/10.1016/0022-4073(88)90009-X.

[40] G. C. Pomraning. "Renewal analysis for higher moments in stochastic transport". In: *Journal of Quantitative Spectroscopy and Radiative Transfer* 57.3 (1997), pp. 295–307. DOI: https://doi.org/10.1016/S0022-4073(96)00137-9.

[41] D. A. Lioce, P. S. Brantley, and A. K. Prinja. "Monte Carlo Particle Transport in Renewal Statistical Media". In: *Proceedings of the International Conference on Mathematics and Computational Methods Applied to Nuclear Science and Engineering (M&C 2025)*. American Nuclear Society. Denver, CO, Apr. 2025, pp. 2070–2080. DOI: https://doi.org/10.13182/xyz-47194.

[42] A. J. Olson and B. C. Franke. "An optimal-cost Monte Carlo approach to stochastic media transport calculations". In: *Transactions of the American Nuclear Society* 118 (2018), pp. 390–393.

[43] Sandia National Laboratories. *PlaybookMC*. Software repository. 2023. URL: https://github.com/sandialabs/PlaybookMC.

[44] P. S. Brantley. "Benchmark Investigation of a 3D Monte Carlo Levermore-Pomraning Algorithm for Binary Stochastic Media". In: *Transactions of the American Nuclear Society* 111 (2014), pp. 655–658.

[45] G. Samba et al. "Evaluation of Memory-Preserving Models for Particle Transport in Random Media". In: *EPJ Web of Conferences* 302 (2024), p. 08001. DOI: https://doi.org/10.1051/epjconf/202430208001.

[46] A. Tentori, G. Samba, and A. Zoia. "Generalized Levermore–Pomraning Equations with Memory Effects". In: *Annals of Nuclear Energy* 214 (2025), p. 111202. DOI: https://doi.org/10.1016/j.anucene.2025.111202.

[47] P. S. Brantley and V. N. Novellino. "Implicit Monte Carlo Thermal Radiative Transfer for Three-Dimensional Binary Stochastic Media: Markovian and Renewal Material Statistics". In: *Proceedings of the International Conference on Mathematics and Computational Methods Applied to Nuclear Science and Engineering (M&C 2025)*. Denver, Colorado, Apr. 2025, pp. 2060–2069. DOI: https://doi.org/10.13182/MC25-47123.

[48] J. A. Fleck and J. D. Cummings. "An Implicit Monte Carlo Scheme for Calculating Time and Frequency Dependent Nonlinear Radiation Transport". In: *Journal of Computational Physics* 8.3 (1971), pp. 313–342. DOI: https://doi.org/10.1016/0021-9991(71)90015-5.

[49] A. B. Wollaber. "Four Decades of Implicit Monte Carlo". In: *Journal of Computational and Theoretical Transport* 45.1–2 (2016), pp. 1–70. DOI: https://doi.org/10.1080/23324309.2016.1138132.

[50] D. S. Miller, F. Graziani, and G. Rodrigue. "Benchmarks and models for time-dependent grey radiation transport with material temperature in binary stochastic media". In: *Journal of Quantitative Spectroscopy and Radiative Transfer* 70.2 (2001), pp. 115–128. DOI: https://doi.org/10.1016/S0022-4073(00)00128-X.

[51] P. S. Brantley, N. A. Gentile, and G. B. Zimmerman. "Beyond Levermore-Pomraning for Implicit Monte Carlo Radiative Transfer in Binary Stochastic Media". In: *Proceedings of the International Conference on Mathematics and Computational Methods Applied to Nuclear Science and Engineering (M&C 2017)*. Jeju, South Korea, Apr. 2017.